THE UNIVERSITY of ADELAIDE

Post-breakup Evolution of the Ceduna Sub-basin and understanding of processes that occur on Rifted Continental Margins

Monica Jimenez Lloreda

ORCID iD: 0000-003-0704-1094

Discipline of Earth Sciences
School of Physics, Chemistry and Earth Sciences
Faculty of Science Engineering and Technology
University of Adelaide

Thesis submitted in fulfilment of the requirements for the degree of Doctor of Philosophy

April 2023

Table of content

List of publications

Conference publications

Jimenez, M., Holford, S., King, R., Bunch, M., 2021. Controls on gravity-driven normal fault geometry and growth in stacked deltaic settings: a case study from the Ceduna Sub-basin. APPEA 61.

Conference abstracts

Jimenez, M., Holford, S., King, R., Bunch, M., n.d. How do detachment properties influence the kinematics of normal growth faults? Insights from 3D seismic reflection data from the Ceduna sub-basin. AEGC Conf. 2021.

Abstract

Understanding the characteristics and evolution of normal growth faults has proved critical for interpreting the geological development of delta systems and the petroleum system of sedimentary basins within passive margins. In general. normal faults control the distribution of sedimentary deposits, the stratigraphic architecture and can provide migration pathways or traps for fluids (e.g. water and hydrocarbons). The interpretation of 3D seismic surveys has permitted a better understanding of fault evolution and control the migration of fluids. However, there are still knowledge gaps regarding the variability of normal growth faults geometrical features (length, strike, dip angle and displacement), fault evolution, changes in the distribution of sediments near the fault planes, and variation in the risk of fault reactivation and their control on magma flow.

This thesis consists of four chapters that detail the structural complexity of normal growth faults in the Ceduna Sub-basin (Great Australian Bight Basin) and provide a detailed interpretation of the Ceduna 3D MSS seismic survey, an analysis and discussion of the normal growth fault complexity in terms of fault evolution, potential risk of reactivation, and influence the transport of magma. The seismic interpretation used in this study permitted a detail characterization of 530 normal growth fault segments in terms of displaced sedimentary sequences, length, dip angle, strike, and changes in displacement along the fault plane. This study classifies these faults segments in the Ceduna Sub-basin in three different fault groups related to the displaced sequences and includes three different analyses: (1) Fault kinematic analyses to assess three different evolution styles that include constant growth and reactivation by either dip-linkage or reactivation during the deposition of upper sequences. (2) Assessment of risk of fault reactivation using the *fault analysis seal technology* to demonstrate that areas of the fault with steep dip angles and oblique strikes from the current maximum horizontal stress are at higher risk of reactivation. (3) Interpretation and statistical lineal alignment prediction to demonstrate the substantial control that normal growth faults have on the geometry and emplacement of eruptive centres magma, flow regions and intrusions.

This is the first study in the Ceduna Sub-basin to include a 3D seismic data that extends 12, 030 km^2 to understand the variation in geometrical characteristics and the variability in the fault evolution of normal growth faults, exposing differences in their evolution styles and the importance of the detachment in the fault displacement configuration in delta systems. It established the importance of the changes in the fault roughness in the prediction of fault reactivation where regions of the faults with steeper dip angles and oblique strike orientations are at higher risk of fault reactivation. It also demonstrates that normal growth faults strongly influence the transport and emplacement of magma by stablishing a preferential northwest-southeast alignment between igneous bodies and the fault strike orientations.

Declaration

I certify that this work contains no material which has been accepted for the award of any other degree or diploma in my name, in any university or other tertiary institution and, to the best of my knowledge and belief, contains no material previously published or written by another person, except where due reference has been made in the text. In addition, I certify that no part of this work will, in the future, be used in a submission in my name, for any other degree or diploma in any university or other tertiary institution without the prior approval of the University of Adelaide and where applicable, any partner institution responsible for the joint award of this degree.

The author acknowledges that copyright of published works contained within the thesis resides with the copyright holder(s) of those works.

I give permission for the digital version of my thesis to be made available on the web, via the University's digital research repository, the Library Search and also through web search engines, unless permission has been granted by the University to restrict access for a period of time.

I acknowledge the support I have received for my research through the provision of an Australian Government Research Training Program Scholarship.

28 /04 /2023

Monica Jimenez Lloreda Date

Acknowledgements

To my wonderful supervisors Simon Holford, Rosalind King and Mark Bunch, thank you so much for all your support, dedication, patience and guidance. It was a privilege to work and learn from you during my PhD.

I would like to thank the Australian Society of Exploration Geophysicists (ASEG) for the extra scholarship support towards my research, which allowed me to participate in conferences and upgrade my research equipment. I would also like to thank the Petroleum Exploration Society of Australia (PESA), Department of Energy and Mining, and Cooper Energy for the 2021 "Best South Australian Focussed Petroleum Geoscience Research project" award and the Institute for Sustainability, Energy and Resources (IMER) for the additional award to this extended abstract. I would also like to thank Ray Adams from *Semiota* for the editorial advice concerning grammar and spelling in the introduction and Chapter 4 sections of this thesis.

A special thank you to Alan for making me an honorary friend of the TES group. Thanks for your support and for letting me to use one of your research offices during my last two years of PhD.

Georgie (a.k.a Easy G beat diamond), Darwin (a.k.a Diggy scratch), and Jarred (a.k.a Jezaaaa), you are the best office team ever! I enjoyed every minute. Thanks for your help, for sharing innumerable snacks and long chats. Morgan, Zara, Alex, Alex, Priya, Jess, thanks for all your support with everything, the chocolate bars, coffee times, lunch plans over the river and your generous friendship. You made my PhD days so much fun. To Tayallen, Shuyan and Yazan for your friendship and good energy during my days in ASPER.

To my parents for all your support during my PhD. Thanks for always believing in me and teaching me that I can dream big. Merich, thanks for being there always. You are my favourite person in the world, and you know I couldn't have done this if you weren't there for me during these four years.

Introduction

Introduction, literature review and thesis outline

Thesis framework

Previous studies in delta systems have shown the importance of normal growth faults in determining both their structure and stratigraphic framework by influencing the geometry of depositional systems and the changes in thickness and distribution of sedimentary sequences *(Gawthorpe and Leeder, 2000; Morley, 2003; Wood, 2012)*. Normal growth faults also control several elements in the petroleum system such as the migration and trapping of fluids and the distribution of seal, source and reservoir rocks within sedimentary basins *(Weber et al., 1978; Hooper, 1991; Caine et al., 1996; Hallett, 2002; Rudolph and Goulding, 2017; Woillez et al., 2017).* From preliminary studies, it can be assumed that variation in the structural characteristics along the fault plane, changes in normal growth fault evolution, and potential events of fault reactivation would have direct implications for the development of delta systems and hydrocarbon exploration.

Previous studies have demonstrated similarities between the Great Australian Bight Basin and other basins that also contain delta systems *(MacDonald et al., 2010)* such as the Gulf of Mexico, Niger Delta, Baram Delta, Amazon fan, Nile Delta, and Sinai Delta. Studies in these delta systems have adanced the understanding of fault evolution *(Schneider et al., 2000; Cobbold et al., 2004; Selim and Omran, 2012; Jackson and Rotevatn, 2013; Jackson et al., 2017),* gravitational extension and structural characteristics of delta systems *(Cohen and McClay, 1996; Morley and Guerin, 1996; Rowan et al., 1999; King et al., 2010)*, and the implications of fault segments in fluid migration (Chapman, 1985; Finkbeiner et al., 2001; Selim and Omran, 2012). However, there are still many questions related to the normal growth fault evolution, risk of fault reactivation due to current stress fields, and the influence of normal growth faults on the transport and emplacement of magma in delta systems within passive margins.

The Ceduna Sub-basin in the Great Australian Bight provides an excellent natural laboratory to study the characteristics, evolution style, and influence of normal faults in stacked deltaic settings containing multiple detachment horizons (The Blue Whale and Tiger supersequences). Recent studies in the Ceduna Sub-basin have analysed the evolution of normal growth faults in the delta top of the Ceduna delta system, providing a starting point in understanding the complexity in the development of structural traps for hydrocarbons (MacDonald et al., 2010; Robson, 2017; Ryan et al., 2017a). Other studies have analysed the impact of the current stress fields on normal growth faults in the Southern Australian margin, suggesting potential reactivation of steep faults that can result in the failure of *seals (Reynolds et al., 2003; Macdonald et al., 2012)*. In recent years authors have also identified post-rift magmatism in the Ceduna Sub-basin associated with the Bight Basin Igneous Complex (BBIC) in the northeast part of the study area. They describe different morphologies for the intrusions and shield volcanic cones contained in a non-volcanic passive margin *(Schofield et al., 2008; Holford et al., 2012, 2017; Jackson et al., 2013; Magee et al., 2013; Robson et al., 2017; Reynolds et al., 2017, 2018)*.

This study is of great importance in the analysis of how the geometrical and structural characteristics (e.g. dip angle, strike, and displacement) of normal growth faults vary along strike and describe their changes in evolution style, potential risk of fault reactivation, and their influence in the transport of magma. It also defines how the changes in the local features of the underlying detachment layer and the fluctuations in the accumulation rate impact the structural configuration with respect to fault displacement and syn-kinematic thickness at the delta top. In terms of the Ceduna Sub-basin, this thesis is the first study that used an extended 3D seismic survey (12,030km^2) to understand in detail

the structural development of normal growth faults including the complexity of their evolution style that includes periods of continuous growth and dip-linkage events. This thesis is also the first in using statistical analysis to define the reactivation potential of normal growth faults and how the variance in fault roughness along the fault plane impact the likelihood of fault reactivation. It is also the first study to demonstrate how normal growth faults influence the magma flow direction and the geometry of extrusions in a non-volcanic passive margin like the Great Australian Bight Basin.

This thesis aims to study in detail normal growth faults that have developed in the delta top of the Ceduna delta system in particular the structural features (geometry, strike, dip, angle and displacement), fault evolution style, fault reactivation potential and the influence of faults on the emplacement and transport of magma. This study includes different techniques such as (1) Interpretation of the Ceduna 3D MSS to interpret a total of 530 fault segments and 11 horizons; (2) Kinematic analyses to graph changes in the evolution style of these normal growth fault segments and define the implications of events such as growth, dip-linkage and reactivation for the petroleum system of sedimentary basins such as the Ceduna Sub-basin. (3) The *fault analysis seal technology* (FAST technique) was used to incorporate several geomechanical parameters from well data and fault roughness features. This technique allows the recognition of the likelihood of a fault to reactivate in terms of the pore pressure needed for the fault to intersect the Mohr-Coulomb envelop within the Mohr circle. This thesis also included the interpretation of magmatic igneous bodies (e.g. intrusions, lava flow regions, eruptive centres and fissures) using the Ceduna 3DMSS seismic survey, which were classified in terms of morphology and structural characteristics (e.g. dip angle, geometry, orientation, etc.). It also incorporates (4) a statistical alignment method to define any potential influence of the strike of normal growth faults in the emplacement and transport of magma from the source points in the intrusions, the geometry and formation of eruptive centres and the lava flow direction.

Literature Review

Location of the study area

The Great Australian Bight Basin extends for 250,000 km^2 along the southern Australian margin and developed between the Middle Jurassic and the Late Santonian ages (Totterdell and Krassay, 2003; Totterdell and Mitchell, 2009; Hughes et al., 2009). It is located between water depths of 0.2 km to 4.0 km and limited at the south by the oceanic crust of the South Australian Abyssal Plain, to the northeast by the Gawler Craton Proterozoic basement, and to the east by the Otway Basin (Totterdell et al., 2000; Hughes et al., 2009)

Structural development of delta systems

Delta systems commonly (but non-exclusively) form in passive margins over gently basinwards-dipping surfaces that mimic classic critical taper wedge models (McClay et al., 2003; Morley, 2003; King and Morley, 2017) and constrain thin-skinned delta systems composed by an extensional region at the delta top and a compressional region at the delta toe (McClay et al., 1998; Morley, 2003a). Delta systems develop when the differential loading in the delta top generates a pressure gradient causing the basinwards displacement of the mobile detachment layer and gravity sliding of the sedimentary sequences due to internal deformation. In the delta toe, the mobile detachment accumulates, creating a great amount of compression stress resulting in the development of Deepwater Fold Thrust Belts *(McClay, 1990; McClay et al., 1998; Morley et al., 2008; King and Backé, 2010).* They are controlled by the large-scale dynamics between tectonics and sedimentation and can vary in geometry and displacement due to the thickness and viscosity of the basal detachment. The delta systems can also contain detachment layers composed by either salt or an overpressured shale layer that works as an incompetent layer which increases the basinwards propagation of deformation *(McClay, 1990; Sapin et al., 2012).*

In terms of the extensional region of delta systems, there are several examples worldwide of modern continental passive margins with synthetic and antithetic normal growth faults that have been interpreted using field work, analogue models and seismic data. Some examples are the northwest (Cohen and McClay, 1996a) and the offshore *(Wiener et al., 2011)* of the Niger Delta; the Province of Brunei Darussalam at the northwest Borneo *(Morley et al., 2008)*; the Hammerhead Delta system (R. King and Backé, 2010; MacDonald et al., 2010) and White Pointer Delta system in the Great Australian Bight (Espurt et al., 2009a; MacDonald et al., 2010), the Amazon fan *(Cobbold et al., 2004)*; the Sinai Delta *(Selim and Omran, 2012)* and the Nile Delta *(Schneider et al., 2000).*

Some authors such as *Weber et al., (1978); Crevello et al., (1997); Alzaga-Ruiz et al., (2009); Sapin et al., (2012)* have proved that delta systems such as the Gulf of Mexico, offshore region of the Niger Delta and Burnei contain excellent petroleum systems with continuing hydrocarbon production. For instance, studies and exploration reports from delta systems such as the Niger Delta *(Jev et al., 1993; Woillez et al., 2017)* and the Gulf of Mexico *(Hood et al., 2002)* have suggested that the normal growth faults in these delta systems can work as either traps against rollover geometries or migration paths for hydrocarbons due to the lateral communication between sandstones and the upwards migration of fluids through the fault plane. These deltas also contain multiple reservoirs from deltaic sequences with intercalated sandstones reservoirs and shales seals that work as caprock and lateral seals. Field and laboratory analyses have demonstrate that delta systems such as the Niger Delta system *(Weber*

et al., 1978) and the Gulf of Mexico *(Hood et al., 2002; Sager et al., 2004)* also display evidences of migration of hydrocarbons from relatively distant source rocks.

Ceduna Sub-basin

The Ceduna Sub-basin is limited to the south with the Recherche Sub-basin, in the west with the Denmark, Bremer and Eyre Sub-basins, in the north with the Madura Shelf, and in the east with the Otway Basin (Hughes et al., 2009). The Ceduna Sub-basin contains a 15.0 km thick sedimentary sequence, and it is characterised by two independent large-scale delta systems as defined by the stratigraphy, stratal geometry, and structural architecture. The Cenomanian White Pointer Delta System formed as a result of the rapid deposition of a large quantity of sediments deposited conformably above the Blue Whale, resulting in the overpressure of the underlying shales and the development of normal growth faults at the delta top *(Totterdell and Krassay, 2003; MacDonald et al., 2010).*

The Santonian-Maastrichtian Hammerhead Delta System formed when the Hammerhead Supersequence was deposited above the Tiger Supersequence; thus reactivating some of the Cenomanian faults from the White Pointer Delta System and also forming new normal growth faults that detached at the top of the Tiger Supersequence (J. Totterdell and Krassay, 2003). Preliminary studies indicated that the Hammerhead Delta System is a near-balance model where the up-dip extension region is linked to the down-dip compression region frozen in time (R. King and Backé, 2010).

Tectonostratigraphic framework of the Great Australian Bight Basin

The Australia and Antarctica rifted margin formed between the Middle Jurassic and the Late Santonian, and follows a northwest-southeast to north-northwest-south-southeast trend which involved the thinning of the lower crust and upper mantle and formed a triple junction between Australia, Antarctica and India *(Sayers et al., 2001; Hughes et al., 2009).* During this extensional period, the basement structures had a strong influence the structural development of the Southern Australian margin. For instance, the Ceduna Sub-basin underwent a northwest-southeast upper crustal extension, while the western Eyre Sub-basin and Recherche Sub-basin showed a northwest-southeast extension oblique to the east- west preliminary basement structures. In contrast, the Duntroon Sub-basin shows a northwest-southeast upper crustal extension which is highly oblique to the north-northwest-south-southeast edge trend in the Gawler Craton-forming echelon half grabens, while the half grabens in the Eyre and Northern Ceduna sub-basins formed due to the interaction between the northwest-southeast rifting and the east-west pre-existing basement structures (Espurt et al., 2009a; G.M Gibson et al., 2013). Unfortunately, the basement pre-existing structures can only be interpreted in the Eyre and Duntroon sub-basins where the sedimentary sequence is thinner in comparison to the thick Middle Jurassic and Eocene sequences in the Ceduna Sub-basin (G.M Gibson et al., 2013)

During the Middle and Late Jurassic periods, the syn-rift Sea Lion and Minke supersequences were respectively deposited and contain fluvial to lacustrine sandstones and shales. During the Late Jurassic and Late Cretaceous (Berriasian Age), the lacustrine to fluvial sandstones and shales from Southern Right Supersequence were deposited, followed by the Valanginian-Aptian age coastal plain sandstones and marginal marine shales from the Bronze Whaler Supersequence (Totterdell et al.,

2000, Hughes et al., 2009). Between the middle Albian and the Cenomanian, the rift continued in the lower crust and upper mantle, causing a global sea level rise. During this period of accelerated subsidence, the siltstones and shales from the Blue Whale Supersequence were deposited *(Totterdell et al., 2000; Sayers et al., 2001; Espurt et al., 2009; Hughes et al., 2009; Stromsoyen et al., 2019).*

The White Pointer Supersequence was deposited conformably above the Blue Whale during the Cenomanian and it is composed by fluvial to deltaic clastic sediments and minor intercalated coal and marine siltstone and mudstone layers, which represent a tidal dominated depositional environment and large shoreface bars basinwards of the coastal plain *(Totterdell et al., 2000; Totterdell and Mitchell, 2009; Stromsoyen et al., 2019)*. Preliminary studies have shown evidence of sediment reworking due to fluvial channels at the nearshore area to shallow marine facies at the lower interval and more deltaic facies at the upper levels *(Tredrea and Horton, 2019).* In the Ceduna Sub-basin, the progradation of 5.0 km of White Pointer deltaic sediments occurred over 6 Ma towards the southwest, resulting in gravity sliding; forming the Mulgara fault system with principal strike orientations towards the northwest-southeast and dipping to the southwest (Espurt et al., 2009a). This fault system corresponds to listric faults that dip basinwards, strike northwest-southeast, and have displaced the Cenomanian-Late Santonian sedimentary sequence between 1.5 and 2.5 km *(Totterdell et al., 2000; Totterdell and Krassay, 2003).* The normal fault growth displacement is considered to be purely gravity controlled, and thus unrelated to regional or local tectonism *(McClay et al., 1998; King and Backé, 2010).* The ductile thinning of the lower crust and the formation of pinch-and-swell features probably increased the sliding gradients, triggering growth faulting and deformation of the sediments *(Totterdell et al., 2000).*

During the Turonian, the last extension period to have occurred which led to the breakup of the outer part of the Australia-Antarctica margin resulted in the formation of a basement ridge at the edge of the continental-oceanic transition zone and the formation of a magnetic anomaly *(Sayers et al., 2001).* In the Ceduna Sub-basin, the Tiger Supersequence was deposited between the Turonian and the Late Santonian during a major flooding event. This 2.8 km thick sequence of marine and marginal marine mudstones and progradational sandstones and shales demonstrate local evidence of meandering channel systems towards the southwest *(Totterdell et al., 2000; Totterdell and Krassay, 2003; Stromsoyen et al., 2019; Tredrea and Horton, 2019).* The upper interval corresponds to an aggradational sequence of finer grain shales and sandstones that can be considered more stable due to the development of a linear basinwards shoreface (Stromsoyen et al., 2019). The top of the Tiger Supersequence represents an unconformity that marks where the continental breakup occurred and the passive margin started (83Ma) (Espurt et al., 2009a; Holford et al., 2011)

The Hammerhead Supersequence was deposited unconformably above the Tiger Supersequence between the Late Santonian and Maastrichtian. It is composed of amalgamated sandstones, interbedded sandstones and shales. The basal sequence of the Hammerhead Supersequence corresponds to progradational deposition towards the centre of the basin forming clinoforms during a period of sea level fall. The middle sequence of the Hammerhead Supersequence displays progradational sediments that thicken gradually towards the centre of the basin and locally shows mass transport facies. The upper sequence of the Hammerhead Supersequence is characterized by aggradational deposits that agrees with a decrease in the basinwards sedimentation rate and the change in the basin dynamics *(Totterdell et al., 2000; Totterdell and Krassay, 2003; Espurt et al., 2009; Stromsoyen et al., 2019; Tredrea and Horton, 2019).*

The Wobbegong Supersequence was unconformably deposited over the top of the Hammerhead Supersequence between the Paleocene and the early Eocene, during a period of very slow sea floor spreading *(Totterdell et al., 2000; Espurt et al., 2009)*. The Dugong Supersequence was deposited above the Wobbegong Supersequence and corresponds to coarse grained sandstones at the base and cool water carbonates at the top, forming a progradational to aggradational geometry (Espurt et al., 2009a). Preliminary studies also suggested structural, stratigraphic and thermo-chronological evidence for recurrent increments of compressional deformation and exhumation during this period that resulted in the inversion of pre-existent normal faults *(Holford et al., 2011).* Other authors have shown high levels of a Neogene-to-Holocene strike-slip to vertical stress in areas such as the Flinders Ranges and Mount Lofty Ranges *(Hillis and Reynolds, 2000).* Recent studies suggested a period of magmatism during the middle Eocene where igneous bodies such as eruptive centres and lava flow regions form at the base of the Wobbegong Supersequence and intrusions were emplaced at the top and middle sequences of the Hammerhead Supersequence *(Schofield and Totterdell, 2008; Hughes et al., 2009)*.

Hydrocarbon system

Preliminary studies used well data, and geochemical and biostratigraphy analyses that included fluid inclusion techniques, samples from drilled wells and natural canyons, grains with oil inclusion (GOI) method (J Totterdell and Mitchell, 2009), and seismic stratigraphy *(Stromsoyen et al., 2019; Tredrea and Horton, 2019)* to establish source, seal and reservoir sequences in the Great Australian Bight. The best quality source rocks are the Late Cenomanian to Turonian ages supersequences (Blue Whale, White Pointer and Tiger). These studies suggested that the best reservoirs in the Ceduna Sub-basin respond to the Cenomanian and Maastrichtian age supersequences (White Pointer, Tiger and Hammerhead) *(Espurt et al., 2009; Mitchell et al., 2009; Klauser-Baumgärtner et al., 2019)*. Some examples are the lower coastal plain sandstones and the deltaic sequences at the upper levels at the White Pointer, the progradational sandstones at the basal Tiger sequence, and the deltaic sandstones and sandy coastal barriers from the Hammerhead *(Tredrea and Horton, 2019).* They also display evidences of source rocks such as the Cenomanian (oil and gas) and Turonian (gas condensate) sequences and a hydrocarbon migration period between the Late Cretaceous (Campanian Age) and Pleistocene epochs, *(Totterdell et al., 2008; Kempton et al., 2019; Bourdet et al., 2020).*

Hydrocarbon exploration history

The exploration in the Southern Australian margin started in the 1960s with the acquisition of gravity and magnetic data after the oil and gas discoveries in the Gippsland Basin. Until the 1990s, twelve wells were drilled in the Great Australian Bight with few hydrocarbons in the Jerboa-1 well in the Eyre-Sub-basin and the Greenly-1 well in the Duntroon Sub-basin. In contrast, the Apollo-1, Borda-1, Columbia-1, Duntroon-1, Echidna-1, Eyre-1, Madura-1, Potoroo-1, Platypus-1 and Vivonne-1 wells unsuccessful results were attributed to inadequate structures, lack of reservoir and source rock, and poor hydrocarbon migration routes (Totterdell et al., 2000; Hughes et al., 2009). In the 2000s, 11 exploration licenses were allocated in the area, which resulted in the acquisition of 2D and 3D seismic data followed by dry wells (Tapley et al., 2005; Department for Energy and Mining, 2020). Additionally, proven evidences of well-preserved marine organic-rich rocks such as the Blue Whale and White Pointer supersequences and sequence stratigraphic analysis that illustrated three potential petroleum systems in the southern Australian margin resulted in the re-stimulation of exploration interest in the

Great Australian Bight Basin (Boreham et al., 2001; Struckmeyer et al., 2001; J. Totterdell and Krassay, 2003). In 2003, Gnarlyknots-1A was drilled through the Hammerhead Supersequence without evidence of hydrocarbons and did not achieve its main target in the White Pointer Supersequence (Tapley et al., 2005a; J Totterdell and Mitchell, 2009). From 2007 to 2012, several companies acquired exploration permits which have resulted in the acquisition of geological and geophysical studies including 3D seismic surveys such as the Ceduna 3D MSS (12,030 km^2), Nerites 3D seismic survey (21,488 km^2), and the Springboard 3D seismic survey (8,013 km^2). Recently, there have not been any additional drilling campaigns is the basin and the permits have been transferred between companies which have left some vacant acreages (Regional Geology of the Bight Basin, 2020)

Thesis outline

Chapter 1: Seismic interpretation of the structural and stratigraphic features of the Ceduna Sub-basin

In this chapter, we explain in detail the methodology we used to interpret the available data (2D seismic lines, well logs and the Ceduna 3DMSS seismic survey). We interpret the Ceduna 3DMSS seismic survey that extends over 12,030 km^2, six 2D seismic lines (W00FDW0003, W00FDW0010, W00FDW0027, W00FDW0027, W00FDW0083, W00FDW0092) and the well logs of the closest drilled wells, Potoroo-1 and Gknarlyknots-1A. We interpreted the four principal supersequence tops in the 2D seismic lines and the Ceduna 3D seismic survey and seven intra-sequence horizons that represent a correlation between the Gamma-Ray and Sonic well logs, changes in seismic amplitude and some relevant stratigraphic structures such as truncations and clinoforms. This correlation allowed us to divide the Hammerhead Supersequence into three sequences, the Tiger Supersequence into four sequences, and the White Pointer into two principal sequences. We also detail how we generated structural and thickness maps of the principal supersequences and detachment layers, respectively. This chapter acts as the starting point for the other chapters as it describes why we selected the specific fault segments we have analysed in each chapter and details the structural characteristics of the study area. Our results from the fault segments demonstrate that normal growth faults show a wide range of characteristics, such as listric to planar fault geometries, rollovers, antiforms and rotated hangingwall blocks, and indicate a broad range of strike orientations (predominance of northwest-southeast strikes, followed by west-east, north-south and a few segments with a northeast-southwest orientation). Most of the interpreted fault segments are synthetic faults with minor antithetic faults that offset the Late Santonian-Maastrichtian sequence and smaller-scale antithetic faults that displace the Cenomanian-Late Santonian sedimentary sequence.

Chapter 2: Kinematic analysis of normal growth faults and their implications in the progression of delta systems and hydrocarbon exploration using the Great Australian Bight Basin as a case study (paper 1)

This chapter uses the seismic interpretation from Chapter 2 and kinematic analyses approaches such as Displacement-Distance, Displacement-Depth and Expansion Index to understand how the normal growth faults evolved in the extensional domain of deltaic sequences in the Ceduna Sub-basin. The selected 20 fault segments are spread broadly across the study area and displaced either the Cenomanian-Late Santonian, Cenomanian-Maastrichtian, or Late Santonian-Maastrichtian sequences.

The results demonstrate that the faults that displace the Cenomanian-Late Santonian and Late Santonian-Maastrichtian sequences constantly grew without evidence of any reactivation events. In contrast, the Cenomanian-Maastrichtian fault segments evolution can be summarized in three different groups that correlate to their location on the delta top: (1) In the north of the study area (region closest to the continent), the fault segments evolve by constant growth; (2) in the centre of the study area, their evolution style includes two periods of dip-linkage at the top and base of the Tiger Supersequence, and; (3) in the southern region (most basinwards region), the fault evolution styles includes one period of dip-linkage at the top of the Tiger Supersequence and one reactivation event at the top of the Hammerhead Supersequence. In all the cases, the evolution of the Cenomanian-Maastrichtian fault segments correlate with the characteristics of the remaining Blue Whale detachment layer where a more consistent and active evacuation of the detachment correlates with non-interrupted fault growth, while a thicker and more complex detachment characteristics (such as changes in lithology, presence of interval structures such as dome-like geometries or thrust faults) has resulted in more complex evolution styles that include reactivation and dip-linkage events. This chapter also explains the implications that fault evolution has for the exploration of hydrocarbons where events of reactivation and dip-linkage can result in result in secondary or tertiary hydrocarbon migration periods.

Chapter 3: Geomechanical analysis of normal growth faults using the Ceduna Sub-basin as a case study (paper 2)

A geochemical study was conducted to define the risk of fault reactivation using the geomechanical parameters from drilled wells in the Ceduna Sub-basin and the stress magnitudes and orientation of the current stress field in the Southern Australian Margin. This chapter defines the methodology and results from the fault analysis seal technology (FAST technique) (S Mildren et al., 2005) which expresses the likelihood of reactivation in terms of the pore pressure needed to reactivate a fault segment using the Mohr circle within the Mohr-Coulomb envelop. This study includes eight different scenarios that use varying geomechanical properties such as two end members of angles of internal friction (one using the coefficient of friction for sandstones and the second using the coefficient of friction for the intercalation of sandstones and shales), two end members for the maximum horizontal stress orientations (well data from the Otway and Perth basins), and two end members for the three principal stress magnitudes (related to the total horizontal stress magnitude at the depth of the principal reservoirs). Using the previous interpretation of fault segments in Chapter 2, four listric and two planar normal growth faults were chosen in this analysis, where five segments have northwest-southeast strike orientation and one a west-east strike orientation. This chapter also includes statistical analysis to define the proportion of the fault and the specific areas along strike, that are at the highest risk of reactivation. The results were compared with the fault roughness characteristics (dip angle and strike) to define what specific structural parameters (in terms of strike and dip angle) mostly encourage the increase pore pressure which can result in the reactivation of fault segments. The results showed that regions along the fault plane with strike orientations that are oblique to the maximum horizontal stress field (10° to 15° away from the maximum horizontal stress orientation) combined with dip angles greater than 45° are at higher risk of reactivation. The analysis also addresses the implications that this risk of fault reactivation has on the exploration of hydrocarbons because the reactivation of normal fault segments can result in the failure of seals and thus, result in the migration of fluids (water and hydrocarbon).

Chapter 4: Structural controls on post-rift magmatism in the Ceduna Sub-basin, Great Australian Bight Basin

This study used the Ceduna 3D MSS seismic survey to map two volcanoes located at the base of the Wobbegong Supersequence and 10 intrusions within the Hammerhead Supersequence (Late Santonian-Maastrichtian sequence). Volcanoes A and B were classified as composite volcanoes within the shield volcanoes category *(Magee et al., 2013; de Silva and Lindsay, 2015).* They are composed of (i) a principal eruptive centre with sub-rounded geometries at the southwest and truncated bases at the northeast, minimum internal variations in seismic amplitude and steep flanks between 53° and 80° that resemble the geometrical characteristics of Mount Schank in South Australia (Government of South Australia, 2001). (ii) lava flow regions around both eruptive centres that flow largely towards the southwest and are truncated towards the northeast against Late Santonian-Maastrichtian fault segments; and (iii) a total of 43 associated minor eruptive centres distributed along the lava flow regions of both volcanoes. In terms of the intrusions, they were emplaced in the Hammerhead Supersequence and were classified using the information from preliminary studies in the Bight Basin Igneous Complex *(Reynolds et al., 2017)*: We identify five saucer-shaped intrusions that are characterised by high to moderate seismic amplitude (70 to 2070% higher than the host rock), circular geometries in map view and concave upwards lateral tips in cross section view. We also identify five compound intrusions with elongate bases in map view that simulate lateral lobes and concave upwards and downwards geometries in cross section view. The compound intrusions locate in shallower depths in comparison to the saucer-shaped intrusions and show high seismic amplitudes (200% to 2070% higher than the host rock). We generate maximum amplitude seismic attribute along the intrusions surfaces and located the deepest area (source point) in the intrusion and define potential flowing patterns. We also extract the "root mean square" (RMS) and *Automatic Gain Control (AGC)* seismic attributes along the fault planes of near normal growth faults without identifying evidence of magma transport along the fault planes.

To quantify the influence of the fault segments in the emplacement and transport of magma in the study area, we use a statistical alignment method (Hammer, 2009a) and demonstrate a northwest-southeast linear correlation between (1) the minor eruptive centres and (2) the source points with the strike orientation of the normal growth faults. Additionally, we demonstrate that the thinning character and the potential de-watered and/or de-gassed of the Tiger detachment layer underlying the Hammerhead Supersequence might result in the transport and emplacement of magma within the Hammerhead Supersequence sandstone and massive transport sequences.

References

Alzaga-Ruiz, H., Granjeon, D., Lopez, M., Seranne, M., Roure, F., 2009. Gravitational collapse and Neogene sediment transfer across the western margin of the Gulf of Mexico: Insights from numerical models. Tectonophysics 470, 21–41. https://doi.org/10.1016/j.tecto.2008.06.017

Bight Basin [WWW Document], 2020. URL https://energymining.sa.gov.au/petroleum/prospectivity/bight_basin

Boreham, C.J., Hope, J.M., Hartung-Kagi, B., 2001. Understanding source, dsitribution and oreservation of australian natural gas: A geochemical perspective. APPEA J. 41, 523. https://doi.org/10.1071/AJ00026

Bourdet, J., Kempton, R.H., Dyja-Person, V., Pironon, J., Gong, S., Ross, A.S., 2020. Constraining the timing and evolution of hydrocarbon migration in the Bight Basin. Mar. Pet. Geol. 114, 104193. https://doi.org/10.1016/j.marpetgeo.2019.104193

Caine, J.S., Evans, J.P., Forster, C.B., 1996. Fault zone architecture and permeability structure. Geology 24, 1025–1028.

Chapman, R.E., 1985. Chapter 10: Origin and migration of petroleum: Geological and geochemical aspects, in: Petroleum Geology, Developments in Petroleum Science. Queensland, Australia, pp. 209–230.

Cobbold, P.R., Mourgues, R., Boyd, K., 2004. Mechanism of thin-skinned detachment in the Amazon Fan: assessing the importance of fluid overpressure and hydrocarbon generation. Mar. Pet. Geol. 21, 1013–1025. https://doi.org/10.1016/j.marpetgeo.2004.05.003

Cohen, H.A., McClay, K., 1996. Sedimentation and shale tectonics of the northwestern Niger Delta front. Mar. Pet. Geol. 13, 313–328. https://doi.org/10.1016/0264-8172(95)00067-4

Crevello, P., Morley, C., Lambiase, J., Simmons, M., 1997. The interaction of tectonics and depositional systems on the stratigraphy of the active tertiary deltaic shelf margin of Brunei Darassalam. Presented at the Proceedings of thePetrleum systems of SE Asia and Australasia, Indonesian Peroleum Association, Indonesia. https://doi.org/10.29118/IPA.443.767.772

de Silva, S., Lindsay, J.M., 2015. Primary Volcanic Landforms, in: The Encyclopedia of Volcanoes. Elsevier, pp. 273–297. https://doi.org/10.1016/B978-0-12-385938-9.00015-8

Espurt, N., Callot, J.-P., Totterdell, J., Struckmeyer, H., Vially, R., 2009. Interactions between continental breakup dynamics and large-scale delta system evolution: Insights from the Cretaceous Ceduna delta system, Bight Basin, Southern Australian margin: CONTINENTAL BREAKUP AND DELTA SYSTEM. Tectonics 28. https://doi.org/10.1029/2009TC002447

Finkbeiner, T., Zoback, M., Flemings, P., Stump, B., 2001. Stress, pore pressure, and dynamically constrained hydrocarbon columns in the South Eugene Island 330 field, northern Gulf of Mexico. AAPG Bull. 85. https://doi.org/10.1306/8626CA55-173B-11D7-8645000102C1865D

Gawthorpe, R.L., Leeder, M.R., 2000. Tectono-sedimentary evolution of active extensional basins. Basin Res. 24.

Gibson, G.M., Totterdell, J., White, L.T., Mitchell, C.R., Stacey, A.R., Morse, M.P., Whitaker, A., 2013. Pre-existing basement structures and its influence on continental rifting and fracture development along Australian's southern rifted margin. J. Geol. Soc. Lond. 170, 365–377. https://doi.org/10.1144/jgs2012-040

Government of South Australia (Ed.), 2001. Volcanoes of the Mount Gambier area.

Hallett, D., 2002. PETROLEUM SYSTEMS, in: Petroleum Geology of Libya. Elsevier, pp. 355–416. https://doi.org/10.1016/B978-044450525-5/50010-X

Hammer, Ø., 2009. New statistical methods for detecting point alignments. Comput. Geosci. 35, 659–666. https://doi.org/10.1016/j.cageo.2008.03.012

Hillis, R.R., Reynolds, S.D., 2000. The Australian Stress Map. J. Geol. Soc. Lond. 157, 915–921.

Holford, S., Hillis, R., Duddy, I., Green, P., Stoker, M., Tuitt, A., Backé, G., Tassone, D., MacDonald, J., 2011. Cenozoic post-breakup compressional deformation and exhumation of the southern Australian margin. APPEA J. 51, 613. https://doi.org/10.1071/AJ10044

Holford, S., Schofield, N., MacDonald, J., Duddy, I., Green, P., 2012. Seismic analysis of igneous systems in sedimentary basins and their impacts on hydrocarbon prospectivity: examples from the southern Australian margin. APPEA J. 52, 229. https://doi.org/10.1071/AJ11017

Holford, S.P., Schofield, N., Reynolds, P., 2017. Subsurface fluid flow focused by buried volcanoes in sedimentary basins: Evidence from 3D seismic data, Bass Basin, offshore southeastern Australia. Interpretation 5, SK39–SK50. https://doi.org/10.1190/INT-2016-0205.1

Hood, K.C., Wenger, L.M., Gross, O.P., Harrison, S.C., 2002. Hydrocarbon Systems Analysis of the Northern Gulf of MexicoDelineation of Hydrocarbon Migration Pathways Using Seeps and Seismic Imaging, in: Surface Exploration Case Histories<subtitle>Applications of Geoschemistry, Magnetics, and Remote Sensing</Subtitle>. American Association of Petroleum Geologists. https://doi.org/10.1306/St48794C2

Hooper, E.C.D., 1991. Fluid migration along growth faults in compacting sediments. J. Pet. Geol. 14, 161–180. https://doi.org/10.1111/j.1747-5457.1991.tb00360.x

Hughes, M., Nichol, S., Przeslawski, R., Totterdell, J., Heap, A., Fellows, M., Daniell, J., 2009. Ceduna Sub-basin: Environmental Summary. Geosci. Aust., 65838 09, 147.

Jackson, C.A., Magee, C., Schofield, N., Golenkov, B., 2013. Seismic Expression and Petroleum System Implications of Igneous Intrusions in Sedimentary Basins: Examples from Offshore Australia. Presented at the AAPG International Conference and Exhibition, AAPG, Singapore, p. 23.

Jackson, C.A.-L., Bell, R.E., Rotevatn, A., Tvedt, A.B.M., 2017. Techniques to determine the kinematics of synsedimentary normal faults and implications for fault growth models. Geol. Soc. Lond. Spec. Publ. 439, 187–217. https://doi.org/10.1144/SP439.22

Jackson, C.A.-L., Rotevatn, A., 2013. 3D seismic analysis of the structure and evolution of a salt-influenced normal fault zone: A test of competing fault growth models. J. Struct. Geol. 54, 215–234. https://doi.org/10.1016/j.jsg.2013.06.012

Jev, B.I., Kaars-Sijpesteijn, C.H., Peters, P.A.M., Watts, N.L., Wilkie, J.T., 1993. Akaso Field, Nigeria: Use of INtegrated 3-D Seismic, Fault Slicing, CLay Smearing and RFT Pressure Data on Fault Trapping and Dynamic leakage. AAPG Bull. 77.

Kempton, R., Bourdet, J., Ross, A., Pironon, J., 2019. Petroleum migration in the Bight Basin: a fluid inclusion approach to constraining source, composition and timing. APPEA 57, 762–766.

King, R., Backé, G., 2010. A balanced 2D strucutral model of the Hammerhead Delta-Deepwater Fold-Thrust Belt, Bight Basin, Australia. Aust. J. Earth Sci. 1005–1012.

King, R.C., Backé, G., Morley, C.K., Hillis, R.R., Tingay, M.R.P., 2010. Balancing deformation in NW Borneo: Quantifying plate-scale vs. gravitational tectonics in a delta and deepwater fold-thrust belt system. Mar. Pet. Geol. 27, 238–246. https://doi.org/10.1016/j.marpetgeo.2009.07.008

King, R.C., Morley, C.K., 2017. Wedge Geometry and Detachment Strength in Deepwater Fold-Thrust Belts. Earth-Sci. Rev. 165, 268–279. https://doi.org/10.1016/j.earscirev.2016.12.012

Klauser-Baumgärtner, D., Reichel, T., Hansen, J.-A., 2019. Regional paleodepositional environment of the Cretaceous in the Great Australian Bight – a support for frontier exploration. APPEA J. 59, 891. https://doi.org/10.1071/AJ18055

Litchfield, N.J., Villamor, P., Dissen, R.J.V., Nicol, A., Barnes, P.M., A. Barrell, D.J., Pettinga, J.R., Langridge, R.M., Little, T.A., Mountjoy, J.J., Ries, W.F., Rowland, J., Fenton, C., Stirling, M.W., Kearse, J., Berryman, K.R., Cochran, U.A., Clark, K.J., Hemphill-Haley, M., Khajavi, N., Jones, K.E., Archibald, G., Upton, P., Asher, C., Benson, A., Cox, S.C., Gasston, C., Hale, D., Hall, B., Hatem, A.E., Heron, D.W., Howarth, J., Kane, T.J., Lamarche, G., Lawson, S., Lukovic, B., McColl, S.T., Madugo, C., Manousakis, J., Noble, D., Pedley, K., Sauer, K., Stahl, T., Strong, D.T., Townsend, D.B., Toy, V., Williams, J., Woelz, S., Zinke, R., 2018. Surface Rupture of Multiple Crustal Faults in the 2016 Mw 7.8 Kaikōura, New Zealand, Earthquake. Bull. Seismol. Soc. Am. 108, 1496–1520. https://doi.org/10.1785/0120170300

Macdonald, J., Backé, G., King, R., Holford, S., Hillis, R., 2012. Geomechanical modelling of fault reactivation in the Ceduna Sub-basin, Bight Basin, Australia. Geol. Soc. Lond. Spec. Publ. 367, 71–89. https://doi.org/10.1144/SP367.6

MacDonald, J., King, R., Hillis, R., Backé, G., 2010. Structural style of the White Pointer and Hammerhead Delta—deepwater fold-thrust belts, Bight Basin, Australia. APPEA J. 50, 487. https://doi.org/10.1071/AJ09029

Magee, C., Hunt-Stewart, E., Jackson, C.A.-L., 2013. Volcano growth mechanisms and the role of sub-volcanic intrusions: Insights from 2D seismic reflection data. Earth Planet. Sci. Lett. 373, 41–53. https://doi.org/10.1016/j.epsl.2013.04.041

McClay, K., Dooley, T., Zamora, G., 2003. Analogue models of delta systems above ductile substrates. Geol. Soc. Lond. Spec. Publ. 216, 411–428. https://doi.org/10.1144/GSL.SP.2003.216.01.27

McClay, K.R., 1990. Deformation mechanics in analogue models of extensional fault systems. Geol. Soc. Lond. Spec. Publ. 54, 445–453. https://doi.org/10.1144/GSL.SP.1990.054.01.40

McClay, K.R., Dooley, T., Lewis, G., 1998. Analog modeling of progradational delta systems. Geology 26, 771. https://doi.org/10.1130/0091-7613(1998)026<0771:AMOPDS>2.3.CO;2

Mildren, S., Hillis, R., Lyon, P., Meyer, J.J., 2005. FAST; A NEw Technique for geomechanical assessment of the risk of reactivation-related breach of fault seals. AAPG Hedberg Ser. 73–85. https://doi.org/10.1306/1060757H23163

Mitchell, C., Boreham, C.J., Totterdell, J., Geoscience Australia, 2009. Bight Basin geological sampling and seepage survey: RV Southern Surveyor survey SS01/2007. Geoscience Australia, Canberra.

Morley, C.K., 2003. Mobile shale related deformation in large deltas developed on passive and active margins. Geol. Soc. Lond. Spec. Publ. 216, 335–357. https://doi.org/10.1144/GSL.SP.2003.216.01.22

Morley, C.K., Guerin, G., 1996. Comparison of gravity-driven deformation styles and behavior associated with mobile shales and salt. Tectonics 15, 1154–1170. https://doi.org/10.1029/96TC01416

Morley, C.K., Tingay, M., Hillis, R., King, R., 2008. Relationship between structural style, overpressures, and modern stress, Baram Delta Province, northwest Borneo. J. Geophys. Res. 113, B09410. https://doi.org/10.1029/2007JB005324

Regional Geology of the Bight Basin (No. 1), 2020. . Geoscience Australia.

Reynolds, P., Holford, S., Schofield, N., Ross, A., 2018. The importance of subsurface lithology in controlling magma storage v. eruption: an example from offshore southern Australia. J. Geol. Soc. 175, 694–703. https://doi.org/10.1144/jgs2017-109

Reynolds, P., Holford, S., Schofield, N., Ross, A., 2017. The shallow depth emplacement of mafic intrusions on a magma-poor rifted margin: An example from the Bight Basin, southern Australia. Mar. Pet. Geol. 88, 605–616. https://doi.org/10.1016/j.marpetgeo.2017.09.008

Reynolds, P., Holford, S., Schofield, N., Ross, A., 12/2017b. The shallow depth emplacement of mafic intrusions on a magma-poor rifted margin: An example from the Bight Basin, southern Australia. Mar. Pet. Geol. 88, 605–616. https://doi.org/10.1016/j.marpetgeo.2017.09.008

Reynolds, S.D., Hillis, R.R., O'Brien, G.W., 2003. Chapter 9: Petroleum Geology of South Australia. Stress Anal. Fault React. Fault Seal Integr. Bight Basin 4.

Robson, A., 2017. Normal fault growth analysis using 3D seismic datasets located along Australia's southern margin (thesis). University of Adelaide, School of Physical Sciences.

Robson, A., King, R., Holford, S., 2017. Structural evolution of a gravitationally detached normal fault array: analysis of 3D seismic data from the Ceduna Sub-Basin, Great Australian Bight. Basin Res. 29, 605–624. https://doi.org/10.1111/bre.12191

Rowan, M., Jackson, M., Trudgill, B., 1999. Salt-Related Fault Families and Fault Welds in the Northern Gulf of Mexico. AAPG Bull. 83, 1454–1484.

Rudolph, K.W., Goulding, F.J., 2017. Benchmarking exploration predictions and performance using 20+ yr of drilling results: One company's experience. AAPG Bull. 101, 161–176. https://doi.org/10.1306/06281616060

Ryan, L., Magee, C., Jackson, C.A.-L., 2017. The kinematics of normal faults in the Ceduna Subbasin, offshore southern Australia: Implications for hydrocarbon trapping in a frontier basin. AAPG Bull. 101, 321–341. https://doi.org/10.1306/08051615234

Sager, W.W., MacDonald, I.R., Hou, R., 2004. Side-scan sonar imaging of hydrocarbon seeps on the Louisiana continental slope. AAPG Bull. 88, 725–746. https://doi.org/10.1306/01260404004

Sapin, F., Ringenbach, J.-C., Rives, T., Pubellier, M., 2012. Counter-regional normal faults in shale-dominated deltas: Origin, mechanism and evolution. Mar. Pet. Geol. 37, 121–128. https://doi.org/10.1016/j.marpetgeo.2012.05.001

Sayers, J., Symonds, P.A., Direen, N.G., Bernardel, G., 2001. Nature of the continent-ocean transition on the non-volcanic rifted margin of the central Great Australian Bight. Geol. Soc. Lond. Spec. Publ. 187, 51–76.

Schneider, R.V., Barkooky, A.E., Gerrits, M., Meyer, H., Schwander, M., Zaki, H., 2000. Tectonic evolution of the Eastern Mediterranean Basin and its significance for. Lead. EDGE.

Schofield, A., Totterdell, J., 2008. Distribution, timing and origin of magmatism in the Bight and Eucla Basins. Geosci. Aust., 67359 1–25.

Selim, E.S.I., Omran, M.A., 2012. Characteristic features of salt tectonics offshore North Sinai, Egypt. Arab. J. Geosci. 5, 371–383. https://doi.org/10.1007/s12517-010-0192-4

Stromsoyen, I., Schomacker, E., Soderstrom, B., Waagan, B.M.T., 2019. The Bight Basin: a tale of three deltaic megasequences, in: APPEA. pp. 952–957. https://doi.org/10.1071/AJ18213

Struckmeyer, H.I.M., Totterdell, J.M., Blevin, J.E., Logan, G.A., Boreham, C.J., Deighton, I., Krassay, A.A., Bradshaw, M.T., 2001. Character, Maturity and Distribution of Potential Cretaceous Oil Source Rocks in the Ceduna Sub-Basin, Bight Basin, Great Australian Bight 12.

Tapley, D., Mee, B.C., King, S.J., Davis, R.C., Leischner, K.R., 2005. Petroleum pontetial of the Ceduna Sub-basin: Impact of Gnarlyknots-1A. APPEA J. 45, 365. https://doi.org/10.1071/AJ04029

Totterdell, J., Krassay, A., 2003. The role of shale deformation and growth faulting in the Late Cretaceous evolution of the Bight Basin, offshore southern Australia. Geol. Scoeity Lond., Subsurface Sediment Mobilization 216, 429–442.

Totterdell, J., Mitchell, C., 2009. Bight Basin geological Sampling and Seepage Survey. RV South. Surv., 68689 24.

Totterdell, J.M., Blevin, J.E., Struckmeyer, H.I.M., Bradshaw, B.E., Colwell, J.B., Kennard, J.M., 2000. A new sequence framework for the Great Australian Bight: Starting with a clean slate. APPEA J. 40, 95. https://doi.org/10.1071/AJ99007

Totterdell, J.M., Struckmeyer, H.I.M., Boreham, C.J., Mitchell, C.H., Monteil, E., Bradshaw, B.E., 2008. Mid–Late Cretaceous organic-rich rocks from the eastern Bight Basin: implications for prospectivity 23.

Tredrea, B., Horton, P., 2019. Seismic evidence for seal and reservoir in the Late Cretaceous Ceduna Delta, Great Australian Bight. Presented at the ASEG Extended Abstracts, ASEG, p. 14.

Weber, K.J., Mandl, G.J., Pilaar, W.F., Lehner, B.V.F., Precious, R.G., 1978. The Role of Faults in hydrocarbon migration and trapping in Nigerian growth fault structures, in: Offshore Technology Conference. Presented at the Offshore Technology Conference, Offshore Technology Conference, Houston, Texas. https://doi.org/10.4043/3356-MS

Wiener, R., Mann, M., Angelich, M., Molyneux, J., 2011. Mobile Shale in the Niger Delta: Characteristics, Structure, and Evolution, in: Shale Tectonics. American Association of Petroleum Geologists, pp. 145–161. https://doi.org/10.1306/13231313M933423

Woillez, M.-N., Souque, C., Rudkiewicz, J.-L., Willien, F., Cornu, T., 2017. Insights in Fault Flow Behaviour from Onshore Nigeria Petroleum System Modelling. Oil Gas Sci. Technol. – Rev. D'IFP Energ. Nouv. 72, 31. https://doi.org/10.2516/ogst/2017029

Wood, L.J., 2012. Shale tectonics, in: Regional Geology and Tectonics: Phanerozoic Passive Margins, Cratonic Basins and Global Tectonic Maps. Elsevier, pp. 42–61. https://doi.org/10.1016/B978-0-444-56357-6.00002-0

Chapter 1: Structural interpretation

Structural interpretation of normal growth faults and detachment layers in the Ceduna sub-basin using the Ceduna 3D MSS seismic survey

Some of the results from this chapter were submitted and presented in the AEGC conferences in 2021.

Structural interpretation of normal growth faults and detachment layers in the Ceduna sub-basin using the Ceduna 3D MSS seismic survey

Introduction

Normal growth faults formed in the extensional region of delta systems as a result of the balance between the rates of sedimentary accumulation and horizontal extension, and depend on the characteristics of the underlying detachment layer *(Bally et al., 1981; Vendeville et al., 1987; McClay, 1990; McClay et al., 2003)*. In this thesis we investigate these aspects for two temporally independent large-scale delta systems that developed in the central region of the Ceduna Sub-basin of the Great Australian Bight (GAB) basin. These delta systems are: (i) the Cenomanian White Pointer Delta System and, (ii) the Late Santonian-Maastrichtian Hammerhead Delta System *(Totterdell and Krassay, 2003; Espurt et al., 2009; Robson et al., 2017; Ryan et al., 2017).* The White Pointer Delta System formed when the progradational White Pointer Supersequence was rapidly deposited over the Blue Whale Supersequence (Albian), forming normal growth faults dipping toward the southwest. The Hammerhead delta system formed during the passive margin phase of the Ceduna Sub-basin when deltaic sediments were rapidly deposited over the Tiger Supersequence, reactivating some Cenomanian-Late Santonian faults and creating distinct Late Santonian-Maastrichtian fault segments *(Totterdell and Krassay, 2003; MacDonald et al., 2010; Ryan et al., 2017).*

Normal growth faults play an important role in passive margins that contain delta systems because they influence the structural and stratigraphic geometry of the sedimentary basin fill. They control the geometry, thickness and distribution of sedimentary sequences *(Gawthorpe and Leeder, 2000; Morley, 2003; Wood, 2012)* and have an important role in the establishment of effective petroleum systems by influencing the distribution of reservoir, seal and source rocks (Caine et al., 1996a; Hooper, 1991). In sedimentary basins hosting deltaic sequences like the Ceduna Sub-basin, it has been demonstrated that normal growth faults control the migration and trapping of fluids such as water and hydrocarbons, providing pathways for hydrocarbons to migrate from deeper sources to shallow reservoirs or forming impermeable barriers that prevent fluid migration. Examples include the Niger Delta, the Gulf of Mexico, the Baram Delta and Offshore Angola *(Thorsen, 1963; Weber et al., 1978; Cohen and McClay, 1996; Marton et al., 2000; Wood, 2012; Woillez et al., 2017*).

In this chapter we explain the processes used to interpret the Ceduna 3D marine seismic survey (MSS) and how we combine available wireline log and 2D seismic reflection survey data to enhance the interpretation. We describe different structural characteristics of the normal fault segments across the study area such as their geometry, strike, and dip direction. We also include a brief description of the seismic characteristics for different stratigraphic sequences, and how they correlate with the Potoroo-1 and Gnarlyknots-1A well log records. We describe the interpretation of structural maps showing the main supersequences (Hammerhead, Tiger, White Pointer and Blue Whale) and thickness maps of the main detachment layer (Tiger upper sequence and Blue Whale) to demonstrate the influence that sedimentary sequences and detachments have had on characteristics of the normal growth faults. This chapter also defines the criteria used for the selection of fault segment candidates, which are examined in subsequent chapters of this thesis (Chapters 2, 3 and 4). In all cases, we select

fault segments that are representative of the geometrical characteristics of the fault segments and are widely distributed in the study area.

Available data

Seismic surveys in the Great Australian Bight Basin (GAB)

The Ceduna 3D MSS is a seismic reflection survey dataset located in the central region of the Ceduna Sub-basin. This 3D seismic survey was acquired as part of the BP Ceduna project between 2011 and 2012, and covers 12,030 km^2 *(GAB 3D Survey Final Report, 2012)*. The seismic record length is 9 seconds two-way-time (TWT) distributed along 16,025 cross-lines oriented 315°N (here perpendicular to the fault strike orientation) and 3,400 inlines oriented 045°N, with a square bin spacing between in-lines and cross-lines of 12.5 metres (m). In Chapter 3, we also interpret the Ceduna 3D MSS in the depth domain (in metres) which resulted from depth conversion during the seismic processing stage *(GAB 3D Survey Final Report, 2012).*

Coverage of 2D seismic profile lines broadly extends along the GAB and covers the Eyre, Ceduna, Recherche and Duntroon sub-basins. We used the closest 2D seismic lines to the Ceduna 3D seismic survey lines from the Flinders Deepwater 2DMSS – W00FDW0003, W00FDW0010, W00FDW0027, W00FDW0027, W00FDW0083, W00FDW0092 – to correlate stratigraphic horizon well tops from the closest exploration wells, Potoroo-1 and Gknarlyknots-1A, with prominent seismic reflectors within the Ceduna 3D MSS seismic survey (Figure 1). These 2D seismic lines are part of the Flinders Deepwater 2D MSS acquired in 2000 by Woodside Energy in the Great Australian Bight.

Potoroo-1 is located 71 km north of the Ceduna 3D MSS and was drilled in 1975 to target the Albian-Maastrichtian sequence. Gnarlyknots-1A is located 42.2 km to the east-northeast of the Ceduna 3D MSS and was drilled in 2003 to target the Late-Santonian-Maastrichtian stratigraphic sequence. Both wells included wireline logs such as Gamma-Ray (GR and GRCDR), Sonic transit time (DT and DTBC) calliper, resistivity, and density, which allowed the correlation and description of the stratigraphic sequences. We incorporate the tops of the supersequences and lithological characteristics from the completion reports to define lithologies within the wireline logs and we incorporate check-shot logs from the Potoroo-1 and Gnarlyknots-1A to generate 2D seismic line well ties (Figure 2).

As both wells are more than 40km away from the study area, there is a great uncertainty in finding a seamless correlation of sequences in the study area. Therefore, in this chapter we will refer to relatively high shale content in the sequences with high values of Gamma-Ray and density, and relatively high sandstone content in the sequence with low values of Gamma-Ray.

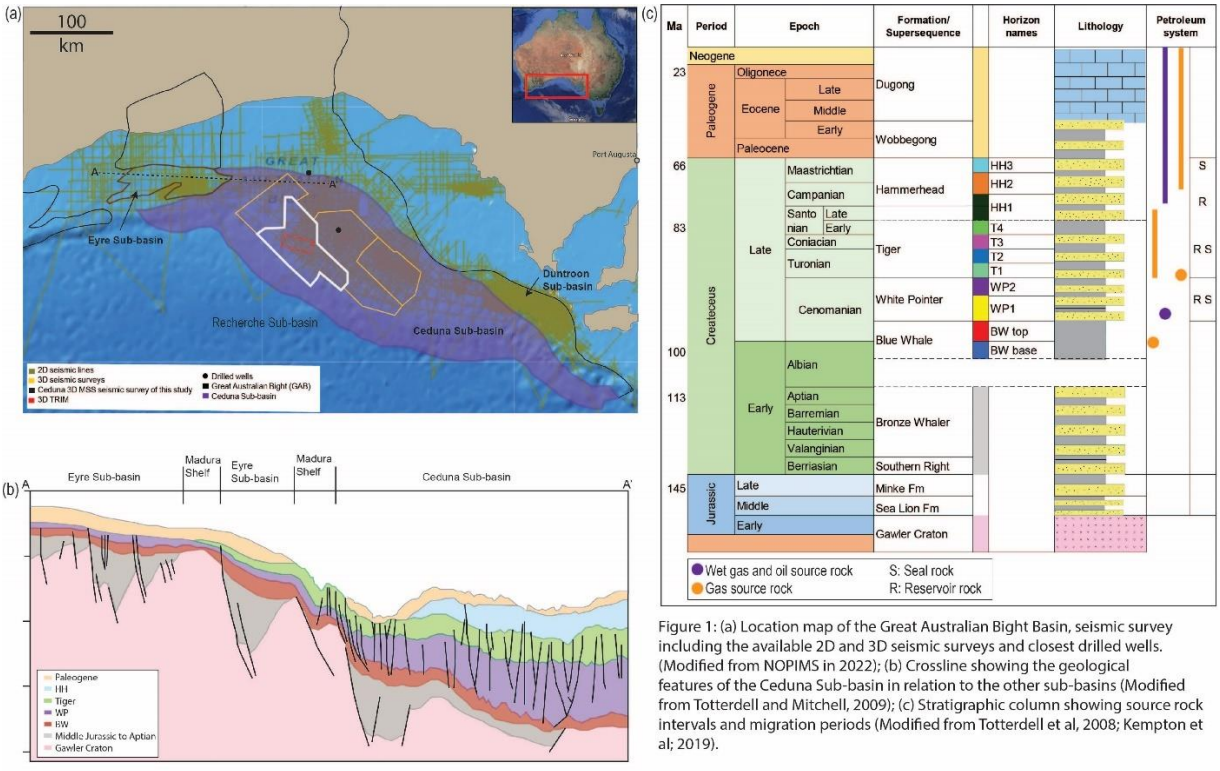

Figure 1: (a) Location map of the Great Australian Bight Basin, seismic survey including the available 2D and 3D seismic surveys and closest drilled wells. (Modified from NOPIMS in 2022); (b) Crossline showing the geological features of the Ceduna Sub-basin in relation to the other sub-basins (Modified from Totterdell and Mitchell, 2009); (c) Stratigraphic column showing source rock intervals and migration periods (Modified from Totterdell et al, 2008; Kempton et al; 2019).

All chapters included in this thesis refer to a detailed interpretation of sedimentary sequences represented within the seismic data; thus, we mapped seven inter-sequence horizons in addition to the four tops of the principal supersequences (Hammerhead, Tiger, White Pointer and Blue Whale). For instance, our kinematic and geomechanical analyses are sensitive to changes in displacement, dip angle and strike of faults determined from these in both vertical and horizontal dimensions. Therefore, near the areas where the wells are located, we correlated Gamma-Ray and Acoustic velocity with the seismic wavelet of the 2D seismic lines to identify smaller-scale changes between sedimentary sequences within each supersequence.

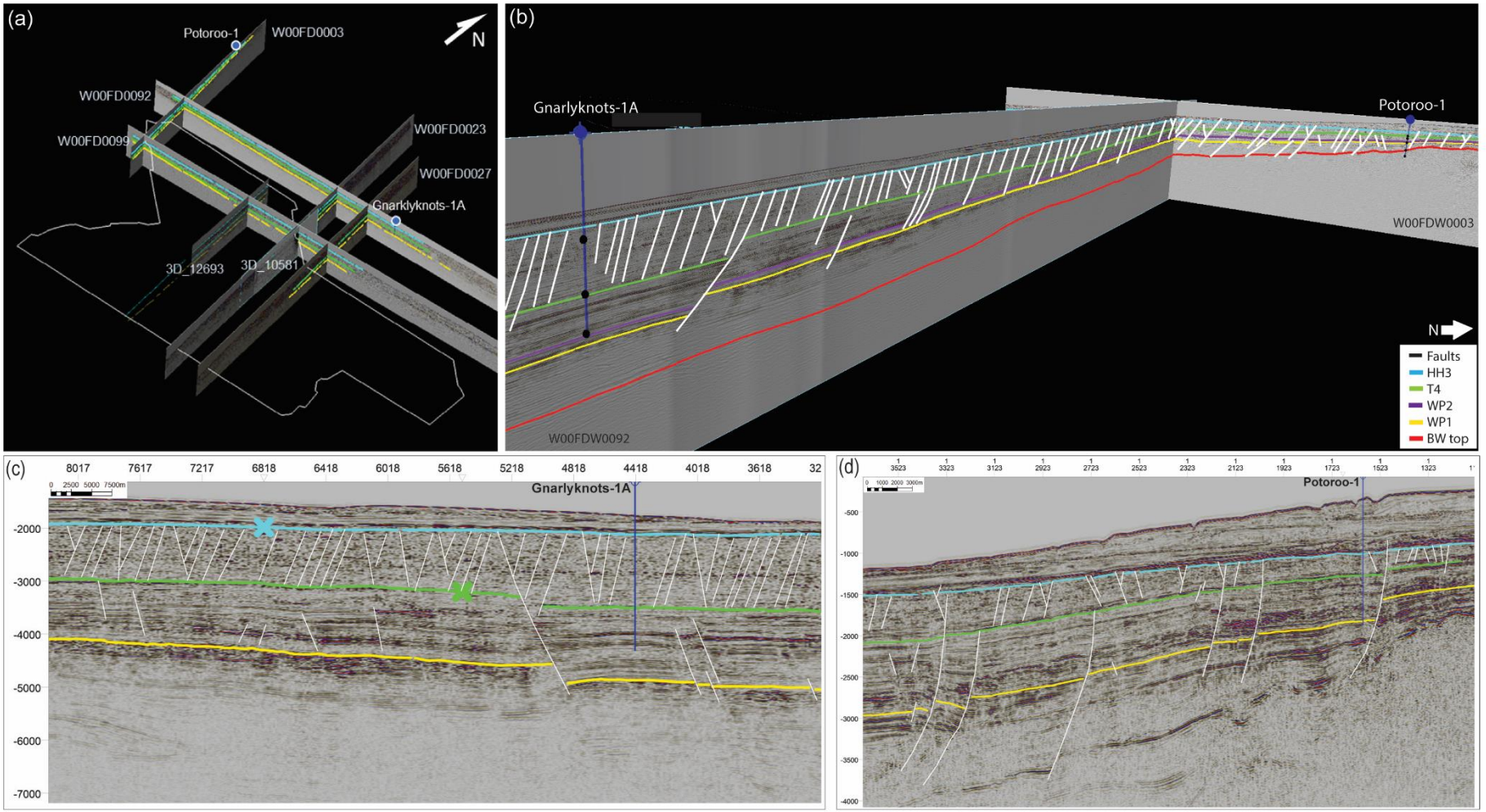

Figure 2: Well-tie of the 2D seismic lines, the Ceduna 3D MSS seismic survey ad the wireline log records from Potoroo-1 and Gnarlyknots-1A exploration wells. (a) 3D map view showing all the interpreted 2D seismic lines and the Ceduna 3D MSS seismic survey. (b) 3D window showing the intersection between seismic lines W00FDW0092 and W00FDW0003 and the wireline log records of the exploration wells Potoroo-1 and Gnarlyknots-1A. Detail of the seismic interpretation of the 2D seismic lines (c) W00FDW0092 and (d) W00FDW0003.

Methodology

As part of this study, 2D seismic lines (from the Flinders Deepwater 2D MSS seismic dataset) W00FDW0003, W00FDW0010, W00FDW0027, W00FDW0027, W00FDW0083, W00FDW0092 were interpreted, which are located between the Ceduna 3D MSS seismic survey and the Potoroo-1 and Gknarlyknots-1A wells. This provided seismic stratigraphic tie-in between the wells and the 3D seismic survey dataset, and regional context for the characterization of major seismic reflectors and other seismic stratigraphic features (e.g., unconformities, syn-kinematic sequences, etc.). As a result, we identified the general structural configuration of the central area of the Ceduna Sub-basin (Figure 2). We interpreted major fault planes to define the principal fault geometry, changes in dip angle in cross section view and principal strikes in map view. This initial interpretation also granted an opportunity to define the behaviour and depth of the detachment layers and define the most appropriate spacing to interpret the Ceduna 3D seismic survey more efficiently, while conserving important regional characteristics (e.g., changes in dip angle due to the detachment, pitchouts, and variations between fault segments). The combination of the regional structural framework interpretation and an overview of the 3D seismic survey processing report allowed the proper characterization of area of interest, including the type of structures in the area, potential regions where the seismic resolution is limited by higher noise-signal rate and outline certain areas that required more attention (Figure 3). For example, the eastern most and southwest most areas of the Ceduna 3D seismic survey show strong noise-signal ratio which can result in human errors during the interpretation of some of the horizons.

Most fault segments, horizons and igneous features were interpreted using the Ceduna 3D MSS survey in *'Two-Way Time'* (TWT) as it is the dataset with the lowest noise-signal ratio. We used our interpretation in depth (m) in the geomechanical analysis to confirm the depths of the intrusions and volcanic cones below the seabed. This depth seismic survey was part of the depth migration seismic processing of the Ceduna 3D seismic survey (*GAB 3D Survey Final Report*, 2012).

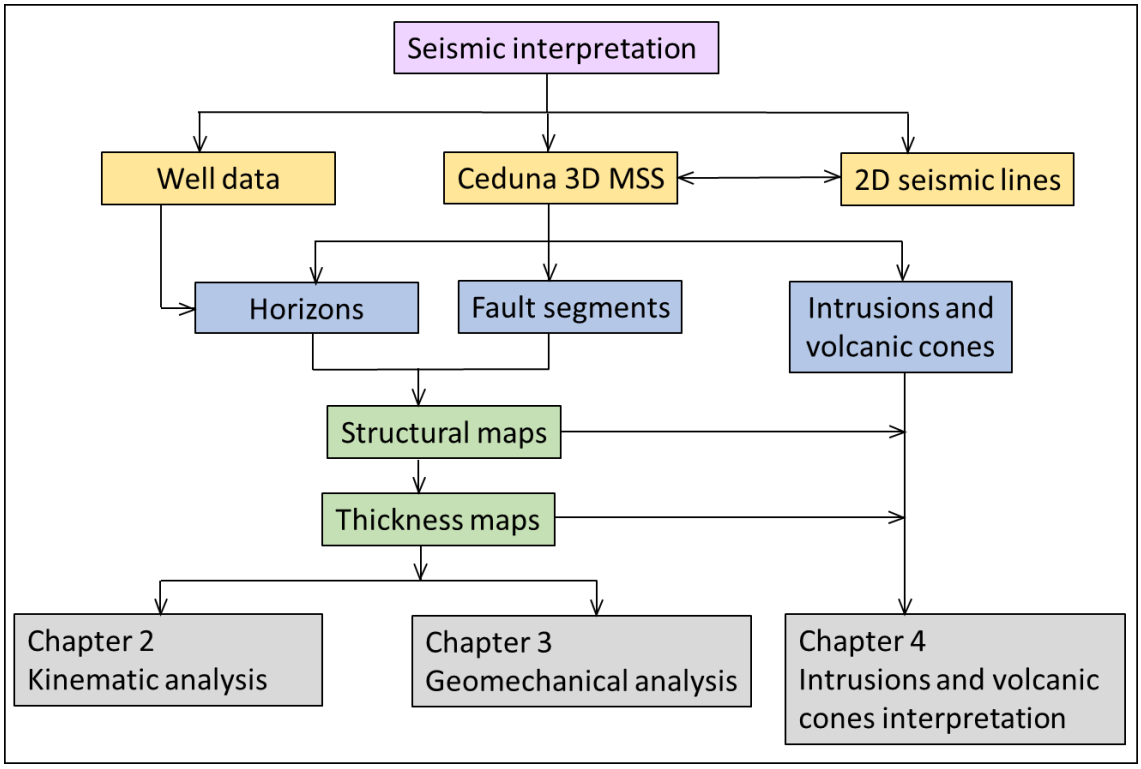

Figure 3: Diagram summarizing the available data and methodology used for the interpretation of sequence tops and normal growth fault segments. We also mentioned the different chapters included in this thesis.

Interpretation of fault segments

Initially we interpreted the Ceduna 3D seismic survey every 32 seismic in-lines and cross-lines and then decreased the interval to every 16 cross-lines, providing enough detail suitable for the kinematic analysis of fault growth (Chapter 2) without losing crucial detail of the main regional structural outline in the area. For the geomechanical analysis (Chapter 3) and the interpretation of fault segments closer to the intrusions and volcanic cones (Chapter 4), we again decreased the interpretation interval to every eight, then four, cross-lines and in-lines to increase the amount of interpreted detail in terms of changes in dip angle and strike along the fault planes. We principally used the cross-lines to map the fault segments as the majority of northeast-southwest faults, and incorporated either the in-lines to interpret northeast-southwest faults and/or arbitrary lines to map north-south and west-east segments, employing the same interpretation intervals (32, 16 and eight and four) we used for the cross-lines.

We generate the variance seismic attribute and utilize time slices with an applied *Automatic Gain Control (AGC)*. The *Variance* helps to reveal discontinuities in seismic data related to stratigraphic or structural discontinuities and highlight changes in strike and geometry between fault traces *(Koson et al., 2014)*. The *AGC* seismic re-scales and amplifies seismic amplitudes at deep seismic regions with low amplitudes. It can be used to balance amplitudes over time intervals whilst largely preserving contrast between successive intervals of high and low amplitude *(Petrel, 2015; Sarhan, 2017)*. *AGC* and *Variance* seismic attributes were also displayed in time slices. This process allowed the verification of changes in strike in each fault segment and identify additional small faults with different strike orientations, which in some cases intersected major northwest-southeast fault planes. In this project

the *Variance* and *AGC* seismic attributes were also projected on to structural maps, especially where the fault segments nucleated or display changes in dip angle.

From the high number of fault segments visible in the Ceduna 3D MSS seismic survey, we focused on detailed mapping of faults with a length equal to or greater than 800 m along strike. This cut-off permitted the definition of the principal fault trends in terms of strike and dip direction, and to differentiate between fault groups from the sedimentary record they displaced. To detail the interaction between the fault segments and the magma flow in the area (Chapter 4), we also interpreted some smaller faults that achieve lengths along strike between 350 and 520m underlying the igneous intrusions and volcanic cones.

In addition to the fault interpretation, we applied seismic attributes such as maximum seismic amplitude and root mean square (RMS) amplitude over certain fault segment planes to define potential magma transport through the fault planes (Chapter 4).

Interpretation of supersequences

To define and tie the tops of the principal supersequences: The Hammerhead (HH), the Tiger, the White Pointer (WP) and the Blue Whale (BW, we made a stratigraphic correlation using wireline logs acquired at Potoroo-1 and Gnarlyknots-1A wells, combined with the 2D seismic lines and the Ceduna 3D MSS seismic survey. We used the Potoroo-1 well logs to interpret the sedimentary record between the base of the BW (Albian-Cenomanian) and the top of the Tiger (Early Santonian) supersequences, and the Gnarlyknots-1A well logs to define the section between the Tiger (Turonian) and the top HH (Maastrichtian) supersequences. We also interpreted the tops of seven stratigraphic sub-sequences that embody vertical variation in the stratigraphical features in the 2D seismic lines at each supersequence (e.g., sequences of low or high seismic amplitude, clinoforms, massive transport sequences, etc), that are also correlated to variations in Sonic transit time and Gamma-Ray well logs (Figure 4). We chose these seven sub-sequences because they represent constant seismic features that were possible to extrapolate from the 2D seismic lines to the Ceduna 3D seismic survey. They are: the upper (HH3) middle (HH2) and lower (HH1) Hammerhead sequences, the upper (T4), upper-middle (T3), lower-middle (T2) and lower (T1) Tiger sequences, and the upper (WP1) and lower (WP2) White Pointer sequences. To outline the changes in thickness the detachments, we interpret the base and top of the BW and T4 and T3 as the top and base of the Tiger detachment layer.

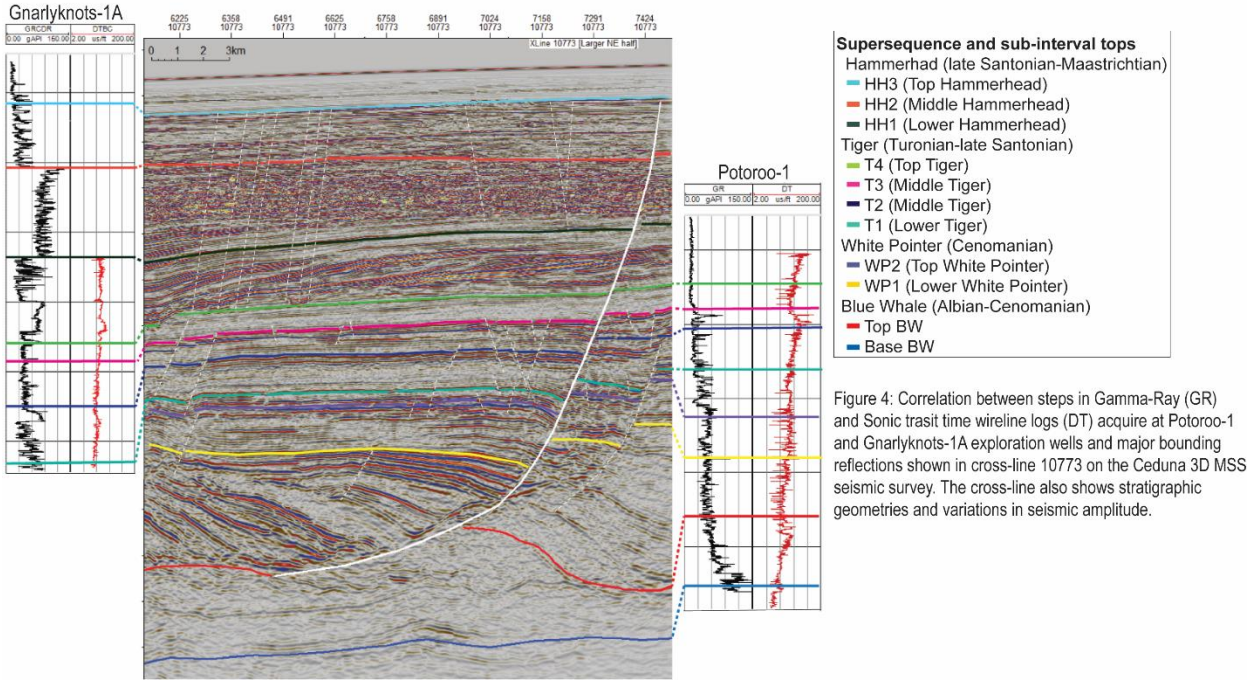

Figure 4: Correlation between steps in Gamma-Ray (GR) and Sonic trasit time wireline logs (DT) acquire at Potoroo-1 and Gnarlyknots-1A exploration wells and major bounding reflections shown in cross-line 10773 on the Ceduna 3D MSS seismic survey. The cross-line also shows stratigraphic geometries and variations in seismic amplitude.

We manually interpreted the eleven horizons every 16 cross-lines and in-lines along most of the Ceduna 3D seismic survey and generated structural maps from the tops of the four principal supersequences and the base of the detachment layers (T3 and base BW). To avoid losing detail related to fault displacement and local changes in dip angle, we used the auto-track along the original seismic interpretation which extrapolated the horizon mapping through a smaller grid. We then generated the structural maps and manually corrected errors in the structural maps and re-interpreted the problematic areas where necessary. To help define regional changes of the detachment layers, we used the structural maps to generate thickness maps of the detachment layers; the Tiger and BW supersequences.

In this chapter we will describe the principal characteristics of the different stratigraphic sequences in terms of variation in seismic amplitude and wireline log data values. As the scope of this thesis is related to the interpretation of normal growth faults, in this chapter we will provide context for the choice of these intervals for the kinematic analysis (Chapter 2) and to frame the risk of fault reactivation (Chapter 3). In addition, we have focused on describing in detail the detachment layers of the BW Supersequence and specifically, T4 (Top of the Tiger detachment layer), as these have been proven to have had a significant impact on the evolution of normal growth faults (Chapter 2) and magma emplacement in the area (Chapter 4).

Characteristics of the structural features in the study area

General characteristics of fault segments

During the seismic interpretation stage, we visualised a substantial number of normal growth fault segments along the study area. As mentioned previously, we mapped fault segments with a length along strike greater than 800 m that restricted the study to a reasonable number of faults of significant scale. This enabled us to define the principal fault trends in terms of strike, dip direction and define group faults using the sedimentary sequences that they displaced. We interpreted a total of 530 normal growth fault segments across the extensional region of the Ceduna Delta system that widely vary in strike, geometry, total displacement, and location along the study area (Figure 5).

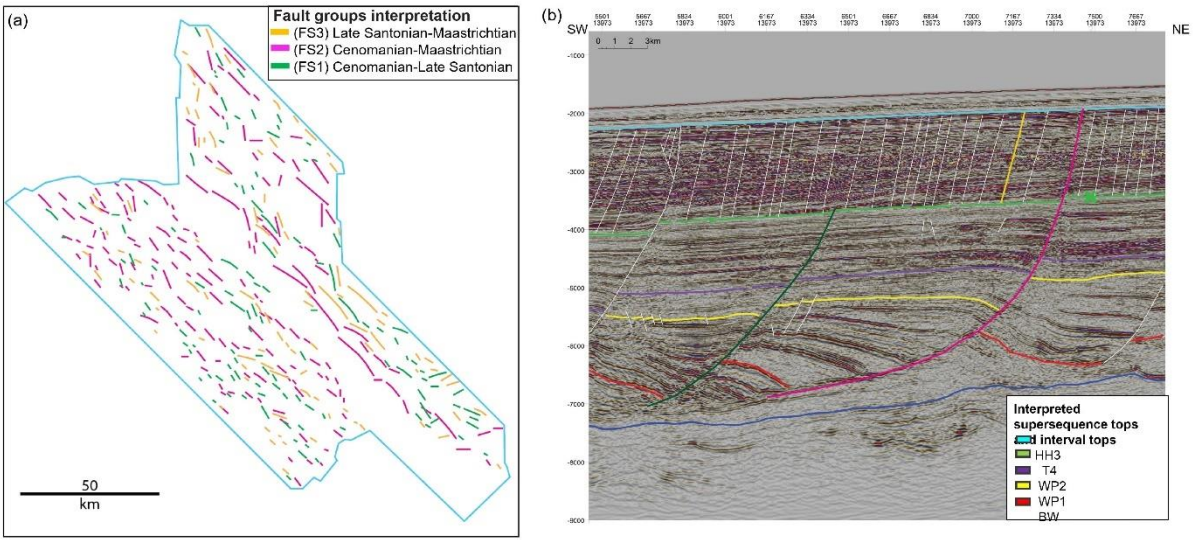

Figure 5: (a) Polylines representing the strike, lateral extension and location of each interpreted fault segment. The Cenomanian-Maastrichtian and the Late Santonian–Maastrichtian fault segment polylines are drawn at the top of the Tiger level and the Cenomanian-Late Santonian fault segment polylines are drawn in the middle White Pointer level. (b) Example of a dip-parallel section in the north showing the three different fault styles interpreted in the study area: FS1, FS2 and FS3

The interpreted fault segments vary in length along strike from 800 m up to 20.8 km and show planar or listric geometries. The listric faults are characterised by changing dip angles in cross-section view from around 85° at the uppermost sedimentary sequences and decreasing to up to 2° at the deeper sequences. In contrast the planar faults display a smaller range of angles from 70° and 38° (Figures 6a, b, c and d).

Most of the interpreted faults correspond to synthetic fault segments with dip directions toward the southwest. We also identified antithetic faults of Cenomanian-Maastrichtian age and minor Early Cenomanian-Late Santonian ages at the east, southwest and south regions. In general, these faults are either related to rollover structures in the footwall of Cenomanian-Maastrichtian fault segments or near the upper tips of Cenomanian-Late Santonian fault segments (Figures 6b to d).

It is difficult to quantify the total number of faults with each strike orientation as not all imaged faults were interpreted in this study. However, from the *Variance* and *AGC* seismic attributes projected to different depths, we can estimate that they share a similar frequency to the longer fault segments (>800 m along strike). Around 461 of the interpreted fault segments had a principal northwest-

southeast strike, 40 showed a west-east strike, 26 a north-south strike and only three showed a northeast-southwest strike. The northeast-southwest faults are mostly concentrated at the southeast of the study area, the north-south strikes can be found throughout the area and are especially concentrated at the north and south to southeast regions, while the west-east and northeast-southeast segments occur throughout the study area (Figure 5).

Classification of fault groups

To classify the interpreted faults, we define three different fault groups in relation to the sedimentary sequences each fault group: (1) Cenomanian-Late Santonian; (2) Cenomanian-Maastrichtian; (3) Late Santonian-Maastrichtian. Regionally, all the fault groups can be found throughout the study area. However, we identified a larger concentration of Cenomanian-Maastrichtian age segments in the northern, western, and central areas, and Cenomanian-Late Santonian and Late Santonian-Maastrichtian in the southern and south-eastern and south-western areas (Figure 5a and b).

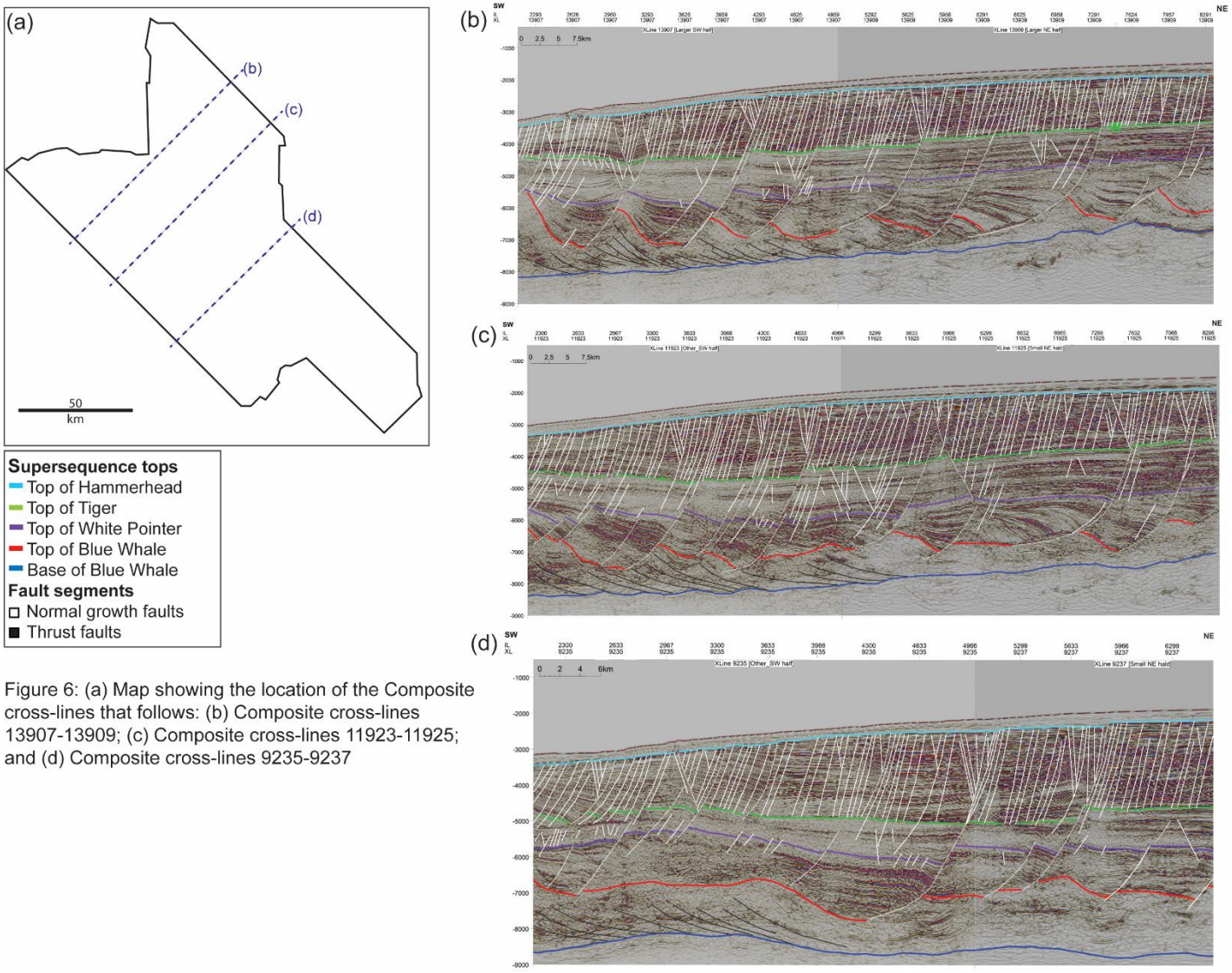

Figure 6: (a) Map showing the location of the Composite cross-lines that follows: (b) Composite cross-lines 13907-13909; (c) Composite cross-lines 11923-11925; and (d) Composite cross-lines 9235-9237

Fault group 1 (FG1)

Fault group 1 (FG1) segments are mostly synthetic segments with lengths along strike that can vary from 0.8km to 6km. The fault total displacements differ between 293ms to 793ms in the Cenomanian and from 27 to 99 ms at the Late Santonian (Figure 5b). The geometry of these faults varies between listric in the north and centre regions of the study area to sub-planar at the southern as eastern region of the study area. They commonly display small rollovers and rotated blocks in the hangingwall (Figure 6b and c). The rotated blocks are more visible towards the southwestern and southeastern regions and are commonly related to areas where the BW detachment is thicker (between 1330 and 2000ms) and in many cases where the BW detachment exhibits folds and 'dome-like' structures that locally change the dip angle of the detachment towards the southwest and modify the regional dipping of the overlying sequences from the southwest to the northeast. (Figure 6d).

The Cenomanian-Late Santonian faults can be categorised as isolated from other fault segments, across the study area, or located near Cenomanian-Maastrichtian faults especially in in the hangingwall were pronounced rollover structures formed (Figure 6c). In some areas, they correspond to an antithetic geometry at the top of either 'dome-like' structures or rollover blocks.

The Variance seismic attribute projected to time slice (-5500ms) between the T4 and WP2 supersequence boundaries supports the seismic interpretation and the WP structural map to suggest that most of the faults exhibit a northwest-southeast strike with few segments with a north-south and northeast-southwest strikes (Figures 7 and 10). The top of the Tiger structural map also shows some fault segments with west-east strikes especially in the south and southeast regions of the study area. The Variance seismic attribute reveals a concentration of Cenomanian-Late Santonian fault segments in southern, southwestern, south-eastern and northern regions.

Fault group 2 (FG2)

Fault group 2 (FG2) corresponds to synthetic faults with lengths along strike from 1km up to 20.8km with displacements that vary from 1 ms to 21 ms at the top of the Maastrichtian stratigraphic level and from 627 to 1172 ms at the Cenomanian level. All the faults of this group show a listric geometry that detaches at the top of the BW with rollover structures in the hangingwall block (Figure 6b). In areas like the south-eastern region where the BW detachment is thicker (1395 to 1511ms), their hangingwall exhibits rotated blocks with small changes in thickness (Figures 6b and d).

Our comparison between the Variance seismic attribute projected to a time slice that are located at the HH1 and Tiger sequences (-5500ms and -4500ms) (Figures 7 and 8) and the tops WP (WP2) and Tiger (T4) structural maps (Figures 10 and 11a) show that Cenomanian-Maastrichtian fault segments are widespread within the study area and relatively decrease in number from around 71 at the west to 30 at the east (Figure 5a). The majority of these faults have a northwest-southeast strike followed by a west-east strike and, in only few cases like the south-eastern and southwestern regions, they exhibit north-south and northeast-southwest strikes (Figure 5a).

Fault group 3 (FG3)

Fault group 3 (FG3) segments exhibit lengths along strike that vary from 1.6km to 14km. They show a listric to planar geometry with changes in displacement that vary from 5ms at the top of the Maastrichtian to 280ms at the top of the Late Santonian (Figure 5b). At the northern and central regions, these faults are found as either isolated fault segments or are related to Cenomanian-Late Santonian segments (Figures 6a, b c, d). In the southern and south-eastern regions, they detach at the upper Tiger Supersequence (T4) and exhibit more prominent listric geometries. We also identify antithetic and synthetic faults in the hangingwall of Cenomanian-Maastrichtian fault segments, were several of these faults develop near the upper tips of the older Cenomanian-Late Santonian fault segments (Figure 6d) forming small normal fault that might response to gravity-slip deformation caused by a near principal normal growth fault *(Harding, 1990; Huang and Liu, 2017)*.

The Variance seismic attribute projected to a time slice at HH1 (-4500ms) (Figure 8) combined with seismic interpretation, shows a prominent increase in the number of Late Santonian-Maastrichtian fault segments in the southern, southwestern, and southeastern regions (Figure 5a). From the cross-lines we identify a rise in the number of antithetic segments towards the eastern, southwestern and southern regions of the study area (Figure 6c and d). In terms of fault strikes, the Variance and AGC attributes show that the faults from FG3 have a predominant northwest-southeast strike across the study area with a few segments exhibiting north-south strikes in the southern and southeastern regions (Figures 7 and 8).

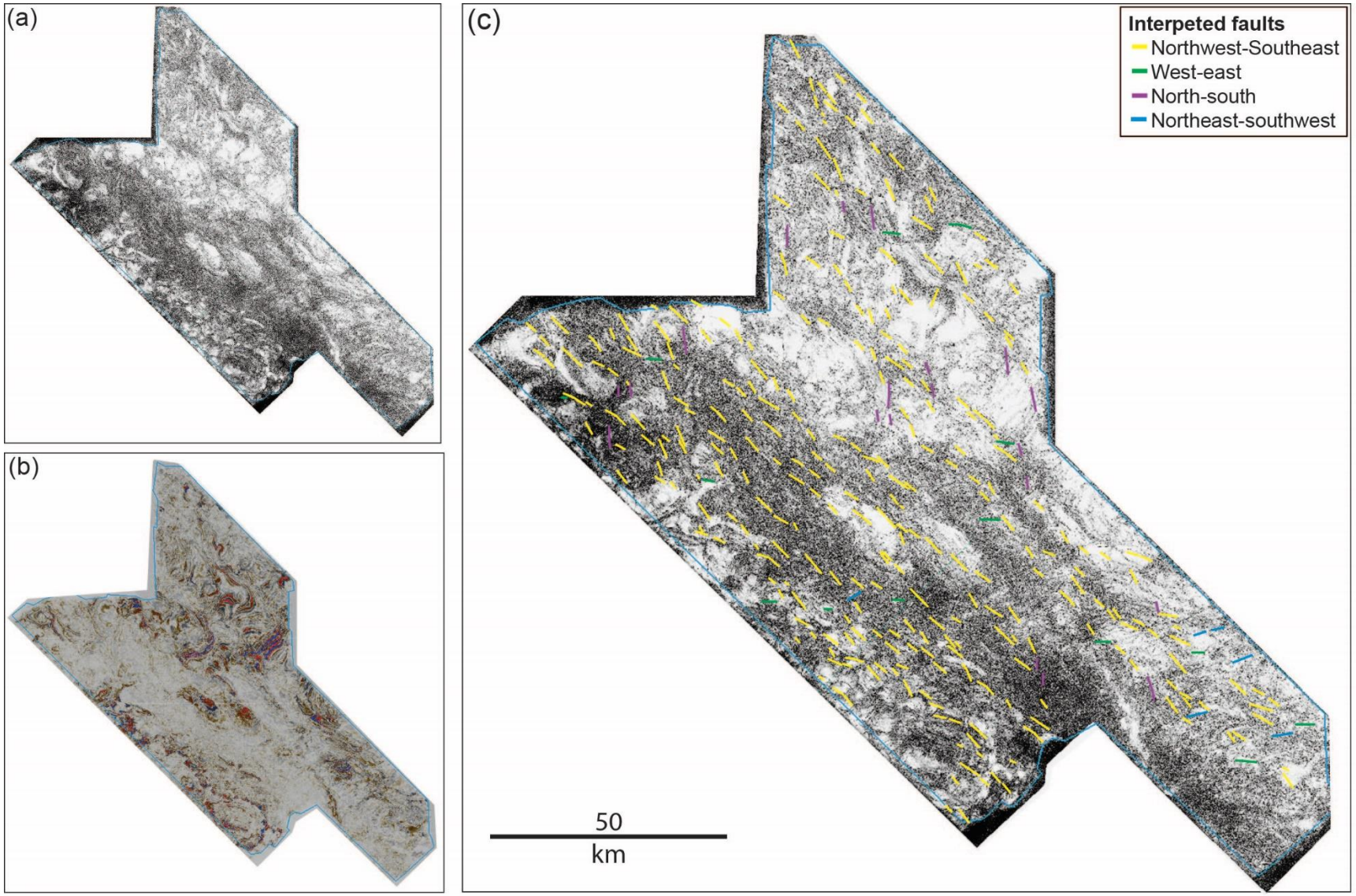

Figure 7: (a) Variance and (b) Automatic Gain Control (AGC) seismic attributes projected to a time slice at the lower Tiger Supequence (-5500ms). Here, the interpeted faults are catalogue by strike orientation to show their distribution along the study area.

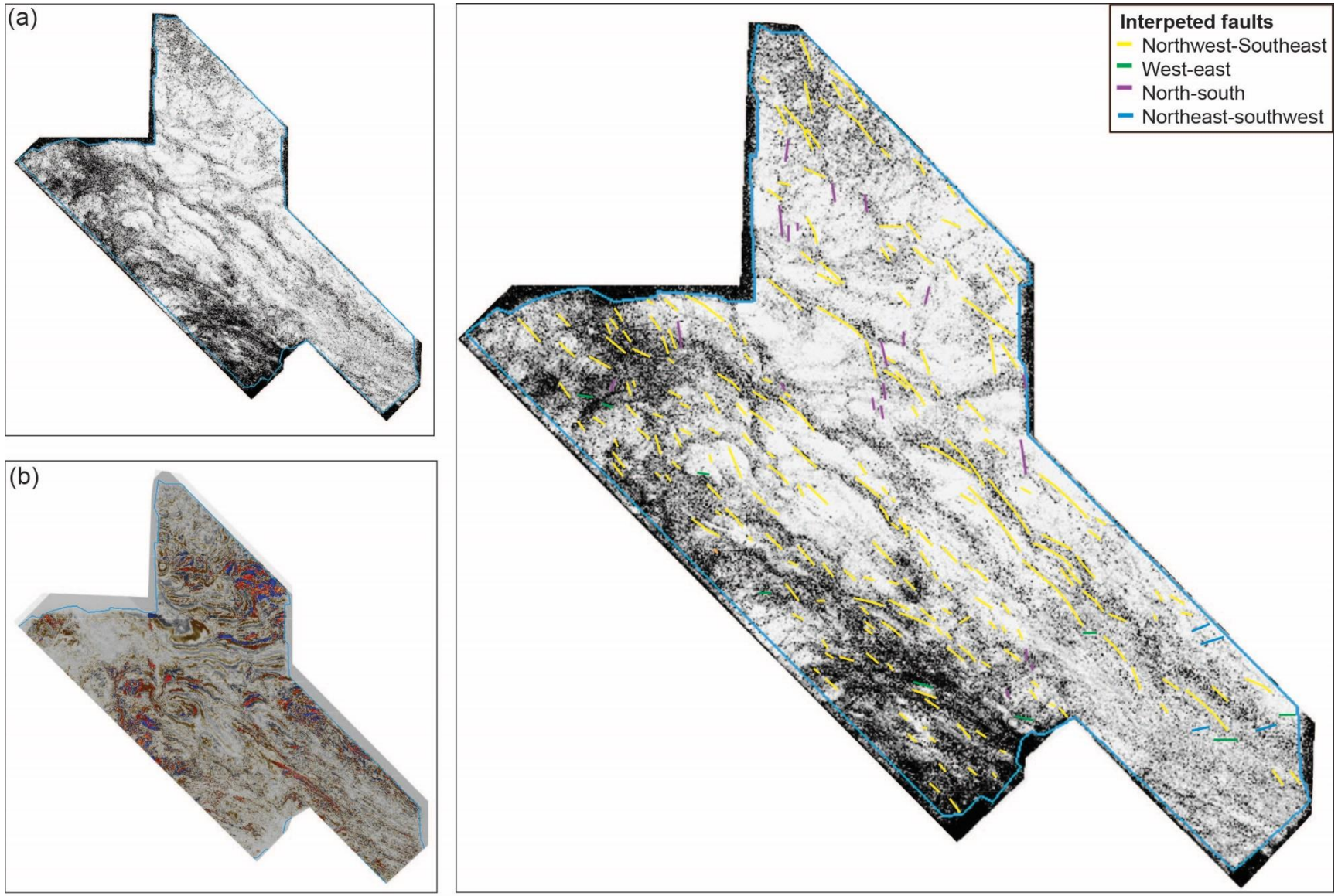

Figure 8: (a) Variance and (b) Automatic Gain Control (AGC) seismic attributes projected to a time slice at the lower Tiger sequence (-4500ms). (c) Here, the interpeted faults are catalogue by strike orientation to show their distribution along the study area.

Seismic expression of the geometry and lateral changes of the interpreted supersequences

Blue Whale Supersequence (BW)

The top and base of the BW Supersequence show low seismic amplitude in the northern and north-central regions with locally chaotic, high seismic amplitude reflection events towards the centre and south (Figure 6b). Seismic interpretation confirms that the FG2 and FG3 detach at the top of the BW Supersequence where listric faults reach angles of about 2° and represent the deeper section of the listric faults. The BW Supersequence exhibits changes in dip angle from 10° in the northern region, to between 5° and 10° in the central area, and <2° in the south and southeast (Figure 6c). These changes are also related to the appearance of 'dome-like' structures and the formation of thrust faults inside the BW Supersequence in the central and southern regions of the study area (Figure 9a). These dip angle variations, and the dome-like structures strongly affect the thickness of the BW Supersequence, which varies from 200ms to 500ms at the north, from 650 and 700ms in the central region and up to 1200ms in the southern and south-eastern areas (Figure 9b).

In the southeast of the study area, the base of the BW Supersequence mimics an antiformal structure at basement level forming a 'dome-like' structure at the detachment layer, where several planar to listric faults detach. The WP and Tiger supersequences mimic this antiform as shown by change of dip angles and broad domal geometry (Figure 6d). It is possible that pre-existing structures such as faults, folds, and other aspects of structural fabric in the basement underlying the BW influence the structural and geometrical characteristics we described in this chapter. However, the lack of coverage below 9ms of the Ceduna 3D MSS seismic survey, the limitations on the seismic data with depth and the lack sampling and well data restrict the ability to evaluate the role that potential pre-existing topography prior to the deposition of the BW detachment layer had in the internal deformation geometry, compaction, and evacuation rate of the BW.

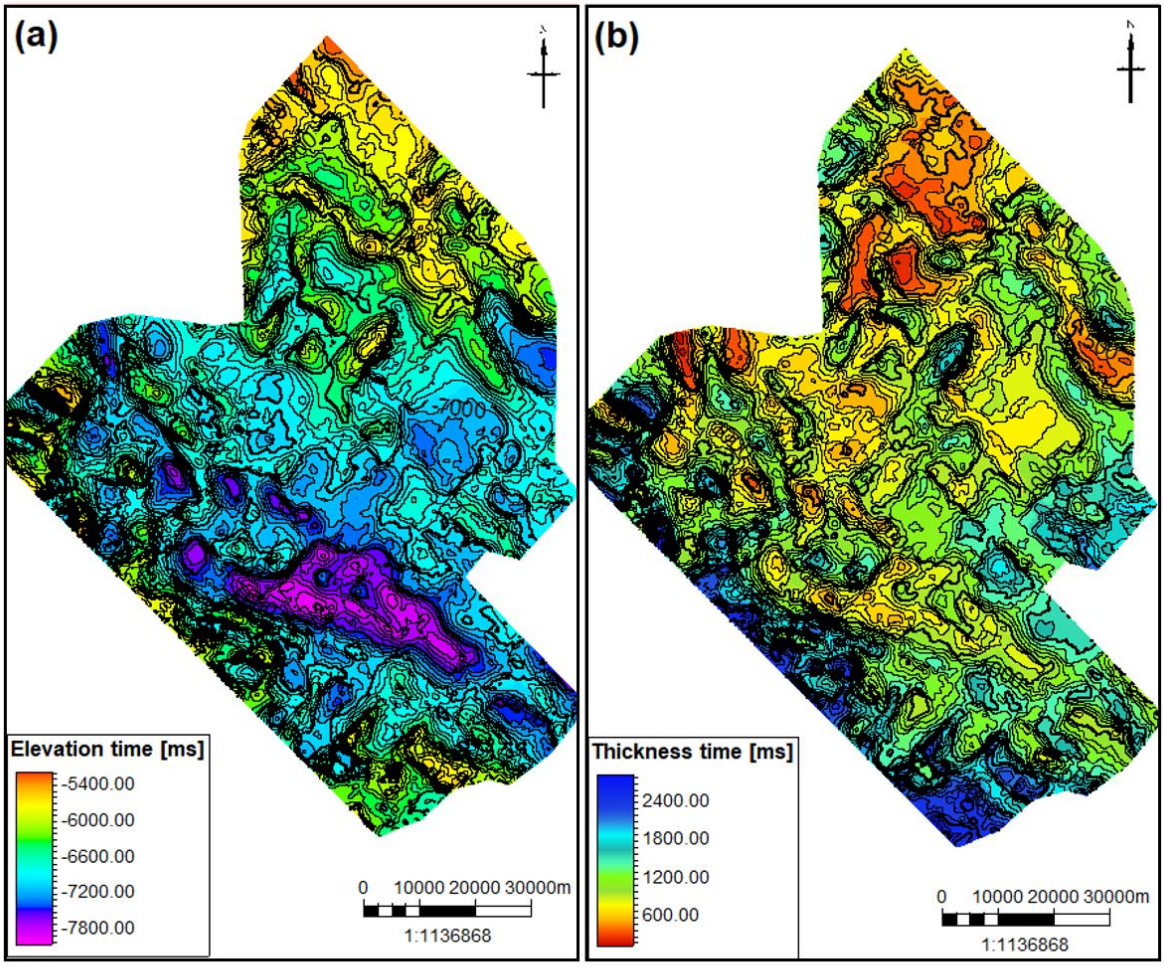

Figure 9: (a) Structural map of the top surface of the Blue Whale Supersequence (b) Thickness map of the Blue Whale detachment interval. Both maps have a contour interval of 100 ms.

White Pointer Supersequence

WP2 is characterised by low to medium seismic amplitude and gentle rollovers in the hangingwall of the fault segments, especially in the northeast region. WP1 displays strong rollover geometries in the hangingwall of normal growth faults and intercalation between reflectors of high (about 3600 to 6620 Hz) and low (about 950 to 1160 hz) to seismic amplitude (Figure 6b and c). WP2 show a more restricted changes in the seismic amplitude (about 1500 to 2290 Hz) in comparison to WP1 and in some cases represent the top sequence of the rollover structures in the hangingwall.

In general, WP exhibits stratigraphic dip angles of about 10° to 15° at the central and northeast regions with local pinch-outs and rotation of blocks in the hangingwall towards the southwest and southeast, where we also identify thinning of the southwestern region within each block between normal faults (Figure 6b). The structural map of the WP2 sequence shows a general deepening towards the south, with strong depth variation between the hangingwall and footwall of fault segments that coincides with changes in fault strike between different fault segments (Figure 10a). In the south and south-eastern regions, WP1 and WP2 show rotated blocks that strongly correlate with areas where the BW thickens to exhibit 'dome-like' structures (Figure 6b and d). The WP also display internal changes in dip angle at the centre and southwest that are possibly associated with changes from pre-kinematic

deposits above the top BW to syn-kinematic deposits within the middle and upper sequences (Figure 6b).

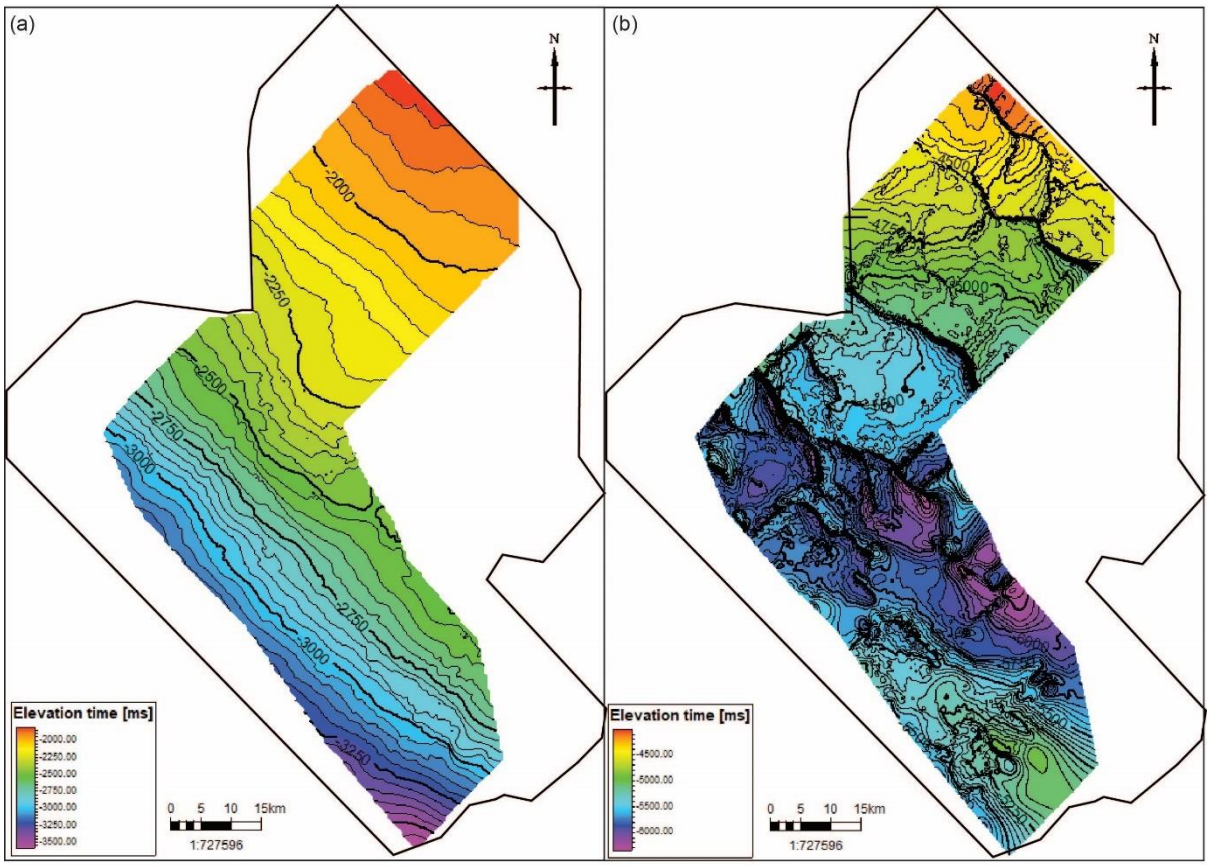

Figure 10: (a) Structural map (ms) of the top Hammerhead Supersequence (b) Structural map (ms) of the top White Pointer Supersequence. Both maps have a contourn interval of 50 ms and include the boundary of the Ceduna 3D MSS seismic survey for reference

Tiger Supersequence

The T1 and T2 sequences exhibit changes between high and low seismic amplitude reflectors across the study area where the northern and central regions exhibit more changes than in the south. In the southwestern and southern regions, we recognise some rotation of the Tiger Supersequence sequence within fault blocks, especially in the areas where the BW detachment thickens and exhibits dome-like structures (Figure 6b). T1 is the only stratigraphic sequence that is not visible across the whole study area. Towards the south we identify a decrease in the thickness of T1 between the footwall and hangingwall of some fault from the FG1 and FG2. For instance, in the southwest the thickness varies from 9307ms at the hangingwall to 456ms at the footwall, to the centre between about 500ms at the hangingwall to about 270ms at the footwall (Figure 11c) and towards the south and southeast from 85ms at the footwall to zero at the hangingwall (Figure 11b) (for more detail refer to Faults F15 and F16 in Chapter 2). These changes in thickness are outside the outline of this thesis, and can be attributed to potential stages of less to non-deposition, erosion and/or inversion of nearby normal faults.

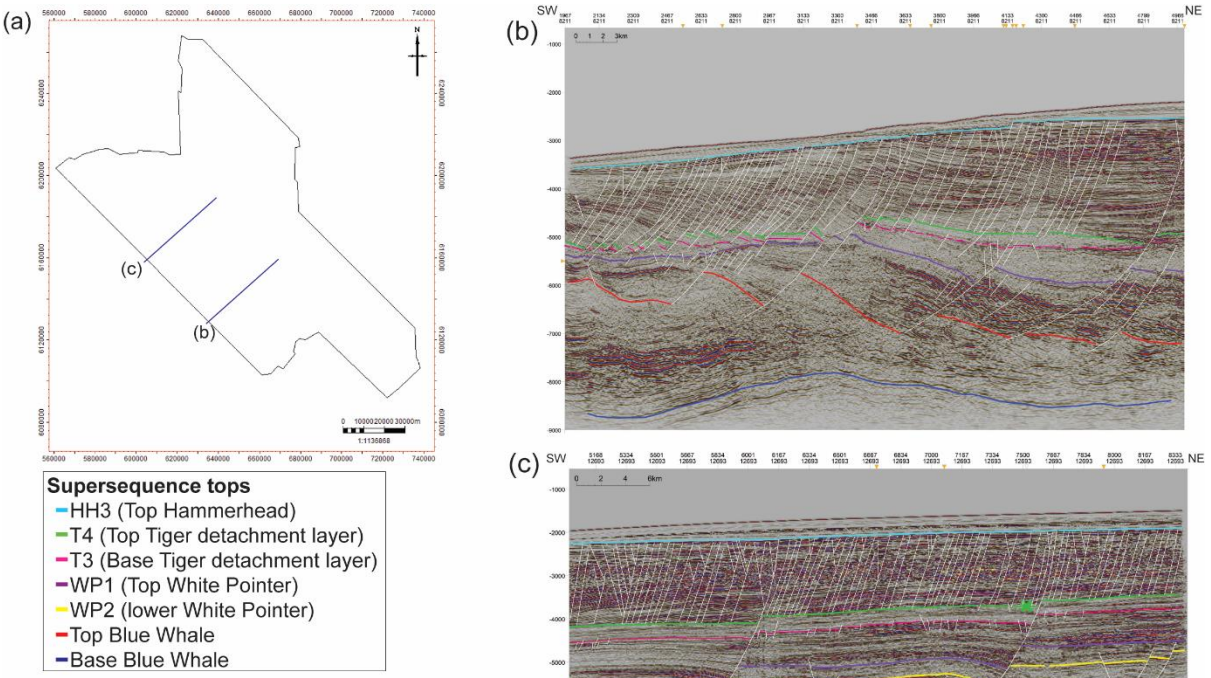

Figure 11: (a) 2D map displaying the cross-line (b) 8211 that shows visible changes in the thickness of the Tiger detachment layer towards the southwest and the (b) cross-line 12693 showing smaller changes in the thickness of the Tiger detachment layer in the central region of the study area.

T3 has high seismic amplitude reflectors, which contrast with the low seismic amplitude from the T2 sequence. The middle and lower T2 sequences show changes in seismic amplitude from high in the north to low in the south, with local high seismic amplitude reflectors especially in the southeast (Figure 6b, c and d).

T4 deepens toward the south (Figure 12a) and shows truncations and local changes of depth in the structural map due to normal faulting, especially towards the southern region. Using cross-lines, we interpret the T4 as a constant low seismic amplitude interval limited in depth with the first high seismic amplitude reflector, which represent the top of the T3 (Figures 6b and c). T4 exhibits a stratigraphic dip angle of about 5° towards the south across the study area. In the northern and central regions, the Tiger Supersequence detachment does not show major changes in seismic amplitude and exhibits a gentle thickness increase from north (about 210ms) to south (about 320ms), with the higher values in the southwest (430ms). Towards the south, we interpret a sharp decrease in thickness (to about 94 to 70ms) that might be related to the basinwards displacement of T4 due to detachment of FG3 segments (Figure 12b).

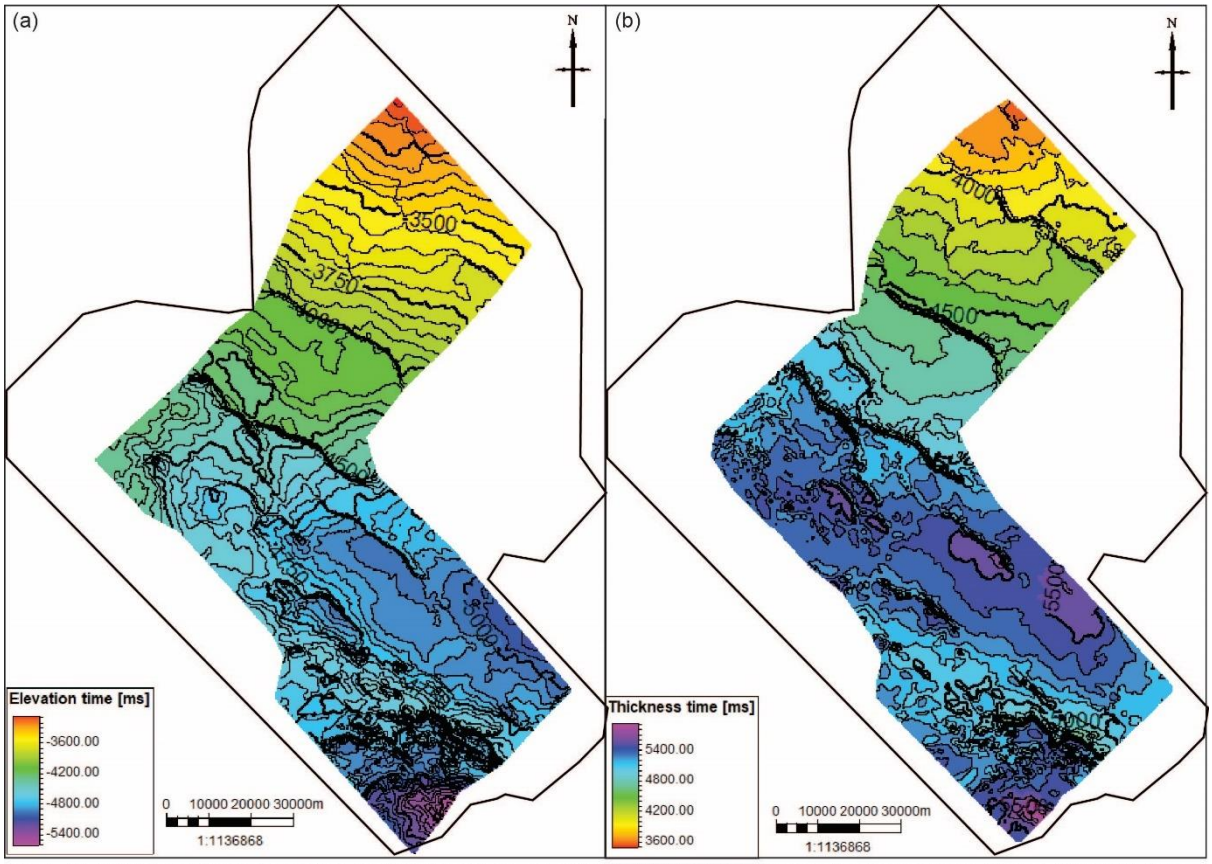

Figure 12: (a) Structural map (ms) of the top Tiger Supersequence (T4) (b) Thickness map of the Tiger detachment interval (T4 to T3). Both maps have a contourn interval of 50 ms and include the boundary of the Ceduna 3D MSS seismic survey for reference.

Hammerhead Supersequence

HH1 is characterised mostly by high seismic amplitude reflectors delineating clinoform structures dipping towards the southwest that show down-lapping reflector geometries terminating within T4 (Figure 6b, c and d). These features are more visible in the north-eastern region.

Above HH1, we identify reflectors with high seismic amplitude where the upper most sequence is sub-parallel to HH3 and pinch-out against HH3 in the southern and south-eastern regions. HH2 is also characterised by chaotic high seismic amplitude reflectors that potentially represent mass transport sedimentary deposits (Figure 6b, c, and d).

The structural map of the top-HH3 shows a gentle deepening from north to south where we did not identify major changes in terms of seismic amplitude or major stratigraphic geometries. We also identify minor changes in displacement as FG2 and FG3 terminates at this sequence (Figure 10b). In the southern region, we interpreted volcanic cones above the HH3 (Chapter 4), which complicated the interpretation of underlying horizons due to the disruption to coherence by high seismic velocity distortion and loss of primary signal energy that masked the sequence between HH3 and HH1 reflectors.

Well log expression of the potential changes in lithology of the interpreted supersequences.

The lack of drilled wells near the study area, make it difficult to differentiate with confidence the changes in lithology between the different sequences we identify using the seismic data. Therefore,

our correlation between sequences and the different stratigraphical variations and seismic amplitude changes are mainly based in the seismic interpretation of the 2D seismic lines near the wells Gnarlyknots-1A and Potorro-1.

White Pointer Supersequence

In general, the wireline logs from the WP exhibit a decrease in the travel time log and oscillation in the Gamma-Ray log that might implies possible intercalation between sandstones and shales where the Porotoo-1 well is located. The wireline logs acquired at Potoroo-1, WP1 exhibits minor changes in the sonic transit time and evidence of sandstone content at the base and a shaly lithology at the top from the Gamma-Ray well logs. (Figure 4).

Tiger Supersequence

The T1 sequence does not exhibit changes in the travel time logs, and it is characterised by a shaly lithology at the base and intercalated sandstones and shales within the middle and top sequences. T2 shows an increase in the travel time logs and potential intercalation between sandstones and shales according to the interpretation of the Gamma-Ray wireline logs at Potoroo-1 and Gnarklyknots-1A wells. T3 exhibits constant travel time at Gnarlyknots-1A whereas prominent changes in the travel time log at Potoroo-1, along potential intercalation of sandstones and shales from the interpretation of the Gamma-Ray wireline log. T4 appears to comprise sandstones shown by a relative decrease in the Gamma-Ray log (Figure 4).

Hammerhead Supersequence

HH1 sequence comprises shales at the base and sandstones at the top. HH2 exhibits high Gamma-Ray response at the base that might be related to high shale content which differs from the more sandstone prone lithology at the top. The Gamma-Ray logs in HH3 slightly decrease which might suggest a similar sandstones lithology than the top of HH2. (Figure 4).

Analysis of the interpretation in the Ceduna Sub-basin

The interpretation of the Ceduna 3D seismic survey allows the interpretation of normal growth faults in deltaic systems like the Hammerhead and White Pointer Delta systems across a wide region of the delta top. The large number of normal growth faults we have interpreted in this study (a total of 530 fault segments) permits a detailed analysis of the structural characteristics of normal faults within the delta top. The detailed interpretation of faults segments was also very valuable in carefully delineating appropriate fault segments, which are utilised for the following chapters of this thesis. For instance, for the Kinematic Analysis (Chapter 2) we interpreted normal fault segments from each of the fault groups we described above (FG1, FG2 and FG3) that are widely found within the study area. Given that the kinematic analysis compares the fault displacement against other parameters such as depth and distance along strike, we chose faults that were isolated segments from other synthetic and

antithetic fault segments that can locally modify fault displacement. For the Geomechanical Analysis (Chapter 3) we selected fault segments with lengths along strike between 1 km and 6km, which were widespread within the study area. To visualize how the changes in some structural parameters impact the risk of fault reactivation we select segments that displaced the Tiger and/or WP supersequences, show principal strike directions either parallel, oblique, or perpendicular to the maximum horizontal stress orientation; display sub-planar or listric geometries, and exhibit local changes in dip angle and strike along the fault plane. In addition, we wanted to predict the risk of fault reactivation in cases where structural traps hold hydrocarbons. Therefore, we included fault segments that show closure against fault planes in the structural maps. Finally, to identify eruptive centres and intrusions in the study area, we referred to the preliminary seismic interpretation to locate areas where magma transport occurred (Chapter 4). Here, normal growth faults near these magmatic intrusions and extrusions were used to determine the potential influence of faults on the transport of magma, while the thickness and structural maps were used to define the influence of the Tiger detachment layer in the emplacement of igneous bodies.

Interpretation of normal growth faults

Previous studies have compared the GAB with the Gulf of Mexico, and the Niger Delta and Baram Delta systems on the basis that interpreted normal growth faults that developed within the delta top and deep-water fold-thrust belts that form in the delta toe (R. King and Backé, 2010; MacDonald et al., 2012b; Robson, 2017). We compared our results with these studies to try and identify similarities that would enable us to understand the implications that normal growth faults have on the development of delta systems in passive margins, and therefore, on the development of petroleum systems.

We propose that the normal growth faults within the Gulf of Mexico, and within the Niger Delta and Baram Delta systems, show similar characteristics to the fault segments we interpreted in this study. These studies suggest that normal faults within the delta top exhibit listric geometries with low intersection angles at the top of detachment layers, syn-kinematic sequence forming rollover structures in the hangingwall and antithetic faults that resulted from the formation of synthetic faults as a response to sediment loading *(Crans et al., 1980; Cohen and McClay, 1996; Sapin et al., 2012).* In this study, we interpret listric and planar geometries that relate to rollovers and rotated block structures in the hangingwall. The fault segments in the GAB extend from 800 m to 20.8 km along strike and show wide variation in strike orientations. We also identified antithetic faults especially at the HH that are either crossed by synthetic faults, rest along pre-existing normal growth faults or formed at the upper tip of nucleated faults (Figure 6c). We propose that the interaction between antithetic and synthetic faults can result from episodes of fault growth that will depend on local gravity sliding.

The wide variations in normal growth faults characteristics within the GAB prove that it was of great importance to classify the fault segments in three different fault groups using the ages of the sedimentary sequence they displaced and recognising changes in their geometry, strike and dip angles. This thesis will address how the fault characteristics parameters in understanding the development of normal growth fault systems, and so have implications for the evolution of sedimentary basins in passive margins and therefore, successful hydrocarbon exploration of delta systems. In the following chapters we will detail these implications using different methods such as

Kinematic Analysis (Chapter 2), Fault Reactivation (Chapter 3) and a detailed interpretation of an example of magma emplacement in sedimentary basins such as the GAB (Chapter 4).

Interpretation of the detachment layers

Analogue models have described the importance of detachments in the formation of delta systems to initiate slope failure. These models produce outcomes that match our interpretation; where the detachment thins basinwards forming the necessary space to accumulate sediment, allowing several slip planes to be active at the same time *(Cohen and McClay, 1996a; Crans et al., 1980; Mandl and Crans, 1981; McClay et al., 1998).* We note that a recent study has suggested that the BW detachment evacuation occurred in two phases including processes of massive shale mobilization and fluidization. These events resulted in the formation of internal unconformities, shale diapirs, wedges and ridges along the BW detachment layer *(Dinc et al., 2023).* This thesis will describe the importance of appropriately characterised and mapped detachment layers in delta systems. We suggest that changes in the Tiger and BW Supersequence detachments in terms of thickness, seismic amplitude (potentially related to changes in lithology) and the presence of internal structures such as thrust faults and dome-like structures, influence the characteristics of the normal growth faults and sediment accumulation. For instance, our structural maps and seismic interpretation propose rotation of faulting blocks, stratigraphic pinch-outs, changes in stratigraphic thickness and an increase in the number of planar faults related to thicker areas of the BW that are also correlated with internal dome-like structures within the BW detachment layer (Chapter 2). Additionally, we identify changes in the Tiger detachment and recognise thinning in the southern and south-eastern regions where the Late Santonian-Maastrichtian fault segments detach (Chapter 2). These changes in the characteristics of the detachment layers might also have implications in other events such as the transport and emplacement of magma in the area. For instance, in Chapter 4 we propose that the de-gassing and de-watering and thinning of the Tiger detachment layer underlying the area where the igneous bodies are located, might influence the emplacement of intrusions in the HH instead of the T4 where we predict a higher shale content.

Summary

- We recognised and identified that the properties of normal growth faults have major implications for the development of delta systems. These concern the interaction between the accumulation, detachment characteristics and interaction with and/or development of other fault segments.
- We believe that it is essential to systematically interpret and describe the characteristics of normal growth faults and underlying detachment layers to understand the structural configuration of the top of delta systems. This detailed interpretation provided the opportunity to classify fault segments (FG1, FG2 and FG3) and define structural patterns that were essential to select the most suitable interpreted fault segment candidates for additional analysis in the following chapters.
- We classified normal growth faults in the GAB by the age(s) of the sedimentary sequence they displaced as Group 1 (FG1): Cenomanian-Late Santonian, Group 2 (FG2): Cenomanian-Maastrichtian, and Group 3 (FG3) Late Santonian-Maastrichtian.

References

Bally, A.W., Bernoulli, D., Davis, G.A., Montadert, L., 1981. Listric Normal Faults. Oceanol. Acta 16.

Caine, J.S., Evans, J.P., Forster, C.B., 1996. Fault zone architecture and permeability structure. Geology 24, 1025–1028.

Cohen, H.A., McClay, K., 1996. Sedimentation and shale tectonics of the northwestern Niger Delta front. Mar. Pet. Geol. 13, 313–328. https://doi.org/10.1016/0264-8172(95)00067-4

Crans, W., Mandl, G., Haremboure, J., 1980. On the theory of growth faulting: a geomechanical delta model based on gravity sliding. J. Petrleum Geol. 2,3, 265–307.

Dinc, G., Callot, J.-P., Ringenbach, J.-C., 2023. Shale mobility: From salt-like shale flow to fluid mobilization in gravity-driven deformation, the late Albian–Turonian White Pointer Delta (Ceduna Subbasin, Great Bight, Australia). Geology XX. https://doi.org/10.1130/G50611.1

Espurt, N., Callot, J.-P., Totterdell, J., Struckmeyer, H., Vially, R., 2009. Interactions between continental breakup dynamics and large-scale delta system evolution: Insights from the Cretaceous Ceduna delta system, Bight Basin, Southern Australian margin: Continental breakup and delta system. Tectonics, TC6002 28. https://doi.org/10.1029/2009TC002447

Fossen, H., 2010. Structural Geology. Cambridge University Press, NY, Cambridge.

GAB 3D Survey Final Report (Seismic Processing), 2012. . PGD Data Processing, Australia.

Gawthorpe, R.L., Leeder, M.R., 2000. Tectono-sedimentary evolution of active extensional basins. Basin Res. 24.

Harding, 1990. Identification of wrench faults using subsurface strauctural data:Crteria and Pitfalla. AAPG Bull. 74, 1590–1609.

Hooper, E.C.D., 1991. Fluid migration along growth faults in compacting sediments. J. Pet. Geol. 14, 161–180. https://doi.org/10.1111/j.1747-5457.1991.tb00360.x

Huang, L., Liu, C., 2017. Three Types of Flower Structures in a Divergent-Wrench Fault Zone: The Third Type of Flower Structures. J. Geophys. Res. Solid Earth 122, 10,478-10,497. https://doi.org/10.1002/2017JB014675

King, R., Backé, G., 2010. A balanced 2D strucutral model of the Hammerhead Delta-Deepwater Fold-Thrust Belt, Bight Basin, Australia. Aust. J. Earth Sci. 1005–1012.

Koson, S., Chenrai, P., Choowong, M., 2014. Seismic Attributes and Their Applications in Seismic Geomorphology 6, 9.

Litchfield, N.J., Villamor, P., Dissen, R.J.V., Nicol, A., Barnes, P.M., A. Barrell, D.J., Pettinga, J.R., Langridge, R.M., Little, T.A., Mountjoy, J.J., Ries, W.F., Rowland, J., Fenton, C., Stirling, M.W., Kearse, J., Berryman, K.R., Cochran, U.A., Clark, K.J., Hemphill-Haley, M., Khajavi, N., Jones, K.E., Archibald, G., Upton, P., Asher, C., Benson, A., Cox, S.C., Gasston, C., Hale, D., Hall, B., Hatem, A.E., Heron, D.W., Howarth, J., Kane, T.J., Lamarche, G., Lawson, S., Lukovic, B., McColl, S.T., Madugo, C., Manousakis, J., Noble, D., Pedley, K., Sauer, K., Stahl, T., Strong, D.T., Townsend, D.B., Toy, V., Williams, J., Woelz, S., Zinke, R., 2018. Surface Rupture of Multiple Crustal Faults in the 2016 Mw 7.8 Kaikōura, New Zealand, Earthquake. Bull. Seismol. Soc. Am. 108, 1496–1520. https://doi.org/10.1785/0120170300

MacDonald, J., Holford, S., King, R., 2012. Structure and Prospectivity of the Delta-Deep-Water Fold-Thrust Belt Systems, Bight Basin, Australia, in: New Understanding of the Petroleum Systems of Continental Margins of the World: 32nd Annual. SOCIETY OF ECONOMIC PALEONTOLOGISTS AND MINERALOGISTS, pp. 779–816.

MacDonald, J., King, R., Hillis, R., Backé, G., 2010. Structural style of the White Pointer and Hammerhead Delta—deepwater fold-thrust belts, Bight Basin, Australia. APPEA J. 50, 487. https://doi.org/10.1071/AJ09029

Mandl, G., Crans, W., 1981. Gravitational gliding in deltas. Geol. Soc. Lond. Spec. Publ. 9, 41–54. https://doi.org/10.1144/GSL.SP.1981.009.01.05

Marton, L.G., Tari, G., Lehmann, C.T., 2000. Evolution of the Angolan Passive Margin, West Africa, with Emphasis on Post-Salt Structral Styles, in: Geophysical Monograph Series, Atlantic Rifts and Continental Margins. American Geophysical Union, Washington DC, USA, pp. 129–149.

McClay, K., Dooley, T., Zamora, G., 2003. Analogue models of delta systems above ductile substrates. Geol. Soc. Lond. Spec. Publ. 216, 411–428. https://doi.org/10.1144/GSL.SP.2003.216.01.27

McClay, K.R., 1990. Deformation mechanics in analogue models of extensional fault systems. Geol. Soc. Lond. Spec. Publ. 54, 445–453. https://doi.org/10.1144/GSL.SP.1990.054.01.40

McClay, K.R., Dooley, T., Lewis, G., 1998. Analog modeling of progradational delta systems. Geology 26, 771. https://doi.org/10.1130/0091-7613(1998)026<0771:AMOPDS>2.3.CO;2

Morley, C.K., 2003. Mobile shale related deformation in large deltas developed on passive and active margins. Geol. Soc. Lond. Spec. Publ. 216, 335–357. https://doi.org/10.1144/GSL.SP.2003.216.01.22

Petrel, 2015. Recommended seismic volume atttrbiutes.

Robson, A., 2017. Normal fault growth analysis using 3D seismic datasets located along Australia's southern margin (thesis). University of Adelaide, School of Physical Sciences.

Robson, A., King, R., Holford, S., 2017. Structural evolution of a gravitationally detached normal fault array: analysis of 3D seismic data from the Ceduna Sub-Basin, Great Australian Bight. Basin Res. 29, 605–624. https://doi.org/10.1111/bre.12191

Ryan, L., Magee, C., Jackson, C.A.-L., 2017. The kinematics of normal faults in the Ceduna Subbasin, offshore southern Australia: Implications for hydrocarbon trapping in a frontier basin. AAPG Bull. 101, 321–341. https://doi.org/10.1306/08051615234

Sapin, F., Ringenbach, J.-C., Rives, T., Pubellier, M., 2012. Counter-regional normal faults in shale-dominated deltas: Origin, mechanism and evolution. Mar. Pet. Geol. 37, 121–128. https://doi.org/10.1016/j.marpetgeo.2012.05.001

Sarhan, M.A., 2017. The efficiency of seismic attributes to differentiate between massive and non-massive carbonate successions for hydrocarbon exploration activity. NRIAG J. Astron. Geophys. 6, 311–325. https://doi.org/10.1016/j.nrjag.2017.06.003

Thorsen, C.E., 1963. Age of Growth Faulting in Southeast Louisiana 13, 8.

Totterdell, J.M., Krassay, A.A., 2003. The role of shale deformation and growth faulting in the Late Cretaceous evolution of the Bight Basin, offshore southern Australia. Geol. Soc. Lond. Spec. Publ. 216, 429–442. https://doi.org/10.1144/GSL.SP.2003.216.01.28

Vendeville, B., Cobbold, P.R., Davy, P., Choukroune, P., Brun, J.P., 1987. Physical models of extensional tectonics at various scales. Geol. Soc. Lond. Spec. Publ. 28, 95–107. https://doi.org/10.1144/GSL.SP.1987.028.01.08

Weber, K.J., Mandl, G.J., Pilaar, W.F., Lehner, B.V.F., Precious, R.G., 1978. The Role of Faults in hydrocarbon migration and trapping in Nigerian growth fault structures, in: Offshore Technology Conference. Presented at the Offshore Technology Conference, Offshore Technology Conference, Houston, Texas. https://doi.org/10.4043/3356-MS

Woillez, M.-N., Souque, C., Rudkiewicz, J.-L., Willien, F., Cornu, T., 2017. Insights in Fault Flow Behaviour from Onshore Nigeria Petroleum System Modelling. Oil Gas Sci. Technol. – Rev. D'IFP Energ. Nouv. 72, 31. https://doi.org/10.2516/ogst/2017029

Wood, L.J., 2012. Shale tectonics, in: Regional Geology and Tectonics: Phanerozoic Passive Margins, Cratonic Basins and Global Tectonic Maps. Elsevier, pp. 42–61. https://doi.org/10.1016/B978-0-444-56357-6.00002-0

Chapter 2: Kinematic analysis

Kinematic analysis of normal growth faults and their implications in the progression of delta systems and the hydrocarbon exploration using as case study the Great Australian Bight Basin

Part of the results from this chapter were submitted and presented in the APPEA and AEGC conferences in 2021 (Refer to list of publications)

Statement of Authorship

Title of Paper	Kinematic analysis of normal growth faults and their implications in the progression of delta systems and the hydrocarbon exploration using as case study the Great Australian Bight Basin
Publication Status	☐ Published ☐ Accepted for Publication ☐ Submitted for Publication ☑ Unpublished and Unsubmitted work written in manuscript style
Publication Details	

Principal Author

Name of Principal Author (Candidate)	Monica Jimenez Lloreda		
Contribution to the Paper	• Data interpretation • Development of methodology • Manuscript drafting		
Overall percentage (%)	70%		
Certification:	This paper reports on original research I conducted during the period of my Higher Degree by Research candidature and is not subject to any obligations or contractual agreements with a third party that would constrain its inclusion in this thesis. I am the primary author of this paper.		
Signature		Date	09/01/2023

Co-Author Contributions

By signing the Statement of Authorship, each author certifies that:

i. the candidate's stated contribution to the publication is accurate (as detailed above);

ii. permission is granted for the candidate in include the publication in the thesis; and

iii. the sum of all co-author contributions is equal to 100% less the candidate's stated contribution.

Name of Co-Author	Simon Holford		
Contribution to the Paper	• Supervision • Manuscript drafting • Method development		
Signature		Date	03/02/23

Name of Co-Author	Rosalind King		
Contribution to the Paper	• Supervision • Manuscript drafting		
Signature		Date	8/2/23

Name of Co-Author	Mark Bunch		
Contribution to the Paper	• Supervision • Manuscript drafting		
Signature		Date	17/03/2023

Kinematic analysis of normal growth faults and their implications in the progression of delta systems and the petroleum hydrocarbon exploration using as case study the Great Australian Bight Basin

Monica Jimenez[1,2], Simon Holford[1,2], Rosalind King[1,2], Mark Bunch[1,2]

[1] Structural, Stress and Seismic Research Group, University of Adelaide (S3)

[2] Discipline of Earth Sciences, University of Adelaide

Abstract

Normal growth faults control the structural and stratigraphic configuration of delta systems and can strongly impact the hydrocarbon system of sedimentary basins. In this paper we use as a case study the Ceduna Sub-basin that contains two stacked delta systems to interpret 530 fault segments using the Ceduna 3DMSS seismic survey. We propose three different fault groups based on the ages of the displaced sedimentary sequences: (i) Cenomanian-Late Santonian, (ii) Cenomanian-Maastrichtian, and (iii) Late Santonian-Maastrichtian. We use kinematic analyses such as Displacement-Distance, Displacement-Depth and Expansion index to demonstrate that the Cenomanian-Late Santonian and Late Santonian-Maastrichtian fault segments constantly grew during their active periods, while the Cenomanian-Maastrichtian fault segments show three different evolution styles that correlate with the localization of the segments and the characteristics of the underlying detachment layer (Blue Whale Supersequence). The three evolution styles are as follows: (1) In the northern region, where the Blue Whale detachment is thin and shows homogeneous seismic amplitudes, the normal growth faults grew constantly; (2) in the central region, where the Blue Whale detachment shows a medium thickness with changes in seismic amplitude with some internal thrust faults and dome-like structures, the faults segments evolution style display two events of dip-linkage at the base and top of the Tiger Supersequence. (3) In the southern region, where the Blue Whale detachment is thicker, shows strong changes in seismic amplitude and internal dome-like structures and thrust faults, the fault segments evolved by one event of dip-linkage at the top of the Tiger Supersequence and one event of reactivation during the deposition of the upper Hammerhead Supersequence sequence above. We also demonstrate that these variations in the evolution style have implications for the hydrocarbon system of the Great Australian Bight by comparing periods of hydrocarbon generation and migration with results from the evolution analysis of the Cenomanian-Maastrichtian fault segments. We demonstrate that the faults which constantly grew are likely to have trapped hydrocarbons that migrated between the Maastrichtian-Pleistocene, while fault segments that show events of dip-linkage and reactivation are expected to have worked as migration pathways for secondary and tertiary hydrocarbon migration within the study area.

Introduction

Growth faults control several elements of the hydrocarbon system such as the distribution of source, reservoir and seal rocks, accumulation of syn-kinematic sequences, and the formation of structural traps for hydrocarbons *(Thorsen, 1963; Ryan et al., 2017; Ze and Alves, 2019)*. Therefore, one of the main considerations in an effective hydrocarbon system is to understand how fault-dependant traps evolve *(Magoon, 1988; Hallett, 2002).*

The kinematic analyses of growth faults such as Displacement-Distance (D-x), Displacement-Depth, (D-z), Expansion Index and thickness maps, allow a more precise understanding of fault evolution, and distinguishes between periods of nucleation, propagation and reactivation in the evolution of faults *(Jackson et al., 2017; Robson et al., 2017).* Such analyses have been proven in analogue models and some production fields in Lybia to provide the main factors involved in potential seismic hazards, breakdown of hydrocarbon seals, and the secondary or tertiary migration periods of hydrocarbons *(Walsh and Watterson, 1991; Bruhn and Schultz, 1996; Hallett, 2002).* In recent years, there has been progress in the implementation of kinematic analysis to understand how normal growth faults grow. However, these studies refer mostly to analogue models and basins where normal faults that are not associated with mechanically weak detachments such as Trescleoux in France, Lancashre and northeastern England in UK, North Sea and California *(Peacock and Sanderson, 1994; Imber et al., 2003; Fazlikhani et al., 2017; Roche et al., 2017).* Therefore, there are still uncertainties related to how growth faults evolve in delta systems that contain detachment layers such as the Great Australian Bight, the Niger Delta, Angola and the Gulf of Mexico *(Rouby and Cobbold, 1996; Totterdell et al., 2000; Alzaga-Ruiz et al., 2009; Dutton and Trudgill, 2009; Wiener et al., 2011; Fazli Khani and Back, 2015; Robson et al., 2017; Ryan et al., 2017).*

The Great Australian Bight (GAB) display stacked deltaic sequences with a detachment unit at the base. This ductile, mechanically weak detachment allows the accommodation of displacement that results in the formation of listric growth faults on the delta top and gravity-driven sliding of the underlying detachment towards the centre of the basin where the slope of the basin floor changes to form fold thrust belts (DWFTB) *(King and Backé, 2010; MacDonald et al., 2010)*. Similar sedimentary basins worldwide containing deltas and fold thrust belts systems have proven that the normal growth faults in the delta top are effective traps for hydrocarbons (e.g. such as in the Niger Delta, Gulf of Mexico, and offshore Angola) *(Cohen and McClay, 1996; Rowan et al., 1998; Marton et al., 2000; Alzaga-Ruiz et al., 2009; Mourgues et al., 2009; Wood, 2012).* These systems could be adopted as analogue systems to advise of exploration potential and risks related to possible fault-dependent plays and timing between fault growth and hydrocarbon migration in the GAB. Therefore, a more complete understanding of temporal and spatial variations in fault geometry and fault kinematics is essential in constraining such exploration risks, thereby attracting future exploration in the GAB.

Two recent studies from *Robson et al., (2017)* and *Ryan et al., (2017)* analysed the kinematic evolution of normal growth faults in the delta top of the Ceduna Sub-basin. Both studies provided a starting point in understanding the development of structural traps in the study area. *Ryan et al., (2017)* used 2D seismic lines and suggested three different fault groups: (1) faults that continuously grew between the Cenomanian and Maastrichtian at the centre of the Ceduna Sub-basin; (2) faults that were reactivated during the Campanian-Maastrichtian in the northeast and proximal areas to the delta source; and (3) faults that nucleated during the Turonian-Campanian in the southwest area of the

Ceduna Sub-basin. *Robson et al., (2017)* interpreted the 3D TRIM seismic survey over a small section in the Ceduna Sub-basin and proposed that the older listric faults that grew between the Cenomanian-Santonian ages control the location and timing of younger Late Santonian-Maastrichtian fault segments by upward propagation and dip-linkage. These two studies use spatially limited datasets in comparison to the Ceduna 3D MSS, which prompt an opportunity to study the nature of growth fault evolution in more detail over a much greater extent of the Ceduna Sub-basin delta system.

The Ceduna 3D MSS seismic survey was acquired over an area of 12,030 km^2 across the central-north section of the Ceduna Sub-basin (Figure 1a). Our study focuses mainly on the vertical growth and interaction of fault segments in cross section view to examine whether these faults evolved by constant growth or by episodic reactivation and examine whether they vertically interact with other fault segments. We show the results of kinematic analysis for 20 fault segments that are widely distributed along the Ceduna 3D seismic survey and represent three faulting periods: (1) Cenomanian-Late Santonian (2) Cenomanian-Maastrichtian, and (3) Late Santonian-Maastrichtian. We also acknowledge that the evolution style of Cenomanian-Maastrichtian fault segments we have interpreted strongly correlates with the current characteristics of the remaining detachment layer underneath (thickness, seismic amplitude, dip angle and presence of internal structures), while small Cenomanian-Late Santonian and Late Santonian-Maastrichtian segments exhibit constant growth. We also compare each of the evolution styles of faults we describe – Cenomanian-Maastrichtian fault segments that constantly grew during their active stage, 3 dip-linked fault segments and 2 dip-linked evolution patterns, Cenomanian-Late Santonian nucleated faults, and Late Santonian-Maastrichtian fault segments – with results from preliminary studies describing potential source rocks and secondary hydrocarbon migration periods within the Ceduna Sub-basin. We predict how the evolution style of these faults could determine whether they acted as trapping structures or as secondary and tertiary migration pathways for hydrocarbons at the time of hydrocarbon generation and expulsion.

Geological background

Delta systems commonly (non-exclusively) form in passive margins over gentle basinwards dipping surfaces that mimic a wedge-shaped model where a weak detachment enables the gravity-driven slide or glide of sediments towards the centre of the basin (e.g., evaporites or overpressured shale layers). Large scale delta systems such as the Niger Delta, Ceduna Sub-basin, Gulf of Mexico and Baram Delta, represent thin-skin models that link gravity-driven extensional faults in the delta top with Deep Water Fold Thrust Belts (DWFTB) in the delta toe. Analogue models suggest that this linkage depends on the rheological properties of the accreting material (e.g. pore pressure, material strength, and lithology), changes in thickness, friction coefficient, dip angle and dip direction of the detachment layer *(McClay et al., 2003; Alzaga-Ruiz et al., 2009; Espurt et al., 2009; King and Backé, 2010; MacDonald et al., 2010; Morley et al., 2011; Sapin et al., 2012; King and Morley, 2017).*

Analogue models that represent the extensional region indicate that the displacement of growth faults depends on the competitive rate between sedimentation and horizontal extension, as well as the geometry and nature of the basal detachment layer that controls the deformation of the sedimentary record above it *(Bally et al., 1981; Vendeville et al., 1987; McClay, 1990; McClay et al., 2003)*. Accretion of deltaic material continues, growth faults dipping basinwards form, displacing the

detachment towards the delta toe. This can result in the massive mobilization of shale basinwards and fluidization that result in the establishment of distal mini-depocentres, wedges, internal unconformities, ridges and shale volcanoes *(Dinc et al., 2023)*. It is possible to speculate that the displacement of the detachment layer would be proportional to the syn-kinematic width and strong changes in thickness along the hanging wall. On the contrary, a stagnant period of fault growth should correspond to a decrease in sediment supply or a sediment starvation period and slow to minimum basinwards displacement of the detachment layer *(Crans et al., 1980; Mandl and Crans, 1981; McClay et al., 2003; Morley, 2003; Totterdell and Krassay, 2003; Espurt et al., 2009).*

In terms of normal fault propagation in the extensional region of delta systems, these analogue models estimate that listric faults cause rollovers in the hangingwall of normal growth faults. They also propose that the displacement of normal growth faults should decrease upwards, indicating that these faults propagate from the base *(McClay and Ellis, 1987)*

Geological characteristics of the study area

The Great Australian Bight (GAB) extends 250,000 km^2 along the Southern Australian Margin and is split into four independent depocentres: the Eyre, Ceduna, Recherche, and Duntroon sub-basins that formed between the Middle Jurassic and the Late Cretaceous (late Santonian) epochs (Figure 1a and 1b) *(Totterdell and Krassay, 2003; Tottendell and Mitchel, 2009 "Department for Energy and Mining," 2020).*

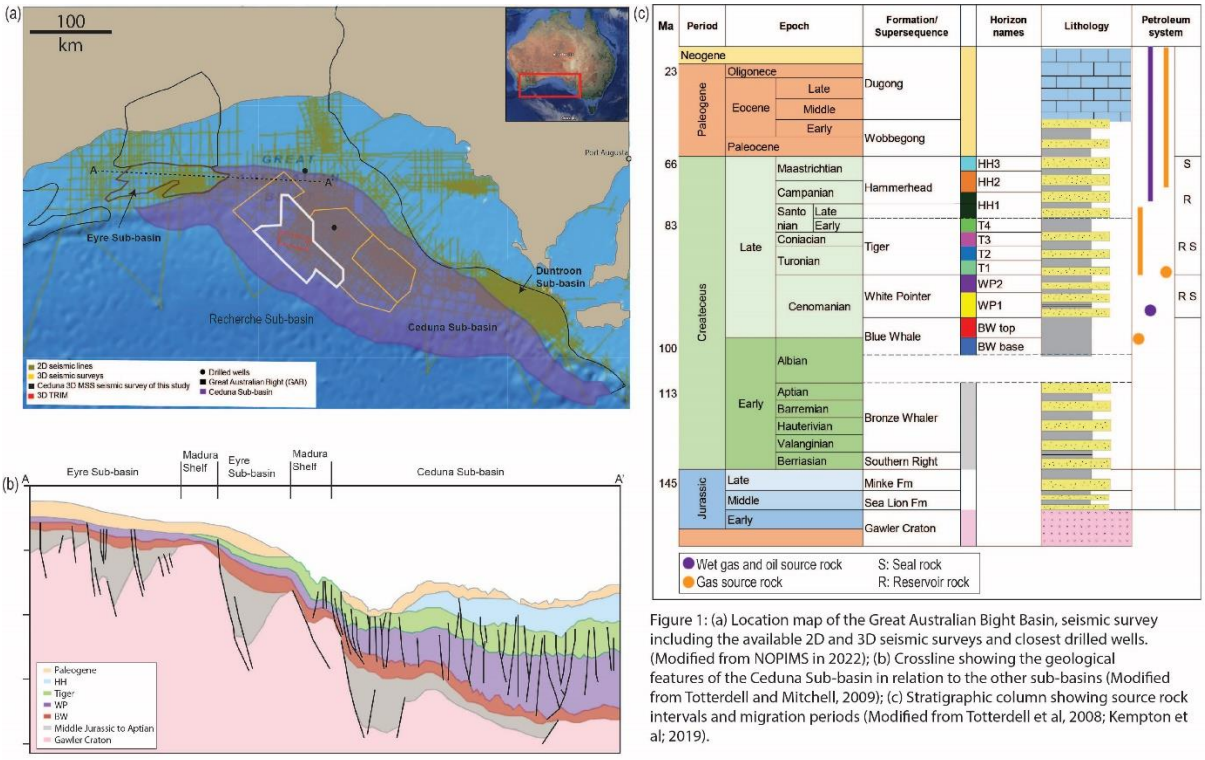

Figure 1: (a) Location map of the Great Australian Bight Basin, seismic survey including the available 2D and 3D seismic surveys and closest drilled wells. (Modified from NOPIMS in 2022); (b) Crossline showing the geological features of the Ceduna Sub-basin in relation to the other sub-basins (Modified from Totterdell and Mitchell, 2009); (c) Stratigraphic column showing source rock intervals and migration periods (Modified from Totterdell et al, 2008; Kempton et al; 2019).

The Ceduna Sub-basin (CSB) is the largest depocentre in the GAB, with a total sedimentary section of approximately 15.0 km that accumulated from the Late Jurassic to Pliocene epochs (Figure 1c) (Sayers et al., 2001; Tapley et al., 2005b). It is bound at the north by Proterozoic terranes, to the east by the Gawler Craton, to the south-east by the Duntroon Sub-basin, to the south by the Recherche Sub-basin, and to the west by the Eyre Sub-basin. It covers an area of 90,000 km^2 with a west-northwest to east-southeast orientation and depth between 0.2 and 4.0 km below sea level *(Totterdell and Krassay, 2003; Espurt et al., 2009).*

The evolution of the Great Australian Bight Basin can be divided in 4 main stages:

(1) The continental rifting between Australia and Antarctica began in the Middle to Late Jurassic, creating a triple junction between India, Australia and Antarctica. It established a northwest-southeast trend and it developed from west to east through continuous steps of crustal extension. The pre-existing basement fabric strongly controlled the extension regime, forming oblique half-grabens and rift basins along the Southern Australian Margin in the Great Australian Bight, and in the Otway, Gippsland, Bass, and Sorell basins (Totterdell and Krassay, 2003; Mitchell et al., 2009; Gibson et al., 2013). In the Ceduna Sub-basin, syn-rift fluvial-lacustrine sandstones and siltstones from the Sea Lion and Minke formations were deposited over the basement between the Middle and Late Jurassic (Figure 1c) *(Mitchell et al., 2009)*

(2) Fluvial sandstones from the Southern Right Supersequence were deposited during the Berriasian, followed by the fluvial and lacustrine sandstones and mudstones from the Bronze Whaler Supersequence between the Valanginian and Aptian during a slow thermal subsidence that also formed a west to east trending open sea (Figure 1c).

(3) The Blue Whale Supersequence (BW) was deposited unconformably over the Bronze Whaler Supersequence and marked the beginning of the rapid thermal subsidence during the Albian-Cenomanian to when global sea level rise ended in the Late Santonian (Figure 1c) *(Tapley et al., 2005; Espurt et al., 2009; Mitchell et al., 2009; Holford et al., 2011).*

The Cenomanian marked deposition of progradational fluvial to deltaic sediments with minor coal in the White Pointer Supersequence (WP) achieving a total thickness of around 4000 m in the CSB. This rapid deposition towards the southwest occurred in a short period and in conjunction with accelerated subsidence, allowing for overpressured conditions at the base of the Blue Whale Supersequence, forming the White Pointer Delta System *(Espurt et al., 2009; Holford et al., 2011)*. Between the Turonian and Santonian, major marine flooding caused deposition of the Tiger Supersequence conformably on top of the White Pointer Supersequence. In the Ceduna Sub-basin, the Tiger Supersequence corresponds to approximately 2800 m of progradational sandstones at its base and aggradational marine to marginal marine mudstones above (Figure 1c) *(Totterdell and Krassay, 2003; Espurt et al., 2009).*

The Late Santonian marked the end of global sea level rise, the commencement of the sea floor spreading between Australia and Antarctica, and the beginning of the passive margin stage of the Southern Australian margin (~83Ma). This is marked by an unconformity in the stratigraphic record

and the formation of gravity anomalies in the central area of the GAB (Figure 1c). The Late Santonian also established the division of the Great Australian Bight basin into three smaller areas that are structurally controlled by the basement architecture: Eyre, Ceduna and Recherche Sub-basins (Figure 1b) *(Espurt et al., 2009; Holford et al., 2011; J.M. Totterdell and Krassay, 2003).*

(4) From the Late Santonian to the Maastrichtian, sandstones, and mudstones from the Hammerhead Supersequence were deposited unconformably on the top of the Tiger Supersequence during a period with remarkably slow seafloor spreading. The Hammerhead Supersequence (HH) is composed at its base by a progradational unit that rapidly deposited towards the SE, forming the Hammerhead Delta System, that has reactivated and been intersected by some of the faults active in the Cenomanian (Figure 1b). The upper sequence comprises an aggradational deposition that correlates a decrease in the basinwards sedimentation rate and the change in the basin dynamics (Totterdell and Krassay, 2003; Tapley et al., 2005; Tottendell and Mitchel, 2009; Reynolds et al., 2017)

Between the end of the Cretaceous and the beginning of the Paleogene, a regional uplift event along the Southern Australian margin is responsible for the erosion of the upper sequence of the HH and Tiger supersequences, thus forming an angular unconformity between the Eucla and GAB basins *(Totterdell and Krassay, 2003)*. In the Ceduna Sub-basin, the Cenozoic Era marked a dramatic drop in the rate of sediment accumulation and thermal subsidence that resulted in a regional hiatus. During the early Eocene Epoch, the marginal marine to deltaic sandstones from the Wobbegong Supersequence were deposited *(Espurt et al., 2009)*, and in the middle Eocene, minor sandstones and cool water carbonates from the Dugong Supersequence accumulated during a period of marine transgression (Figure 1c). Today, the GAB Basin forms a large continental shelf (260 km extension) *(Totterdell and Krassay, 2003; Reynolds et al., 2017).*

Characteristics of the Ceduna Delta System

The Ceduna Sub-basin is characterised by two independent large-scale delta systems: The Cenomanian White Pointer Delta System and the Santonian-Maastrichtian Hammerhead Delta System *(Totterdell and Krassay, 2003; MacDonald et al., 2010).* The White Pointer Delta System was formed in the Cenomanian when the progradational WP rapidly deposited over the BW (Albian), forming normal growth faults with northwest to southeast, to west-northwest to east-southeast, strikes and a southwest dip direction (Figure 1b) *(Totterdell and Krassay, 2003; MacDonald et al., 2010; Ryan et al., 2017)*. The BW acts as the principal detachment layer of this delta system, due to its overpressured characteristics *(Espurt et al., 2009; ; Mitchell et al., 2009; MacDonald et al., 2010).*

The Hammerhead Delta System formed in the Late Santonian-Maastrichtian Age after the passive margin developed. It is divided into extensional and compressional regions with normal growth faults at the head of the delta and DWFTB at the delta toe. Faults fully or partially intersect the full thickness of the Hammerhead Supersequence (Late Santonian-Maastrichtian) and have northwest to southeast strikes and a dip direction towards the south-west. The base and top of the Tiger Supersequence (Turonian-early Santonian) act as detachment layers for the Hammerhead Delta System *(King and Backé, 2010; MacDonald et al., 2010).* In the study area, this detachment layer is visible predominantly in the south and south-east regions. We have focused our analysis on the evolution of normal growth faults that formed in the extensional region of both delta systems.

Hydrocarbon system in the Ceduna Sub-basin

Recent studies used 2D seismic lines to identify possible structural closures in the footwall at the Turonian (Tiger Supersequence), and younger crest closures at the hanging wall against southwest to northeast strike bounding faults. (Somerville, 2001a).

Preliminary studies using well data, geochemical and biostratigraphy analyses demonstrated that the best quality source rocks correspond to the Late Cenomanian to Turonian stratigraphic intervals. They also identify a potential reservoir between Cenomanian and Maastrichtian ages in the Ceduna Sub-basin *(Espurt et al., 2009; Mitchell et al., 2009; Klauser-Baumgärtner et al., 2019).* In the central Ceduna Sub-basin, they highlight strong evidence of hydrocarbon migration from Cenomanian (oil and gas) and Turonian (gas condensate) source rocks during the Campanian-Pleistocene, gas from Cenomanian, and oil and gas from Turonian source *rocks (Totterdell et al., 2008; Kempton et al., 2019; Bourdet et al., 2020).*

Exploration history

Exploration in the GAB started in 1960 but has been without economic discoveries due to invalid closures, lack of reservoir and source rock, and poor hydrocarbon migration routes. In the 2000s, the Australian government granted 11 exploration licenses, which permitted the acquisition of 2D and 3D seismic data and promoted new geological and geophysical studies that resulted in new unsuccessful drilled wells *(Tapley et al., 2005; Department for Energy and Mining, 2020; Geoscience Australia, 2020)*. It is evident that the spares well data coverage has become a challenge for a complete evaluation of the Hydrocarbon system in the basin *(Ryan et al., 2017)*.

Data set and methodology

To understand how normal growth faults developed in the Ceduna Sub-basin, we interpreted the Ceduna 3D MSS seismic reflection survey that was acquired as part of the BP Ceduna project between 2011 and 2012. This high-quality 3D seismic survey covers 12,030 km^2 *(GAB 3D Survey Final Report, 2012)* and it is located approximately 350 km southeast from Eucla and 380 km southwest from Ceduna in the offshore Great Australian Bight (Figure 1a). The seismic sampling is 2ms with a total vertical length of 9 seconds two-way-time (TWT) distributed along 16,025 cross-lines (perpendicular to the modal strike of faults) oriented 315°N and 3,400 inlines oriented 045°N, with a square bin spacing between in-lines and cross-lines of 12.5 metres (m).

Seismic interpretation

We interpreted the Ceduna 3D seismic survey every 16 cross-lines (200 m) which provides enough detail suitable for the kinematic analysis without losing critical resolution of the main regional structural outline in the area.

From the large number of fault segments visible in the 3D seismic survey, we mapped those with a length equal to or greater than 800 m along their strike. This cut-off allowed us to define the main fault trends in terms of strike and dip direction, and to differentiate between fault groups on the basis of the specific sedimentary sequences they displaced.

Well data

The closest drilled wells to the Ceduna 3D MSS seismic survey are Potoroo-1 and Gknarlyknots-1. Potoroo-1 was drilled in 1975 and it is located 71 km north of the Ceduna 3D seismic survey and targeted the Middle to Late Cretaceous interval. Gnarlyknots-1A was drilled in 2003 and it is located 42.2 km to the east-northeast of the Ceduna 3D seismic survey. It was drilled away from 3-way closures and terminated without reaching the lower targets of the WP and the lower Tiger supersequences (Figure 1a) (Tapley et al., 2005b).

Preliminary studies have shown that kinematic analyses are susceptible to bias in data sampling *(Ze and Alves, 2019).* Therefore, we mapped seven horizons including the tops of the four principal supersequences and seven sub-sequence stratigraphic tops that correlate to main changes in the seismic amplitude corresponding to variations in Sonic transit time (DT) and Gamma-Ray (GR, GRCDR) wireline log data. We use stratigraphy intersected by Potoroo-1 to interpret the sedimentary record between the base of the BW and top of the Tiger supersequences. Similarly, we use the Gknarklyknots-1A to define the sequences between the Tiger (Turonian) and top HH supersequences (Figure 2a). We interpret 2D seismic reflection survey lines W00FDW0003, W00FDW0092, W00FDW0023, W00FDW0027 and W00FDW0099 to correlate formation tops interpreted from Potoroo-1 and Gknarlyknots-1A wireline logs with seismic reflectors interpreted from the Ceduna 3D MSS seismic survey (Figure 2b).

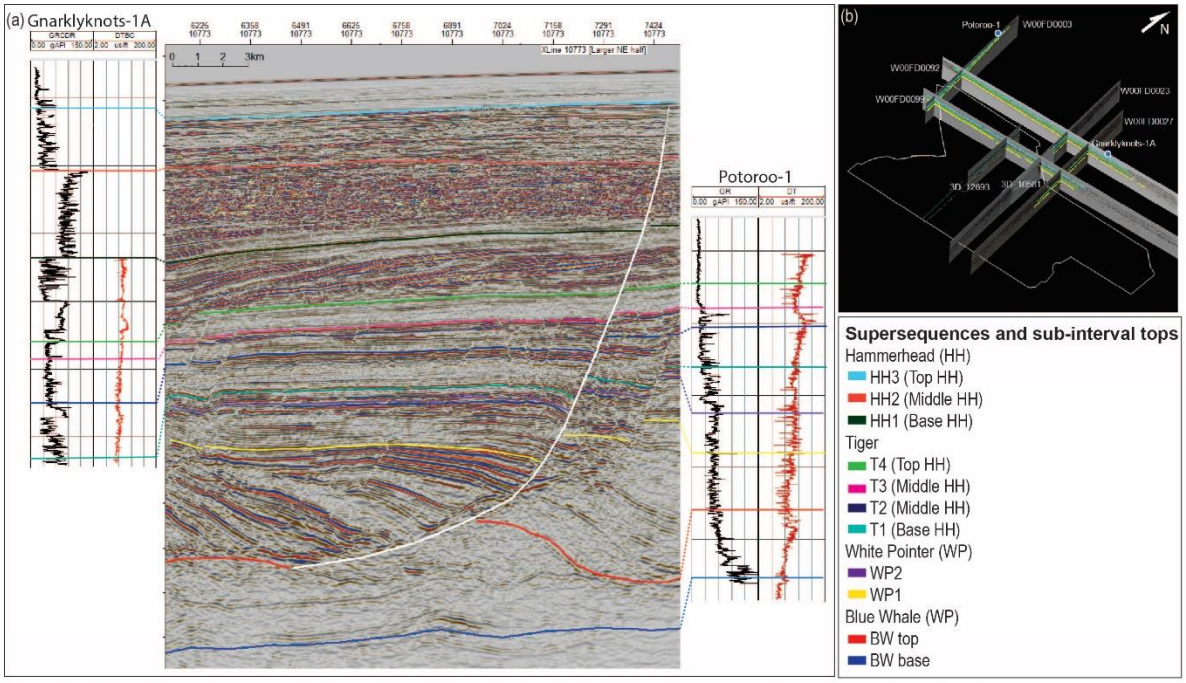

Figure 2: (a) Correlation between steps in Gamma-Ray (GR) and Sonic velocity (DT) wireline logs acquired at Potoroo-1 and Gnarlyknots-1A exploration wells. (b) Major reflectors interpreted on crossline 10773 of the Ceduna 3D MSS seismic survey. The crossline also shows stratigraphic geometries, thickness variations and changes in seismic amplitude.

Kinematic analyses techniques

Preliminary studies have described the use of kinematic analyses from seismic reflection survey data to define the evolution style of normal faults. They use the displacement measurements from control

points along a fault strike at several horizons to define growth and quiescence periods in the evolution of fault segments. These kinematic results depend mainly on the vertical and horizontal resolution of seismic data. Therefore, a zero displacement measurement will represent the minimum detectable fault throw at that specific part of the seismic reflection survey dataset *(Walsh and Watterson, 1991; Osagiede et al., 2014).*

Fossen, (2010) described fault displacement (D) as the relative motion of two adjacent points at each side of a fault. In this paper, we use this terminology and take vertical component between the hangingwall and footwall of a fault at points perpendicular to strike (on the horizontal axis) at equidistance control points (every 200m). In addition, we use the following terms as stages of fault growth (Figure 3d): (1) Continuous fault growth as a period of vertical and/or horizontal constant growth *(Jackson et al., 2017)*. (2) Reactivation as the period when a normal fault passes from a quiescence or fault nucleation stage to a period of growth. *(Bellahsen and Daniel, 2005; Baudon and Cartwright, 2008)*. (3) Dip-linkage refers to the event when an nucleated fault segment is dip-linked to a younger fault segment eventually becoming dip hard-linked through relay-ramp between them *(Mansfield and Cartwright, 1996; Camanni et al., 2019)* (Figure 3 a, b and c).

Several authors have recorded similarities between fault growth plots in time (TWT) and depth (m), especially in areas with minor changes in lateral velocity (Mahon and Wallace, 2020). In this study we measure the displacement data in time (ms), which provides more confidence in the collected data as no depth conversion has been undertaken. Thus, potential errors from a hypothetical velocity model may increase mistakes in the measurement of fault displacement and interval depth.

Figure 3: Diagram explaining the three kinematic analysis methods we used in this study. (a) Displacement-Distance, (b) Displacement-depth, (c) Expansion Index. (d) Diagram modified from Fossen (2010) to show the components of true displacement. In this study we will focus on the vertical component of displacement to measure the displacement (D) between the hangingwall and footwall.

We use three different kinematic techniques:

Displacement-distance (D-x) to describe the changes in displacement along strike, and compare these changes between the different interpreted sequences *(Jackson and Rotevatn, 2013; Fazlikhani et al., 2016; Wang et al., 2018)*. Preliminary studies suggest that a single normal fault should concentrate

the maximum displacement at the middle section with less displacement at the lateral tips *(Jackson et al., 2017)* (Figure 3a).

Displacement-depth (D-z) to identify changes in displacement between horizons. This technique enables the definition of (a) a continuous growth interval which is associated with an upwards increase in displacement with depth *(Jackson et al., 2017; Robson et al., 2017).*; (b) a reactivation interval that represents non-changes to minimum decreases in the displacement gradient between two continuous growth intervals *(Baudon and Cartwright, 2008; Robson et al., 2017).* (c) a dip-linkage event between an older nucleated fault and a young fault segment. This event is established by an interval of an upwards increase in displacement between two continuous growth intervals *(Mansfield and Cartwright, 1996; Tvedt et al., 2013).* We also define a minimum decrease in displacement as a change of less than +/-5 ms between consecutive units. This 5 ms cut-off also represents possible issues in the interpretation related to the vertical seismic resolution and human error. It is expected that a single normal fault should vertically concentrates the maximum displacement at the middle sequence and display less displacement at the top and base tips *(Jackson et al., 2017)* (Figure 3b).

Expansion index (EI) to recognize the magnitude of the growth of strata in a certain time interval on the hanging wall side of a normal fault. This method divides the total thickness of the hangingwall by the total thickness of the footwall to discriminate between a period of fault growth represented by an EI higher than one (EI>1) and a period of fault inactivity represented by an expansion index equals to one (EI=1) *(Thorsen, 1963; Jackson et al., 2017).* As a normal distribution of EI from base to top, a single fault segment should display the higher EI values in the middle section forming a bell-shaped curve with the minimum EI at the upper and lower tips *(Osagiede et al., 2014)*. We denote the EI results in two different ways: (a) By comparing the EI between units at each control point. This permits us to define possible dip-linkage between fault segments. (b) By comparing the EI values of each horizon along strike (EI-x). This allows us to identify possible horizontal linkage events that could affect the displacement measurements, and to establish periods when the fault was more active (Figure 3c). In this study we assume that when EI is less than 1, it represents a period of non-deposition or potential erosion of the sedimentary sequence at the hangingwall.

Limitations

The Ceduna 3D seismic survey can present some limitations related to the vertical and horizontal resolution associated with signal-noise ratio, burial depth, compaction, porosity and fluid content *(Osagiede et al., 2014)*. In addition, seismic processing can also challenge the seismic interpretation by forming fault shadow effects at the footwall in the upper levels. We also identify rollovers, folding, fault drag, and minor listric faults at the footwall, and antithetic faults at the hanging wall that can alter the fault displacement along the strike. Additionally, an overpressure condition and possible local changes in lithology of the detachment layers (BW and Tiger top sequences), might reduce acoustic impedance contrasts that inhibit the interpretation of fault tips in profile view and complicate accurate detection of seismic horizons (Figure 7)

Given the discussed limitations we estimate an error margin of ±10% for the interpretation of fault segments (location, geometry, tip depth) and horizons (observing from each side of the fault and extrapolation of stratigraphic intervals from a well outside the study and data area). This percentage also covers a +/- 5ms cut-off which we approximate in the measurement of fault displacement for kinematic analysis. This cut-off also considers the seismic time sampling (2ms) and the visual resolution from the interpretation software (Petrel®) that interpolates the processed data for viewing and interpretation.

Results

Characteristics of the Blue Whale and Tiger detachment layers

Blue Whale detachment layer

We interpret the top and base of the detachment layer and find a regional dip angle of approximately 5 to 10 ° towards the south (basinwards) where it is at its maximum thickness. Locally, we map "dome-like" and "depression-like" structures that strongly change the detachment thickness (Figure 4b). To the north, the top of the BW displays a low seismic amplitude reflection event. To the south and south-east the top-detachment reflector shows lateral changes in seismic amplitude with structural complexity that includes thrust faulting, folding, and local changes in the dip angle (e.g., from 10° to less than 5°) (Figure 7). To the south-east we also identify a large "dome-like" structure that mimics the antiform geometry of the underlying basement (Figure 4a). The lateral changes in lithology and geometry of the BW detachment agrees with the recent study of *Dinc et al., (2023)* that suggests that the presence of internal unconformities, shale diapirs, and internal structures such as ridges and wedges was due to processes such as the massive basinwards mobilization of shale and fluidization.

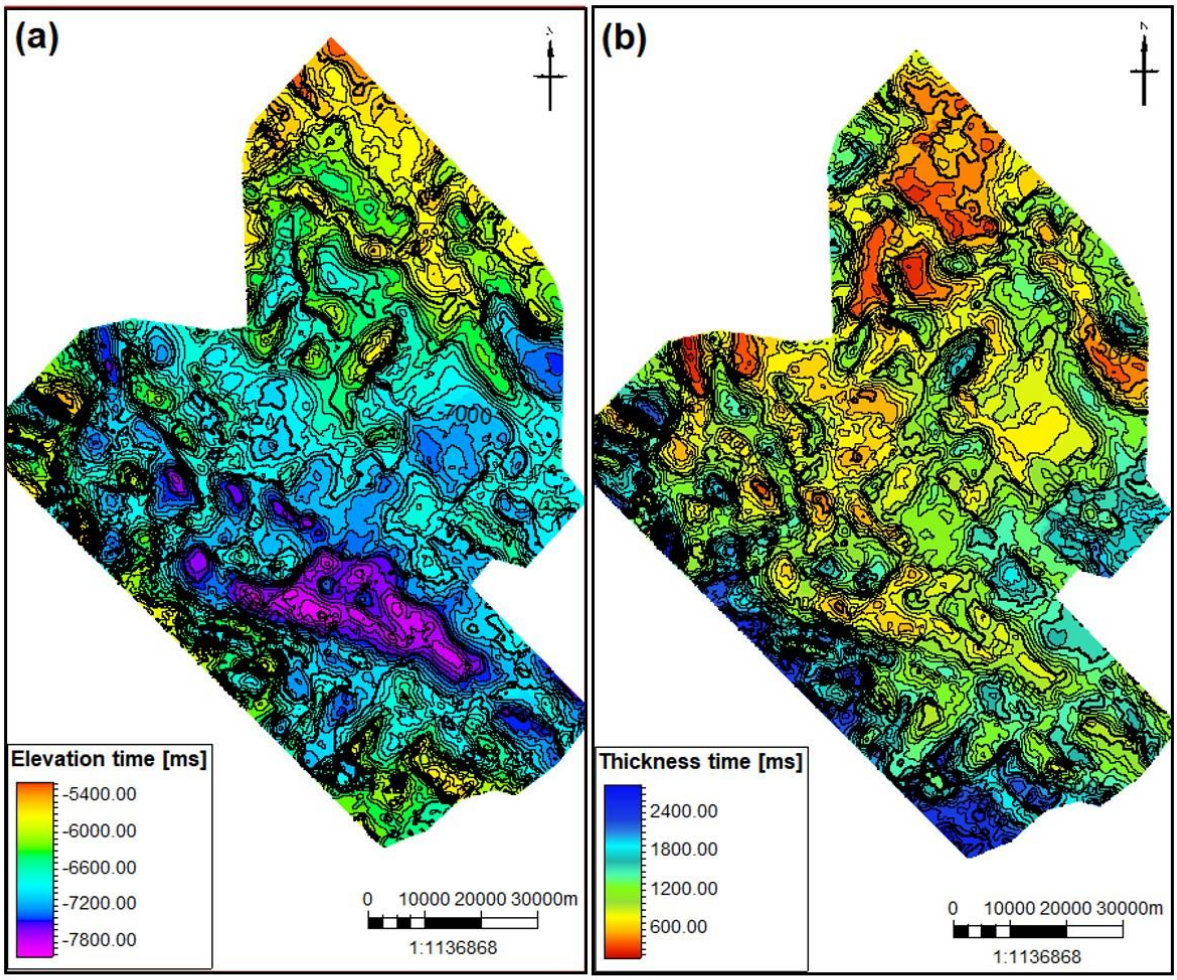

Figure 4: (a) Structural map (ms) of the top Blue Whale Supersequence. (b) Thickness map (ms) of the Blue Whale detachment interval. Both maps have a contour interval of 100 ms

Tiger detachment layer

The Tiger detachment unit corresponds to the upper Tiger sequence and display a dip angle of approximately 5° toward the southwest (basinwards). In the north and central areas, the Tiger detachment does not present major changes, and the Late Santonian-Maastrichtian fault segments seem to be mainly associated with Cenomanian-Late Santonian faults. However, in the south and southeast areas, the Tiger detachment works as a detachment unit for the Late Santonian-Maastrichtian fault segments (Figure 5a). In general, the upper Tiger sequence shows a low seismic amplitude with minimal lateral changes and non-visible thrust or fold structures (Figure 2a). The Tiger detachment layer thickness increases from north (approximately 210ms) to south (approximately 320ms) with the higher values towards the southwest (approximately 430ms). To the southeast, the Tiger detachment tilts approximately 5° to 10° that imitates the dome structures of the Blue Whale detachment layer and reaches a thickness of between 20 and 50ms (Figure 5b).

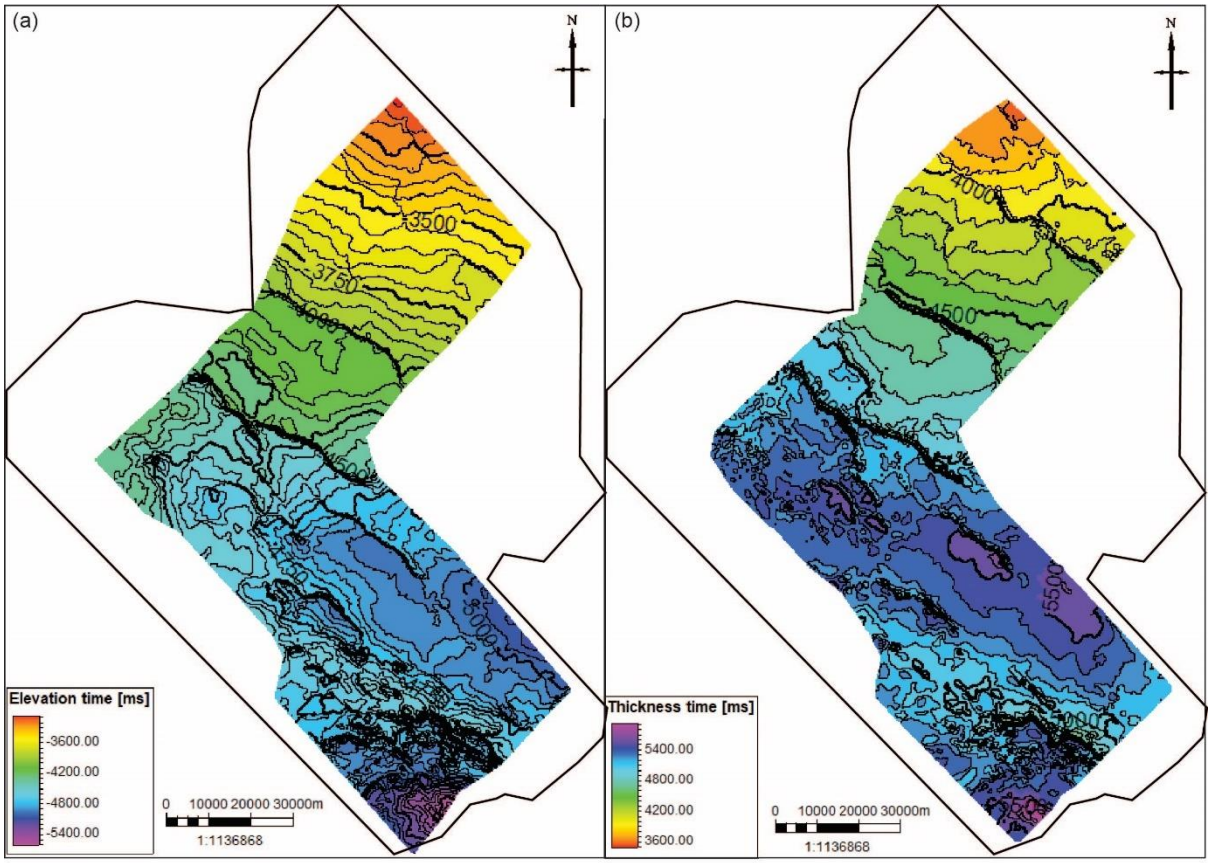

Figure 5: (a) Structural map (ms) of the top Tiger Supersequence (T4) (b) Thickness map of the Tiger detachment interval (T4 to T3). Both maps have a contourn interval of 50 ms and include the boundary of the Ceduna 3D MSS seismic survey for reference.

Characteristics of all the fault segments

We interpreted 530 fault segments in the Ceduna 3D MSS seismic survey (Figure 6a). Of these, 476 have northwest-southeast strikes (110°N-145°N), 28 have north to south strikes (150°N-170°N), and 14 have west to east strike. (075°N-105°N) (Figure 6b)

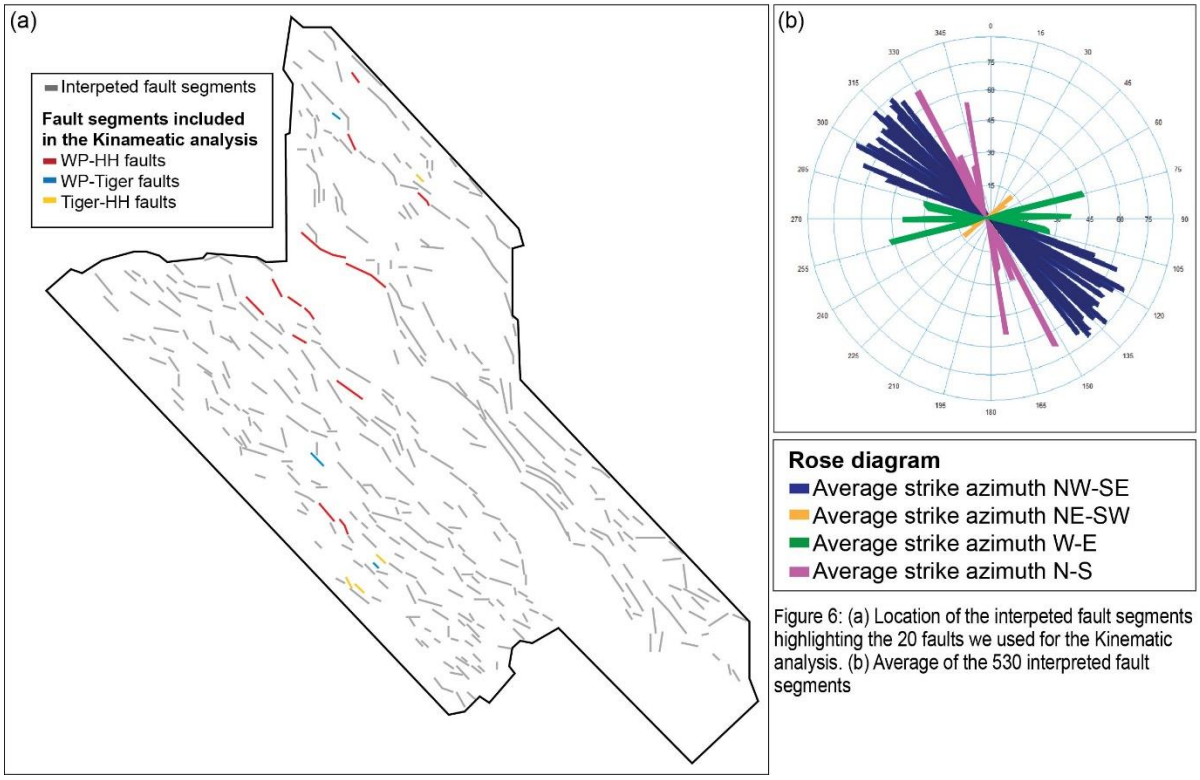

Figure 6: (a) Location of the interpeted fault segments highlighting the 20 faults we used for the Kinematic analysis. (b) Average of the 530 interpreted fault segments

Most of the interpreted faults correspond to synthetic fault segments with dip direction towards the southwest. We identified minor antithetic faults mostly located at the top of rollovers (Figure 7). These antithetic fault segments offset the sequence between T4 and HH3 (Late Santonian-Maastrichtian) in the east and the sequence between WP1-T4 in the southeast area (Cenomanian-Late Santonian).

From the seismic interpretation, we identified three different fault groups corresponding to ages of the displaced sedimentary record: (1) Cenomanian-Late Santonian, (2) Cenomanian-Maastrichtian, and (3) Late Santonian-Maastrichtian (Figure 6a). Regionally, all groups of faults are spread along the study area, with a larger concentration of Cenomanian-Maastrichtian fault segments in the north, west and central areas, and Cenomanian-Late Santonian and Late Santonian-Maastrichtian in the south and southeast areas (Figure 6a).

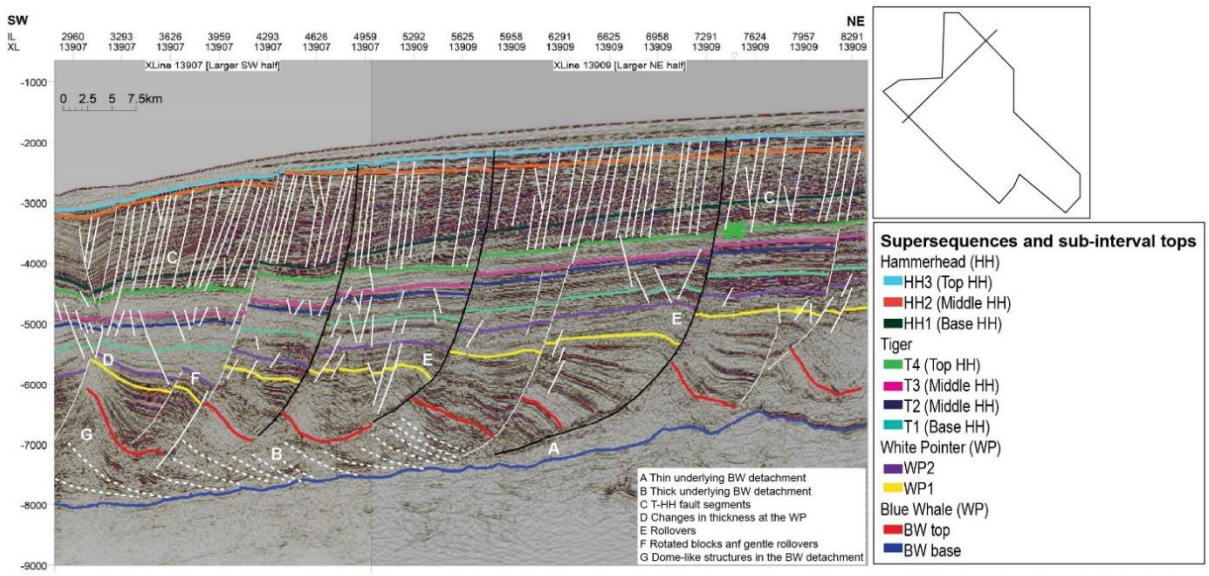

Figure 7: Composite seismic line showing differences in the fault styles characteristics from northwest to southeast. We also show the principal structural Characteristics of the different stratigraphyc sequences, such as changes in thixkness and hangingwall structures. In black are some fault segments from the Fault style 2 and in white are some examples of the interpeted fault segments from Fault style 1 and 3. In dash lines we plot examples of thrust faults at the Bluw Whale detshcment layer

Interpretation of formation intervals

To measure the fault displacement values for the kinematic analysis, we map the supersequence tops of the HH, Tiger, WP and BW that were previously interpreted at the Gnarlyknots-1A and Potoroo-1 wells. We also interpret seven additional intra-sequence intervals that correspond to variations in the Gamma-Ray (GR) and Sonic transit time (DT) log data within the principal supersequences and that also represent visible changes in seismic amplitude and stratigraphic changes across the study area (Figure 2a). As a result, the HH is defined as having top (HH3), middle (HH2) and base (HH1) intervals, the Tiger Supersequence (T) as having top (T4), upper middle (T3), lower middle (T2) and a base (T1) unit, and the WP as having top (WP2) and base (WP1) sections. We also divide the BW into top and base units to properly characterize and calculate its thickness (Figures 4 and 5).

Kinematic analysis results

We select 20 fault segments as the best candidates in the study area, which collectively represent the main fault groups, are distributed across in the study area, and show minimum interaction with small synthetic and antithetic faults (Figure 7). In general, they represent the average strike of all interpreted fault segments, northwest to southeast (approximately 110°N-290°N and 145°N-325°N) and reach a total length along the strike of faults between 1.6 and 12.0 km (Figure 6a and b).

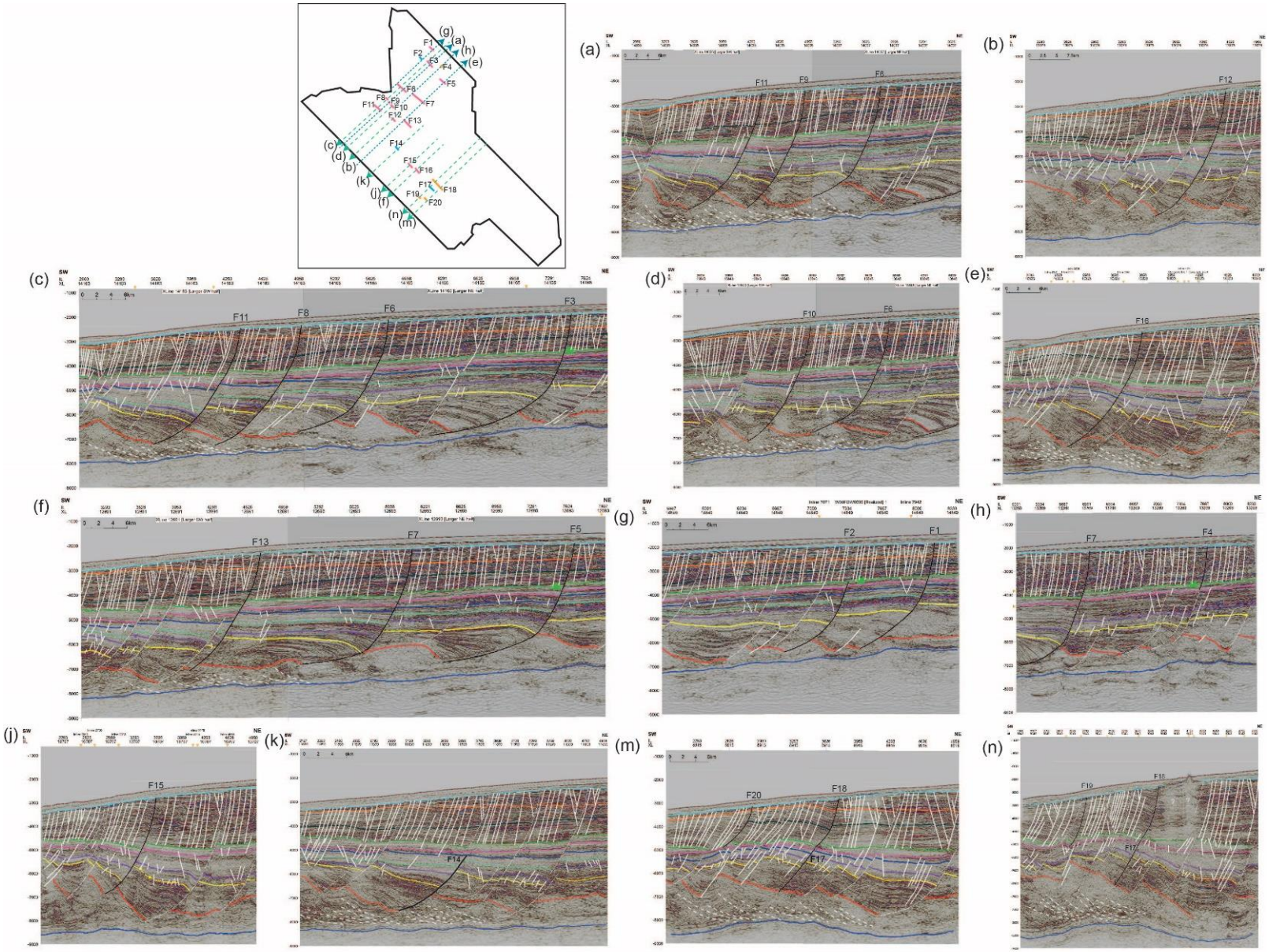

Figure 8: Interpetation of the fault segments along (a) Crossline 14035-14037 (F9, F11, F3, F6), (b) Crossline 13075 (F12), (c) Crossline 14163-14165 (F3, F8, F6, F11), (d) Crossline 13843 (F10, F6), (e) Crossline 10323 (F16), (f) Crossline 12691-12693 (F5, F13, F7), (g) Crossline 14549 (F1, F2), (h) Crossline 13269 (F4), (j) Crossline 10707 (F15), (k) Crossline 11859 (F14), (m) Crossline 8915 (F20, F17, F18), (n) Crossline 9043 (F19, F17, F18)

Fault group 1: Cenomanian-Late Santonian

This group describes the fault segments that began in the early Cenomanian and then terminated in the Late Santonian. These faults have a listric to planar geometry with gentle rollovers (in the northern and central area) and rotated blocks (in the southern and south-eastern area) in their hanging wall. They strike between 123°N-303°N and 131°N-311°N. We interpret three fault segments in this group: F2 (Figure 8g) is 2.5 km along strike and it is located in the northern area, where the top-BW underlying detachment shows low seismic amplitude and an average thickness of approximately 365 ms. F17 (Figure 8m and n) is 4.0 km along strike and is interpreted in the south-eastern area over an antiformal basement structure. The BW detachment underneath F17 is approximately 1228 ms thick with visible thrust faults and strong changes in seismic amplitude. This fault is located below a Tiger-HH fault segment that according to our seismic interpretation, is evidently not connected. As F17 does not contain T1, we have measured displacement of the T2 unit between the tops of WP1 and T2. F14 (Figure 8k) is 4.0 km along strike and is located in the central-southern area, where the BW detachment reaches a thickness of approximately 968 ms. Underneath F14, the top-BW also shows strong changes in seismic amplitude and thrust faults.

In the D-x analysis, all these faults show a proportional decrease in displacement from the lower (BW) to the upper (WP1 to Tiger) levels. For instance, F2 shows high displacement at the Blue Whale (BW top) and is terminates at T4. F17 unevenly displaces the BW top, which represents the period with the lowest displacement values, and it is terminated at T2. F14 shows the highest displacement values at the BW and ends at the T1. At the Tiger levels (T1 to T4), F14 shows similar displacement values to F2 along strike, indicating a similar growth rate between adjacent sequences (Figure 9a).

The D-z analysis of F2 and F17 exhibits an upwards increase in displacement between BW and WP1, which suggests the faults might either not have been active during this period or that it illustrates the termination of the fault segment at the deeper tip. At F14, the BW to WP1 interval shows a decrease in displacement gradient in the west and central sections that contrasts with an increase in displacement at the eastern tip. This change in the upwards displacement can be associated with an uneven growth of the fault where the east section did not grow during this period. In all the faults, WP2 shows highest displacement gradients that gently decrease between T1 at F2 and F14, and T2 at F17. This trend shows that all these faults constantly grew without being reactivated or dip-linked to another fault segment (Figure 10a).

The Expansion index (EI) analysis display a normal distribution with the higher EI in the central section, indicating that all these faults grew as independent fault segments. F2 and F17 show EI=1 along the strike in WP1. This result correlates with the upwards decrease in displacement at this unit in the D-z analysis. The same is apparent for the eastern section of F14, which reaffirms the uneven growth of the fault at WP1, where the eastern section did not grow. WP2 in F14 and F2 exhibit the highest EI rate, while F17 shows the highest EI at T2. In all cases, the faults reach their maximum length along strike at WP2. F2 exhibits an EI rate that oscillates along the strike between T2 and T3, where EI=1 correlates with the displacement trend values of the D-x analysis (Figure 11a).

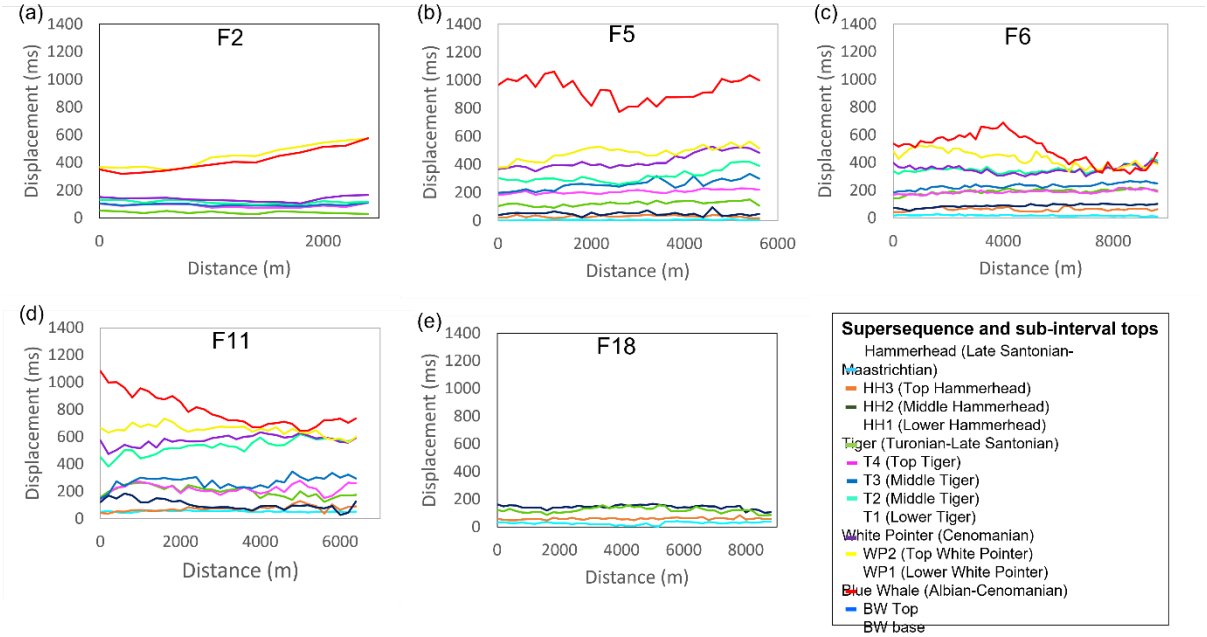

Figure 9: Kinematic result of the Displacement-Distance method (D-x). We included one fault as an examples of each fault style we interpreted. (a) fault group 1, (b) Fault evolution style 2a, (c) Fault evolution style 2b, (d) Fault evolution style 2c and (e) Fault group 3.

Fault group 2: Cenomanian-Maastrichtian

This group represents faults that grew between the Cenomanian and the Maastrichtian. These listric faults form rotated blocks and gentle to major rollovers in the hanging wall. They are distributed from north to south and mostly concentrated in the western and central areas. We analysed 13 fault segments with these characteristics: F1, F3 and F5 in the north, F6, F7, F8, F9, F10 in the centre, F11, F12, F13 in the central south, and F15 and F16 in the southeast.

Results from the kinematic analyses and characteristics of the underlying BW detachment layer, we distinguish 3 different fault sub-groups thar represent different evolution styles: (2a) fault segments that constantly grew between the Cenomanian-Maastrichtian, (2b) three fault segments connected by two events of dip-linkage, and (2c) two fault segments connected by a dip-linked events. Each of these sub-groups is located in a different region of the study area, and each shows differences in the remaining BW (Albian-Cenomanian) detachment layer in terms of thickness, internal structures (e.g. thrust folds), and top boundary seismic amplitude.

Fault evolution style 2a: Constant growth fault segments

F1 (Figure 8g), F3 (Figure 8c) and F5 (Figure 8f) fault lengths along the strike are 3.2 km, 4.8 km and 5.6 km respectively. They are principally located in the north of the study area with a general strike between 129°N-309°N and 140°N-320°N and dip direction towards the southwest. The underlying BW detachment layer shows minimum changes in seismic amplitudes, which inhibits interpretation of internal structures such as thrust faults below the interpreted fault segments. However, the boundaries of the detachment layer are well enough resolved to exhibit variation in thickness of between 270 and 460ms.

D-x analysis shows the highest displacement values for all of these faults occurs at the BW top. F3 shows a lineal increase in displacement towards the east. In F1 and F5, the higher values of displacement are at the western and eastern tips. From WP1 to HH3, the displacement values

decrease proportionally towards the upper levels. Only two faults show minimum displacement changes between consecutive units: F3 in WP2 and T1 along the strike, and F5 in T3 and T2 at the western tip (Figure 9b).

The D-z analysis at F3 displays a linear increase in displacement gradient between BW and WP1 that correlates with the D-x analysis, where the higher displacement values are in the east. Similarly, F5 shows a slight upwards decrease in displacement between BW and WP1 at the centre in comparison to the western and eastern tips. Between WP2 and HH3, all the faults show a constant upward decrease in the displacement gradient, which demonstrates that they constantly grew during accumulation of the WP, Tiger and HH supersequences (Figure 10b).

The EI analysis exhibits a bell shape in a cross-section view with the higher values at the Tiger interval (T3 and T2 at F1, T4 and T3 at F5, and T4 and T2 at F3). The EI-x analysis also shows EI>1 along the strike at WP1, which suggests that these segments reached their total length from the beginning of their evolution style. F1 and F3 show relatively lower EI at T1 in comparison with that at WP2 and T2. In both cases, the EI is higher than 1, which indicates that the faults grew but at a gentler rate during this period in comparison to the proximal lower and upper levels. Both faults show an increase in EI at T1 in the east and a slight decrease in EI in T2. Similarly, F5 exhibits a smaller EI at WP2 (Ei>1), but higher values at WP1 and T1. In F3 and F5, WP1 and WP2 respectively exhibit the highest EI values, which could be a result of the major rollover geometry we found in the hanging wall of both faults. In all for the Hammerhead units (HH1, HH2, and HH3), EI rate is smaller and behaves as a trend along strike (Figure 11b).

Fault evolution style 2b: Three fault segments with two dip-linked events

The fault segments F6 (Figure 8a, c and d), F8 (Figure 8c), F9 (Figure 8a) , F10 (Figure 8d), F12 (Figure 8b) and F13 (Figure 8f) represent fault evolution style 2b. They have a listric fault geometry and locates in the central section of the study area with a length along strike of 9.6 km, 3.8 km, 1.6 km, 3.2 km, 4.2 km and 8 km, respectively. They show a dip direction towards the southwest and strikes between 112°N-292°N and 143°N-323°N. The BW detachment thickness changes between 565 and 670 ms and shows thrust faults and strong variations in the seismic amplitude.

The D-x analysis for all the faults shows higher displacements at BW with an uneven trend along strike. Above BW, F13 exhibits lower displacement at WP2 than at T1, and slightly higher displacement at T4 than at T3. F9 and F10 show higher displacement results at T1 than at WP1 or WP2, with displacement at WP1 being consistently higher than WP2. These two segments also show higher displacement values at HH1 than at T4. F8 shows minimal variations in displacement between WP1, WP2 and T1 in the central and eastern sections, and higher displacement values at HH1 than at T4. F6 exhibits minimal variations in displacement between T1 and WP2, though displacement at T1 is slightly higher than at WP2. It also demonstrates that T3 and T4 show similar displacement values. T12 shows the lowest displacement at T1 and similar displacement values between T2 and T3. In contrast, F12 exhibits higher displacement at HH1 than at T4 (Figure 9c).

The D-z analysis shows changes in upwards displacement along the strike between BW and WP1. In F8, F9 and F12, there is an upwards increase in displacement towards the east. F6, F10 and F13 show steeper displacement slopes in the central section in comparison to the western and eastern tips. This

trend correlates to the uneven changes in displacement along strike in the D-x analysis at BW. In addition, we identify two periods in which the displacement increases upwards, corresponding to two dip-linkage events that characterize this fault evolution style. F6, F9, F10 and F13 represent the first dip-linkage period at T1. In all cases, the results correlate with the D-x analysis at WP2 where it exhibits lower displacement values than at T1. F8 shows the first dip-linkage event at WP2 and minimum to zero upwards displacement at T1. In this case, F8 presents minimum displacement variation between WP1, WP2 and T1. F12 exhibits the first dip-linkage event at T2, which correlates with the D-x analysis showing lower values of displacement at T1 than at T2, and minimum displacement variation between T2 and T3. F6 and F13 show the second dip-linkage event occurred at T4, while F8, F9, F10 and F12 show it occurred at HH1. This second dip-linkage event also correlates with the displacement distribution revealed by the D-z analysis where displacement value at T4 is higher than at T3 for F6 and F13. Elsewhere, the displacement value at HH1 is higher than at T4 for F9, F10, and F12. Between the two dip-linkage events, all faults show an upwards decrease in displacement. F6, F8, F9 and F10 show a steep upwards displacement (between 50° and 70°), in comparison with those of F12 and F13 (from 15° to 30°). This decrease in displacement indicates a period of fault growth in all the faults. After the second dip-linkage event, all segments show an upwards decrease in displacement, which again represents a period of fault growth until all faults terminate at HH3 (Figure 10c).

Between WP1 and HH3, the EI analysis shows three separate distributions. F6, F9, F10 and F13 display a bell-shaped distribution between WP1 and T1. For F13, we find an EI=1 at T1, whereas for F9 and F10, EI<1 for the same interval. All the faults exhibit a dip-linkage event at T1 that is also shown by the D-z analysis. F8 exhibits the first bell-shaped curve between WP1 and WP2; WP2 in the central area shows E1=1, which correlates with the first dip-linkage event. F12 exhibits the first normal distribution tendency at T2 with an EI=1 in the central and eastern sections that correlates with the first dip-linkage event shown by the D-z analysis. F8, F9 and F10 show a second bell-shaped distribution between T1 and HH1. As for F12, the second normal distribution begins at T2 and ends at HH1. In all the cases, EI=1 at HH1 correlates with the second dip-linkage event in this unit shown by the D-z analysis. F6 and F13 show the second bell distribution between T1 and T4. In this case, the EI=1 rate at T4 correlates with the second dip-linkage event. F8, F9, F10 and F12 show the third distribution bell shape between HH1 and HH3, while F6 and F13 show the third EI normal distribution between T4 and HH3 (Figure 11c).

In the EI-x analysis, F8, F9 and F10 display EI>1 at WP1. Therefore, we can infer that they reach their maximum lateral length in this period. F6, F12 and F13 show an uneven distribution of EI along strike at WP1. For example, F12 and F13 exhibit EI=1 in its western section, whereas the same is true for F6 at both eastern and western tips. This demonstrates that these faults did not reach their total lengths within the period where these sequences were deposited. These results correlate with the higher displacement gradients in the D-z analysis in the central and eastern sections of F6, F12 and F13. F12 attains maximum length at WP1, which can be inferred from the constant EI>1 along its strike. In contrast, F13 grew slightly towards the eastern and western tips during WP2, T1 and T2, reaching its maximum length at T3. This result correlates with the D-z analysis, which shows the eastern and western sections of F13 exhibit minimal variation in displacement gradient between WP1 and T2. As for F6, it grew towards the western tip at WP2, and at T2 it reached its maximum length. These results are also clear between WP1 and T1 in the D-z analysis, which shows the eastern tip exhibits minimal

variation to the displacement gradient. Above the second dip-linkage event, all faults show EI>1 up to their termination at HH3 (Figure 11c).

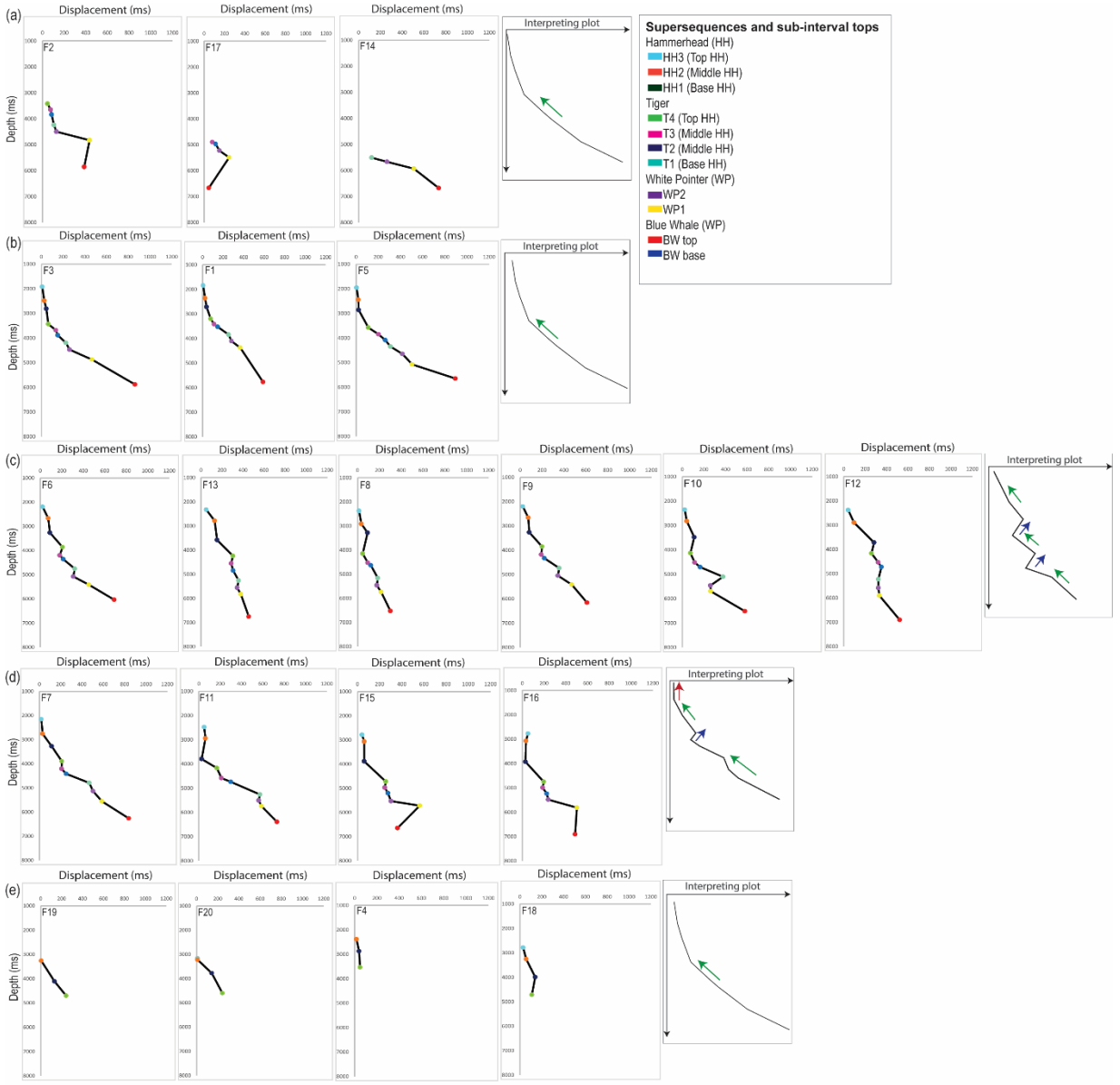

Figure 10: Kinematic result of the Displacement-Depth method (D-z). (a) Fault group 1, (b) Fault evolution style 2a, (c) Fault evolution style 2b, (d) Fault evolution style 2c, (d) Fault style 2c, (e) Fault group 3.

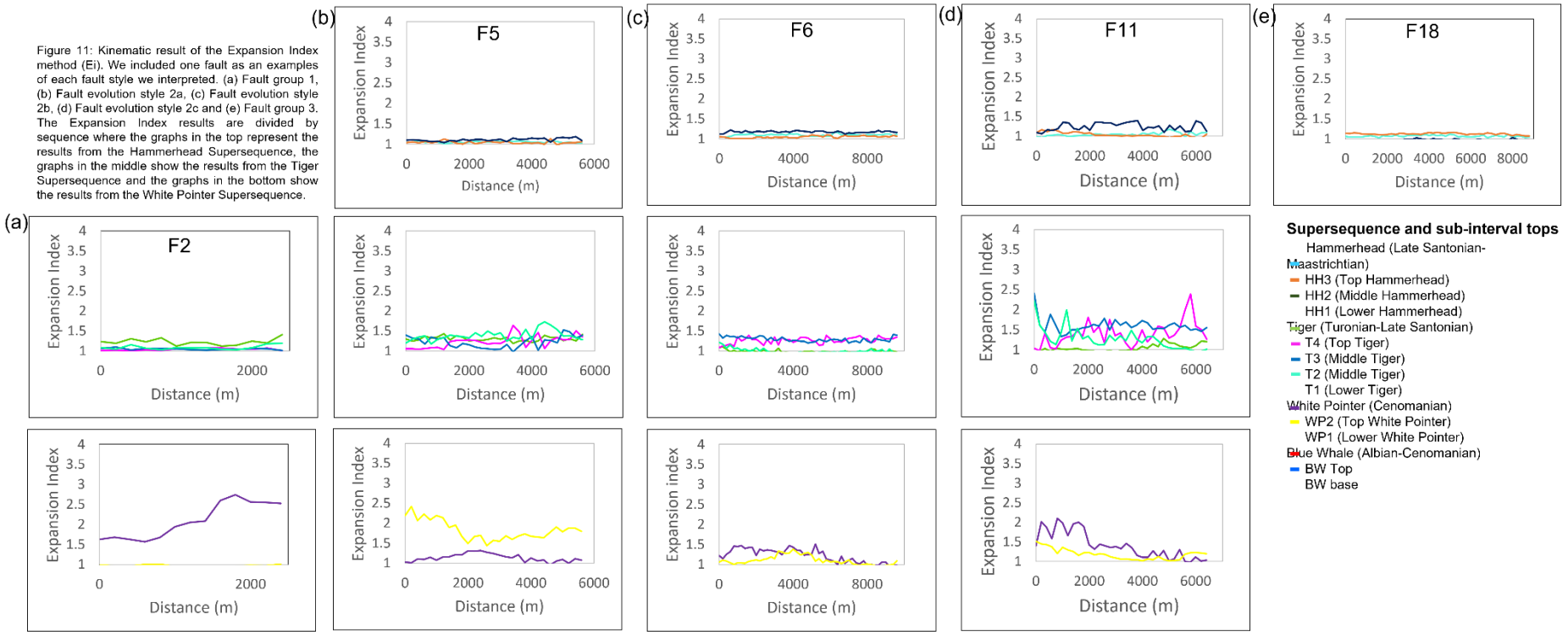

Figure 11: Kinematic result of the Expansion Index method (Ei). We included one fault as an examples of each fault style we interpreted. (a) Fault group 1, (b) Fault evolution style 2a, (c) Fault evolution style 2b, (d) Fault evolution style 2c and (e) Fault group 3. The Expansion Index results are divided by sequence where the graphs in the top represent the results from the Hammerhead Supersequence, the graphs in the middle show the results from the Tiger Supersequence and the graphs in the bottom show the results from the White Pointer Supersequence.

Fault evolution style 2c: 2 fault segments with a dip-linkage event

This group corresponds to the fault segments F7 (Figure 8f) and F11 (Figure 8a and c) in the central area with lengths along the strike of 11.2 km and 6.4 km, and F15 (Figure 8j) and F16 (Figure 8e) in the southern area with lengths along the strike of 5.6 km and 4.0 km respectively. They have a listric geometry, a dip direction towards the southwest and strikes between 122°N- 302°N and 140°N-320°N. The underlying BW detachment thickness varies between 685 and 1430 ms with strong internal changes in seismic amplitude showing variation in the amplitude, thrust faults and "dome-like" structures. The central and eastern sections of F16 are located over a basement anti-form, while for F15 western and central sections are situated over a thicker Blue Whale detachment layer that forms a "dome-like" structure underneath. In both cases, T1 is not present, so we measure displacement of the T2 unit between the tops of WP1 and T2.

The D-x analysis displays strong changes in displacement at the BW unit along strike for each fault. For instance, F7 and F16 display lower displacement values in the central section in comparison to those at the eastern and western tips. F11 shows a decrease in displacement towards the east. In contrast, F15 shows an increase in displacement at the BW interval with lower values in the west than at the Tiger interval (T2, T3 and T4) and slightly higher values in the east than at WP1 (Figure 9d).

The D-x analysis shows three main displacement trends that mark changes in the displacement values between high, middle and low trends along strike. The highest displacement values in F7 and F11 occur at BW, WP1, WP2 and T1 sequences, for F15 at WP1, and for F16 at BW and WP1. F7 and F11 exhibit the highest displacements values at T2, T3 and T4. F15 and F16 exhibit slightly higher displacement values along strike at T4 than at T3. A trend of intermediate displacement values for F15 and F16 begins at WP2, T2, T3 and T4; for F16 and at the central and east sections of F15, these trends continue to T2, T3 and T4. The lowest displacement values for all these faults coincide with HH1, HH2 and HH3 units. In the central and eastern sections of F11 and the western and central sections of F16, HH1 and HH2 show minimal variation in displacement values. In F15 and F7, there are proportional upwards decreases in displacement between HH1, HH2 and HH3 (Figure 9d).

D-z kinematics analysis shows changes along fault strikes within the BW unit. For instance, in the central sections of F7 and F16, and the eastern section of F11, the displacement at BW is close to zero. These values correlate to the lower displacement values of the D-x analysis in these same sections. F15 shows an upwards increase in the displacement at BW along strike that correlates to the low displacement values in BW. Between WP1 and T3, all faults show an upwards decrease in displacement that represents a period of constant growth at this interval, followed by an upwards increase in the displacement at T4, which represents a dip-linkage event. This dip-linkage event correlates with sections of the D-z analysis where displacement values at T4 were slightly higher than those at T3. In the Hammerhead interval (HH1 to HH3), F7 and F15 exhibit an upwards decrease in displacement between HH1 and HH3 that correlates with a similar decrease in displacement in the D-z graph. The implication is that both faults grew constantly between HH1 and HH3. F11 and F16 display a upwards decrease in the displacement at HH1 and upward changes in displacement closer to zero at HH2. In both cases, an upwards decrease in displacement at HH3 indicates that these faults did not grow during the deposition of HH2 and were unevenly reactivated during the deposition of HH3 (Figure 10d).

The EI analysis shows two periods with normal distributions separated at T4 where EI=1. The first is located between WP1 and T4 and the second between T4 and HH3. F15 shows EI<1 in its central and eastern sections at WP1 that correlates with the increase in displacement shown by the D-z analysis. We can infer that the fault grew slightly in the east during this period. At WP1, F7, F11 and F16 exhibit E1=1 in the central area and EI>1 at their eastern and western tips. These results correlate to the zero-displacement gradient in the central sections of these faults. The D-z analysis shows that all the fault segments reach their maximum length along the strike at WP2. In the Hammerhead interval, F15 shows EI=1 at HH2 and HH3, which can be related to the truncation of HH2 towards HH1, as interpreted in the Ceduna 3D seismic survey. Central and eastern sections of F11 and F16 exhibit EI=1 at HH2, which marks a quiescence period for the faults. In both cases, an irregular distribution of EI values at HH1 that correlate with the uneven reactivation periods at both faults described at the D-z analysis (Figure 11d).

Fault group 3: Late Santonian-Maastrichtian

Faults that were active between the late Santonian and Maastrichtian and show a strike between 123°N-303°N and 131°N-311°N. These segments have a listric to slightly planar geometry with rotated blocks and gentle rollover structures in the hanging wall. F4 (Figure 8h) is located in the northern area and shows a length along strike of 2.4 km, where the T4 detachment layer reaches a thickness of approximately 42 ms. In the south, we interpret F18 (Figure 8m and n), which shows a length along strike of 8.8 km at T4 with a thickness of 53 ms. Both faults are associated with Cenomanian fault segments. In contrast, F19 (Figure 8n) and F20 (Figure 8m) are located in the southeastern area, where they are detached at the upper Tiger interval (T4) and extends along strike 2.0 km and 1.6 km respectively. In this area, the T4 detachment layer is only between 13 and 18ms thick.

In the D-x analyses, all fault segments show their maximum displacement values at T4. F18 is the only fault with slightly higher displacement values at H1 in comparison to T4 along strike. This can be related to the influence of the F17 fault segment below, which terminates just before T4. F4 and F47ML exhibit minimal variation in displacement between T4 and H1. Only F18 and F20 terminate in HH3 where they show their minimum displacement values, while F4 and F19 terminate just below HH3. Our seismic interpretation proposes that the top of HH2 is truncated against HH3 towards the southwest where F18, F19 and F20 faults are located, which can have implications in the displacement and thicknesses of HH2 calculated between the footwall and hanging wall of this faults (Figure 9e).

The D-z analysis shows an upwards decrease in displacement between T4 and HH3 for all the fault segments, which indicates that these faults constantly grew during the deposition of HH (HH1 to HH3). F19 and F20 show higher displacement values at HH1 and HH2 (between 20° and 50°), which demonstrate differences in displacement between consecutive units in the D-x analysis. F4 and F18 exhibit a gentler upwards displacement from T4 to HH2, and T4 to HH3 (lower than 15°) respectively (Figure 10e).

The EI analysis shows a normal distribution of displacement gradients that correlates with the constant growth pattern shown by the D-z analysis for all faults, demonstrating that they evolved as independent fault segments. F4 and F47ML show EI=1 at HH1, which demonstrates that these faults did not grow until HH2, when both faults reached their maximum length along strike (EI>1). In

contrast, F19 and F20 display values of EI>1 at HH1 along strike, which indicates that these faults reached their maximum length early in their evolution style (Figure 11e).

Interpretation of kinematic results

Displacement distribution with depth

Analogue models of growth faulting over salt detachments suggests that the difference in displacement between successive units represents an increment of displacement in the period marked between both horizons. Therefore, where consecutive units in the study area show similar displacement trends along strike, it resulted in a gentle displacement slope in the D-z analysis and low EI values (close to 1). Therefore, this can indicate a minimum growth rate in this period. In contrast, strong changes in displacement in the D-x between consecutive units, produces steeper displacement slopes in the D-z analysis and higher EI values. In terms of fault growth, major changes in displacement in the D-x analysis represent a stronger growth period that also characterizes the formation of a thicker syn-kinematic interval on the hanging wall of the fault *(McClay and Ellis, 1987).*

In the D-z analysis, a constant upwards increase in displacement represents continuous fault growth, which relates to the standard evolution of listric faults in analogue models when they propagate from the base *(McClay and Ellis, 1987; Jackson et al., 2017; Robson et al., 2017).* Therefore, we propose that the dip-linkage episodes described by fault group 2 (fault evolution style 2b and 2c) are represented by "abnormal" distributions of displacement between consecutive units in the D-x analysis. In all cases, the older units show lower displacement values in comparison with younger successive units. For example, for F6 and F13, displacement at T1 is higher than at WP2, and displacement at T3 is higher than at T4. T1 and T4 in this context represent the two dip-linkage events in the fault segments. Similarly, F11 and F16 show higher displacement values at T3 than at T4. We propose that these faults were dip-linked during the deposition of T4.

Relationship between sediment accumulation and fault displacement

Preliminary kinematic analysis of normal faults have shown a correlation between a EI=1 and the nucleation of fault segments (Thorsen, 1963b). However, we identified several faults with EI>1 in the uppermost sequences. For example, F2 at T4, F14 at T1 and F17 at T3and F6, F8, F10, F12 F13 and F16 at HH3. We propose that the higher EI rate at the top tips of the faults might be related to local changes in deposition that have resulted in increased fault displacement. F10, F12 and F16 show visible changes in thickness at HH2 and HH3 in their footwall and truncation of the top of HH2 towards the HH3, which may result in a smaller EI than HH3.

The EI graphs allow also to compare changes along strike in EI between the different sequences. In this case, most of the fault segments exhibit oscillation of the Expansion Index along strike. For instance, when a control point shows EI=1, the successive sequence above shows a higher EI. These changes along strike are thought to be related to pulses of sediment entering the basin causing an EI=1 in a sequence which initially had minimal accumulation of sediments and later receive a greater thickness of deposits. This changes in accumulation resulted in levelling the syn-kinematic interval from T4 to HH2. For example, F1, F3, F5, F6, F8, F9, F10, F11, F13, F16 and F17 show some control

points with an EI rate closer to 1 at T2. At the same reference points, the EI at T3 is not only higher than 1 but slightly greater than the points with constant EI>1. A similar distribution occurs for F5 and F11 between WP2 and T1, for F7, F8 and F9 between WP1 and WP2, for F1 and F11 between T3 and T2, and for F8 between T3 and T4.

Similarly, we interpret EI<1 at T1 for F9 and F10, and at HH3 for F15. These values are not thought to represent measurement issues in seismic interpretation of displacement, but local changes in the sedimentary record and/or the stratigraphical configuration. It is important to remember that these faults did not respond to external tectonic stresses but rather to the accumulation of sediment, locally affecting the accumulation rate between the hanging wall and the footwall. These observations can be related to studies that have discussed the implications of the sedimentary record on normal fault evolution, which have examined the role that stratigraphy and rock composition have on the control of fault propagation, nucleation, displacement, and brittle failure *(Vendeville and Cobbold, 1988; Ferrill et al., 2017; Redpath et al., 2022).*

Our seismic interpretation determines that T1 is not present at F15, F16 or F17. We do not have well data close enough to these fault segments that can predict either that the current thickness of this unit or the presence of local changes in the sedimentary facies may challenge the accuracy of our seismic interpretation. However, we know that this outcome occurs for all faults in the southern to eastern area, which might indicate that (1) it can be a result of the dynamics between the BW detachment and the accumulation of sediments, where the high BW thickness and the low dip angle would not leave enough space for T1 to accumulate, making it harder for the gravity-driven sliding of the BW detachment basinwards, or (2) it can be a consequence of erosion due to external factors (tectonic or structural) that uplifted and exposed the T1 unit to erosion in the southeast.

Fault interaction with the detachment layer

An analogue model of an extensional fault system (McClay, 1990) proposed that the geometry of the basal detachment is a fundamental parameter in the control deformation of overlying stratigraphy. The faults classified in Fault evolution style 2c (F7, F11, and F16) show EI=1 in the central section of each fault. These EI results along strike might demonstrate that the faults did not reach their maximum length until WP2, where in all the cases they show EI>1 and a decrease in displacement gradient along strike. We believe that there may be two explanations: (1) the thick underlying BW detachment layer might not permit an even accumulation of the WP1 unit on the hanging wall side. As WP2 accumulated, the fault would fully develop along strike, forming a syn-kinematic interval on the hanging wall side. (2) the EI=1 rate and zero to an upwards decrease in displacement during the accumulation of WP1 might be related to a scenario where in map view two independent fault segments formed at this time that later grew far enough laterally during WP2 accumulation to link and form one single fault.

We find a strong correlation between the evolution of Cenomanian-Maastrichtian fault segments and characteristics of the remaining BW detachment layer such as thickness, composition (assumed from variation in the seismic amplitude), and internal structures (“dome-like”, folds, “depression-like” and thrust faults). For example, we recognised that in areas where the BW detachment layer is thinner and shows a more homogenous seismic amplitude without visible interval structural features, the Cenomanian-Maastrichtian fault segments constantly grew. In cases when the detachment thickens

and shows changes in the seismic amplitude and an increase in the diversity and frequency of internal structures (e.g. thrust faults, or folds), the Cenomanian-Maastrichtian fault segments exhibit periods of dip-linkage and changes along strike in their displacement values. We also find strong differences in thickness of the remaining BW detachment layer underlying Cenomanian-Late Santonian fault segments (365 to 1228 ms). However, these faults constantly grew without showing evidence of vertical linkage.

We identify some differences in the kinematic analysis between F19 and F20 that detach at T4, and F4 and F18, that are directly above older Cenomanian-Late Santonian fault segments. In these cases, faults that visibly detach from the T4 unit exhibit higher displacement values from the D-x analysis and higher displacement gradients from the D-z analysis, even when all the faults constantly grew during their evolution style. This result agrees with the observation of *Robson et al (2017)* that suggests the areas where younger faults form above older fault segments, the Cenomanian-Late Santonian faults have a strong influence on evolution of the Late Santonian-Maastrichtian fault segments. Additionally, when comparing the kinematic results between FG1 and FG3 we do not find major changes, which suggest that both groups evolve similarly. However, the fault kinematic results are not enough in this case to assume similar geometrical and internal characteristics (lithology, evacuation rate) between the BW and T4 detachments, and a more detail analysis would be necessarily.

Implications of fault evolution on petroleum systems

Preliminary studies suggested that gas from the BW source rock (Albian-Cenomanian) migrated between the Turonian and Late Santonian, oil and wet gas from the WP (Cenomanian) migrated between the early Campanian and Pleistocene, and gas from the Tiger (Turonian) migrated during the Late Campanian and Pleistocene ages *(Totterdell et al., 2008; Kempton et al., 2019)* (Figure 2c). We compared these outcomes with the D-z kinematic analysis results to predict how events in the evolution on each fault group can determine whether the faults acted as trapping structures or migration pathways for hydrocarbons in their current locations. Unfortunately, there are several components in the analysis of fault seal and trapping that are not included in this study. For instance, we do not address the impact of shale gouge ratio and shale smear, neo-tectonics, juxtaposition relationships *(Allard, 1997; Ogilvie et al., 2020)*, and local changes in pore pressure, porosity and permeability along the fault plane *(Fitzenz and Miller, 2003).* This study only account 3D seismic data and lack the high resolution of core sampling or well data that can permit the incorporation of more detail factors into the study. Therefore, we will evaluate the mechanical significance that fault reactivation and linkage have in the seal and tap of hydrocarbons in the Ceduna Sub-basin.

In this study, we differentiate geological ages for stratigraphic intervals (taken from well data) for this analysis by employing dark colours to mark older ages and lighter colours to highlight younger ages. Given the lack of hydrocarbon production in the area, we suppose that hydrocarbon migrated upwards in the structure towards the delta top at a constant rate, and that in each example it corresponds to the first stage of migration from the source rock interval (secondary migration) rather than a consequence of tertiary migration from an intermediary containment system, for example, a fault-dependant trapping system located basinwards and unsealed an initial hydrocarbon accumulation.

Fault group 1: Cenomanian-Late Santonian

The faults from this fault group evolved by constant growth between the accumulation of the WP and Tiger supersequences. For this analysis, we use as example Fault F2 since it displaces strata from WP1 to T4 and it is located in the northern part of the study area.

F2 constantly grew between the Cenomanian and Late Santonian which suggest that it can be. active while gas migrates from the BW source between the Turonian and early Santonian. However, it was likely nucleated when the gas from the Late Santonian migrates, which can suggest potential trapping. Similarly, wet gas and oil from the WP that migrated between the early Campanian and Pleistocene, and the gas from the Tiger Supersequence that migrated between the Late Campanian and the Pleistocene would have been trapped, given that the fault terminated at T4 (early Santonian) (Figure 12a)

Fault group 2: Cenomanian-Maastrichtian

Fault evolution style 2a: Constant growth fault segments

This fault evolution style includes fault segments in the northern area that constantly grew between the Cenomanian and Maastrichtian where the underlying BW detachment layer is between 270 and 460ms thick, with low and constant top reflector seismic amplitude. We choose Fault F5 as our example to define the implications of the evolution history of these faults for hydrocarbon migration, given that all these fault segments show similar evolutionary histories in D-z analysis (Figure 10). F5 constantly grew between the Cenomanian and Maastrichtian and can potentially work as a migration path for BW gas, and for WP and Tiger hydrocarbon which migrated between the Campanian and Maastrichtian. Similarly, fault segments with a similar evolution style than F5 might trap oil and wet gas from the WP and gas from the Tiger Supersequence that migrated between the Paleocene and Pleistocene (Figure 12b).

Fault evolution style 2b: 3 dip-linked fault segments

This fault evolution style corresponds to fault segments located in the central area that show 2 dip-linkage events at WP to WP2 or T1 and T4 to HH3 sequences. They also correspond to a BW detachment layer thickness of approximately 565 and 670ms with changes in top reflector seismic amplitude and thrust faults. To predict the effects of the pattern of fault evolution on the petroleum system, we use Fault F6 as representative as it exhibits 2 dip-linkage events at T1 and T4.

The F6 fault segment shows dip-linkage events at T1 (Turonian) and late Santonian (T4) which suggest that the BW-WP2 fault segments (within the Cenomanian sequence) likely traps gas from the BW that migrated during the Turonian. However, there is chance of seal breakage when this BW-WP2 fault segment linked to the T2-T3 fault segment (late Turonian-Coniacian). Similarly, gas from the BW that migrates during the Coniacian-early Santonian might have escaped when BW-T3 faults (Late Cenomanian-Coniacian) linked with the HH1-HH3 faults (late Santonian-Maastrichtian). These final BW-HH1 linked fault would also have acted as migration pathways between the Campanian and Maastrichtian, whereas Paleocene to Pleistocene oil and gas would likely have been trapped by these faults (Figure 12c).

Fault evolution style 2c: 2 dip-linked fault segments

This evolution style shows one dip-linkage event at T4 (early Santonian) and either reactivation or minimum displacement during the accumulation of HH2 (Campanian). All these faults exhibit an underlying BW thickness of approximately 680 and 1430ms with strong changes in internal seismic amplitude, "dome-like" structures and thrust faulting. We choose Fault F11 as the example of this type, which is located at the west-central part of the study area.

BW gas migrated during the Turonian Age would have travelled through Fault F11 given that the BW-T3 (late Cenomanian-Coniacian) fault segment was likely active during this period. A secondary migration event might occur when gas from the Coniacian-late Santonian likely migrates when the BW-T3 (Cenomanian-Coniacian) linked with the T4-HH3 (early Santonian-Maastrichtian) fault segment. The hydrocarbons that migrated in the late Santonian and Campanian to Maastrichtian may not have been trapped but rather may have migrated on due to reactivation of the T4-HH3 (early Santonian-Maastrichtian) fault segment at HH2 (Campanian) time. Therefore, only gas and oil from the WP and Tiger that migrated between the Paleocene and Pleistocene would have been trapped (Figure 12d).

Fault group 3: Late Santonian-Maastrichtian:

We state that this fault group evolved by constant growth between the late Santonian and Maastrichtian. Asan example of this fault group, we use Fault F18, located at the south-east of the study area, as the example of a fault located above a preliminary nucleated Cenomanian-late Santonian fault segment.

Gas from BW source rocks that migrated during the Santonian might have passed through Fault F18, given that it only started to develop at the early Santonian and reached its total length along strike as HH2 (Campanian) was deposited. Similarly, oil and wet gas from the WP and gas from the Tiger Supersequence that migrated between the Campanian and Maastrichtian would not have been trapped, whereas hydrocarbons generated during the Paleocene to Pleistocene could have been (Figure 12e).

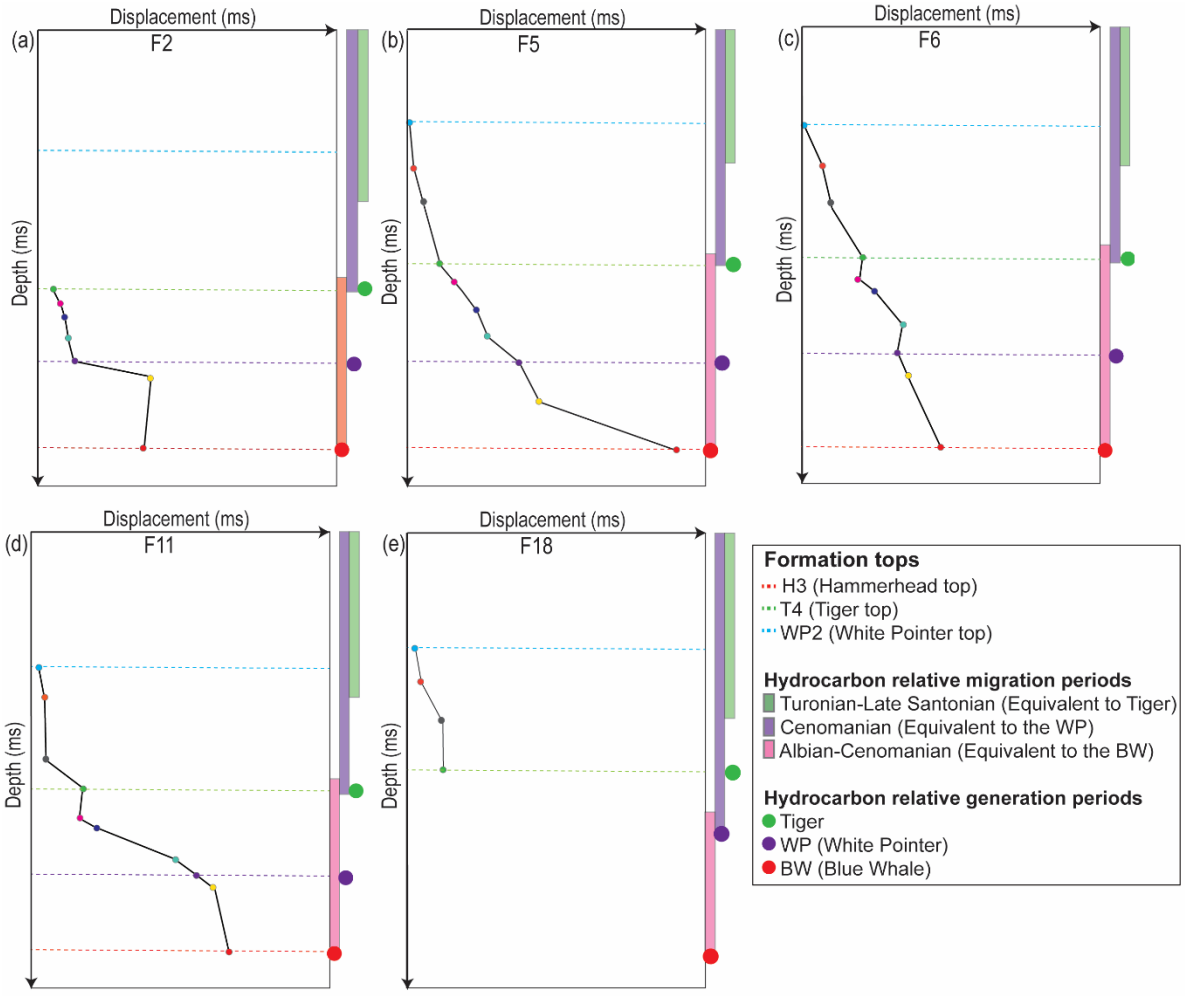

Figure 12: Diagram comparing the results from the Displacement-Depth Kinematic method (D-z) with the information about hydrocarbon generation and migration contain in Walsh and Watterson, (1991; Bruhn and Schultz, (1996); and Hallett, (2002) studies. We used one example from each fault group we previously interpeted: (a) Fault group 1, (b) Fault evolution style 2a, (c) Fault evolution style 2b, (d) Fault evolution style 2c, and (e) Fault evolution 3.

Implications of results for other delta systems

Previous studies have suggested that there are strong similarities between the characteristics and evolution of the Great Australian Bight Basin and other sedimentary basins with large delta systems such as those of the Niger Delta, Gulf of Mexico and Nile Delta *(King and Backé, 2010; MacDonald et al., 2010; King and Morley, 2017)*. Some findings of the current study should be applicable to these and other large delta systems prone to gravity-driven fault propagation. For instance, our results confirm that kinematic analyses are an effective tool to study and identify changes in the evolution of normal growth faults in delta systems where a overpressured shale detachment is present and normal faults grow in response to accumulation rate.

Our results show that fault segments with similar geometries that displace the same stratigraphic section can nonetheless exhibit different evolutionary styles. We identified a strong correlation between the behaviour and characteristics (e.g. thickness, lithology,

internal structures) of the underlying detachment and the evolution styles of normal growth faults. For instance, fault segments from fault evolution styles 2b and 2c in the central and southern regions of the study area and record events of dip-linkage and reactivation. These faults are also located in areas where the underlying BW detachment layer shows internal variation in the seismic amplitude (e.g., lithology) inside the detachment layer, increase in the detachment thickness and both the diversity and frequency of visible internal structures. In contrast faults with evolution style 2a are principally located in the northern region of the study area where the underlying detachment layers thinner and homogeneous both in terms of the internal seismic amplitude and without visible internal structures. These differences can suggest that it might be possible to predict the evolution style of the normal growth faults in the Ceduna Delta system within similar settings by understanding the characteristics of the underlying BW detachment layer.

Our results demonstrate that local changes in the expansion Index (EI) between adjacent units might represent a response to local changes in sediment accumulation. This result has significant implications for the petroleum system: distribution of reservoir, seal, and source rocks; distribution of trapping elements; timing of the critical moment. These findings can be applicable to sedimentary systems where underlying detachment layers are present. The characteristics of the underlying detachment layer can be responsible for local changes in the accumulation and the evolution of the normal growth faults in the extensional region of delta systems.

Conclusions

Kinematic analysis has been proven in the past an excellent method to understand the evolution of normal faults in terms of their growth and reactivation. In this study, we demonstrated that it is an excellent tool for describing such faults that develop in response to the accumulation of sediments in delta systems.

We interpreted 530 fault segments in the study area using the Ceduna 3D MSS seismic survey which represents a structurally complex area of the Ceduna Sub-basin containing faults with a range of strike orientations and lengths along strike. We demonstrated that the fault system varies with the thickness of different stratigraphic intervals and exhibits variation in the presence or extent of development of rollovers and rotation blocks in the hangingwall in response to variations in characteristics of the underlying Tiger and BW detachment layers (e.g., “dome-like” and “depression-like” structures, changes in lithology and thickness). This structural complexity is also evident in the evolution style of the normal growth faults that can denote periods of constant fault growth, dip-linkage and reactivation.

We identified three fault groups that relate faults offsets of the stratigraphic record (WP-Tiger, WP-HH and Tiger-HH) and define three evolution styles that involved constant fault growth, or either one or two events of dip-linkage and reactivation of already nucleated fault segments. Our detailed

analysis includes fault segments distributed across the study area that permitted correlation between the location of WP-HH fault segments and their evolution styles. We believe that in the case of delta systems, evolution studies can result from the interaction between two parameters: (1) changes in sediment accumulation along the study area. As these faults are controlled by the amount of sediment entering the basin, these local changes in lithology and thickness can result in variations to fault displacement and fault growth in terms of the thickness of the syn-kinematic interval, and specifically between adjacent layers; (2) displacement of the underlaying detachment basinwards. Our seismic interpretation and structural maps indicate that the BW and Tiger detachments vary in thickness, lithology (inferred from changes in the internal seismic amplitude), and the diversity and frequency of internal structures (thrust faults, "dome-like" and "depression-like" geometries). Our analysis demonstrates that more complex characteristics of the detachment layer result in a more complex evolution styles of the overlying growth fault segments.

These findings have implications for hydrocarbon system of the basin. The timing between hydrocarbon generation, migration and trapping is a key risk in determining the formation of structural traps or migration paths throughout the fault segments. This study has shown the importance for the exploration of hydrocarbons of understanding in detail how normal growth faults have evolved within delta systems. In this study, we correlated the information from earlier studies showing potential periods of hydrocarbon generation and secondary migration with the history of growth fault development in the Ceduna Sub-basin. This comparison demonstrates that faults developed between the White Pointer and Hammerhead supersequences that comprised events of dip-linkage and reactivation evets (especially in the south and southeast areas of the study) might represent a risk of failure in the containment of any hydrocarbon fluids that had accumulated following secondary or tertiary migration from either Blue Whale or Tiger supersequence source rocks. These results show that in all cases faults displacing the WP-HH and Tiger-HH sequences are more likely to have trapped hydrocarbons that migrated after the deposition of the HH3 sequence, either by secondary or tertiary migration events. In, while faults that evolved between deposition of the WP and Tiger supersequences might have been able to trap hydrocarbon fluids migrating since the Turonian.

References

Allard, D.M., 1997. Fault leak controlled trap fill: Rift basn examples. AAPG Mem. Chapter 9, 135–142.

Alzaga-Ruiz, H., Granjeon, D., Lopez, M., Seranne, M., Roure, F., 2009. Gravitational collapse and Neogene sediment transfer across the western margin of the Gulf of Mexico: Insights from numerical models. Tectonophysics 470, 21–41. https://doi.org/10.1016/j.tecto.2008.06.017

Bally, A.W., Bernoulli, D., Davis, G.A., Montadert, L., 1981. Listric Normal Faults. Oceanol. Acta 16.

Baudon, C., Cartwright, J., 2008a. The kinematics of reactivation of normal faults using high resolution throw mapping. J. Struct. Geol. 30, 1072–1084. https://doi.org/10.1016/j.jsg.2008.04.008

Baudon, C., Cartwright, J., 2008b. The kinematics of reactivation of normal faults using high resolution throw mapping. J. Struct. Geol. 30, 1072–1084. https://doi.org/10.1016/j.jsg.2008.04.008

Bellahsen, N., Daniel, J.M., 2005. Fault reactivation control on normal fault growth: an experimental study. J. Struct. Geol. 27, 769–780. https://doi.org/10.1016/j.jsg.2004.12.003

Bourdet, J., Kempton, R.H., Dyja-Person, V., Pironon, J., Gong, S., Ross, A.S., 2020. Constraining the timing and evolution of hydrocarbon migration in the Bight Basin. Mar. Pet. Geol. 114, 104193. https://doi.org/10.1016/j.marpetgeo.2019.104193

Bruhn, R.L., Schultz, R.A., 1996. Geometry and slip distribution in normal fault systems: Implications for mechanics and fault-related hazards. J. Geophys. Res. Solid Earth 101, 3401–3412. https://doi.org/10.1029/95JB03253

Camanni, G., Roche, V., Childs, C., Manzocchi, T., Walsh, J., Conneally, J., Saqab, M.M., Delogkos, E., 2019. The three-dimensional geometry of relay zones within segmented normal faults. J. Struct. Geol. 129, 103895. https://doi.org/10.1016/j.jsg.2019.103895

Cohen, H.A., McClay, K., 1996. Sedimentation and shale tectonics of the northwestern Niger Delta front. Mar. Pet. Geol. 13, 313–328. https://doi.org/10.1016/0264-8172(95)00067-4

Crans, W., Mandl, G., Haremboure, J., 1980. On the theory of growth faulting: a geomechanical delta model based on gravity sliding. J. Petrleum Geol. 2,3, 265–307.

Department for Energy and Mining [WWW Document], 2020. . Bight Basin. URL https://energymining.sa.gov.au/petroleum/prospectivity/bight_basin

Dinc, G., Callot, J.-P., Ringenbach, J.-C., 2023. Shale mobility: From salt-like shale flow to fluid mobilization in gravity-driven deformation, the late Albian–Turonian White Pointer Delta (Ceduna Subbasin, Great Bight, Australia). Geology XX. https://doi.org/10.1130/G50611.1

Dutton, D.M., Trudgill, B.D., 2009. Four-dimensional analysis of the Sembo relay system, offshore Angola: Implications for fault growth in salt-detached settings. AAPG Bull. 93, 763–794. https://doi.org/10.1306/02230908094

Espurt, N., Callot, J.-P., Totterdell, J., Struckmeyer, H., Vially, R., 2009a. Interactions between continental breakup dynamics and large-scale delta system evolution: Insights from the Cretaceous Ceduna delta system, Bight Basin, Southern Australian margin: Continental breakup and delta system. Tectonics, TC6002 28. https://doi.org/10.1029/2009TC002447

Espurt, N., Callot, J.-P., Totterdell, J., Struckmeyer, H., Vially, R., 2009b. Interactions between continental breakup dynamics and large-scale delta system evolution: Insights from the

Cretaceous Ceduna delta system, Bight Basin, Southern Australian margin: CONTINENTAL BREAKUP AND DELTA SYSTEM. Tectonics 28. https://doi.org/10.1029/2009TC002447

Fazli Khani, H., Back, S., 2015. The influence of pre-existing structure on the growth of syn-sedimentary normal faults in a deltaic setting, Niger Delta. J. Struct. Geol. 73, 18–32. https://doi.org/10.1016/j.jsg.2015.01.011

Fazlikhani, H., Back, S., Kukla, P.A., Fossen, H., 2017. Interaction between gravity-driven listric normal fault linkage and their hanging-wall rollover development: a case study from the western Niger Delta, Nigeria. Geol. Soc. Lond. Spec. Publ. 439, 169–186. https://doi.org/10.1144/SP439.20

Fazlikhani, H., Back, S., Kukla, P.A., Fossen, H., 2016. Interaction between gravity-driven listric normal fault linkage and their hanging-wall rollover development: a case study from the western Niger Delta, Nigeria. Geol. Soc. Lond. Spec. Publ. 439, 169–186. https://doi.org/10.1144/SP439.20

Ferrill, D.A., Morris, A.P., McGinnis, R.N., Smart, K.J., Wigginton, S.S., Hill, N.J., 2017. Mechanical stratigraphy and normal faulting. J. Struct. Geol. 94, 275–302. https://doi.org/10.1016/j.jsg.2016.11.010

Fitzenz, D.D., Miller, S.A., 2003. Fault compaction and overpressured faults: results from a 3-D model of a ductile fault zone. Geophys. J. Int. 155, 111–125. https://doi.org/10.1046/j.1365-246X.2003.02008.x

Fossen, H., 2010. Structural Geology. Cambridge University Press, NY, Cambridge.

GAB 3D Survey Final Report (Seismic Processing), 2012. . PGD Data Processing, Australia.

Geoscience Australia [WWW Document], 2020. . Gt. Aust. Bight. URL https://www.ga.gov.au/scientific-topics/energy/province-sedimentary-basin-geology/petroleum/offshore-southern-australia/bight

Gibson, G.M., Totterdell, J.M., White, L.T., Mitchell, C.H., Stacey, A.R., Morse, M.P., Whitaker, A., 2013. Pre-existing basement structure and its influence on continental rifting and fracture zone development along Australia's southern rifted margin. J. Geol. Soc. 170, 365–377. https://doi.org/10.1144/jgs2012-040

Hallett, D., 2002a. PETROLEUM SYSTEMS, in: Petroleum Geology of Libya. Elsevier, pp. 355–416. https://doi.org/10.1016/B978-044450525-5/50010-X

Hallett, D., 2002b. Petroleum Systems, in: Petroleum Geology of Libya. Elsevier, pp. 355–416. https://doi.org/10.1016/B978-044450525-5/50010-X

Holford, S., Hillis, R., Duddy, I., Green, P., Stoker, M., Tuitt, A., Backé, G., Tassone, D., MacDonald, J., 2011. Cenozoic post-breakup compressional deformation and exhumation of the southern Australian margin. APPEA J. 51, 613. https://doi.org/10.1071/AJ10044

Imber, J., Childs, C., Nell, P.A.R., Walsh, J.J., Hodgetts, D., Flint, S., 2003. Hanging wall fault kinematics and footwall collapse in listric growth fault systems. J. Struct. Geol. 25, 197–208. https://doi.org/10.1016/S0191-8141(02)00034-2

Jackson, C.A.-L., Bell, R.E., Rotevatn, A., Tvedt, A.B.M., 2017. Techniques to determine the kinematics of synsedimentary normal faults and implications for fault growth models. Geol. Soc. Lond. Spec. Publ. 439, 187–217. https://doi.org/10.1144/SP439.22

Jackson, C.A.-L., Rotevatn, A., 2013. 3D seismic analysis of the structure and evolution of a salt-influenced normal fault zone: A test of competing fault growth models. J. Struct. Geol. 54, 215–234. https://doi.org/10.1016/j.jsg.2013.06.012

Kempton, R., Bourdet, J., Ross, A., Pironon, J., 2019. Petroleum migration in the Bight Basin: a fluid inclusion approach to constraining source, composition and timing. APPEA 57, 762–766.

King, R., Backé, G., 2010. A balanced 2D strucutral model of the Hammerhead Delta-Deepwater Fold-Thrust Belt, Bight Basin, Australia. Aust. J. Earth Sci. 1005–1012.

King, R.C., Backé, G., 2010. A balanced 2D structural model of the Hammerhead Delta–Deepwater Fold-Thrust Belt, Bight Basin, Australia. Aust. J. Earth Sci. 57, 1005–1012. https://doi.org/10.1080/08120099.2010.509409

King, R.C., Morley, C.K., 2017. Wedge Geometry and Detachment Strength in Deepwater Fold-Thrust Belts. Earth-Sci. Rev. 165, 268–279. https://doi.org/10.1016/j.earscirev.2016.12.012

Klauser-Baumgärtner, D., Reichel, T., Hansen, J.-A., 2019. Regional paleodepositional environment of the Cretaceous in the Great Australian Bight – a support for frontier exploration. APPEA J. 59, 891. https://doi.org/10.1071/AJ18055

MacDonald, J., King, R., Hillis, R., Backé, G., 2010. Structural style of the White Pointer and Hammerhead Delta—deepwater fold-thrust belts, Bight Basin, Australia. APPEA J. 50, 487. https://doi.org/10.1071/AJ09029

Magoon, L.B., 1988. Petroleum Systems of the United States (Bulletin No. 1870). U.S. Geological Survey, Washington DC, USA.

Mahon, E.M., Wallace, M.W., 2020. Cenozoic structural history of the Gippsland Basin: Early Oligocene onset for compressional tectonics in SE Australia. Mar. Pet. Geol. 114, 104243. https://doi.org/10.1016/j.marpetgeo.2020.104243

Mandl, G., Crans, W., 1981. Gravitational gliding in deltas. Geol. Soc. Lond. Spec. Publ. 9, 41–54. https://doi.org/10.1144/GSL.SP.1981.009.01.05

Mansfield, C.S., Cartwright, J.A., 1996. High resolution fault displacement mapping from three-dimensional seismic data: evidence for dip linkage during fault growth. J. Struct. Geol. 18, 249–263. https://doi.org/10.1016/S0191-8141(96)80048-4

Marton, L.G., Tari, G., Lehmann, C.T., 2000. Evolution of the Angolan Passive Margin, West Africa, with Emphasis on Post-Salt Structural Styles. Geophys. Monogr. 115, 129–150.

McClay, K., Dooley, T., Zamora, G., 2003. Analogue models of delta systems above ductile substrates. Geol. Soc. Lond. Spec. Publ. 216, 411–428. https://doi.org/10.1144/GSL.SP.2003.216.01.27

McClay, K.R., 1990. Deformation mechanics in analogue models of extensional fault systems. Geol. Soc. Lond. Spec. Publ. 54, 445–453. https://doi.org/10.1144/GSL.SP.1990.054.01.40

McClay, K.R., Ellis, P.G., 1987. Analogue models of extensional fault geometries. Geol. Soc. Lond. Spec. Publ. 28, 109–125. https://doi.org/10.1144/GSL.SP.1987.028.01.09

Mitchell, C., Boreham, C.J., Totterdell, J., Geoscience Australia, 2009. Bight Basin geological sampling and seepage survey: RV Southern Surveyor survey SS01/2007. Geoscience Australia, Canberra.

Morley, C.K., 2003. Mobile shale related deformation in large deltas developed on passive and active margins. Geol. Soc. Lond. Spec. Publ. 216, 335–357. https://doi.org/10.1144/GSL.SP.2003.216.01.22

Morley, C.K., King, R., Hillis, R., Tingay, M., Backe, G., 2011. Deepwater fold and thrust belt classification, tectonics, structure and hydrocarbon prospectivity: A review. Earth-Sci. Rev. 104, 41–91. https://doi.org/10.1016/j.earscirev.2010.09.010

Mourgues, R., Lecomte, E., Vendeville, B., Raillard, S., 2009. An experimental investigation of gravity-driven shale tectonics in progradational delta. Tectonophysics 474, 643–656. https://doi.org/10.1016/j.tecto.2009.05.003

Ogilvie, S.R., Dee, S.J., Wilson, R.W., Bailey, W.R., 2020. Integrated Fault Seal Analysis: An Introduction. Geol. Soc. Lond. Spec. Publ. 496, 1–8. https://doi.org/10.1144/SP496-2020-51

Osagiede, E., Duffy, O., Jackson, C.A.-L., Wrona, T., 2014. Quantifying the growth history of seismically imaged normal faults. J. Struct. Geol. 66, 382–399.

Peacock, D., Sanderson, D., 1994. Geometry and Development of Relay Ramps in Normal Fault Systems. AAPG Bull. 78. https://doi.org/10.1306/BDFF9046-1718-11D7-8645000102C1865D

Redpath, D., Jackson, C.A. -L., Bell, R.E., 2022. Mechanical Stratigraphy Controls Normal Fault Growth and Dimensions, Outer Kwanza Basin, Offshore Angola. Tectonics 41. https://doi.org/10.1029/2021TC006823

Reynolds, P., Holford, S., Schofield, N., Ross, A., 2017. The shallow depth emplacement of mafic intrusions on a magma-poor rifted margin: An example from the Bight Basin, southern Australia. Mar. Pet. Geol. 88, 605–616. https://doi.org/10.1016/j.marpetgeo.2017.09.008

Robson, A., King, R., Holford, S., 2017. Structural evolution of a gravitationally detached normal fault array: analysis of 3D seismic data from the Ceduna Sub-Basin, Great Australian Bight. Basin Res. 29, 605–624. https://doi.org/10.1111/bre.12191

Robson, A.G., King, R.C., Holford, S.P., 2017. Structural evolution of a gravitationally detached normal fault array: analysis of 3D seismic data from the Ceduna Sub-Basin, Great Australian Bight. Basin Res. 29, 605–624. https://doi.org/10.1111/bre.12191

Roche, V., Homberg, C., van der Baan, M., Rocher, M., 2017. Widening of normal fault zones due to the inhibition of vertical propagation. Geol. Soc. Lond. Spec. Publ. 439, 271–288. https://doi.org/10.1144/SP439.5

Rouby, D., Cobbold, P.R., 1996. Kinematic analysis of a growth fault system in the Niger Delta from restoration in map view. Mar. Pet. Geol. 13, 565–580. https://doi.org/10.1016/0264-8172(95)00076-3

Rowan, M.G., Hart, B.S., Nelson, S., Flemings, P.B., Trudgill, B.D., 1998. Three-dimensional geometry and evolution of a salt-related growth-fault array: Eugene Island 330 field, offshore Louisiana, Gulf of Mexico. Mar. Pet. Geol. 15, 309–328. https://doi.org/10.1016/S0264-8172(98)00021-X

Ryan, L., Magee, C., Jackson, C.A.-L., 2017a. The kinematics of normal faults in the Ceduna Subbasin, offshore southern Australia: Implications for hydrocarbon trapping in a frontier basin. AAPG Bull. 101, 321–341. https://doi.org/10.1306/08051615234

Ryan, L., Magee, C., Jackson, C.A.-L., 2017b. The kinematics of normal faults in the Ceduna Subbasin, offshore southern Australia: Implications for hydrocarbon trapping in a frontier basin. AAPG Bull. 101, 321–341. https://doi.org/10.1306/08051615234

Sapin, F., Ringenbach, J.-C., Rives, T., Pubellier, M., 2012. Counter-regional normal faults in shale-dominated deltas: Origin, mechanism and evolution. Mar. Pet. Geol. 37, 121–128. https://doi.org/10.1016/j.marpetgeo.2012.05.001

Sayers, J., Symonds, P.A., Direen, N.G., Bernardel, G., 2001. Nature of the continent-ocean transition on the non-volcanic rifted margin of the central Great Australian Bight. Geol. Soc. Lond. Spec. Publ. 187, 51–76.

Somerville, R., 2001. The Ceduna Sub-basin—A Snapshot of prospectivity. APPEA J. 41, 321. https://doi.org/10.1071/AJ00015

Tapley, D., Mee, B.C., King, S.J., Davis, R.C., Leischner, K.R., 2005. Petroleum potential of the Ceduna Sub-Basin: Impact of Gnarlyknots–1A. APPEA J. 45, 365. https://doi.org/10.1071/AJ04029

Thorsen, C.E., 1963. Age of Growth Faulting in Southeast Louisiana. AAPG, Gulf Coast Association of Geological Societies Transactions 13, 103–110.

Tottendell, J., Mitchel, C., 2009. Bight Basin geological sampling and seepage survey: RV Southern Surveyor survey SS01/2007. Geosci. Aust., 68689 24, 1–134.

Totterdell, J., Krassay, A., 2003. The role of shale deformation and growth faulting in the Late Cretaceous evolution of the Bight Basin, offshore southern Australia. Geol. Scoeity Lond., Subsurface Sediment Mobilization 216, 429–442.

Totterdell, J.M., Blevin, J.E., Struckmeyer, H.I.M., Bradshaw, B.E., Colwell, J.B., Kennard, J.M., 2000. A new sequence framework for the Great Australian Bight: Starting with a clean slate. APPEA J. 40, 95. https://doi.org/10.1071/AJ99007

Totterdell, J.M., Krassay, A.A., 2003. The role of shale deformation and growth faulting in the Late Cretaceous evolution of the Bight Basin, offshore southern Australia. Geol. Soc. Lond. Spec. Publ. 216, 429–442. https://doi.org/10.1144/GSL.SP.2003.216.01.28

Totterdell, J.M., Struckmeyer, H.I.M., Boreham, C.J., Mitchell, C.H., Monteil, E., Bradshaw, B.E., 2008. Mid–Late Cretaceous organic-rich rocks from the eastern Bight Basin: implications for prospectivity 23.

Tvedt, A.B.M., Rotevatn, A., Jackson, C.A.-L., Fossen, H., Gawthorpe, R.L., 2013. Growth of normal faults in multilayer sequences: A 3D seismic case study from the Egersund Basin, Norwegian North Sea. J. Struct. Geol. 55, 1–20. https://doi.org/10.1016/j.jsg.2013.08.002

Vendeville, B., Cobbold, P.R., 1988. How normal faulting and sedimentation interact to produce listric fault profiles and stratigraphic wedges. J. Struct. Geol. 10, 649–659. https://doi.org/10.1016/0191-8141(88)90073-9

Vendeville, B., Cobbold, P.R., Davy, P., Choukroune, P., Brun, J.P., 1987. Physical models of extensional tectonics at various scales. Geol. Soc. Lond. Spec. Publ. 28, 95–107. https://doi.org/10.1144/GSL.SP.1987.028.01.08

Walsh, J.J., Watterson, J., 1991. Geometric and kinematic coherence and scale effects in normal fault systems. Geol. Soc. Lond. Spec. Publ. 56, 193–203. https://doi.org/10.1144/GSL.SP.1991.056.01.13

Wang, H.X., Fu, X.F., Liu, S.R., Chu, R., Liu, B., Shi, P.P., 2018. Quantitative discrimination of normal fault segment growth and its geological significance: example from the Tanan Depression, Tamtsag Basin, Mongolia. Aust. J. Earth Sci. 65, 711–725. https://doi.org/10.1080/08120099.2018.1462850

Wiener, R., Mann, M., Angelich, M., Molyneux, J., 2011. Mobile Shale in the Niger Delta: Characteristics, Structure, and Evolution, in: Shale Tectonics. American Association of Petroleum Geologists, pp. 145–161. https://doi.org/10.1306/13231313M933423

Wood, L.J., 2012. Shale tectonics, in: Regional Geology and Tectonics: Phanerozoic Passive Margins, Cratonic Basins and Global Tectonic Maps. Elsevier, pp. 42–61. https://doi.org/10.1016/B978-0-444-56357-6.00002-0

Ze, T., Alves, T.M., 2019. Impacts of data sampling on the interpetation of normal fault propagation and segment linkage. Tectonophysics 762, 79–96.

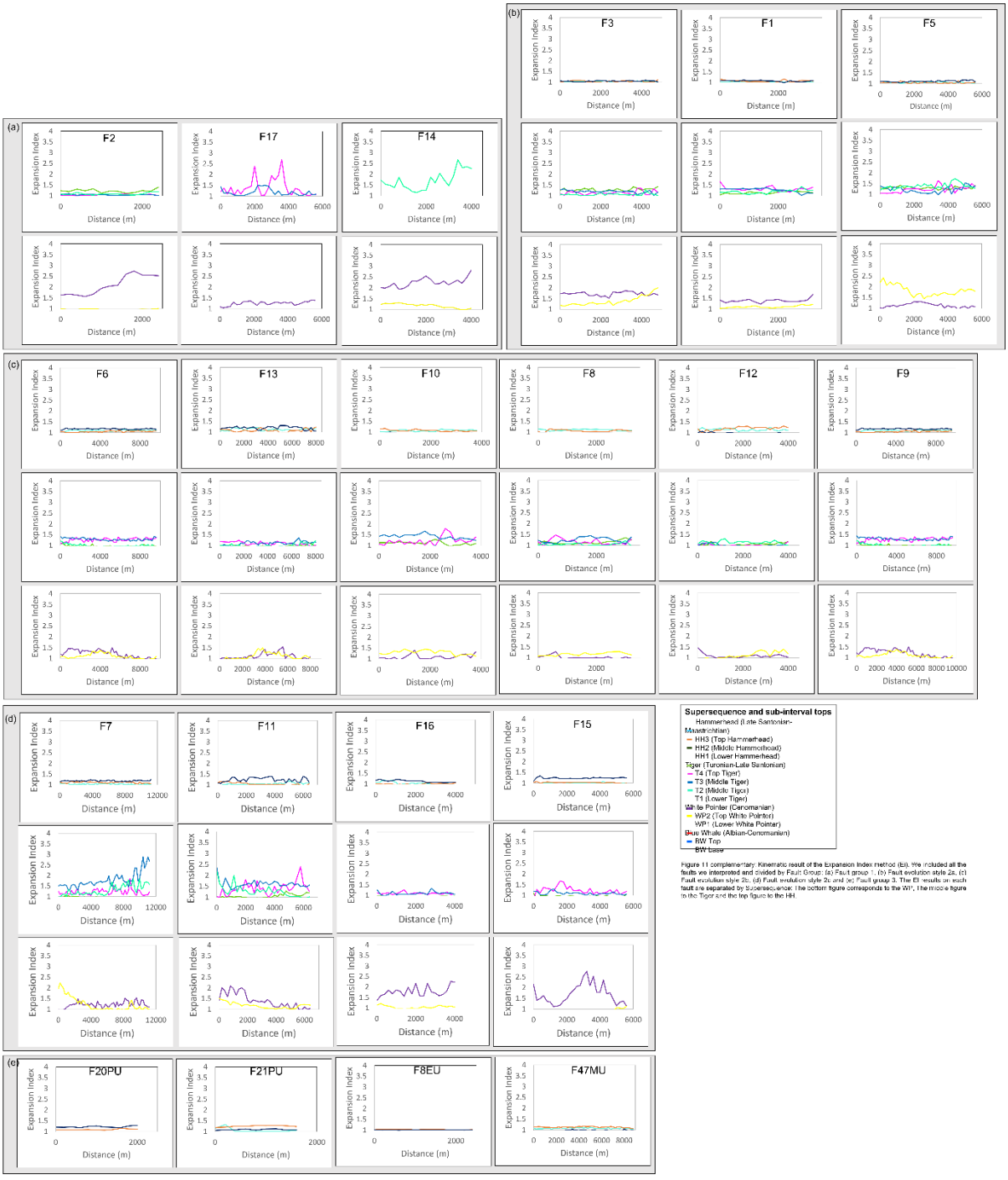

Figure 11 complementary Kinematic result of the Expansion Index method (EI). We included all the faults we interpreted and divided by Fault Group: (a) Fault group 1, (b) Fault evolution style 2a, (c) Fault evolution style 2b, (d) Fault evolution style 2c and (e) Fault group 3. The EI results on each fault are separated by Supersequence. The bottom figure corresponds to the WP, the middle figure to the Tiger and the top figure to the HH.

Chapter 3: Geomechanical analysis

Geomechanical analysis of normal growth fault reactivation in the Ceduna Sub-basin

Statement of Authorship

Title of Paper	Geomechanical analysis of normal growth fault reactivation in the Ceduna Sub-basin
Publication Status	☐ Published ☐ Accepted for Publication ☐ Submitted for Publication ☑ Unpublished and Unsubmitted work written in manuscript style
Publication Details	

Principal Author

Name of Principal Author (Candidate)	Monica Jimenez Lloreda
Contribution to the Paper	• Data interpretation • Development of methodology • Manuscript drafting
Overall percentage (%)	70%
Certification:	This paper reports on original research I conducted during the period of my Higher Degree by Research candidature and is not subject to any obligations or contractual agreements with a third party that would constrain its inclusion in this thesis. I am the primary author of this paper.
Signature	Date 09/01/2023

Co-Author Contributions

By signing the Statement of Authorship, each author certifies that:

i. the candidate's stated contribution to the publication is accurate (as detailed above);

ii. permission is granted for the candidate in include the publication in the thesis; and

iii. the sum of all co-author contributions is equal to 100% less the candidate's stated contribution.

Name of Co-Author	Simon Holford
Contribution to the Paper	• Supervision • Manuscript drafting • Method development
Signature	Date 03/02/23

Name of Co-Author	Rosalind King
Contribution to the Paper	• Supervision • Manuscript drafting
Signature	Date 8/2/23

Name of Co-Author	Mark Bunch		
Contribution to the Paper	• Supervision • Manuscript drafting		
Signature		Date	17/03/2023

Geomechanical analysis of normal growth fault reactivation in the Ceduna Sub-Basin

Monica Jimenez[1,2], Rosalind King[1,2], Simon Holford[1,2], Mark Bunch[1,2]

[1] Structural, Stress and Seismic Research Group (S3)

[2] Discipline of Earth Sciences, University of Adelaide

Abstract

The reactivation of normal faults results in seismicity that can cause traps and seals to fail and allow fluids to migrate in sedimentary basins. In terms of petroleum operations, active faults can cause damage to and changes in the geometry of boreholes drilled as exploration and development wells. This study is focused in the Ceduna Sub-basin in the Great Australian Bight where recent studies have defined a Neogene-to-present-day strike-slip stress field in the Southern Australian Margin. We aim to analyse the likelihood that nucleated normal growth faults in the up-dip region of the Ceduna Delta system can reactivate with the present-day stress field. We used the Fault analysis seal technology (FAST) technique to create eight different parameter sets (scenarios) that consist of different geomechanical values of angle of friction, total stress magnitudes, maximum horizontal stress orientations, pore pressures, and cohesion. We analysed six fault segments with different structural attributes such as length, strike, and geometry to test how the changes in fault roughness along strike impact the pore pressure threshold required to reactivate faults in the area. We also include statistical analysis to define the proportion of fault surfaces that are at higher risk of reactivation along strike using each scenario. Given that fault reactivation can strongly affect multiple elements of the petroleum system, we test two fault traps in two leads where we map good quality reservoir and seal rocks, and potential hydrocarbon accumulations. These leads represent rollover structures against fault planes that might be good traps for hydrocarbons. Our results demonstrate that areas of a fault with steep dip angles (>40°) and strikes oblique to the maximum stress orientation (within 10° to 15°) are more likely to reactivate, which demonstrates that fault roughness (changes in dip angle and strike) have a strong impact on the risk of fault reactivation, and it is an important factor to consider in future normal fault reactivation analysis.

Introduction

Reactivation of fault segments has an enormous impact on the evolution of sedimentary basins in terms of the development of accommodation space and sedimentation patterns during extended periods of time, and on both seismicity and fluid migration (e.g. water, hydrocarbons). Therefore it has implications for the exploration of hydrocarbons as it influences the distribution of petroleum system elements *(Worum et al., 2004)* and can damage exploration and development boreholes by causing failure of the borehole wall and hydraulic fractures *(Brudy et al., 1997)*. Normal faults can either trap hydrocarbons during inactive periods or work as periodic migration pathways during active stages (e.g. growth or reactivation periods). Some properties such as variability in the permeability and thickness of the fault zone can potentially result in (1) water displacement; (2) oil and/or gas migration from deep source rocks to shallow intervals, and (3) increase in pore pressure within reservoir intervals. It is possible to define potential interactions between a fault and the fluid content of adjoining rock given that these interactions leave evidence such as: anomalies in salinity, pore pressure or temperature; local mineralization of sandstones; grain crushing (as seen in the Gulf of Mexico), and; changes in reservoir pressure as the basin develops (e.g. Niger Delta and North Sea), *(Weber et al., 1978; Hooper, 1991; Caine et al., 1996; Karstens and Berndt, 2015; Woillez et al., 2017).*

Two aspects of a petroleum system that are essential for the exploration of hydrocarbons are the effectiveness of faults forming closures to trap hydrocarbons, and the relative timing of hydrocarbon migration with respect to the development of traps *(Thorsen, 1963; Streit, 1999, Mildren et al., 2002; Selley and Sonnenberg, 2015)*. Normal faults prone to reactivation pose a risk to trap effectiveness. Reactivation events or periods of reactivation would depend on the strike, dip and spatial organization of the structural heterogeneities, stress field and local pressure conditions *(Bellahsen and Daniel, 2005)*. This study focuses in the Ceduna Sub-basin of the Great Australian Bight Basin (GAB), which contains two stacked delta systems (the White Pointer and the Hammerhead delta systems). These deltas are linked by systems of normal growth faults at the delta top and deep water fault thrust belts at the delta toe *(Totterdell and Krassay, 2003; King and Backé, 2010; MacDonald, 2012).*

Preliminary studies suggested that gas from the Blue Whale source rock (Albian-Cenomanian) migrated between the Turonian and late Santonian, oil and wet gas from the WP (Cenomanian) migrated between the early Campanian and Pleistocene, and gas from the Tiger (Turonian) migrated during the late Campanian and Pleistocene (*Totterdell et al., 2008; Kempton et al., 2019)*. Drilled wells such as Gnarlyknots-1A and Greenly-1 intersected potential sandstone reservoirs and favourable fault-dependant closures that could potentially trap hydrocarbons *(Tapley et al., 2005; MacDonald et al., 2012).* However, these drilling campaigns highlighted potential hydrocarbon leakage at Jerboa-1 due to reactivation of faults in the late Santonian *(Totterdell et al., 2000; Somerville, 2001).* More specifically, recent studies in the Ceduna Sub-basin proposed fluid escape through pipe-like geometries along fault planes at the top of the Tiger and Hammerhead supersequences (*Velayatham* et al., 2021). Therefore, for a future exploration campaign in the Ceduna Sub-basin, it is vital to predict whether prospective fault-bound closures represent a risk of geologically recent or future reactivation under the present-day stress field along the Australian Southern Margin.

Preliminary studies have identified Neogene-to-Holocene tectonic activity in the Flinders Rangers, Mount Lofty Ranges, southwest Western Australia, Northwest Shelf and southeast Australia, that suggest active strain in response to regional stress in these areas *(Hillis and Reynolds, 2000; Reynolds et al., 2003; Hillis et al., 2008; Rajabi et al., 2017; Lubiniecki et al., 2020)*. These stresses could therefore reactivate faults forming a breaching component of pre-existing hydrocarbon traps, and unstable boreholes (S. Reynolds et al., 2003). For instance, *Reynolds et al., (2005)* analysed several 2D seismic lines over the GAB and suggested that in a strike-slip stress regime, the vertical faults with northwest-southeast and east-west strike orientations have higher risk of reactivation, while the faults with northeast-southwest strike have the smallest risk. *MacDonald et al., (2012)* interpreted the Trim3D seismic survey (TWT) to map the risk of reactivation in synthetic and antithetic northwest-southeast striking faults. They tested three different stress regimes: (a) strike slip, (b) strike slip-normal, and (c) normal. The results showed that moderately dipping faults are at the highest risk of reactivation, while fault with dips greater than 70° or shallower than 40° have a lower risk of reactivation. They also used two maximum horizontal stress orientations of 130°N (eastern Australian margin) and 090°N (south-western Australian margin and Perth Basin), and concluded that the orientation of the maximum horizontal stress (SH_{max}) (i.e. orientation of SH_{max} with respect to fault strike) has a greater impact on fault reactivation than the stress regime.

Preliminary work in this study involved interpretation of more than 520 fault segments in the study area using the Ceduna 3D MSS seismic survey and concluded that normal growth faults show a wide variability of lengths along strike (from 0.8 km to 12 km), geometries (planar and listric), strikes (northwest-southeast, northeast-southwest, north-south and west-east) and diverse evolution styles that include dip-linkage and reactivation events. These fault segments also show strong changes in dip angle along the fault plane. Interpreted listric faults exhibit dip angles from about 85° to 2° in cross-section, while planar faults exhibit dip angles that vary from about 70° to 38° It is reasonable to expect variations in risk of reactivation given the strong changes in dip angle and strike along the fault planes.

Some studies have advanced understanding of the influence that fault plane roughness has on the risk of fault reactivation and seismicity. This influence is mostly related to variability of fault dip angles than to local changes in strike orientation *(MacDonald et al., 2012, Litchfield et al., 2018).* There is limited information regarding the location of areas more likely to reactivate along fault planes. We consider that a statistical approach would be the most useful way to analyse results in detail. The incorporation of percentiles is also a common practice in the oil and gas industry to classify exploration projects as low (P10), middle (P50) and high (P90) risk. This approach is used to calibrate hydrocarbon exploration uncertainty *(Otis and Haryott, 2010).*

In this study, we created eight different parameter sets (scenarios) that consist of different values for the angle of friction, total stress magnitudes, SH_{max} orientations, pore pressures, and cohesion to analyse six fault segments. From the seismic data we also mapped two leads that represent two areas where we identified potential closures against fault segments to test if they are suitable candidates to trap hydrocarbons. We also generated seismic attributes such as sweetness and instantaneous frequency over the structural surfaces of the principal targets (Tiger and White Pointer) to define the potential presence of good quality reservoirs and hydrocarbon content along these structures. Fault segments were interpreted using the Ceduna 3D MSS seismic survey and represent synthetic faults that collectively vary in their geometry (listric vs. planar), principal strike orientation (northwest-southeast or east-west) and in terms of the stratigraphic units they offset. We applied these parameters to the Fault analysis seal technology (FAST) technique (Scott Mildren et al., 2005) that determines likelihood of fault reactivation in a given stress regime with respect to

fracture stability in terms of pore pressure and the Mohr-Coulomb criterion. We highlight the areas where mapped faults are closer to failure and included statistical percentiles to differentiate distributions of pore pressure data. We compare results for sections along fault planes showing changes in strike and dip angle to identify and define the structural features that influence the risk of fault reactivation. Finally, we plot our results over 3D maps of each fault and lead to show fault sections that are at the highest risk of reactivation.

The FAST technique proved to be an effective method to analyse the risk of fault reactivation in the Ceduna Sub-basin. In addition, the incorporation of percentiles allowed an improved and more detailed analysis of the distribution of pore pressure along fault planes, and how the structural features of the fault influence likelihood of reactivation. Our analysis demonstrates that angle of friction, SH_{max} orientation and stress magnitude all have a major effect on the risk of fault reactivation. We recognized that the angle of friction is the geomechanical parameter that is most strongly related to the risk of fault reactivation. Our results demonstrate that when the angle of friction is decreased to comprised lithologies of shales intercalated with sandstones faults are likely to reactivate as the pore pressure required to achieve fault failure decreases by 10 MPa. In addition, changes in fault plane roughness prove to be a major factor in the likelihood of fault reactivation where dip angles exceed 44° and oblique strike orientations that are at 10° to 15° from the SH_{max} orientation.

Geological background

Location of the Great Australian Bight and the Ceduna Sub-basin

The GAB developed between the Middle Jurassic and the Late Cretaceous epochs and covers ~250,000 km^2 of the Southern Australian Margin. It contains four structurally independent sub-basins: The Eyre, Duntroon, Ceduna, and Recherche. Water depths vary considerably from about 200m in the Eyre Sub-basin to more than 4,000m in the Recherche Sub-basin. The Northern boundary of the GAB is the Madura Shelf and the Gawler Craton; the eastern boundary is the western boundary of the Otway Basin; the southern boundary occurs at the continental-oceanic crust transition; the western boundary is the eastern boundary of the Perth Basin (*Reynolds and Hillis, 2000; Totterdell and Krassay, 2003; Totterdell and Mitchell, 2009; Department for Energy and Mining, 2020)* (Figure 1a and b).

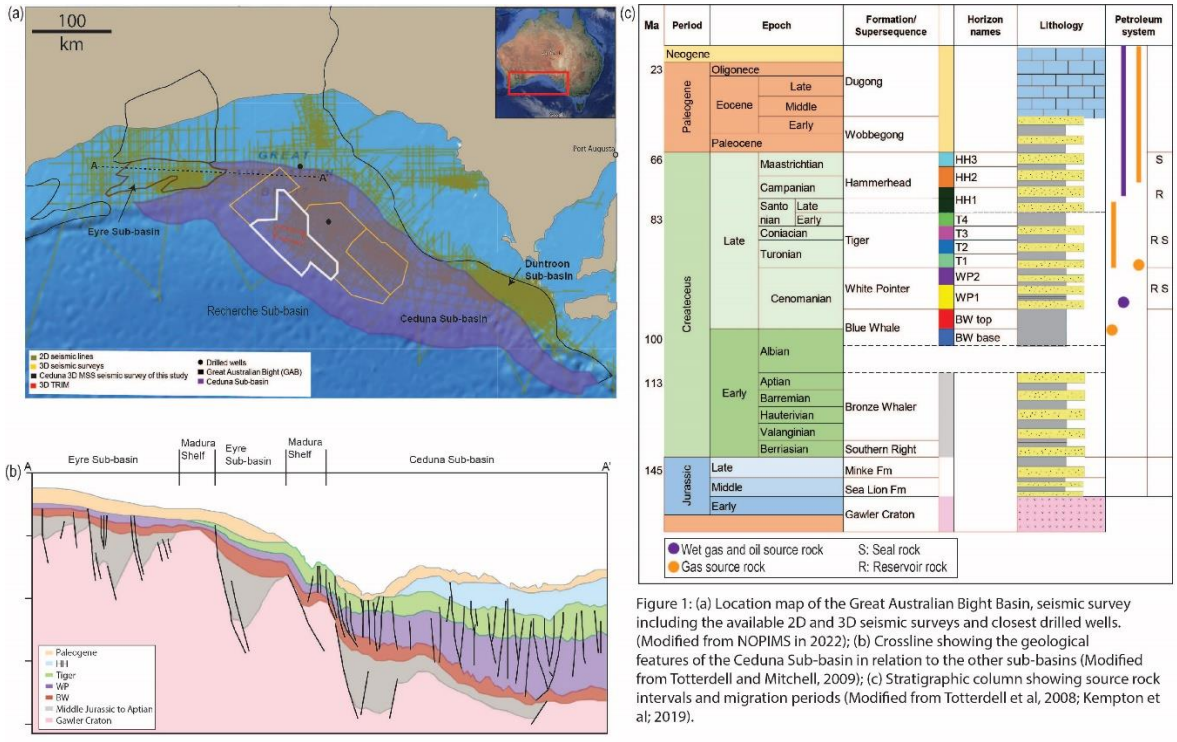

Figure 1: (a) Location map of the Great Australian Bight Basin, seismic survey including the available 2D and 3D seismic surveys and closest drilled wells. (Modified from NOPIMS in 2022); (b) Crossline showing the geological features of the Ceduna Sub-basin in relation to the other sub-basins (Modified from Totterdell and Mitchell, 2009); (c) Stratigraphic column showing source rock intervals and migration periods (Modified from Totterdell et al, 2008; Kempton et al; 2019).

The Ceduna Sub-basin (CSB) contains the thickest stratigraphic sequence of 15,000 m of Middle Jurassic to Neogene age sediments. The CSB extends to the Proterozoic terranes to the north, the Gawler craton to the north-east, the Duntroon Sub-basin to the south-east, and the Recherche Sub-basin to the south and west *(Sayers et al., 2001; Totterdell and Krassay, 2003; Tapley et al., 2005; Espurt et al., 2009).*

Geological evolution of the Great Australian Bight

The Great Australian Bight developed between the start of Australia-Antarctica rifting during the Middle Jurassic and the beginning of the passive margin at the Late Cretaceous (late Santonian) *(Totterdell et al., 2000; Holford et al., 2011; Gibson et al., 2013)*. Four different phases define this basin development (Figure 2)

Stage 1: During the Middle Jurassic a continental rift formed a triple junction between India, Australia and Antarctica. This rift started from the west to east as continuous steps of crustal extension that were strongly controlled by basement fabric creating oblique grabens and rift-basins (Great Australian Bight, Otway, Gippsland, Bass and Sorell basins *(Totterdell and Krassay, 2003; Totterdell and Mitchell, 2009; Gibson et al., 2013)* (Figure 2a)

Stage 2: The Southern Right Supersequence was deposited during a period of slow thermal subsidence. This Supersequence is characterized by fluvial sandstones of Berriasian Age. The Bronze Whaler Supersequence was deposited subsequently and is composed of fluvial lacustrine sandstones and shales of Valanginian-Aptian ages (Figure 1c) *(Tapley et al., 2005; Totterdell and Mitchell, 2009; Holford et al., 2011).*

Stage 3: After an erosional event the Blue Whale Supersequence (BW) was deposited unconformably during the Albian-Cenomanian. Above the BW, 4000m of progradational fluvial-deltaic sediments

from the White Pointer Supersequence (WP) were deposited in the GAB. Rapid deposition of the WP sediments combined with rapid subsidence produced overpressure in the underlying BW shales forming the White Pointer Delta System. This delta contains the BW and WP supersequences and includes normal growth faults that detach at the top of the BW in the delta top *(Totterdell and Krassay, 2003; Espurt et al., 2009; Holford et al., 2011)* (Figure 1b and c)

During the Turonian-Santonian, the Tiger Supersequence was deposited conformably over the WP through a major marine flooding event. The Tiger Supersequence interval reaches a maximum thickness of 2,800 m within the CSB and transitions from base to top from progradational sandstones and shales to aggradational shales (Figure 1c) *(Totterdell and Krassay, 2003; Espurt et al., 2009).*

During the late Santonian (~83Ma), the rift transitioned to a passive margin that resulted from sea floor spreading. Evidence of this is preserved in gravity anomalies in the central area between Australia and Antarctica and an unconformity in the stratigraphic record (Figure 1c). The passive margin also resulted in the formation of smaller sub-basins within the GAB (Eyre, Ceduna, Recherche Sub-basins). Each sub-basin is structurally controlled by the basement architecture *(Totterdell and Mitchell, 2009; Holford et al., 2011).* (Figure 2b)

Stage 4: The Hammerhead Supersequence (HH) was deposited between the late Santonian and the Maastrichtian ages. This sequence contains 4,000m of sandstones and shales that were rapidly deposited to form the Hammerhead Delta system (Figure 1c). This rapid accumulation event reactivated some faults from the Cenomanian that propagate upwards into younger sediments, and created new faults that detach at the top of the Tiger Supersequence (Figure 1b). The HH represents a progressive change from a progradational regime at the base to an aggradational regime at the top, which changed the dynamics of the basin and resulted in nucleation of the normal growth faults *(Totterdell and Krassay, 2003; Tapley et al., 2005; Totterdell and Mitchell, 2009)* (Figure 2c)

During the Paleogene, a regional uplift event reactivated some of the normal growth faults and eroded most of the HH and upper Tiger intervals in the Eucla Sub-basin area, forming an angular unconformity between the GAB and the Eucla Basin and a hiatus in the stratigraphy in the CSB. Above the hiatus, fluvial sandstones from the Wobbegong Supersequence were deposited during the early Eocene and followed by transgressive cool water carbonates of the Dugong Formation during the later Eocene. *(Totterdell and Krassay, 2003; Espurt et al., 2009).* During the middle Eocene, several intrusions and eruptive centres formed in the GAB. This igneous bodies are described as complex magma network systems of basaltic composition that intruded different levels inside the HH and lava flows and volcanoes above the top of the Wobbegong Supersequence *(Magee et al., 2013; Reynolds et al., 2017; 2018)*

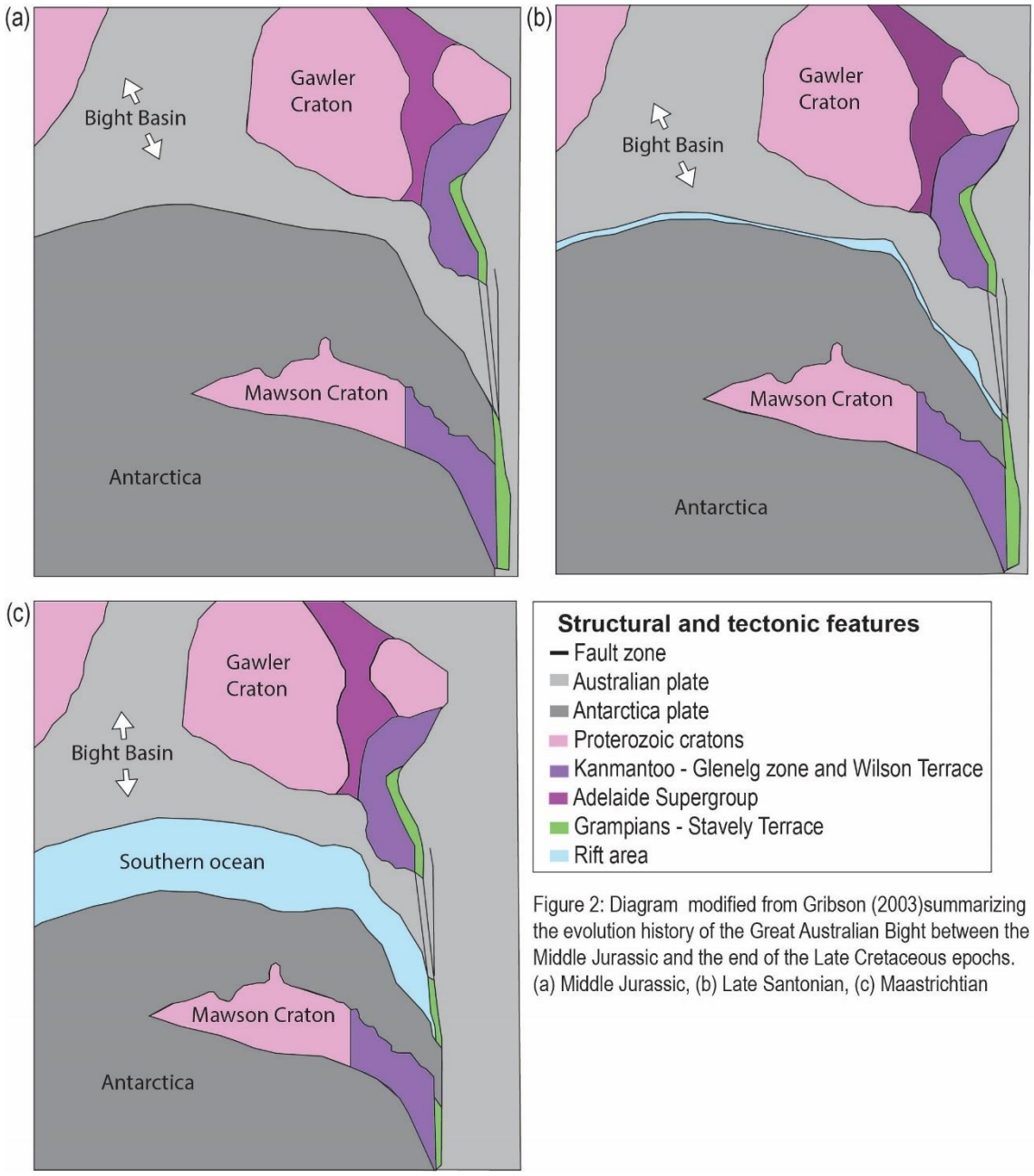

Figure 2: Diagram modified from Gribson (2003)summarizing the evolution history of the Great Australian Bight between the Middle Jurassic and the end of the Late Cretaceous epochs. (a) Middle Jurassic, (b) Late Santonian, (c) Maastrichtian

The petroleum system of the Great Australian Bight

Recent studies include the interpretation of 3D seismic surveys and 2D seismic lines, samples from canyons and cores (Eyre and Ceduna Sub-basins). We summarize in Figure 1c the results from preliminary studies that suggest three different source rock intervals: the BW generating gas, the WP generating wet-gas and oil, and the Tiger generating gas. These fluid products are hypothesised to have migrated during the Turonian-late Santonian, early Campanian-Pleistocene and late Campanian-Pleistocene respectively. Reservoir rocks proposed to have hosted these fluids following secondary migration are fluvial and deltaic sandstones of the WP, Tiger sandstones and HH deltaic sandstones and aggradational shales *(Tapley et al., 2005; Totterdell et al., 2008; Kempton et al., 2019; Langhi et al., 2020).* Sealing units are assumed to have been intercalated shales of the WP and Tiger

supersequences, and thick shales intervals at the top of the HH *(Espurt et al., 2009; Totterdell and Mitchell, 2009; Klauser-Baumgärtner et al., 2019).*

Exploration history in the Great Australian Bight

Since the 1960's there has been great interest in exploration of the GAB. Seven dry holes have been drilled that failed to intersect a hydrocarbon column due to possible deficit of reservoir, seal or effective structural closure; only Greenly-1 and Duntroon-1 have shown potential economical hydrocarbon discoveries. There are 11 petroleum exploration licenses in the GAB with several 2D seismic survey profile lines having been acquired in addition to 3D seismic survey data and seafloor sub-crop rock samples *(Tapley et al., 2005; Totterdell et al., 2008; Department for Energy and Mining, 2020).*

Importance of Fault Plane Roughness

Listric faults are described as normal faults with steep dip angles at the upper tip and shallow dip at the base (Bally et al., 1981b). They are likely to exhibit variations in dip and trend in cross-section view. Preliminary studies have demonstrated the importance of fault plane roughness for fault reactivation. It is well defined in field and laboratory observations and can occur at all spatial scales. It also has strong implications for frictional properties along strike and the complexity of fracture development as roughness influences stress concentration and stress changes along fault planes *(Renard and Candela, 2017).* This can be translated to represent a considerable control on the risk of fault reactivation and seismicity in specific sections of faults with moderate dip angles *(MacDonald et al., 2012; Litchfield et al., 2018).*

Available data

Parameters for the Reactivation Analysis

The Mohr-Coulomb Criterion constrains several geomechanical parameters that control the formation or reactivation of pre-existing faults. These are parameters such as rock mechanics properties (e.g. cohesion coefficient of friction and pore pressure), stress characteristics (orientation and magnitude) and tectonic regime (shear or normal stress) *(Paul, 1961; Sibson, 1985)*. To assess the risk of reactivation of normal growth faults in detail within the Ceduna Sub-basin, we incorporate the following geomechanical parameters from preliminary studies:

Stress orientation and magnitudes: We use stress orientations from preliminary studies in the GAB to identify a current stress field in the Southern Australian Margin. Studies in the western Otway and Ceduna Sub-basin calculated a maximum horizontal stress (S_{Hmax}) from dipmeter (HDT) logs for four drilled wells (Duntroon-1, Echidna-1, Platypus-1 and Columbia-1) and image logs (FMS) for two wells (Greenly-1 and Borda-1). These preliminary studies used elliptical boreholes from the six wells as evidence of *in situ* SH_{max} stress orientation towards the 130°N. They also a SH_{max} orientation towards 090°N in the Perth basin from borehole breakouts and drilling-induced tensile fracture analysis (DITF) *(Hillis et al., 1998; Hillis and Reynolds, 2000; Reynolds et al., 2003; King et al., 2008, 2012).* Numerical modelling undertaken to refine the Australian stress map provides a reasonable estimate of SH_{max} in the CSB *(Hillis et al., 1998; Hillis and Reynolds, 2000; Rajabi et al., 2017)*. In this study we use information from the Perth Basin, western Otway Basin and the CSB to postulate two potential SH_{max} stress orientations of 130°N and 090°N in the study area.

Reynolds et al., (2003) estimated a strike-slip stress ($Sh_{min} < S_v < SH_{max}$) in the GAB with a vertical stress (S_v) gradient of 10.5MPa/km, a minimum horizontal stress (Sh_{min}) gradient of 6MPa/km and a calculated a maximum horizontal stress (SH_{max}) gradient of 18.7MPa/km. Given the strong changes in water depth within the GAB (ranging from 200m to 4,000m), they assumed effective stress magnitudes at a depth of 1,000 m below sea bed. In this study we use the information from *Reynolds et al., (2003)* to calculate effective stress magnitudes for Sh_{min}, S_v, and SH_{max} using average depths to the tops of the HH, Tiger, WP and BW, and a standard water depth within the study area from seismic survey data of 1500 to 2000m.

Using the results from previous studies we consider that WP, Tiger and HH sequences host the principal prospective reservoirs within the CSB *(Totterdell et al., 2000Tapley et al., 2005; Langhi et al., 2020).* The WP and Tiger are composed of sandstones that are thinning towards the southeast and shales that work as a combined sequence of intercalated reservoir and seals (Totterdell et al., 2008; Langhi et al., 2020). We expect a ratio of 50-50 and 60-40 between sandstone and shale content of the Tiger and WP respectively. Therefore, it can be speculated that these supersequences have good potential to store and trap hydrocarbons. In contrast, well logs at the Gnarlyknots-1 well demonstrate that the HH is composed of thick sandstone packages with thin sealing shale units between that would result in a thinner fault gouge membrane seal for any fault-dependent trap *(Tapley et al., 2005). Totterdell et al., (2008)* proposed that the HH has a ratio of 80:20 between sandstones and shales. Therefore, we focus our study on the impact that the current stress field in the Southern Australian Margin has on the most prospective sequences of the CSB, and we use effective stress magnitudes calculated for the Tiger and WP of 53.24MPa and 65.04MPa respectively.

Failure envelope: We used two different angles of friction in the fault reactivation analysis. This incorporates information from preliminary studies in the GAB that used a coefficient of friction (μ) of 0.6 and a cohesive strength of 5MPa *(Reynolds et al., 2003, MacDonald et al., 2012)*. Additionally, from the calculated composition ratios between sandstones and shales in the WP and Tiger in *Totterdell et al., (2008)*, we include a coefficient of friction of 0.4, which represents a larger proportion of shales in the sequences. From coefficients of friction of 0.4 and 0.6, we calculate the angle of friction using the equation $\beta = \tan^{-1}(\mu)$, resulting in angles of friction of 22˚ and 31˚ respectively *(Wyllie and Norrish, 1996; Chan et al., 2014).*

Pore pressure: Repeat Formation Tests (RFT) from the Jerboa-1 and Greenly-1 wells demonstrated a hydrostatic pore pressure within the upper sequence with mild overpressure below 3,600 m only at Greenly-1. *Reynolds et al., (2003)* estimated a regional normal hydrostatic pressure within the GAB with slight overpressure below depths below 3,600 m. We calculate a pore pressure gradient using RFT data from Jerboa-1 and Greenly-1, projecting an increase in pore pressure with depth. This gradient also allows us to estimate the pore pressure at the depth of the reservoir. Our results show that pore pressure varies from 53 to 65 MPa between the Tiger and WP supersequences.

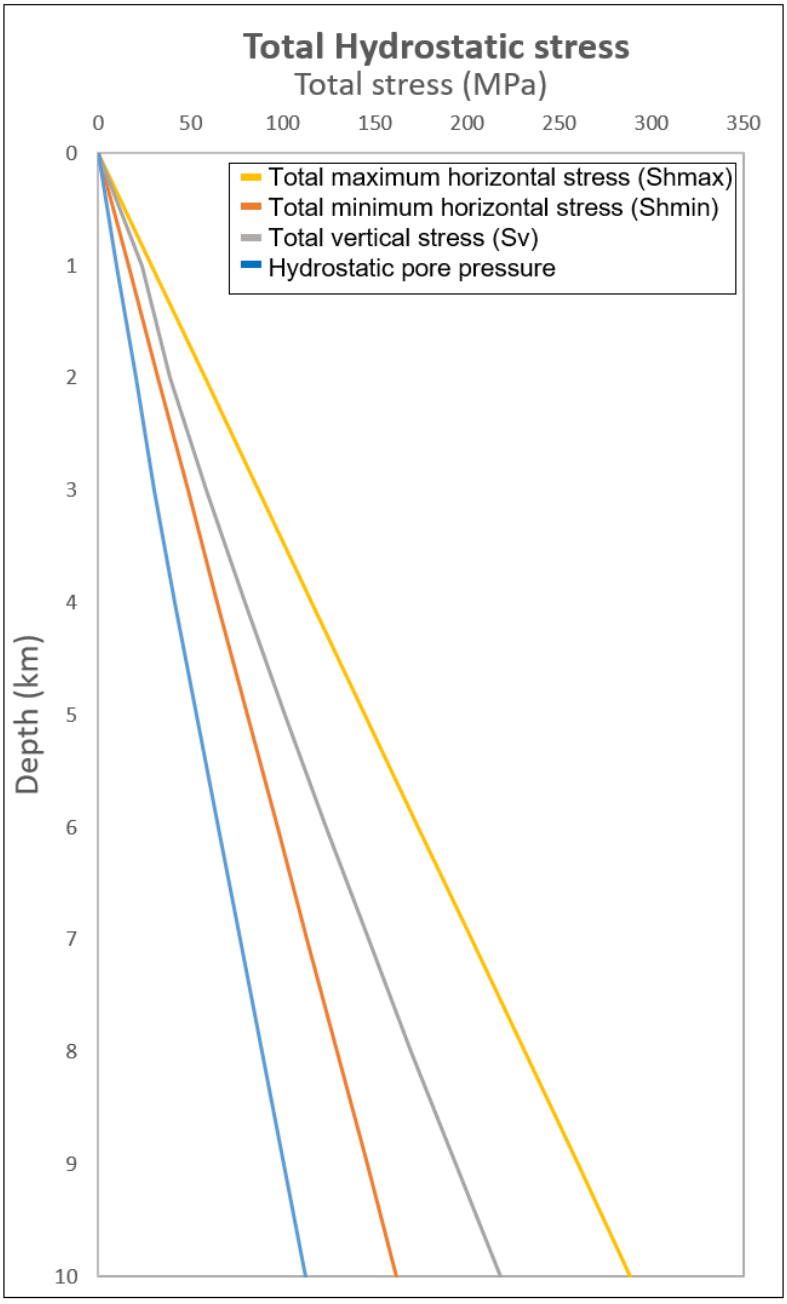

Figure 3: (a) Graph showing the calculated absolute hydrostatic stress: Maximum horizontal stress (SHmax), minimum horizontal stress (Shmin) and vertical stress (Sv) and the pore pressure gradient.

Seismic reflection data in the Ceduna Sub-basin

We have interpreted Ceduna 3D seismic survey in depth (m) domain to map fault segments and formation tops. This seismic reflection survey was acquired by PGS between 2011 and 2012. It is located approximately 350 km southeast from the Eucla Basin and 380 km southwest from the town of Ceduna offshore within the GAB. It extends horizontally 12,030 km^2 and vertically up to 13,300 m. The survey contains a total of 14,600 cross-lines oriented 135°N (perpendicular to the strike of the large-scale bounding faults) and 6343 inlines oriented 045°N.

Methodology

Definition of geomechanical scenarios

We use several geomechanical parameters to evaluate the risk of reactivation of normal growth faults within the present-day stress field of the CSB. We consider eight different parameter sets (scenarios) with a range of different geomechanical constraints including two stress magnitudes, two SH_{max} orientations, and two angles of friction. (Table 1)

Table 1: Summary of the geomechanical parameters we included for each scenario.

Scenario	Stress applied at reservoir depths		Stress orientation		Angle of friction	
	WP	Tiger	130°N	090°N	31°	22°
WP-130-31	X		X		X	
WP-130-22	X		X			X
WP-90-31	X			X	X	
WP-90-22	X			X		X
T-130-31		X	X		X	
T-130-22		X	X			X
T-90-31		X		X	X	
T-90-22		X		X		X

Fault Interpretation

We interpreted 11 horizons using standard wireline logs (gamma ray and sonic velocity) acquired at the Potoroo-1 and Gnarlyknots-1A wells. We interpreted four horizons as the top of the principal supersequences within the Ceduna Sub-basin (HH, Tiger, Wp and BW) and seven horizons that represent variations in seismic amplitude that correlate with changes in gamma ray (GR) and sonic velocity (DT) log values.

We chose six faults within the Ceduna 3D seismic survey for reactivation analysis. They represent the most typical fault features defined through our interpretation in the study area. In this study we refer to dip angles as shallow (≤30°) moderate (31° to 59°) or steep (≥ 60°). We also use the term planar to denote faults with steep angles along a cross section view (> 40°) and listric faults when the fault plane shows in cross-section dip angles that vary from steep through the upper stratigraphic sequences to shallow through the bottom intervals *(Fossen, 2010).*

Interpretation of Leads

From structural maps and our fault interpretation, we selected two potential structures that comprise hanging wall rollover structural traps proposed in *Tapley et al., (2005)* at the WP and Tiger intervals. To confirm the potential presence of good quality reservoir rocks, we generated a sweetness seismic attribute in cross-section view. The Sweetness seismic attribute results from dividing the instantaneous amplitude by the square root of instantaneous frequency and is

commonly used to distinguish between high porosity sandstone intervals and shale accumulations. It allows mapping of lateral and vertical continuity when there is high acoustic impedance contrast from lithology changes (e.g. channels and coastal planes) *(Azeem et al., 2016; Hart, 2008).* In some cases it is also use to predict hydrocarbon reservoirs as high Sweetness anomalies values that represent areas with high amplitude and low frequency *(Hart, 2008)*. However, we will only refer to the results from the Sweetness seismic attribute in terms of reservoir quality (high porosity-prone sandstones) because we do not have well data or sampling along the Ceduna 3DMSS to properly calibrate the response from the sweetness seismic attribute that can allow us to correctly imply the presence of hydrocarbons.

The FAST Technique

The FAST (Fault Analysis Seal Technology) technique uses the Coulomb-Mohr envelope method and expresses the reactivation potential as the increase in pore pressure required for failure to occur. We used MOVE® software which incorporates the FAST technique to build the eight scenarios and plot changes in strike and dip along fault planes on steronets as poles to planes. Colours are according to the position of a fault on a Mohr circle for a given stress regime. Here, a fault that sits closest to the failure envelope requires the smallest increase pore pressure to induce failure and will be considered most likely to fail. A low fracture stability value represents a state where the fault segment is at higher risk of reactivation as it requires a small pore pressure to cause failure (red and pink colours). In contrast, a high fracture stability value represents a state where the fault segment is at a low risk of reactivation (stable) as it requires a higher pore pressure to cause failure (blue and green colours) *(Mildren et al., 2002, 2005; Reynolds et al., 2003, 2005).*

Statistical analysis of fault reactivation

We plotted the six fault segments as poles to planes in the MOVE® software to define the fracture stability of each fault segment along the fault plane in terms of relative frequency (%). We differentiated our results between percentile regions as P10 (low case), P50 (base case) and P90 (high case) to diagnose how likely a fault is to reactivate in terms of how much pore pressure is needed between 0 (high risk of reactivation) and 110MPa (low risk of reactivation). For each scenario we present a stereonet showing each fault segment as poles to planes. We highlighted the sections of the fault that are most likely to reactivate and applied again the percentiles (P10, P50 and P90) to the poles to planes contained in the highlighted section. We then used the results from the P50 case in histograms and 3D fault maps to define the likelihood of reactivation along strike. In this study we will refer to the section of the fault at highest risk of reactivation as the highlighted section.

The number of results from each scenario and fault segment will depend on the sedimentary sequences that each fault offsets. We included the faults F1, F8, F9, F10 and F11 in scenarios that comprised SH_{max} applied at the depth of the WP reservoir (WP-130-31, WP-130-22, WP-90-31 and WP-90-22) and F1, F8, F10 and F11 in the scenarios where we used SH_{max} at the Tiger level (T-130-31, T-130-22, T-90-31 and T-90-22).

We present our results of risk of fault reactivation as low, moderate and high relative to selected fault segments using the P50 results of the highlighted section at each fault. To standardize our

results, we will refer to similar pore pressures when two faults show no more than 2MPa between their pore pressure required to activate the fault.

Fault plane roughness

In this study we refer to fault roughness as the changes in dip angle and strike along the fault plane. Each pole to plane in the stereonets and 3D maps, represent a single section of the fault that contain a different measurement of dip angle and strike. As we interpreted faults with different average strike using the in the Ceduna 3D MSS in depth domain, we will only mention the eastern hemisphere of the stereonet (between 000°N and 180°N) as it replicates the average strike we find at the western hemisphere.

Limitations

Due to the lack of well data information close to the Ceduna 3D seismic survey, the available rock mechanics properties are from wells some distance away (> 40 km) and may not accurately represent the area of study. Likewise, there is not enough information from drilling reports and well logs inside the study area that can provide in-situ stress orientations and magnitudes and pore pressure data from the Tiger and WP reservoirs.

The faults and tops were interpreted in Petrel® using a 3D seismic survey (Ceduna 3D seismic survey). This will carry some limitation in terms of the distance between crosslines and inlines (12.5m), the vertical resolution of the seismic survey, and any inaccuracy caused by human error in seismic interpretation.

Results

Characteristics of faults in the Ceduna Sub-basin

Individual fault segments

To assess the risk of fault reactivation within the Ceduna Sub-basin, we interpreted six faults using the Ceduna 3D seismic survey in depth (m). These faults are excellent candidates because they are well distributed along the study area and represent the principal characteristics of the normal growth faults in the extensional region of the Ceduna Delta System (Figure 4a)

We analysed two planar faults (F10 and F11) with a main northwest-southeast strike. These faults detach at the BW where we interpreted local thrust faults resulting in the thickening of the detachment (1160 to 2400m). F10 is located at the central-east area of the study and covers a distance along strike of 2.5 km and offsets the sedimentary sequences between the base of the WP (WP1) and HH3. It shows changes in dip angle along the fault plane between 30° and 50° and variations in strike from 000°N to 025°N and from 100°N to 180°N (Figure 4b). The second fault segment corresponds to F11 and it is situated at the southern area of the study. It extends 1.6 km along strike and displays variations in dip of 40° to 50° and strike variations between 121°N to 143°N. F11 displaced the sedimentary sequences between WP1 and the T1 (Figure 4c).

We include four listric faults in our analysis located in geographic areas where the BW detachment has a thin (750 and 950m in F1, F8 and F9) to medium thickness of (1100m in F16). Each of these

listric faults show rollover structures in their hangingwall, were three (F1, F8 and F9) shows an average strike northwest-southeast and one (F16) an east-west strike. Fault F1 is located in the northern area of the study and extends along strike for 5.4 km. It offsets the sedimentary sequences between WP1 and T4 sequences. The fault at this level exhibits dip variation between 02° to 65°, while the strike changes between 045°N to 180°N along the fault plane (Figure 4d). The second fault is F8, which is located at the centre-west part of the study and extends 5.2 km along strike. Along the fault plane, F8 varies in dip and strike between 8° and 70°, and 112°N to 143°N, respectively (Figure 4e). Like F1, this fault displaces the sedimentary sequence between WP1 and HH3. The third fault is F9, which is located at the southern area of the study and extends along strike for 5.9 km. This fault offsets the sequence between WP1 and WP2 (the top of the White Pointer). It shows changes in dip angle between 03° and 46° and variations in strike between 000°N to 011°N and 062°N to 180°N along the fault plane (Figure 4f). The fourth listric fault is F16, which is located in the northern area of the study. It extends 2.1 km along strike and displaces sedimentary sequence between WP1 and WP2. In F16, we identified changes in dip and strike that range from 10° to 60° and 015°N to 090°N, respectively (Figure 4g).

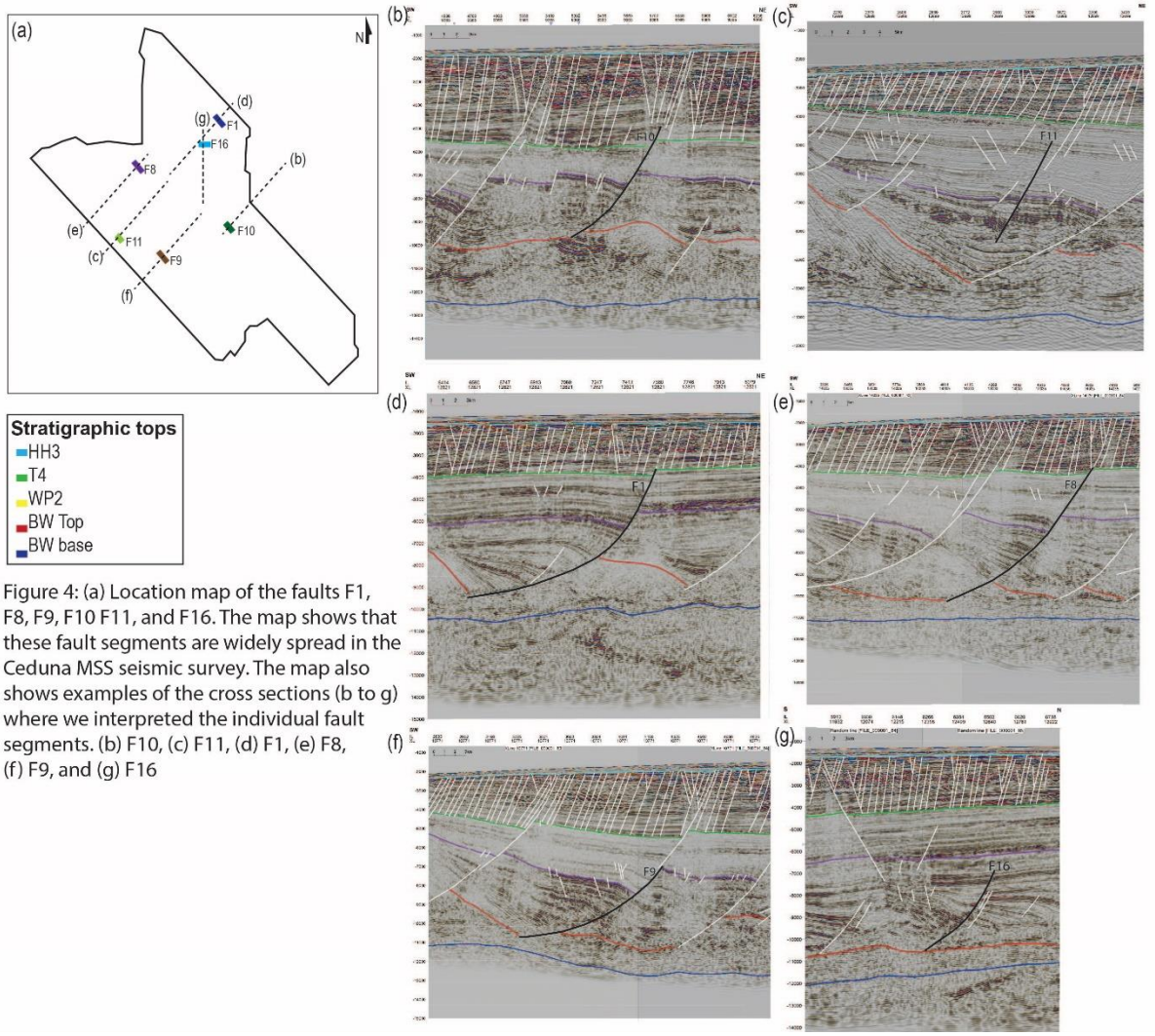

Figure 4: (a) Location map of the faults F1, F8, F9, F10 F11, and F16. The map shows that these fault segments are widely spread in the Ceduna MSS seismic survey. The map also shows examples of the cross sections (b to g) where we interpreted the individual fault segments. (b) F10, (c) F11, (d) F1, (e) F8, (f) F9, and (g) F16

Leads

Using the structural maps, we identified leads with potential fault-dependant closures composed by two fault segments F2-F4 and F5-F6 (Figure 5a). We included in Figure 5d the depth map of WP1, showing the structural closure against the fault segments F2-F4 towards the northwest section of the map. We also show in Figures 5e the structural map of WP1, where we interpreted F5 and F6 as the principal structural component of the potential structural closure. These structural maps also show the changes in the strike between F5 (east-west) and F6 (northwest-southeast) (Figure 5e and f). These maps also show evidence of minor fault segments with different strikes that might be contributing to the development of a hydrocarbon trap. However, we did not include these small faults in our reactivation risk assessment as they are too short in map view (less than 1.0 km along strike) and displacement. The structural closures that are represented in the leads are also potentially associated with porosity-prone sandstones that can work as good quality reservoir rocks due to the high anomaly values in the sweetness attribute we generated in cross-section. In this study we used two examples at the north and south section of the study area.

The first lead (F2-F4) linked the listric faults F2 and F4 at the southern section of the study area (Figure 5a and b). In this case, the main target corresponds to the footwall at the WP1 sequence (Figure 5d). In conjunction, the faults display a main north-west strike, changing in dip between 01° and 45° and strike between 032°N and 178°N, with a total length of 3.6 km (Figure 5a).

The Sweetness seismic attribute projected along cross-sections of faults F2 and F4 at the WP1 level, indicate a high porosity-prone reservoir (low anomaly values) and seal rocks (high anomaly values) at the hanginwall of F2 and F4 (Figure 6a). The low values in the Sweetness response at the footwall can be also associated to problems with the seismic velocity and noise-ratio due to the fault shadow as the footwall region with low seismic amplitude contrast is below the steeper section of the faults F2-F4. *(Fagin, 1996)*. Therefore, we are not assured about the presence of good quality reservoir in WP1 near the F2-F4 closure.

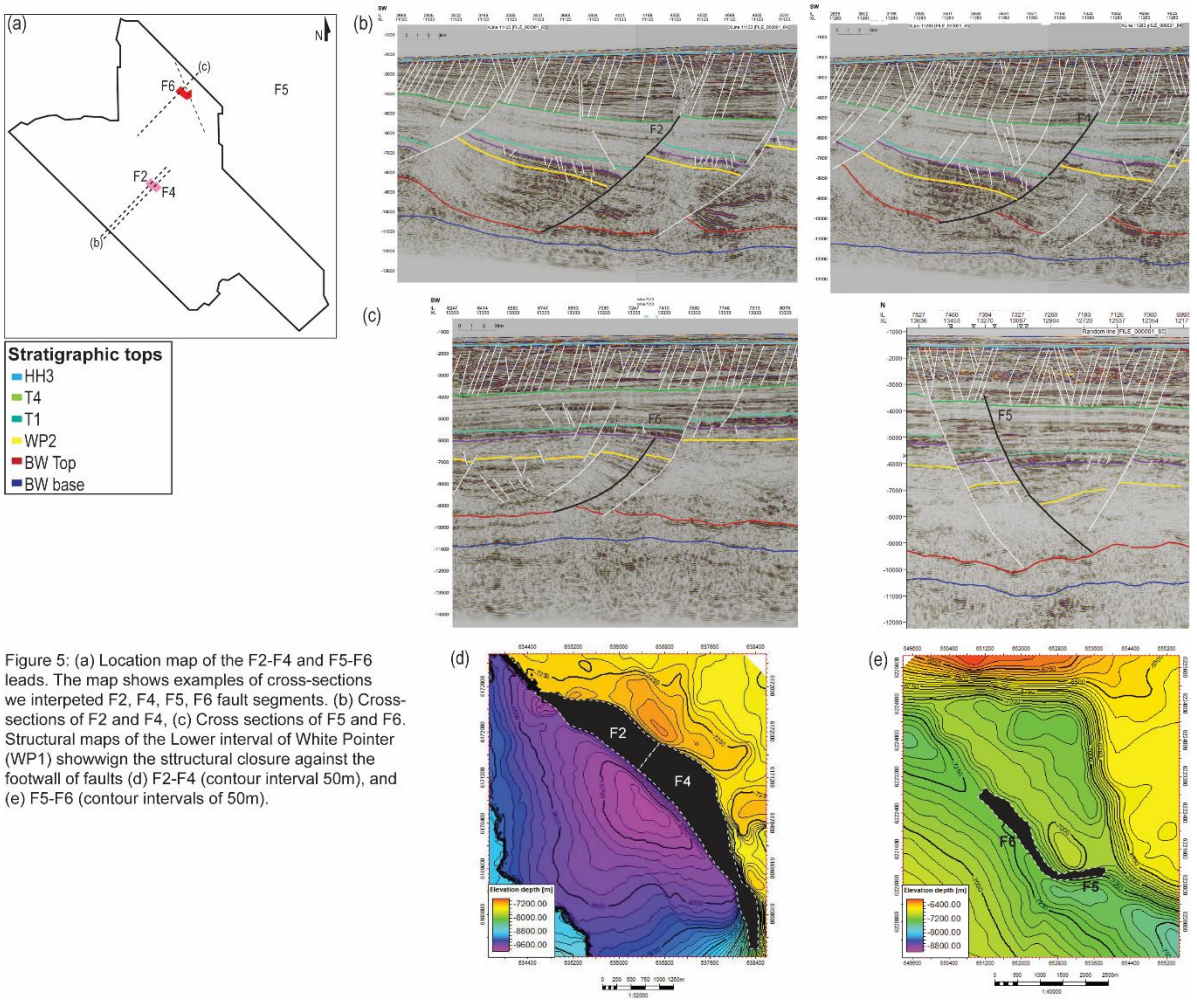

Figure 5: (a) Location map of the F2-F4 and F5-F6 leads. The map shows examples of cross-sections we interpeted F2, F4, F5, F6 fault segments. (b) Cross-sections of F2 and F4, (c) Cross sections of F5 and F6. Structural maps of the Lower interval of White Pointer (WP1) showwign the sttructural closure against the footwall of faults (d) F2-F4 (contour interval 50m), and (e) F5-F6 (contour intervals of 50m).

The second lead (F5-F6) contains the fault segments F5 and F6 at the northern section of the study area (Figure 5a) and combined, they extend 3.9 km along strike and show structural closure in the footwall at the WP1 sequence (Figure 5e and f). Overall, these listric faults exhibit changes in dip and strike between 05° and 60°, and 040°N to 180°N, respectively (Figure 5a).

We generated the Sweetness seismic attribute along the cross-sections perpendicular to F5 and F6 strikes. Here we interpret good quality reservoir at WP1 that is defined by boundaries with potential seal rocks at the top and at the hangingwall section of both faults (Figure 6b).

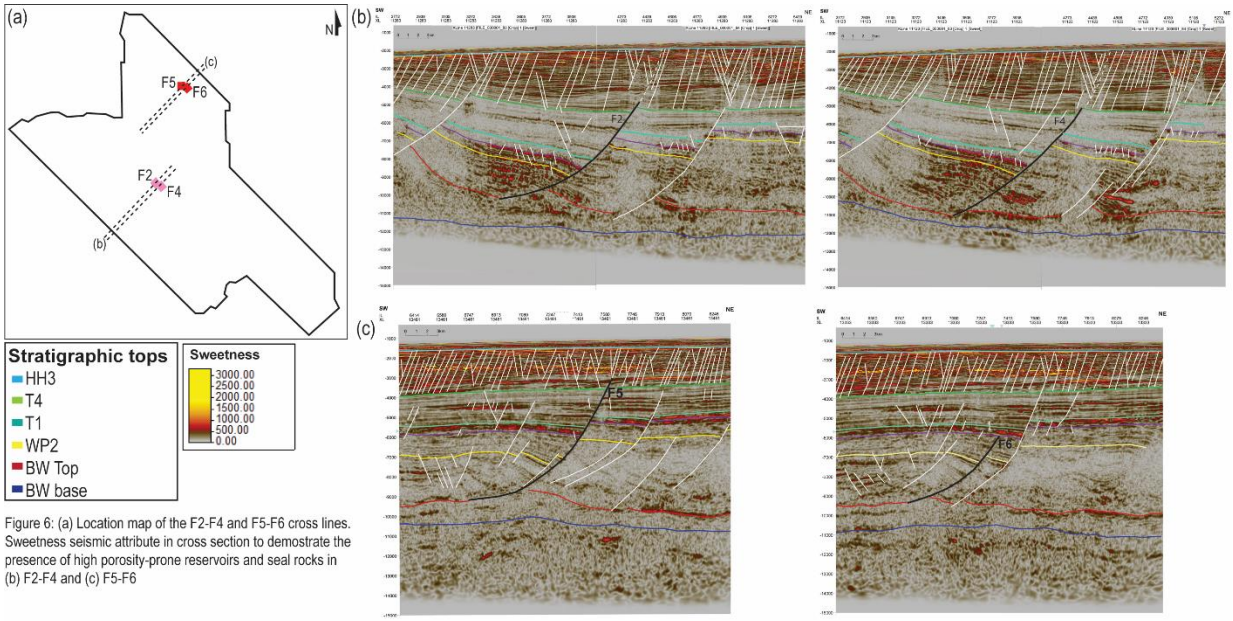

Figure 6: (a) Location map of the F2-F4 and F5-F6 cross lines. Sweetness seismic attribute in cross section to demostrate the presence of high porosity-prone reservoirs and seal rocks in (b) F2-F4 and (c) F5-F6

Distribution of the risk of reactivation along fault segments

The FAST technique proved to be an effective tool to analyse the risk of reactivation of faults in the Ceduna Sub-basin. Our results demonstrate a wide range of values along fault segments with strong variations in pore pressure. We provide a statistical analysis to define in more detail how the risk of reactivation is distributed along strike (Table 2). This statistical analysis helped to investigate in more detail the sections of faults that are at risk of reactivation, enabling a comparison of pore pressure results with the fault roughness (Table 3). As mentioned in the methodology, we will refer to the section of the fault that is at risk of reactivation as the "highlighted section".

Pore pressure results as histograms

Our results show that the risk of fault reactivation strongly varies along a fault plane in all the fault segments (Table 2). We use histograms (Figure 7) to represent these results by relative frequency (%) of points along a fault. Considering a single fault segment, the pore pressure required to reactivation to occur can vary from 12 to 66MPa in a single scenario. We identify changes in pore pressure between the different scenarios, which suggest that the geomechanical parameters included in this study indicate risk of fault reactivation in the Ceduna Sub-basin. For instance, where the angle of friction is 31° (≤43MPa) the highlighted section shows lower risk of reactivation than where the angle of friction is 22° (≤26MPa) (Figure 7). At the planar faults F10 and F11 (e.g. WP-130-31 with WP-130-22 or between T130-31 and T130-22), we identify a variation in pressure of at least 10MPa. In all the fault segments, the risk of fault reactivation slightly varies when we compare scenarios with stress orientations of 130°N and 090°N (e.g. between WP-130-31 and WP-90-31, or between T-130-32 and T90-31). Similarly, when stress is applied at the Tiger and WP supersequences, changes to the risk of fault reactivation results do not exceed 3MPa (Figure 7).

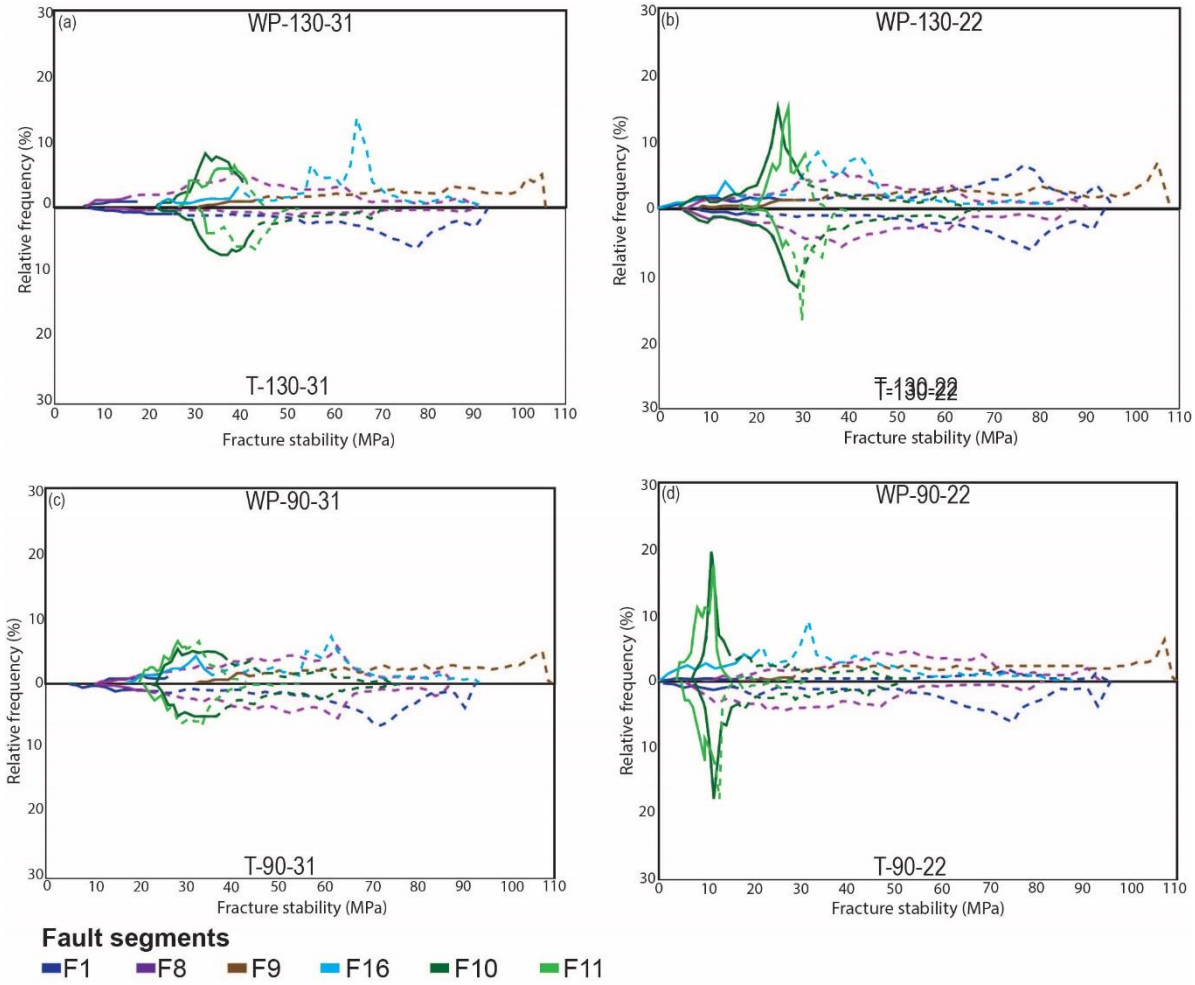

Figure 7: Histograms comparing the results of risk of faut reactivation (as fracture stability) at F1, F8, F9, F10, F11, and F16. We divided the results into different scenarios: (a) WP-130-31 and T-130-31, (b) WP-130-22 and T-130-22, (c) WP-90-31 and T-90-31, (d) WP-90-22 and T-90-22. The dashed line rerpesents the risk of reactivation results along each fault plane and the solid line denotes the results from the P50 case from the highlighted section of the fault.

Comparing results from the combined faults at the structural leads (F2-F4 and F5-F6), we do not distinguish major changes in the pore pressure required for the reactivation to occur between the scenarios where we applied SH_{max} at the WP and Tiger sequences (e.g. Between WP130-31 and T130-31, or between WP-90-22 and T-90-22) or between the scenarios where we used SH_{max} of 130°N and 090°N (e.g. Between WP103-31 and W-P90-31 or T130-31 and T90-31) (Figure 8 and Table 2). However, for the combined fault segments the risk of fault reactivation increases in scenarios where the angle of friction is 22° compared to where it is 31° (Figure 8).

In Table 2 to we can see that none of the fault segments in this study can be considered active faults as they all require a pore pressure increase greater than 2 MPa to reactivate. However, when we compare pore pressure results for each fault segment, they can be differentiated between higher, moderate and lower risk of fault reactivation. For instance, F9 can be considered the most stable fault in this study in all the scenarios (low risk of reactivation). In contrast, F1 and F8 show intermediate pore pressure results in comparison to the other faults, which suggests that they are at higher risk of reactivation. F10 and F11 show lower risk of reactivation than F1 and F8 and higher

likelihood to reactivate than F9. Therefore, we consider these faults to be at moderate risk of reactivation. F16 results are greatly influenced by the angle of friction and the SH_{max} orientation. It shows similar pore pressure results to F10 and F11 when the angle of friction is 31° but similar to F8 when the angle of friction is 22°. We consider this fault to be at moderate to high risk of reactivation.

The histograms and Table 2 also show that F5-F6 pore pressure results are similar to F1 and F8 (with variations up to 2 MPa). Therefore, we believe that F5-F6 is at higher risk of reactivation. F2-F4 show lower risk of reactivation with values similar to F10 and F11 and slightly smaller than F9. We believe that this lead is at low to moderate-to-low risk of reactivation (Figure 8)

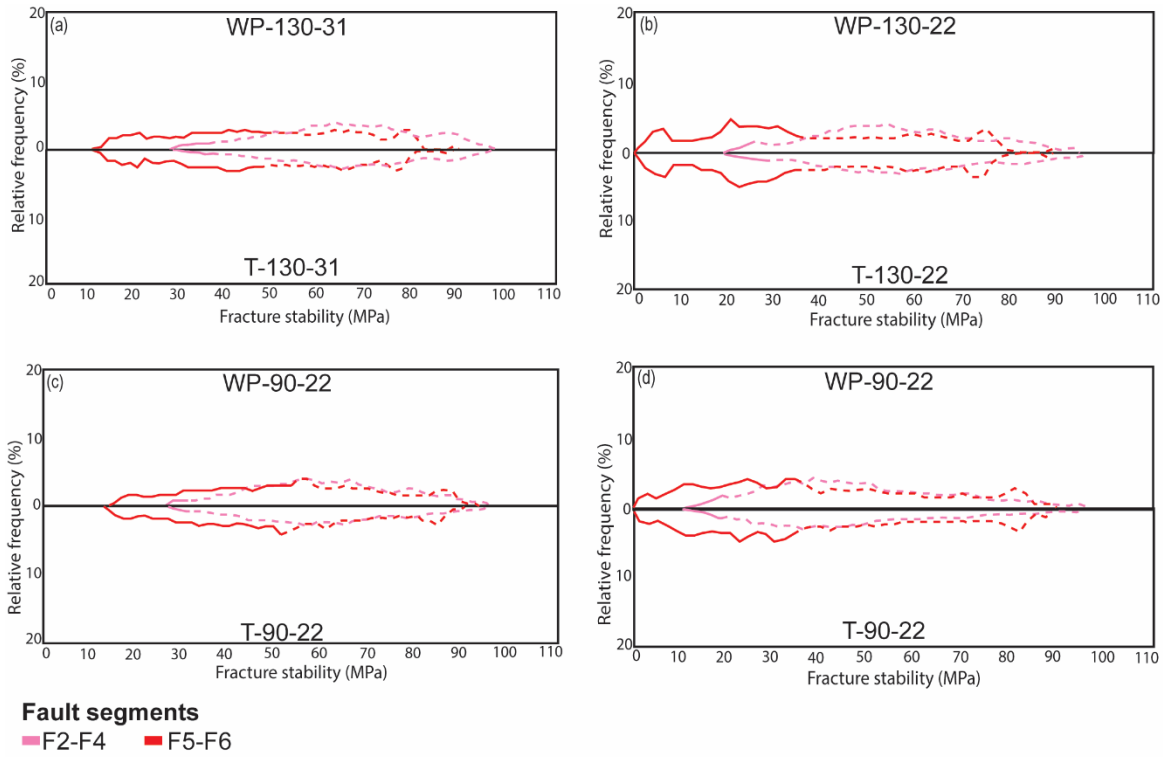

Figure 8: Histograms comparing the results of risk of faut reactivation (as fracture stability) at F2-F4 and F5-F6. We divided the results into different scenarios: (a) WP-130-31 and T-130-31, (b) WP-130-22 and T-130-22, (c) WP-90-31 and T-90-31, (d) WP-90-22 and T-90-22. The dashed line prerpesents the risk of reactivation results along each fault plane and the solid line denotes the results from the P50 case from the highlighted section of the fault.

Projection of fault data on stereonet

Stereonets have enabled us to differentiate changes in dip and strike for each fault segment and to compare these structural features with the risk of fault reactivation results. As expected, faults with greater lengths along strike cover a wider area of the stereonets, which confirms a broader range of variations in dip angle and strike along the fault plane (vertically and horizontally). The colour scale of the diagrams helps to visually distinguish between the sections at higher risk of reactivation (red and pink areas) from the ones that are more stable (blue and green) (Figures 9 and 10).

We note that the highlighted section of faults exhibits moderate to steep dip angles that vary from 36° to 71°. In general, F1 and F8 exhibit steeper dip angles at the highlighted section between 45° and 71° than the other faults. In contrast, F9 is the fault with the shallower dip angles in the

highlighted section, with small changes between 38° and 47°. F10, F11 and F16 show moderate dip angles that vary from 36° to 60°. The stereonets also indicate that there are regions of the faults with steep dip angles that do not belong to the highlighted section. For instance, F1 and F8 exhibit dip angles of about 60° and 70° that are not included in the highlighted section. Similarly, F10 and F11 show regions of the fault with dip angles between 45° and 50° that are at low risk of reactivation (Figure 9 and 10). Likewise, the dip angle at the highlighted section varies in F2-F4 from 31° to 45° and in F5-F6 from 45° to 59°. In both cases, these angles are shallower than F1 and F8 and in a similar range to F9, F10, F11 and F16 (Figure 9 and 10).

Most faults exhibit strong variations in strike independently of their planar or listric geometry. The number of these changes in strike are proportional to the length along the fault plane. For instance, F11 is the fault with the least changes in strike (from 121°N to 143°N) and the shortest length (1.6 km), while F1 is one of the longest faults (5.4 km) and exhibits a greater range of strikes (from 045°N to 180°N) along the fault plane (Figure 9 and 10). We have combined data for each of these faults with others at each lead in the stereonet diagrams in Figure 9 and 10; the broader envelope of data values shown for F1 demonstrates that it covers a wider range of strikes and dip angles than the other faults (F8, F9, F10, F11 and F16). Generally, length along strike is proportional to the area shown in the stereonet, as is the case shown when comparing between F2-F4 and F5-F6 (3.6 km and 5.5 km respectively) in Figure 11.

The stereonets also show that F8, F10 and F11 exhibit a variation between one or two separate areas at risk of fault reactivation along the fault plane. This can be interpreted as (1) a wider variation in strike and dip angle in the regions of the fault that are at high risk of reactivation, (2) the influence that the geomechanical parameters in this study have in different arrangements of strike and dip, or (3) a combination between the two. For instance, F10 and F11 vary between two stratigraphic sections for the scenarios when SH_{max} orientation is 130°N (Figure 9 and 10) to the one when SH_{max} orientation is at 090°N (Figure 9 and 10). F8 shows two regions at risk of reactivation in scenarios when SH_{max} orientation is at 090°N and is applied at the WP (Figure 9 and 10), and where the angle of friction is 31° and the SH_{max} orientation is applied at the Tiger (Figure 9 and 10). F1 is the only segment that exhibits two separate sections at high risk of reactivation in all scenarios. In contrast, F9 and F16 exhibit a single section at high risk of reactivation in all the scenarios. In F9 and F16, the stereonets exhibit minor changes in strike and dip angle in the highlighted section (Figure 9 and 10). Similar to F1, F5-F6 show two sections of the fault at high risk of reactivation (Figure 11). F2-F4 exhibit two highlighted regions of the fault in the scenarios where SH_{max} is at 130°N and one when the SH_{max} orientation is 090°N (Table 3).

Table 3 summarises the information of dip and strike from the highlighted section at each fault including the faults at the two leads. We include pore pressure results (P50 case) for the highlighted sections.

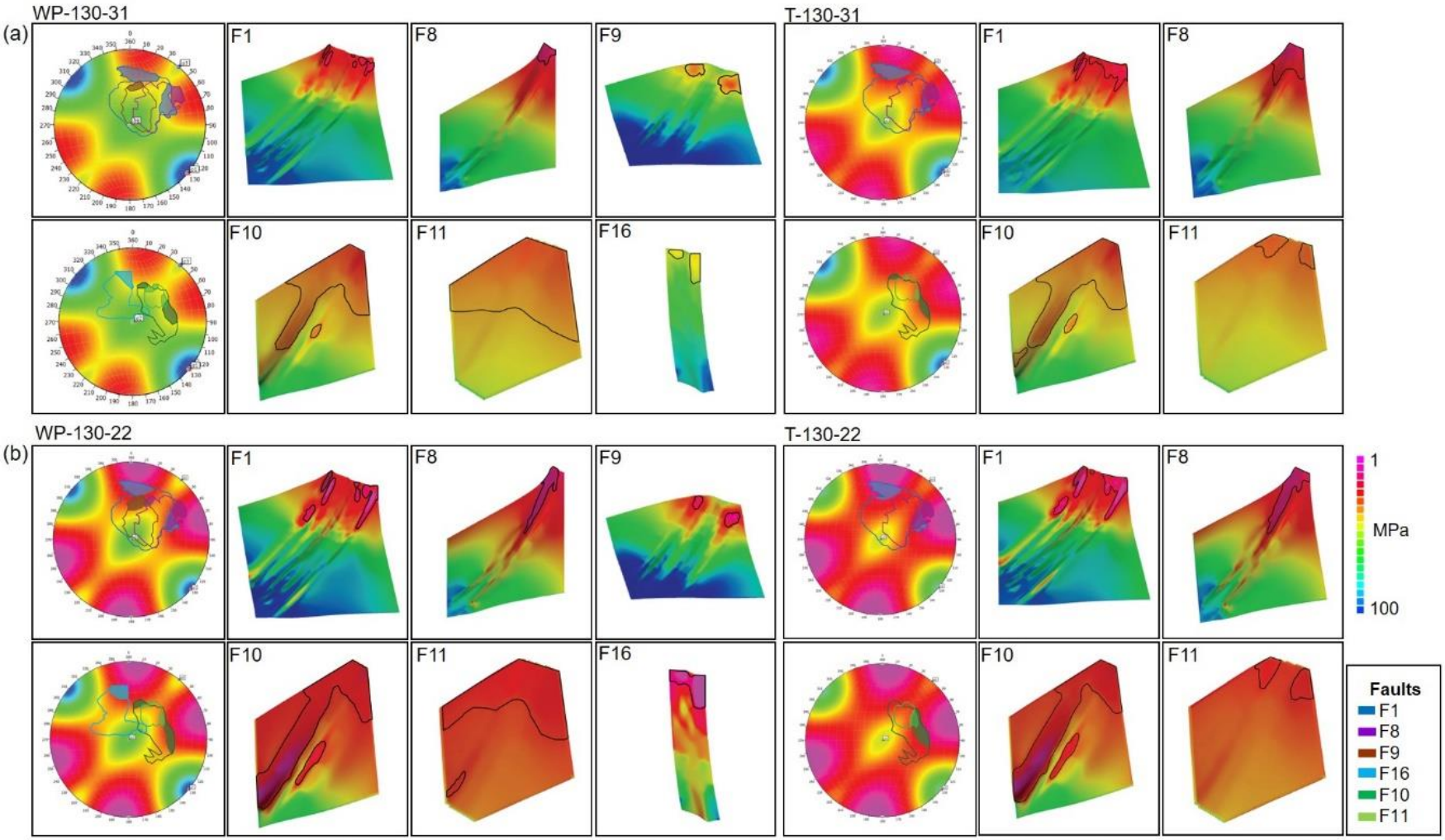

Figure 9: (a) At the left we present the steronets showing as a line the boundary of the area where the poles to planes of the faults F1, F8,F9, F10, F11 and F16 are projected. The filled area at each fault indicated the section at high risk of reactivation. In the text, we refer to these areas as the highlighted section. In the middle and right we also include the 3D fault maps of the same faults where the black polygon represents the boundary of the highlighted section. We divide the information between the different scenarios (a) WP-130-31 and T-130-31, (b) WP-130-22 and T-130-22.

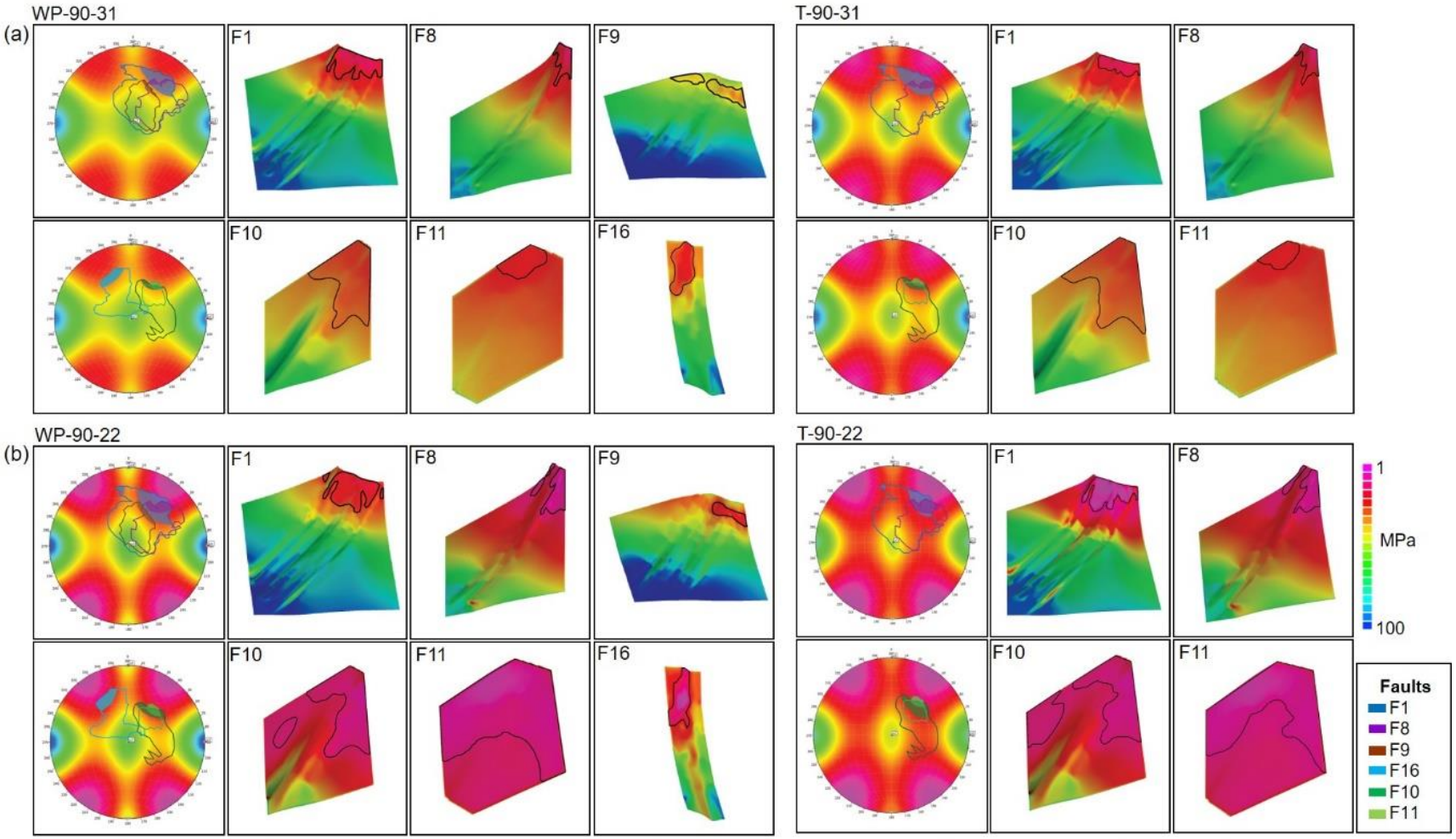

Figure 10: (a) At the left we present the steronets showing as a line the boundary of the area where the poles to planes of the faults F1, F8,F9, F10, F11 and F16 are projected. The filled area at each fault indicated the section at high risk of reactivation. In the text, we refer to these areas as the highlighted section. In the middle and right we also include the 3D fault maps of the same faults where the black polygon represents the boundary of the highlighted section. We divide the information between the different scenarios (a) WP-90-31 and T-90-31, (b) WP-90-22 and T-90-22.

Table 2: Pore pressure results of the P10, P50 and P90 cases from the fault segments and leads.

Fault		Pore pressure results (MPa)																							
		WP-130-31			WP-130-22			WP-90-31			WP-90-22			T-130-31			T-130-22			T-90-31			T-90-22		
		P10	P50	P90	P10	P50	P90	P10	P50	P90	P10	P50	P90	P10	P50	P90	P10	P50	P90	P10	P50	P90	P10	P50	P90
Fault segments	F1	34	72	87	25	68	86	31	71	86	18	65	84	27	68	81	27	68	86	27	68	86	19	64	83
	F8	27	52	75	20	42	70	28	51	72	14	34	60	28	52	77	22	42	70	28	52	77	14	32	57
	F9	47	78	102	35	70	102	47	78	102	35	70	101												
	F16	37	78	87	12	37	61	29	56	78	10	35	68												
	F10	31	38	57	23	27	31	28	38	60	10	16	40	32	39	51	17	28	48	32	39	58	10	16	38
	F11	30	36	42	23	27	31	26	28	31	6	10	14	31	38	44	26	30	34	32	38	44	6	10	13
Leads	F2-F4	42	63	84	33	55	80	40	59	81	25	45	74	42	63	84	35	55	80	39	58	80	24	43	73
	F5-F6	22	48	75	25	39	74	24	49	80	8	36	73	23	49	76	7	24	71	25	49	79	11	33	75

In this table, smaller numbers in this table (pink) indicates less pore pressure required to cause failure, while greater numbers (blue) correspond to a higher pore pressure required to cause failure.

Table 3: Summary of the pore pressure results from the fault sections that are at risk of reactivation and the dip and strike information.

		Fault	Pore pressure results (MPa)											
			PP	Dip (°)	Strike (°N)	PP	Dip (°)	Strike (°N)	PP	Dip (°)	Strike (°N)	PP	Dip (°)	Strike (°N)
			WP-130-31			WP-130-22			WP-90-31			WP-90-22		
WP	Fault segments	F1	12	45-65	85-115 143-165	13	45-65	84-116 145-168	20	50-65	51-81 104-140	8	45-65	53-86 100-142
		F8	16	47-71	140-160	11	47-71	138-160	18	45-62	100-120	10	46-71	112-125 140-162
		F9	38	40-47	84-120	22	38-47	85-115	43	40-47	85-143	24	38-47	95-142
		F16	31	40-60	70-90	11 (P10=0)	40-60	70-90	29	45-60	49-79	11 (P10=0)	40-60	49-85
		F10	34	38-50	102-109 150-185	24	38-50	102-115 150-185	31	37-70	103-145	11	39-50	103-148
		F11	36	40-46	121-126 140-143	11	41-43	121-124 140-144	26	44-50	122-134	11	45-50	121-137
	Leads	F2-F4	35	32-45	108-120 130-176	25	31-45	104-118 142-172	30	32-45	105-144	18	32-45	108-145
		F5-F6	17	50-58	88-112 143-167	4	43-58	86-107 145-180	19	53-69	50-65 105-135	4	52-60	47-67 108-140
			T-130-31			T-130-22			T-90-31			T-90-22		
Tiger	Fault segments	F1	18	45-65	85-125 140-165	16	48-65	87-115 157-160	16	48-65	51-79 105-145	6	49-71	50-84 104-144
		F8	20	48-71	87-115 157-162	14	42-65	140-165	18	44-62	117-125 140-162	8	48-65	125-142
		F10	36	39-50	102-119 138-180	26	36-50	103-145	32	36-50	103-145	9	36-50	122-136
		F11	30	40-46	121-125 142-145	25	45-50	121-131	22	41-50	121-131	10	42-50	109-145
	Leads	F2-F4	34	32-45	110-118 133-175	27	32-45	110-120 135-177	30	32-45	108-142	17	32-45	110-145
		F5-F6	18	51-59	87-111 146-174	8	50-57	87-106 148-178	16	52-60	48-69 105-130	3	53-63	48-60 112-131

In this table, smaller numbers in this table (pink) indicates less pore pressure required to cause failure, while greater numbers (blue) correspond to a higher pore pressure required to cause failure.

Pore Pressure results along fault planes shown in 3D fault maps

3D maps show the section or sections of faults that are at high risk of fault reactivation. We identify changes in these sections when geomechanical parameters are varied for each scenario and how the dip angle and strike vary along the fault planes. All faults show high risk of reactivation at their topmost sedimentary sequence. Apart from F9, when we varied the angle of friction or the SH_{max} orientation, the section at risk of fault reactivation increases along strike and in cross-section view. For instance, when the angle of friction is 31°, faults F1, F8 exhibit high risk of fault reactivation at the T4 sequence. In contrast, when we use an angle of friction of 22°, the section at risk of reactivation is randomly distributed between the T4, T3 and T2 sequences. F16 exhibits a broader area at risk of fault reactivation in cross-section when SH_{max} orientation is 090°N in comparison to 130°N (Figure 9 and 10).

Similar to the individual fault segments, F2-F4 and F5-F6 show that the upper sedimentary sequence is at risk of reactivation in all the scenarios. Additionally, both fault sets show a wider section along strike and in cross-section view at risk of reactivation in the scenarios when we changed the angle of friction from 31° to 22°. (Figure 11).

In Table 4, we summarise the results from Figures 9, 10 and 11. We include sedimentary sequences and describe the section of the fault that exhibits higher risk of reactivation.

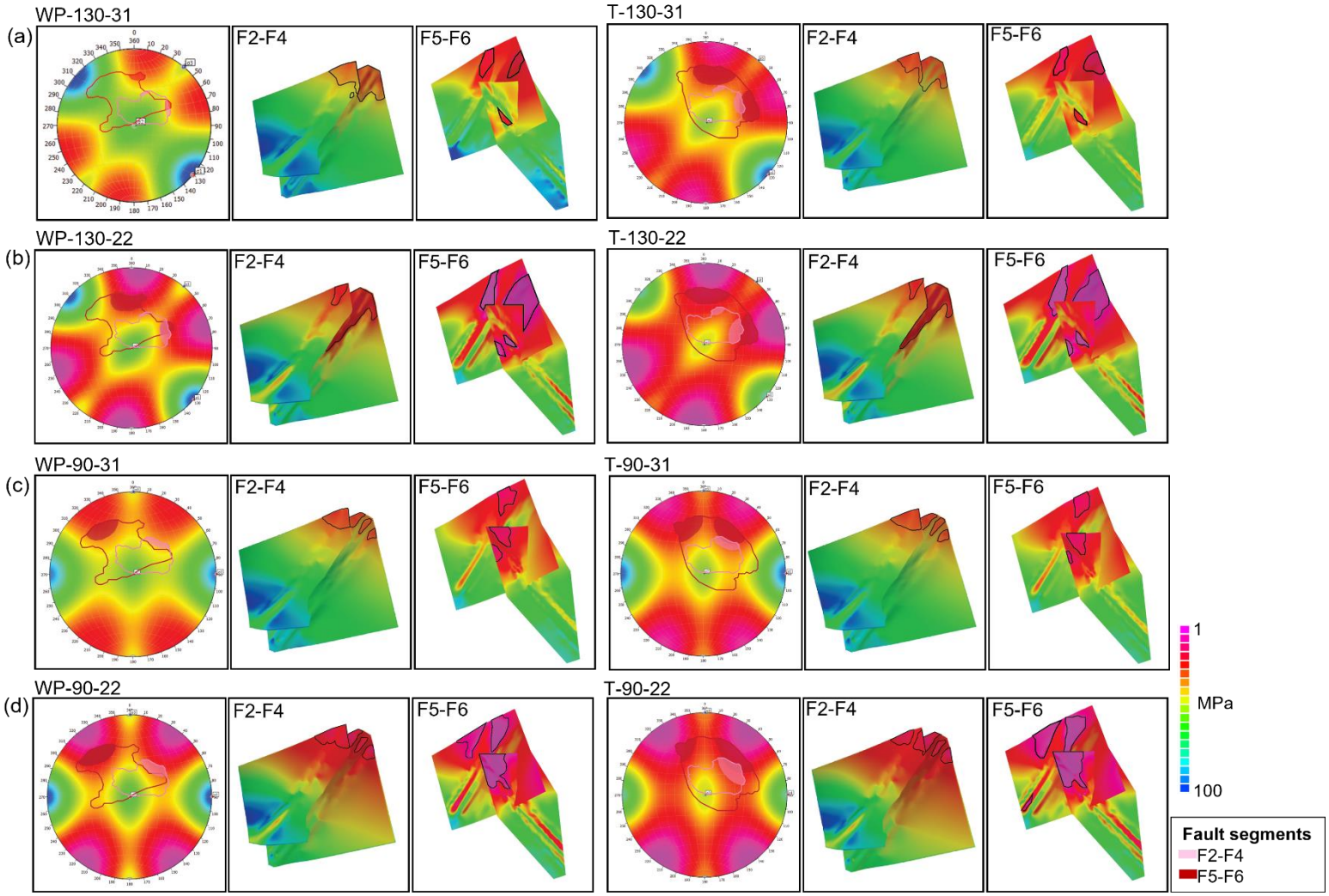

Figure 11: (a) At the left we present the stereonets showing as a line the boundary of the area where the poles to planes of the faults F2-F4 and F5-F6 are projected. The filled area at each fault indicated the section at high risk of reactivation. In the text, we refer to these areas as the highlighted section. In the middle and right we also include the 3D fault maps of the same faults where the black polygon represents the boundary of the highlighted section. We divide the information between the different scenarios (a) WP-130-31 and T-130-31, (b) WP-130-22 and T-130-22, (c) WP-90-31 and T-90-31, (d) WP-90-22 and T-90-22.

Table 4: Summary of the pore pressure results over the 3D fault maps.

	Fault	Section of the fault at higher risk of reactivation	Stratigraphic unit	Section of the fault at higher risk of reactivation	Stratigraphic unit	Section of the fault at higher risk of reactivation	Stratigraphic unit	Section of the fault at higher risk of reactivation	Stratigraphic unit
		WP-130-31		**WP-130-22**		**WP-90-31**		**WP-90-22**	
Fault segments	F1	Randomly distributed along strike	T4	Concentrated at the NW and SE tips	T4 and T3	Wide distributed along strike	T4	Wide distributed along strike	T4 and T3
	F8	Concentrated at the centre and northwest tip	T4	Concentrated in the centre	T4, T3, T2	Distributed along strike and deepens towards the SE tip	T4	Mainly at the SE tip where it deepens to T3. Minor distribution at the NW tip	T4 and T3
	F9	Located in the northwest and southeast tips	WP2	Concentrated at the NW and SE tips	WP2	Randomly distributed along strike	WP2	Cocnetrated at the SE tip	WP2
	F16	Concentrated at the east tip	WP2	Concentrated in the central section and east tips (P10: east)	WP1	Centre of th fault and deepens towards the west	WP2 and WP1	Centre and depends towards the west tip	WP2 and WP1
	F10	Distributed between the centre and NW and SE tips	T1, WP2, WP1	Concentrated in the centre	T1, WP2, WP1	Wide distributed along strike. Deepends towards the SE tip	T1 and WP2	Wide distributed along strike in T1 and deepends at the centre of the fault. Randomly distributed in WP2 and WP1	T1, WP2, WP1
	F11	Distributed between the centre and NW and SE tips	T2, T1, WP2	Mostly concentrated at the NW tip with minor section at the centre	T2, T1, WP2	Mainly between the centre and the west tip	T2	Wide distributed along strike and deepens at NW tip	T2, T1, WP2
Leads	F2-F4	Wide distributed along strike. Slightly deepend at centre specisly in F4	T4 and T3	Randomly distributed along strike and deepends at centre	T4, T3, T2	Wide distributed along strike in F5 and randomly distributed in F4	T4	Wide distributed along strike in F2 and randomly distributed in F4	T4, T3, T2
	F5-F6	Along strike in F5 and towards NW and SE tips in F6	T4	Randomly distributed along strike in F5 and deepends at centre in F6	T4, T3, T2	Wide distributed in F5 and deepens towards the west tip. Concentrated at the west tip and centre in F6	T4, T3, T2	Randomly distributed between T4 and T3. Concentrated at the centre in T2 in F5. Concentrated at the centre in F6	T4, T3, T2
		T-130-31		**T-130-22**		**T-90-31**		**T-90-22**	
Fault segments	F1	Randomly distributed along strike	T4	Randomly distributed along strike and deepens at NW and Se tips	T4 and T3	Concentrated at the Centre	T4	Randomly distributed along strike	T4
	F8	Wide distributed along strike	T4	Randomly distributed along strike and deepens at the centre	T4, T3, T2	Wide distributed along strike and deepens at SE tip	T4 anf T3	Randomly distributed and slightly deepens at the SE tip	T4
	F10	Wide distributed along strike. Deepends at NW and SE tips	T1, WP2, WP1	Wide distributed along strike. Deepends at NW tip	T1, WP2, WP1	Wide distributed along strike and deepens at SE tip	T1 and WP2	Wide distributed along strike in T1. Randomly concentrated at WP2 and WP1 at the NW and Se tips	T1, WP2, WP1
	F11	Concentrated at the NW and SE tips	T2	Concetrated at NW and Se tips	T2	Concentrated only at the NW tip	T2	Wide distributed along strike in T2 and T1. Depends at NW and SE tips	T2, T1, WP2, WP1
Leads	F2-F4	Wide dstributed along strike and deepens at the centre in F4	T4 and T3	Concentrated at the centre in F2 and randomly deepens a the centre in F4	T4, T3, T2	Concentrated at the centre in F2 a randomly distributed in F4 where it deepends at the centre	T4, T3, T2	Wide concentrated along strike in F2. Randomly distributed at the NW, centre and SE in F4	T4
	F5-F6	Wide dstributed along strike in F5 and concentrated at the SE tips in F4	T4 and T3	Wide distributed along strike in F5 and deepens at centre and SE tips in F6	T4, T3, T2	Wide distributed at F5 and concentrated st the SE tip in F4	T4, T3	Concentrated at west and east tips in F5 and at NW tip in F6	T4, T3 and WP1

Discussion of results

Similarly to preliminary studies in the CSB *(Reynolds et al., 2003, 2005; Macdonald et al., 2012)*, we used the FAST technique, which proved to be an useful tool to determine the likelihood of fault reactivation of normal growth faults. Doing so permitted incorporation of a variety of geomechanical parameters such as angle of friction, SH_{max} orientation, and the depth where the SH_{max} is applied (WP and Tiger) to evaluate six faults with different characteristics in terms of their principal strike orientation, length along strike, and diverse displaced sedimentary sequences.

Percentiles were used to estimate how the risk of fault reactivation varies along the fault plane and to compare our results with fault roughness along strike (Table 3). The statistical analysis enabled a more detailed evaluation of the highlighted section at each fault in every scenario. As the pore pressure results vary strongly along fault planes for all scenarios (Table 2), it was necessary to focus on highlighted section to understand what proportion of the fault is represented and where these segments are located along strike. This strong variation in pore pressure also confirms the importance of incorporating percentiles in future risk of fault reactivation analyses.

Geomechanical parameters

In this study we applied the same geomechanical parameters that preliminary studies in the CSB used such as cohesion, angle of friction, and SH_{max} orientation. These studies also used stress gradients to define a strike-slip stress regime and pore pressures *(Reynolds et al., 2003, 2005; Macdonald et al., 2012)*. In this paper we added the calculation of effective stress magnitude at the depth of the principal reservoirs Tiger and WP, and two coefficients of friction associated with the occurrence of sandstones and shales within the reservoir intervals.

Changes in pore pressure results between the different scenarios suggest that particular geomechanical parameters included in this study influence the risk of fault reactivation in the Ceduna Sub-basin. Our results show that the angle of friction is the geomechanical parameter that has the strongest impact on the risk of fault reactivation. For instance, our results show that changes of 2 to 5 MPa in pore pressure occur between scenarios when we changed either the SH_{max} orientation or SH_{max} at WP and Tiger stratigraphic levels, and when we leave the angle of friction constant (e.g. between WP-130-31 and T-130-31, or T-130-22 and T-90-22). In contrast, we see changes in pore pressure from 8 to 20 MPa between scenarios where we change the angle of friction, but maintain other parameters as unchanged (e.g., between WP-130-31 and WP-90-22, or between T-90-31 and T90-22). The impact of the angle of friction on the risk of fault reactivation is also evident in the 3D maps where we identified a wider sector of the fault at risk of reactivation along the fault plane for the scenarios where the angle of friction is 22° in comparison to the scenarios where the angle of friction is 31°. For instance, in the scenario WP-130-31, F1 and F8 show risk of reactivation in the T4 sequence. However, in the scenario WP-130-22, the area at risk of reactivation covers the T4 and T3 sequences. Similarly, in the scenario WP-90-31, F10 shows risk of reactivation at T1 and WP2. However, in the scenario WP-90-22 this fault exhibits risk of reactivation in the T1, WP2 and WP1 sequences.

Influence of fault plane roughness on the risk of fault reactivation

Results from stereonet and 3D map analyses confirm the importance of assembling a detailed seismic interpretation of fault segments to identify changes in fault roughness along strike. We believe that in this case, the 3D seismic survey proved to be a good tool to map these changes of strike and dip angle for all the fault planes regardless of their length along strike and their geometry (listric vs. planar).

In this study we included listric and planar faults of different length along strike. We were not surprised to find greater variety of dip angles in the listric faults in cross-section view than the planar faults, because the seismic interpretation confirmed that listric faults exhibit changes in dip angle from steep in the upper intervals to shallow in the lower intervals. However, we also identified a correlation between variations in fault plane roughness and the length along strike for all faults. F1, F8 and F9, are interpreted with distances along strike greater than 5.0 km and cover a large area of the stereonets, denoting a wider range of strikes and dip angles along the fault plane. In contrast, F16, F10 and F11 are interpreted with lengths along strike of 2.1 km, 2.5 km and 1.6 km respectively covering a smaller range of strikes and dip angles on stereonets.

Our results show that sections of faults that show dip angles steeper than 40° are at risk of reactivation. F1 and F8 are faults with higher risk of reactivation for all scenarios. These faults also exhibit steeper dip angles along their highlighted section. In contrast, F9 is the most stable fault in this study and exhibits shallow dip angles along its highlighted area. These observations agree with preliminary studies which suggest that the vertical faults and sections of listric faults with dip angles between 55° and 70° are at higher risk of reactivation *(Reynolds et al., 2005; MacDonald et al., 2012)*. However, we also demonstrate on stereonets that not all fault sections with steep dip angles are likely to reactivate, which suggests that the angle of friction is not the only structural feature within the faults that can influence the risk of fault reactivation.

Our results show similarities with those of *Reynolds et al., (2003)*, suggesting that faults with a strike between 100°N and 160°N are at higher risk of reactivation when the maximum horizontal stress orientation is either 130°N or 090°N. However, they only evaluated fault segments with northwest-southeast average strikes and did not consider outcomes for faults with other average strikes in the CSB. This study included a total of eight faults with northwest-southeast strike (F1, F8, F9, F10, F11, F2 and F4) and two faults with east-west average strike (F16 and F5). Therefore, we were able to differentiate the impact that changes in SH_{max} orientation have for different fault strike orientations. In all cases we see that the faults show one or two sections of the same segment that are at risk of reactivation. Faults at higher risk of reactivation like F1, F8 and F16 have sections of the fault with strikes that are oblique to Sh_{max} (10° to 15° from Sh_{max}) regardless of SH_{max} orientation. We used these faults to set a strike cut-off that can predict the section of faults that are likely to reactivate. We propose that (1) when the maximum horizontal stress orientation is 130°N, faults with general strikes of 070°N and 115°N or 140°N and 165°N are at highest risk of reactivation; and (2) when the maximum horizontal stress orientation is 090°N, fault sections with strikes between 046°N and 079°N or 104°N and 165°N are at highest risk of reactivation. We test these strike cut-offs for faults that are at low risk of reactivation (F9, F10 and F11) and confirm that the sections with strikes parallel to sub-parallel (<10°) to the SH_{max} orientation, and in most cases did not coincide with our proposed fault strike cut-offs. However, these faults also exhibit sections with similar strikes to the trends we delimit for other faults, which might suggest that the fault strike structural feature is not the only important factor in

the likelihood of reactivation. Considering the result from the dip angle we propose that the risk must be influenced by a combination between fault strike and dip angle.

3D maps confirm the variability in fault strike and dip angle along strike, and so demonstrates both variations in fault roughness along strike and how these variations are associated with the changes in the risk of fault reactivation. The 3D fault maps corroborate that the steeper dipping parts of these faults are mostly concentrated in the upper stratigraphic sections and are in most of the cases at higher risk of reactivation. These changes in fault roughness along the fault plane were first observed in *Macdonald et al., (2012)*, where 3D maps of the four interpreted faults showed areas at risk of reactivation that vary in cross-section view and along strike.

Implications for the exploration of hydrocarbons

Faults are a principal structural element to trap or provide migration pathways for immiscible buoyant fluids such as hydrocarbons. Fault reactivation can lead to sealing system breach, seismicity and development of new trapping structures for migrating fluids *(Thorsen, 1963; Streit, 1999; Mildren et al., 2002; Selley and Sonnenberg, 2015).*

In this study we apply our proposed scenarios to two fault sets forming trapping elements for potential hydrocarbon leads in the study area to identify the impact that the risk of fault reactivation analysis has for hydrocarbon exploration in the CSB. To properly define the leads, we previously confirmed other petroleum system elements in the lead areas such as the presence of good quality reservoir and seal rocks and the prospect for hydrocarbon content.

Results from the fault sets comprising trapping elements of this leads show higher risk of reactivation when the angle of friction decreases. These results confirm the importance of evaluating different geomechanical parameters for risk assessment of exploration campaigns. Therefore, we emphasise the importance of properly defining the coefficient of friction to reduce hydrocarbon exploration uncertainties.

The results for the combined faults F2-F4 and F5-F6 show similar results to those for individual fault segments. We identify a strong correlation between fault roughness along strike and the likelihood of reactivation. Both hydrocarbon lead fault sets confirm that areas of a fault with steeper angles of dip and oblique strikes from the SH_{max} orientation are at higher risk of reactivation. Results shown in stereonets and 3D maps also show that the risk of fault reactivation can be distributed differently on each of the fault segments even though they are part of the same hydrocarbon trapping system. For instance, the highlighted sections for F5-F6 show different strikes than those of F2-F4 and in consequence differences in the risk of fault reactivation results. We believe that these differences are mainly associated with the principal west-east strike in F5 that differs from the more northwest-southeast strikes in F2, F4 and F6.

Implications for other sedimentary basins

The FAST technique has been already applied to other sedimentary basins at passive margins like the Timur Sea, to evaluate the risk of fault reactivation in normal faults *(Mildren et al., 2002)*. In addition, our results demonstrate the importance of integrating percentiles in cases where fault planes exhibit strong changes in fault roughness that can lead to variation in fault reactivation risk along strike. some

studies related to active tectonic margins with existing seismicity activity, like those of New Zealand and the west coast of the United States of America, have incorporated the analysis of fault roughness as a way to estimate structural parameters involved during earthquake-related fault displacement *(Streit, 1999; Litchfield et al., 2018).* However, there are few studies like *Macdonald et al., (2012*) that incorporate fault roughness information in geomechanical studies of passive margins.

We demonstrate that normal growth faults are not homogenous planes but rather planes that can vary in dip angle and orientation along strike. We also demonstrate that in the case of normal growth faults these changes in roughness are proportional to the length of analysed fault segment in map view. Therefore, we believe that for more detailed geomechanical analyses of growth faults it is essential to incorporate the changes in fault roughness. We also demonstrate how the risk of reactivation can strongly vary along the fault strike. Therefore, we propose the addition of percentiles in fault risk assessments to identify variation in fault reactivation risk along strike as they enable to define the areas at greatest risk of reactivation along the fault plane, which is an essential information in the exploration of hydrocarbons and in the prediction of potential seismicity hazards.

Conclusions

This paper is one of very few studies that analyse the likelihood of contemporary fault reactivation in normal growth faults in passive margins. It demonstrates that the heterogeneity planes of faults can outcome in variations in the likelihood of fault reactivation which is an important factor in the exploration of hydrocarbons as it signifies potential seal breakage and possible risk of seismicity activity. We demonstrate how the fault roughness has a significant impact on the risk of reactivation, where the region that combines steep dip angles (>40°) and strikes oblique to SH_{max} (10°-15° from the stress orientation) are at highest risk of reactivation.

This study proves the importance of a detailed seismic interpretation to define fault segments in the CSB that exhibit different characteristics in terms of geometry, length along strike, and average strike orientation. It also demonstrates that the FAST technique is an excellent tool to analyse the risk of fault reactivation of normal growth faults as it allowed to analyse the influence that the present-day stress field in the Southern Australian Margin. We also demonstrated the importance of including percentiles in the analysis of fault reactivation risk to define what percentage of a fault is at risk and where these unstable areas are located along strike.

Of the geomechanical parameters we used in this study, the angle of friction was demonstrated to be the parameter that most strongly influences the risk of fault reactivation. We propose that for future rock mechanics analyses it is essential to properly define this parameter, ideally using well data.

We also tested our results by applying these hypotheses to two independent hydrocarbon accumulation leads at the northern and southern regions of the study area. We determined the importance of including the fault reactivation risk analysis as part of future exploration campaign planning. We demonstrated that specific sections of the fault along strike that delimited the structural closure in the leads are at risk of reactivation given their particular dip angle and strike, which varies from those of the fault planes in general.

References

Azeem, T., Yanchun, W., Khalid, P., Xueqing, L., Yuan, F., Lifang, C., 2016. An application of seismic attributes analysis for mapping of gas bearing sand zones in the sawan gas field, Pakistan. Acta Geod. Geophys. 51, 723–744. https://doi.org/10.1007/s40328-015-0155-z

Bally, A.W., Bernoulli, D., Davis, G.A., Montadert, L., 1981. Listric Normal Faults. Oceanol. Acta 16.

Bellahsen, N., Daniel, J.M., 2005. Fault reactivation control on normal fault growth: an experimental study. J. Struct. Geol. 27, 769–780. https://doi.org/10.1016/j.jsg.2004.12.003

Bight Basin [WWW Document], 2020. URL https://energymining.sa.gov.au/petroleum/prospectivity/bight_basin

Brudy, M., Zoback, M.D., Fuchs, K., Rummel, F., Baumgartner, J., 1997. Estimation of the complete stress tensor to 8km depth in the KTB scientific drill holes: Implications for crustal strengtj 102.

Caine, J.S., Evans, J.P., Forster, C.B., 1996. Fault zone architecture and permeability structure. Geology 24, 1025–1028. https://doi.org/10.1130/0091-7613(1996)024<1025:FZAAPS>2.3CO;2

Chan, A.W., Hauser, M., Couzens-Schultz, B.A., Gray, G., 2014. The Role of Shear Failure on Stress Characterization. Rock Mech. Rock Eng. 47, 1641–1646. https://doi.org/10.1007/s00603-014-0585-x

Espurt, N., Callot, J.-P., Totterdell, J., Struckmeyer, H., Vially, R., 2009. Interactions between continental breakup dynamics and large-scale delta system evolution: Insights from the Cretaceous Ceduna delta system, Bight Basin, Southern Australian margin: CONTINENTAL BREAKUP AND DELTA SYSTEM. Tectonics 28. https://doi.org/10.1029/2009TC002447

Fagin, S., 1996. The fault shadw problem; its nature and elimination. Corpus Christi Geol. Soc. Corpus Christi TX U. S. November, 6.

Fossen, H., 2010. Structural Geology. Cambridge University Press, NY, Cambridge.

Gibson, G.M., Totterdell, J., White, L.T., Mitchell, C.R., Stacey, A.R., Morse, M.P., Whitaker, A., 2013. Pre-existing basement structures and its influence on continental rifting and fracture development along Australian's southern rifted margin. J. Geol. Soc. Lond. 170, 365–377. https://doi.org/10.1144/jgs2012-040

Hart, B.S., 2008. Channel detection in 3-D seismic data using sweetness. AAPG Bull. 92, 733–742. https://doi.org/10.1306/02050807127

Hillis, R.R., Meyer, J.J., Reynolds, S.D., 1998. The Australian stress map. Explor. Geophys. 29, 420–427. https://doi.org/10.1071/EG998420

Hillis, R.R., Reynolds, S.D., 2000. The Australian Stress Map. J. Geol. Soc. Lond. 157, 915–921.

Hillis, R.R., Sandiford, M., Reynolds, S.D., Quigley, M.C., 2008. Present-day stresses, seismicity and Neogene-to-Recent tectonics of Australia's 'passive' margins: intraplate deformation controlled by plate boundary forces. Geol. Soc. Lond. Spec. Publ. 306, 71–90. https://doi.org/10.1144/SP306.3

Holford, S., Hillis, R., Duddy, I., Green, P., Stoker, M., Tuitt, A., Backé, G., Tassone, D., MacDonald, J., 2011. Cenozoic post-breakup compressional deformation and exhumation of the southern Australian margin. APPEA J. 51, 613. https://doi.org/10.1071/AJ10044

Hooper, E.C.D., 1991. Fluid migration along growth faults in compacting sediments. J. Pet. Geol. 14, 161–180. https://doi.org/10.1111/j.1747-5457.1991.tb00360.x

Karstens, J., Berndt, C., 2015. Seismic chimneys in the Southern Viking Graben – Implications for palaeo fluid migration and overpressure evolution. Earth Planet. Sci. Lett. 412, 88–100. https://doi.org/10.1016/j.epsl.2014.12.017

Kempton, R., Bourdet, J., Ross, A., Pironon, J., 2019. Petroleum migration in the Bight Basin: a fluid inclusion approach to constraining source, composition and timing. APPEA 57, 762–766.

King, R., Hillis, R.R., Reynolds, S.D., 2008. In-situ stresses and natural fractures in the Northern Perth Basin, Australia. Aust. J. Earth Sci. 55, 685–701. https://doi.org/10.1080/08120090801982843

King, R., Holford, S., Hillis, R., Tuitt, A., Swierczek, E., Backé, G., Tassone, D., Tingay, M., 2012. Reassessing the in-situ stress regimes of Australian petroleum basins 12.

King, R.C., Backé, G., 2010. A balanced 2D structural model of the Hammerhead Delta–Deepwater Fold-Thrust Belt, Bight Basin, Australia. Aust. J. Earth Sci. 57, 1005–1012. https://doi.org/10.1080/08120099.2010.509409

Klauser-Baumgärtner, D., Reichel, T., Hansen, J.-A., 2019. Regional paleodepositional environment of the Cretaceous in the Great Australian Bight – a support for frontier exploration. APPEA J. 59, 891. https://doi.org/10.1071/AJ18055

Langhi, L., Strand, J., Ross, A., 2020. Stratigraphic and structural trapping frameworks in the central Ceduna Sub-basin. Mar. Pet. Geol. 120, 104523. https://doi.org/10.1016/j.marpetgeo.2020.104523

Litchfield, N.J., Villamor, P., Dissen, R.J.V., Nicol, A., Barnes, P.M., A. Barrell, D.J., Pettinga, J.R., Langridge, R.M., Little, T.A., Mountjoy, J.J., Ries, W.F., Rowland, J., Fenton, C., Stirling, M.W., Kearse, J., Berryman, K.R., Cochran, U.A., Clark, K.J., Hemphill-Haley, M., Khajavi, N., Jones, K.E., Archibald, G., Upton, P., Asher, C., Benson, A., Cox, S.C., Gasston, C., Hale, D., Hall, B., Hatem, A.E., Heron, D.W., Howarth, J., Kane, T.J., Lamarche, G., Lawson, S., Lukovic, B., McColl, S.T., Madugo, C., Manousakis, J., Noble, D., Pedley, K., Sauer, K., Stahl, T., Strong, D.T., Townsend, D.B., Toy, V., Williams, J., Woelz, S., Zinke, R., 2018. Surface Rupture of Multiple Crustal Faults in the 2016 Mw 7.8 Kaikōura, New Zealand, Earthquake. Bull. Seismol. Soc. Am. 108, 1496–1520. https://doi.org/10.1785/0120170300

Lubiniecki, D.C., King, R.C., Holford, S.P., Bunch, M.A., Hore, S.B., Hill, S.M., 2020. Cenozoic structural evolution of the Mount Lofty Ranges and Flinders Ranges, South Australia, constrained by analysis of deformation bands. Aust. J. Earth Sci. 67, 1097–1115. https://doi.org/10.1080/08120099.2019.1695227

MacDonald, J., 2012. Origin and structure of the Ceduna Delta System, offshore South Australia (thesis). University of Adelaide.

MacDonald, J., Backé, G., King, R., Holford, S., Hillis, R., 2012a. Geomechanical modelling of fault reactivation in the Ceduna Sub-basin, Bight Basin, Australia. Geol. Soc. Lond. Spec. Publ. 367, 71–89. https://doi.org/10.1144/SP367.6

Macdonald, J., Backé, G., King, R., Holford, S., Hillis, R., 2012. Geomechanical modelling of fault reactivation in the Ceduna Sub-basin, Bight Basin, Australia. Geol. Soc. Lond. Spec. Publ. 367, 71–89. https://doi.org/10.1144/SP367.6

MacDonald, J., Holford, S., King, R., 2012b. Structure and Prospectivity of the Delta-Deep-Water Fold-Thrust Belt Systems, Bight Basin, Australia, in: New Understanding of the Petroleum Systems of Continental Margins of the World: 32nd Annual. SOCIETY OF ECONOMIC PALEONTOLOGISTS AND MINERALOGISTS, pp. 779–816.

Magee, C., Hunt-Stewart, E., Jackson, C.A.-L., 2013. Volcano growth mechanisms and the role of sub-volcanic intrusions: Insights from 2D seismic reflection data. Earth Planet. Sci. Lett. 373, 41–53. https://doi.org/10.1016/j.epsl.2013.04.041

Mildren, S., Hillis, R., Lyon, P., Meyer, J., Dewhurst, D., Boult, P., 2005. FAST: A New Technique for Geomechanical Assessment of the Risk of Reactivation-related Breach of Fault Seals. AAPG Bull., Hedberg 2, 73–85. https://doi.org/10.1306/1060757H23163

Mildren, S.D., Hillis, R.R., J.Kaldi, 2002. Calibrating predictions of fault seal Reactivation in the Timor Sea. APPEA J. 42, 187. https://doi.org/10.1071/AJ01011

Otis, R., Haryott, P., 2010. Calibration of Uncertainty (P10/P90) in Exploration Prospects; #40609 (2010), in: AAPG. p. 23.

Paul, B., 1961. A Modification of the Coulomb-Mohr Theory of Fracture. J. Appl. Mech. 28, 259–268. https://doi.org/10.1115/1.3641665

Rajabi, M., Tingay, M., Heidbach, O., Hillis, R., Reynolds, S., 2017. The present-day stress field of Australia. Earth-Sci. Rev. 168, 165–189. https://doi.org/10.1016/j.earscirev.2017.04.003

Renard, F., Candela, T., 2017. Scaling of Fault Roughness and Implications for Earthquake Mechanics, in: Thomas, M.Y., Mitchell, T.M., Bhat, H.S. (Eds.), Geophysical Monograph Series. John Wiley & Sons, Inc., Hoboken, NJ, USA, pp. 195–215. https://doi.org/10.1002/9781119156895.ch10

Reynolds, P., Holford, S., Schofield, N., Ross, A., 2018. The importance of subsurface lithology in controlling magma storage v. eruption: an example from offshore southern Australia. J. Geol. Soc. 175, 694–703. https://doi.org/10.1144/jgs2017-109

Reynolds, P., Holford, S., Schofield, N., Ross, A., 12/2017b. The shallow depth emplacement of mafic intrusions on a magma-poor rifted margin: An example from the Bight Basin, southern Australia. Mar. Pet. Geol. 88, 605–616. https://doi.org/10.1016/j.marpetgeo.2017.09.008

Reynolds, S., Hillis, R., Paraschivoiu, E., 2003. In situ stress field, fault reactivation and seal integrity in the Bight Basin, South Australia. Explor. Geophys. 34, 174–181. https://doi.org/10.1071/EG03174

Reynolds, S.D., Hillis, R.R., 2000. The in situ stress field of the Perth Basin, Australia. Geophys. Res. Lett. 27, 3421–3424. https://doi.org/10.1029/2000GL011538

Reynolds, S.D., Paraschivoiu, E., Hillis, R.R., O'Brien, G.W., 2005. A Regional Analysis of Fault Reactivation and Seal Integrity Based on Geomechanical Modeling: An Example from the Bight Basin, Australia. AAPG Hedberg Ser., 2 57–71. https://doi.org/10.1303/1060756H23162

Sayers, J., Symonds, P.A., Direen, N.G., Bernardel, G., 2001. Nature of the continent-ocean transition on the non-volcanic rifted margin of the central Great Australian Bight. Geol. Soc. Lond. Spec. Publ. 187, 51–76.

Selley, R.C., Sonnenberg, S.A., 2015. Chapter 7: Traps and Seals, in: Elements of Petroleum Geology. Elsevier, UK, pp. 321–375.

Sibson, R.H., 1985. A note on fault reactivation. J. Struct. Geol. 7, 751–754. https://doi.org/10.1016/0191-8141(85)90150-6

Somerville, R., 2001. The Ceduna Sub-basin - A snapshot of prospectivity. APPEA 41, 321–346.

Streit, J.E., 1999. Conditions for earthquake surface rupture along the San Andreas Fault System, California. J. Geophys. Res. Solid Earth 104, 17929–17939. https://doi.org/10.1029/1999JB900131

Tapley, D., Mee, B.C., King, S.J., Davis, R.C., Leischner, K.R., 2005a. Petroleum potential of the Ceduna Sub-Basin: Impact of Gnarlyknots–1A. APPEA J. 45, 365. https://doi.org/10.1071/AJ04029

Tapley, D., Mee, B.C., King, S.J., Davis, R.C., Leischner, K.R., 2005b. Petroleum Potential of the Ceduna Sub-basin: Impact of Gnarlyknots-1A. APPEA 365–380.

Tapley, D., Mee, B.C., King, S.J., Davis, R.C., Leischner, K.R., 2005c. Petroleum pontetial of the Ceduna Sub-basin: Impact of Gnarlyknots-1A. APPEA J. 45, 365. https://doi.org/10.1071/AJ04029

Thorsen, C.E., 1963. Age of Growth Faulting in Southeast Louisiana. AAPG, Gulf Coast Association of Geological Societies Transactions 13, 103–110.

Totterdell, J., Mitchell, C., 2009. Bight Basin Geological Sampling and Seepage Survey. Geosci. Aust.

Totterdell, J., Struckmeyer, H.I.M., Boreham, C.J., Mitchell, C.H., Monteil, E., Bradshaw, B.E., 2008. Mid–Late Cretaceous organic-rich rocks from the eastern Bight Basin: implications for prospectivity 23.

Totterdell, J.M., Blevin, J.E., Struckmeyer, H.I.M., Bradshaw, B.E., Colwell, J.B., Kennard, J.M., 2000. A new sequence framework for the Great Australian Bight: Starting with a clean slate. APPEA J. 40, 95. https://doi.org/10.1071/AJ99007

Totterdell, J.M., Krassay, A.A., 2003. The role of shale deformation and growth faulting in the Late Cretaceous evolution of the Bight Basin, offshore southern Australia. Geol. Soc. Lond. Spec. Publ. 216, 429–442. https://doi.org/10.1144/GSL.SP.2003.216.01.28

Totterdell, J.M., Struckmeyer, H.I.M., Boreham, C.J., Mitchell, C.H., Monteil, E., Bradshaw, B.E., 2008. Mid–Late Cretaceous organic-rich rocks from the eastern Bight Basin: implications for prospectivity 23.

Velayatham, T., Holford, S., Bunch, M., King, R., 2021. Fault controlled focused fluid flow in the Ceduna Sub-Basin, offshore South Australia; evidence from 3D seismic reflection data. Mar. Pet. Geol. 127, 49.

Weber, K.J., Mandl, G.J., Pilaar, W.F., Lehner, B.V.F., Precious, R.G., 1978. The Role of Faults in hydrocarbon migration and trapping in Nigerian growth fault structures, in: Offshore Technology Conference. Presented at the Offshore Technology Conference, Offshore Technology Conference, Houston, Texas. https://doi.org/10.4043/3356-MS

Woillez, M.-N., Souque, C., Rudkiewicz, J.-L., Willien, F., Cornu, T., 2017. Insights in Fault Flow Behaviour from Onshore Nigeria Petroleum System Modelling. Oil Gas Sci. Technol. – Rev. D'IFP Energ. Nouv. 72, 31. https://doi.org/10.2516/ogst/2017029

Worum, G., van Wees, J.-D., Bada, G., van Balen, R.T., Cloetingh, S., Pagnier, H., 2004. Slip tendency analysis as a tool to constrain fault reactivation: A numerical approach applied to three-dimensional fault models in the Roer Valley rift system (southeast Netherlands): SLIP TENDENCY ANALYSIS OF THREE-DIMENSIONAL FAULT MODELS. J. Geophys. Res. Solid Earth 109. https://doi.org/10.1029/2003JB002586

Wyllie, D., Norrish, N., 1996. Chapter 14: Rock strenght properties and their measurement., in: Landslides: Investigation and Migration. The National Academies of Sciences, Engineering and Medicine, US, pp. 372–390.

Chapter 4: Interpretation of magmatic systems

Structural controls on post-rift magmatism in the Ceduna Sub-basin, Great Australian Bight Basin

Statement of Authorship

Title of Paper	Structural controls on post-rift magmatism in the Ceduna Sub-basin, Great Australian Bight Basin
Publication Status	☐ Published ☐ Accepted for Publication ☐ Submitted for Publication ☑ Unpublished and Unsubmitted work written in manuscript style
Publication Details	

Principal Author

Name of Principal Author (Candidate)	Monica Jimenez Lloreda		
Contribution to the Paper	• Data interpretation • Development of methodology • Manuscript drafting		
Overall percentage (%)	70%		
Certification:	This paper reports on original research I conducted during the period of my Higher Degree by Research candidature and is not subject to any obligations or contractual agreements with a third party that would constrain its inclusion in this thesis. I am the primary author of this paper.		
Signature		Date	09/01/2023

Co-Author Contributions

By signing the Statement of Authorship, each author certifies that:

i. the candidate's stated contribution to the publication is accurate (as detailed above);

ii. permission is granted for the candidate in include the publication in the thesis; and

iii. the sum of all co-author contributions is equal to 100% less the candidate's stated contribution.

Name of Co-Author	Simon Holford		
Contribution to the Paper	• Supervision • Manuscript drafting • Method development		
Signature		Date	03/02/02

Name of Co-Author	Rosalind King		
Contribution to the Paper	• Supervision • Manuscript drafting		
Signature		Date	8/2/23

Name of Co-Author	Mark Bunch		
Contribution to the Paper	• Supervision • Manuscript drafting		
Signature		Date	17/08/2023

Structural controls on post-rift magmatism in the Ceduna-Sub-basin, Great Australian Bight

Monica Jimenez [1,2], Simon Holford [1,2], Rosalind King [1,3], Mark Bunch [1,2]

[1] Structural, Stress and Seismic Research Group, University of Adelaide (S3)

[2] Australian School of Petroleum and Energy Resources, University of Adelaide

[3] Department of Earth Sciences, University of Adelaide

Abstract

Igneous bodies in the Great Australian Bight Basin have mostly been interpreted using 2D and small 3D seismic surveys. These interpretations suggest complex magma network systems that occurred during the Paleogene that include multiple magmatic levels within the Hammerhead Supersequence. In this study we use the Ceduna 3D MSS seismic survey that extends across 12,030 km^2 of the central region of the Ceduna Sub-basin to interpret two composite volcanoes (Volcano A and Volcano B) that include steep principal eruptive centres surrounded by regions of lava that mostly flowed towards the southwest, and 43 minor eruptive centres. We also map ten intrusive igneous bodies, a potential pipe-like structure underlying Volcano B, and two potential fissures connected to underlying intrusions at the southeast region of Volcano B. The 10 intrusions consist of (a) five intrusions with a compound morphology that are located in the middle and base sequences of the Hammerhead Supersequence, that represent mostly isolated igneous bodies, and (b) five intrusions with saucer-shaped morphology that are situated at the top section of the Hammerhead Supersequence and are clustered beneath the lava flow and eruptive centres. We also investigate the influence of normal growth faults in the transport and emplacement of magma in the study area. Our seismic interpretation proposes that the sharp geometry of the eruptive centres and the truncation of the lava flow in the northeast of the study area can be strongly influenced by near-normal growth fault segments that might work as structural boundaries. We use seismic attributes (e.g., maximum amplitude and RMS) to demonstrate the absence of evidences of magma transport along the fault planes and a statistical point alignment method to quantify a clear northwest-southeast alignment between normal growth fault strikes in the Ceduna Sub-basin, eruptive centres and source points of intrusions. Despite the presence of the Tiger detachment layer in the Ceduna Sub-basin the intrusions were emplaced and transported along sandstones and mass transport sediments of the Hammerhead Supersequence rather than through the underlying Tiger detachment layer. We propose that this might be a consequence of a decrease in thickness of the Tiger detachment layer or its dewatering and/or degassing through the formation of vertical chimneys.

Introduction

The Bight Basin Igneous Complex (BBIC) is located in the central region of the Ceduna Sub-basin in the Great Australian Bight. The BBIC comprises basaltic sills, dykes and laccolith morphologies, lava and fissure flows, and shield volcanic cones interpreted using 2D and small 3D seismic surveys, which have proven excellent tools for characterising complex magma network systems preserved in the subsurface *(Schofield and Totterdell, 2008. Holford et al., 2012, 2017; Jackson et al., 2013; Magee et al., 2013; Reynolds et al., 2017a, 2018; Robson et al., 2017*).The BBIC include multiple levels within the Hammerhead Supersequence composed of saucer-shaped, hybrid intrusions and laccolith morphologies *(Reynolds et al., 2017b)*, shield volcanoes and stratovolcanoes *(Magee et al., 2013b).* In both cases it is thought the magma transport occurred in the Middle Eocene Epoch after the beginning of the passive margin stage of this part of the Australian Continental Shelf.

The Ceduna Sub-basin is a passive margin basin with two independent delta systems (White Pointer and Hammerhead delta systems) that structurally exhibit normal growth faulting in the delta tops and Deep-Water Fold-Fault Thrust belts basinwards *(Totterdell and Krassay, 2003; Totterdell and Mitchell, 2009; King and Backé, 2010; MacDonald et al., 2010; Robson et al., 2017).* The extensional region of the White Pointer Delta System shows Cenomanian normal growth faults that detach at the top of the Blue Whale Supersequence, while the extensional region of the Hammerhead Delta System shows Late Santonian-Maastrichtian normal growth faults that are either dip-linked with Cenomanian faults or detach at the top of the intervening Tiger Supersequence (Jimenez et al., 2021; MacDonald et al., 2010; Robson, 2017; Ryan et al., 2017b).

Interpretation of 2D and 3D seismic surveys has shown the influence that faults have in the transport, morphology, distribution and emplacement of igneous bodies, where normal faults influence the transport of magma and geometry of magma systems. Many of these studies are related to active margins (e.g. subduction, rift) *(Magee et al., 2013, 2018; Olivia et al., 2019; Hillman et al., 2020),* leaving many questions regarding how normal growth faults interact with magma transport processes elsewhere. In addition, studies suggest that ductile shale sequences and over-pressurised zones (e.g. shale detachment layers) *(Thomson, 2007)*, and salt layers *(Schofield et al., 2014; Magee et al., 2021; Pindell and Heyn, 2022)* are commonly preferential sequences for the transport and emplacement of magma. Hydrate lithologies in particular are more favourable given the capacity of the hot magma to increase internal pore pressure, weakening the internal rock fabric and leaving greater space for magma to be transported laterally *(Schofield et al., 2014).* Detachment layers in passive margin delta systems, especially those comprising a source for hydrocarbons, are similarly prone owing to their mechanical weakness and potentially volatile pore fluids. The Ceduna Sub-basin provides a great opportunity to examine the potential effect that growth faults and mechanical discontinuities/boundaries such as shale detachments, have on shallow magma plumbing systems.

In this paper we interpret the Ceduna 3D seismic survey to provide new insights into structural controls on paleo magma transport and eruption within the Ceduna Sub-basin. We describe the morphologies of 10 intrusive igneous bodies and two volcanoes that comprise principal eruptive centres, minor eruptive centres and lava flow regions, to demonstrate the strong influence that normal growth faults had on the morphology of extrusions. In addition, we quantify the influence of normal growth faults on the transport of magma using a statistical point alignment method and rose diagrams to demonstrate a linear northwest-southeast correlation between igneous bodies and Late

Santonian-Maastrichtian normal growth faults in the Ceduna Sub-basin. We also investigate how the potential lack of overpressure in the upper Tiger detachment layer due to dewatering and degassing influenced the emplacement of intrusive bodies within the Hammerhead Supersequence

Geological settings

Geological evolution of the Great Australian Bight

The Great Australian Bight (GAB) is located along the Southern Australian Margin and extends for 250,000 km^2 (Figure 1a). It includes four independent depocentres: the Eyre, Ceduna, Recherche, and Duntroon sub-basins that developed between the Middle Jurassic and Late Cretaceous epochs. The Ceduna Sub-basin (CSB) is the largest depocentre in the GAB and covers an area of 90,000 km^2 with a west-northwest trend and a total sedimentary thickness of 15 km that was deposited from the Late Jurassic to the Tertiary *(Sayers et al., 2001; Totterdell and Krassay, 2003; Espurt et al., 2009; Totterdell and Mitchell, 2009).* (Figure 1b)

The geological evolution of the GAB can be divided in four main stages, as follows:

(1) A continental rift between Australia and Antarctica formed in the Middle to Late Jurassic Period and established a northwest-southeast trend that formed oblique half-grabens and rift basins along the Southern Australian Margin (e.g. the Great Australian Bight, the Otway, Gippsland, Bass, and Sorell basins*) (Totterdell and Krassay, 2003; Totterdell and Mitchell, 2009; Gibson et al., 2013)*. (Figure 1b)

(2) During the Berriasian, syn-rift fluvial sandstones from the Southern Right Supersequence were deposited followed by Valanginian to Aptian Age sandstones and mudstones of the Bronze Whaler Supersequence *(Espurt et al, 2009; Totterdell and Mitchell, 2009).* (Figure 1c)

(3) Between the Albian-Campanian, shales of the Blue Whale Supersequence (BW) were unconformably deposited above the Bronze Whaler Supersequence and marked the beginning of the rapid thermal subsidence that ended at the Late Santonian *(Tapley et al., 2005; Espurt et al., 2009; Totterdell and Mitchell, 2009; Holford et al., 2011).* During the Cenomanian progradational fluvial and deltaic sediments of White Pointer Supersequence (WP) were rapidly deposited in a short period of time towards the Southwest, which in conjunction with an accelerated subsidence, resulted in overpressure characteristics of the Blue Whale shales at the base and the formation of the White Pointer Delta System *(Espurt et al., 2009; Holford et al., 2011).* Between the Turonian and Santonian, progradational sandstones were followed by aggradational marine mudstones from the Tiger Supersequence that were conformably deposited over the White Pointer Supersequence *(Totterdell and Krassay, 2003; Espurt et al., 2009).* A Late Santonian unconformity represents the end of the global sea level rise, the commencement of the sea floor spreading between Australia and Antarctica, and the beginning of the passive margin (~83Ma). During the Late Santonian the Great Australian Bight (GAB) basin became divided into three smaller depocentres that are structurally controlled by the basement architecture: Eyre, Ceduna and Recherche Sub-basins *(Totterdell and Krassay, 2003; Espurt et al., 2009; Holford et al., 2011)*. (4) Between the Late Santonian-Maastrichtian, sandstones and mudstones of the Hammerhead Supersequence (HH) were deposited unconformably during a period of slow seafloor spreading. The base (HH1) and middle (HH2) are progradational sequences of sandstones and shales that was rapidly deposited towards the southeast, forming the Hammerhead

Delta System. The rapid accumulation reactivated some of the faults from the Cenomanian sequence and created new faults that detached at the top of the Tiger Supersequence. The topmost unit of the Hammerhead Supersequence (HH3) corresponds to an aggradational accumulation phase that reduced basinwards sedimentation and thus, produced a change in basin dynamics *(Totterdell and Krassay, 2003; Tapley et al., 2005; Tottendell and Mitchel, 2009; Reynolds et al., 2017).* (Figure 1c)

Regional uplift between the end of the Cretaceous and the beginning of the Paleogene eroded part of the Hammerhead Supersequence and the top of the Tiger Supersequence, forming an angular unconformity between the Eucla and the Great Australian Bight basins *(Totterdell and Krassay, 2003).* In the CSB, the Cenozoic era is represented by a dramatic drop in sedimentation, which in conjunction with a period of thermal subsidence resulted in a regional hiatus. During the Early Eocene, marginal marine to deltaic sandstones of the Wobbegong Supersequence were deposited *(Espurt et al., 2009),* and in the middle Eocene unconformably above the Wobbegong Supersequence, minor sandstones and carbonate platforms of cool-water carbonates from the Dugong Supersequence accumulated during a period of marine transgression (Figure 1b). Today, the GAB is part of the Australian Continental Shelf and included the continental slope of 260 km*(Totterdell and Krassay, 2003; Reynolds et al., 2017; Stoker et al., 2022).* (Figure 1c)

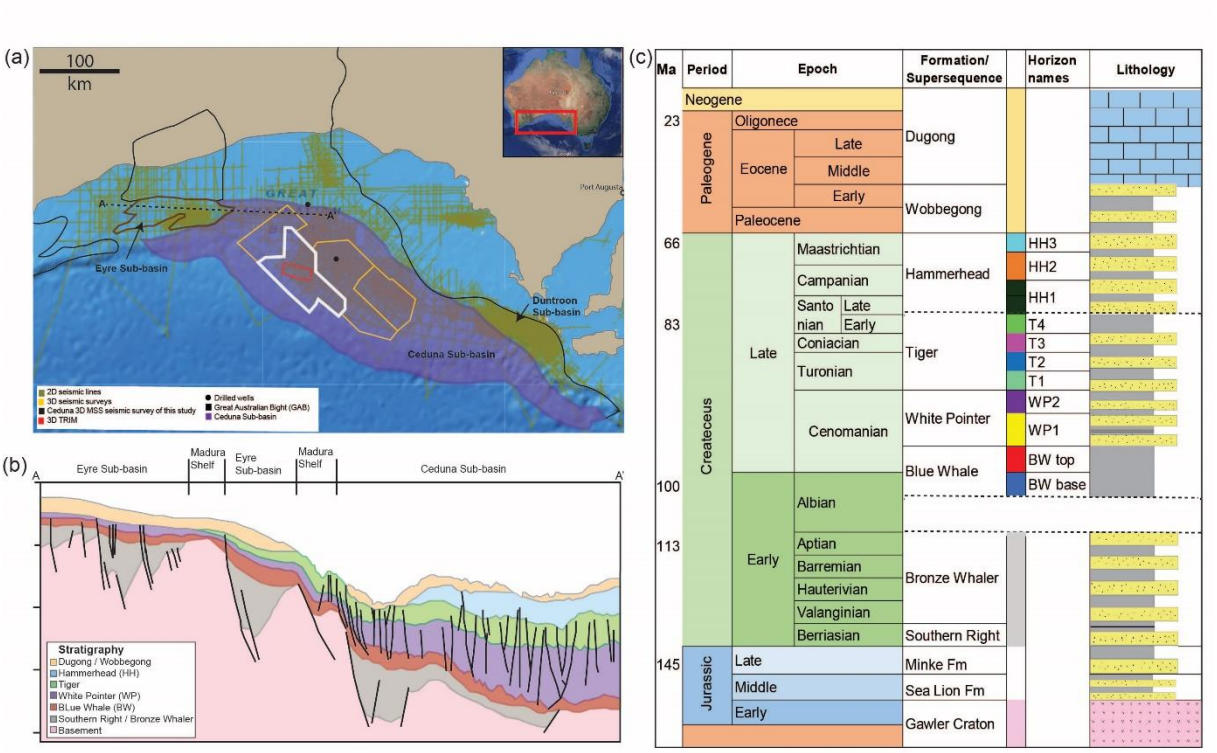

Figure 1: (a) Location map of the Great Australian Bight Basin, seismic survey including the available 2D and 3D seismic surveys in the Ceduna Sub-basin and closest drilled wells. (Modified from NOPIMS in 2022); (b) Cross-section line showing the geological features of the Ceduna Sub-basin in relation to the other sub-basins (Modified from Totterdell and Mitchell, 2009); (c) Stratigraphic column showing source rock intervals and migration periods (Kempton et al, 2019; Totterdell et al, 2008)

The Ceduna Sub-basin (CSB) is characterised by two independent large-scale delta systems: The Cenomanian White Pointer Delta System and the Late Santonian-Maastrichtian Hammerhead Delta System *(Totterdell and Krassay, 2003; Espurt et al., 2009; Robson et al., 2017; Ryan et al., 2017)*. The White Pointer Delta System formed during the Cenomanian when the progradational White Pointer Supersequence rapidly deposited over the BW (Albian Age), forming normal growth faults with northwest-southeast, west northwest-east southeast, and mainly southwest strikes within the delta

top. *(Totterdell and Krassay, 2003; King and Backé, 2010; MacDonald et al., 2010; Ryan et al., 2017)*. In both delta systems, the rapid accumulation of deltaic sediments and subsidence resulted in over pressure of both the BW and Tiger units respectively, which act as detachment layers for overlying listric growth faults *(Espurt et al., 2009; Mitchell et al., 2009).* (Figure 1b)

The Hammerhead Delta System formed in the Late Santonian-Maastrichtian after the passive margin developed following continental breakup between Australia and Antarctica. Deposition of HH1 and HH2 sequences reactivated some of the faults that formed during the Cenomanian and led to the development of normal growth faults at the delta top that totally or partially offset the HH with northwest-southeast strikes and a main dip direction towards the south-west *(MacDonald et al., 2010).* In the study area, which is covered by the Ceduna 3D MSS seismic survey, the Late-Santonian-Maastrichtian faults are only visibly detached over the Tiger detachment layer (T4) in the south and south-east regions close to the location of the igneous intrusion and eruptive centres. In this study we will focus on the delta top (extensional region) of the Ceduna Delta System where the main structure corresponds to normal growth faults detached at the base of the Tiger and BW.

Delta systems commonly (but non-exclusively) form in passive margins over gentle basinwards-dipping surfaces that mimic a wedge-shaped model where a weak detachment enables the gravity-driven slide of sediments towards the centre of the basin (e.g. evaporites or overpressured shale layers) *(Rowan et al., 1999; McClay et al., 2003; Morley et al., 2011)*. In large-scale delta systems, this thin-skinned model links gravity-driven extensional faults in the delta top with a transition region in the middle and Deepwater fold thrust belts (DWFTBs) at the delta toe. Development of these structural features, including listric normal faults and the DWFTB, depends on the rheological properties of the accreting material (e.g. material strength, lithology and pore pressure), changes in thickness, friction coefficient, dip angle and dip direction of the detachment layer *(McClay et al., 2003; Alzaga-Ruiz et al., 2009; Espurt et al., 2009; King and Backé, 2010; MacDonald et al., 2010; Sapin et al., 2012; King and Morley, 2017)*. The overpressured state of the detachment layers responds to compaction of the top of the shale unit, forming an impermeable skin-like surface that prevents dehydration of the layer during the burial process *(Morley et al., 2008).*

Analogue models have shown that shale detachments layers in delta systems will progressively continue to displace basinwards as long as the overpressure condition is maintained. However. dewatering or degassing can reduce pore pressure until it reaches hydrostatic pressure, which immobilizes the shale layer *(Wood, 2012).* Some authors propose that fluid escape pipes can appear as a result of hydraulic fracturing, differential compaction or a combination of these processes *(Holford et al., 2017)*. These processes can release fluids (water and hydrocarbons) from the main overpressured source level *(Morley et al., 2008).* In the Ceduna Sub-basin, *Velayatham et al., (2021)* interpreted three sets of vertical escape pipes that allowed the migration of fluids (gas) from T4 (southeast area) and from HH1 to HH3 through chimneys at the upper tips of polygonal and normal growth faults. They appear as vertical fluid escape chimneys associated with natural seeps or overpressured sources. Using the Ceduna 3D seismic survey, they mapped contrasting high seismic amplitude chimneys in the northeast, southwest, south-centre and south-east regions. Their results suggest that in the northeast region, the chimneys are randomly distributed and associated with polygonal faults, while towards the southern region they appear to be aligned with normal growth faults that have northwest-southeast strikes.

Magmatic history

Previous regional studies have identified igneous intrusions and volcanic cones in the Otway, GAB, Sorell, Bass and Gippsland basins of the Southern Australian Margin using 2D and 3D seismic surveys *(Holford et al., 2012b, 2017; Meeuws et al., 2016; Watson et al., 2019)*. In terms of the GAB, volcanic cones are mainly located at the base of the Dugong Supersequence *(Schofield et al., 2008; Reynolds et al., 2017).* The magmatic activity in the Southern Australian Margin occurred between the Cretaceous and the Paleogene periods and can be related to tectonic events such as cessation of Tasman sea spreading, collision between India and Asia, and accelerated seafloor spreading in the Southern Ocean *(Clarke and Alley, 1992; Schofield and Totterdell, 2008, Holford et al., 2012; Meeuws et al., 2016; Reynolds et al., 2018).* Volcanic activity in the GAB appears to have been structurally and magmatically controlled, with faults substantially affecting both the original migration of fluids and present-day interpretation of interconnected magmatic complexes e.g., the BBIC. The BBIC contains volcanic cones linked to shallow tips of underground dykes and sills *(Schofield et al., 2012; Magee et al., 2013; Reynolds et al., 2018).*

Bight Basin Igneous Complex

The BBIC is interpreted as an extinct northwest-southeast oriented igneous field with a series of volcanic cones, lava flow fields, sills, laccoliths and dykes *(Schofield et al., 2008; Magee et al., 2013b; Reynolds et al., 2018).* Recovered samples from the Eyre Sub-basin show that the volcanoes have a pillowed alkaline basaltic composition with local alterations of silica and carbonates of Late Cretaceous to Paleogene periods *(Clarke and Alley, 1992).*

Extrusive morphologies

Magee et al., (2013b) used 2D seismic data over an area of about 23,370km^2 in the GAB and interpreted 56 mounds and grouped their results into two distinctive morphologies: Group 1 is the most common type which embody a shield-like morphology with slightly rounded cones, sub-angular bases and flanks with dip angles of up to 12°. They are described as (a) direct extrusions without a "lava-channel" feeder during their initial growth stages or (b) layered eruptive centres that resulted from intermittent eruptions of magmatic activity. The eruptive centres also show relatively high seismic velocities (2365-6739 m/s) that contrast with the lower seismic velocities from the host rock layers (an average of 2215 m/s) of the Dugong and Wobbegong Supersequences.

Group 2 represents dome-shaped hydrothermal vents and volcanogenic cones of low seismic amplitude due to the intercalation between igneous and sedimentary layers. They show a general conical geometry and are linked to underlying sills through sub-vertical zones of low seismic amplitude and chaotic seismic reflectors associated with intervals of low seismic velocities (2215 m/s). In general Group 2 shows smaller basal diameters (1.09-1.98 km) than Group 1 (about 1.8 to 19 km) and steeper flanks with dip angles between 7° and 13°.

Reynolds et al., (2017a) interpreted buried lava flows of 0.5 to 34 km in length transported during the middle Eocene Epoch as part of the BBIC. They are associated with volcanoes that vary between 0.3 and 10 km in diameter. They classified the lava flows into two different geometries: (1) Tabular flows that are characterized by continuous reflection of high seismic amplitude. The tabular flows also show a gradual decrease in thickness from the centre to the edges. (2) Dendritic flows which are non-

continuous seismic reflection lobes, pathways and plateaus morphologies that cover longer and wider areas than the tabular flows.

Other extrusions have been mapped onshore in South Australia during the Pleistocene Epoch. These eruptions represent linear features of crustal fissuring, small flows of basaltic lava, and eruptive centres that expelled ash and scoria material. Some examples like Mount Gambier and Mount Schank are dated as being of more recent magmatic activity in the offshore area. Mount Schank shows evidence of two phases of magmatic activity that occurred 4,500 years ago where an older small eruptive centre over a wider, more recent principal cone. It also exhibits a linear fissure that contains smaller eruptive centres forming a northwest-southeast trend at the northwest, some blowholes at the southeast and a lava flow region towards the west *(Government of South Australia, 2001)*

Intrusive morphologies

Reynolds et al., (2017b), defined four different morphologies to describe 39 mapped intrusions in the BBIC using the Nerites 3D seismic survey. Roughly half of the intrusions are (1) saucer-shaped with sub-circular and flat inner saucer geometries in map and cross-sectional views respectively. They show sub-parallel top and base reflectors with a thicker middle section in relation to the lateral tips that were emplaced at depths of 60 and 1200 m below the paleo-seabed. Around 10% of the intrusions that *Reynolds et al., (2017b)* interpreted are (2) compound morphologies with multiple lobes of elongate irregular shapes in map view and either concave upwards and downwards, or planar geometries in cross-section view. They also show flat top and base contacts and are located at depths of between 60 and 1000 m as part of the BBIC. Only a third of the sills are (3) *hybrid* with elongate sinuous lava-like morphologies that formed in shallow depths of around 180-800 m beneath the seabed. They exhibit a thinning upwards geometry and contain multiple elongate or sub-circular lobes. The rest of the intrusions (5%) are considered (4) *laccoliths* with an elongate geometry at the centre and distinct marginal lobes that transgress host rock strata. The laccoliths also show sinuous seismic amplitude along the lobes and were emplaced between 260 and 1200 m below the seabed.

Interpretation of 2D and 3D seismic surveys acquired across the BBIC indicate that around 60% of the lava vents are located directly above the upper tips of sills and laccoliths, while 40% do not seem related to underlying intrusions. Preliminary interpretations proposed that some feeding sources are situated near to faults that can function as upwards transport pathways. The lack of mapped dykes underlying the lava flows could be a consequence of either poor seismic data (e.g. 2D seismic lines) or vertical intrusions with dimensions too small to be detected by the seismic resolution (Holford et al., 2012; Magee et al., 2013a; Reynolds et al., 2017a, 2017b, 2018).

Analogue field sites (e.g., High Cup Nick in UK, Coal-seam Cliff in Antarctica, Midland Valley in Scotland) suggest that unlike laccoliths, intrusions normally exhibit little to no evidence of forced-folds in the underlying host-rock. However, more complex morphologies commonly include upwards stepping in cross-section view, and rounded or elongate lobe geometries in map view *(Breitkreuz and Rocchi, 2018).* In terms of the GAB, the interpreted intrusions within the middle region of the sub-basin exhibit overlying forced-folds that are normally controlled by the geometry of the underlying intrusions and resulted from the pure elastic deformation in the host-rock during magma emplacement *(Pollard and Johnson, 1973; Kumar et al., 2022).* They mostly occur in shallower depths and are thinner than the underlying intrusions as a result of the amplitude characteristics of the folds. This relationship can be

affected by post-intrusion erosion, the burial-related association between the intrusion and forced-folding, variations in strain due to the emplacement depth, and host-rock heterogeneity *(Jackson et al., 2013).* In contrast, magma intrusions in the western Ceduna Sub-basin are not associated with forced-folds, which might may occur as a result of low magma volumes forming small-scale igneous bodies (e.g. intrusions and dykes) in the area *(Schofield and Totterdell, 2008).*

Magma emplacement

Worldwide there are still many questions regarding how magma emplacement occurs in sedimentary sequences where the outcome can range from simple to more complex magma flow networks producing different morphologies such as fissures, eruptive centres, sub-horizontal intrusions, laccoliths and dykes. In general, magma transport occurs outwards and upwards from the source *(Thomson, 2007; Schofield et al., 2012; Breitkreuz and Rocchi, 2018)* forming vertical and lateral igneous bodies where ductile sequences appear to be more suitable candidates to be intruded (e.g. shale sequences, salt, or overpressure sequences). These transport stages also include climbing of intrusions across the sedimentary sequences, sometimes forming forced-folds and fractures in the overburden host-rock. The emplacement and evolution of magma systems can also result in underdeveloped morphologies caused when intrusion ceases and the intrusive body cools to freeze in place during at any of the mentioned stages *(Thomson, 2007).*

Studies has shown that magma emplacement can happened by brittle mechanisms where normal faults can control the morphology and emplacement of intrusions *(Magee et al., 2013a; Breitkreuz and Rocchi, 2018; Mark et al., 2020)* and fractures can appear during the magma cooling stages (Hansen and Cartwright, 2006; Schofield et al., 2014). Pre-existing structural features (e.g. faults and fractures) can provide preferential pathways and influence the transport of magma fluid by rotating or raising sub-horizontal intrusions to steeper dip angles *(Magee et al., 2013a; Mark et al., 2020)*. Typically, intrusion geometries occur parallel to the orientation of the maximum stress and there are several examples where magma have intruded normal fault segments which can result from (1) variations in the fault dip angle, (2) changes in fault rock properties, or (3) rotation of the minimum stress to an orthogonal orientation from the fault plane *(Magee et al., 2013a).* Examples from the Northwest Shelf in Australia indicate that generally saucer-shaped intrusions do not propagate through steep normal faults (40°-50°) *(Mark et al., 2020)*. Laboratory and field studies have also shown that magma emplacement is strongly controlled by the layering and composition of the host rock, where shales have proven to be more favourable sequences as they tend to deform by ductile shear stresses at depth, that sometimes favour the formation of fractures and faults in the tips *(Magee et al., 2013a)*

Magma emplacement can occur most dominantly by non-brittle mechanisms where the magma is transported through ductile sequences such as salt *(Schofield et al., 2014; Magee et al., 2021),* sequences with prominent shale content *(Mark et al., 2020)* and overpressured shale layers *(Thomson, 2007).* In this type of sequence, it is easy for the magma to increase the pore fluid pressure reducing the effective horizontal stress and facilitating the magma transport throughout the layer *(Thomson, 2007)*. For example, studies in areas where magma is shown to have intruded salt layers such as in Brazil, the salt can influence the distribution of magma flow and therefore, the geometry and size of intrusions resulting from the transport of magma along several stratigraphic levels *(Magee et al., 2021)*. Other areas such as the North Atlantic Igneous Province, show that magma predominantly

intruded salt lithologies with high water content such as carnallite. In these lithologies the hot magma is transported by a viscous fluid-to-fluid interaction that displaced and dehydrated the salt *(Schofield et al., 2014).* In addition, a few studies have investigated areas where magma has intruded overpressured shale layers such as the Faeroe-Shetland Basin in the northwest European continental margin. In such cases the pore pressure reduction that normally occurs during the emplacement of magma becomes more dramatic, providing more space for magma to be transported along the layer. This process forms sub-horizontal intrusions and dewatering of the shale layer by hydrothermal contraction until the host rock fractures and the intrusion cools and thickens *(Thomson, 2007).*

Data and methodology

Previous studies have demonstrated that 3D seismic reflection data provides a unique opportunity to characterise and map the distribution and infer the emplacement sequence of igneous intrusions, eruptive centres and lava flows *(Holford et al., 2012; Planke et al., 2017; Reynolds et al., 20107a; 2017b, Magee and Jackson, 2020)*. To map igneous bodies in the study area, we interpreted the Ceduna 3D MSS seismic reflection survey which covers an area of 12,030 km^2 and lies approximately 350 km southeast from Eucla and 380 km southwest from Ceduna in the offshore Great Australian Bight. The Ceduna 3D MSS seismic survey extends vertically down to 9 seconds in two-way-time (TWT) with a spacing between crosslines and inlines of 12.5m. The 16,025 crosslines and 3,400 inlines are oriented 315°N (perpendicular to the main fault's strike) and 45°N respectively *(GAB 3D Survey Final Report, 2012)*. The vertical resolution was estimated to be between 4-8 ms at the sequence where the volcanoes are located and between 8 and 12 ms where the intrusions are emplaced.

Seismic interpretation

Interpretation of faults and horizons

We interpret the Ceduna 3D seismic survey in time (TWT) using Schlumberger Petrel Seismic-to-simulation Software® along the central area of the Ceduna sub-basin and we create a seismic well tie with W00FDW0003, W00FDW0092, W00FDW0023, W00FDW0027 and W00FDW0099 2D seismic survey lines to correlate formation tops interpreted from wireline logs acquired at Potoroo-1 and Gnarlyknots-1A wells (Figure 2a). We interpret eleven horizons that correspond to the four main Supersequence tops: BW, White Pointer WP, Tiger and HH, and seven intra-sequence horizons that correlate to main changes in the seismic amplitude and represent variations in the acoustic sonic (DT) and Gamma-Ray (GR) well logs. From horizon interpretations we generate structural maps of the top of each supersequence and thickness maps of the BW and Tiger detachment layers. (Figure b)

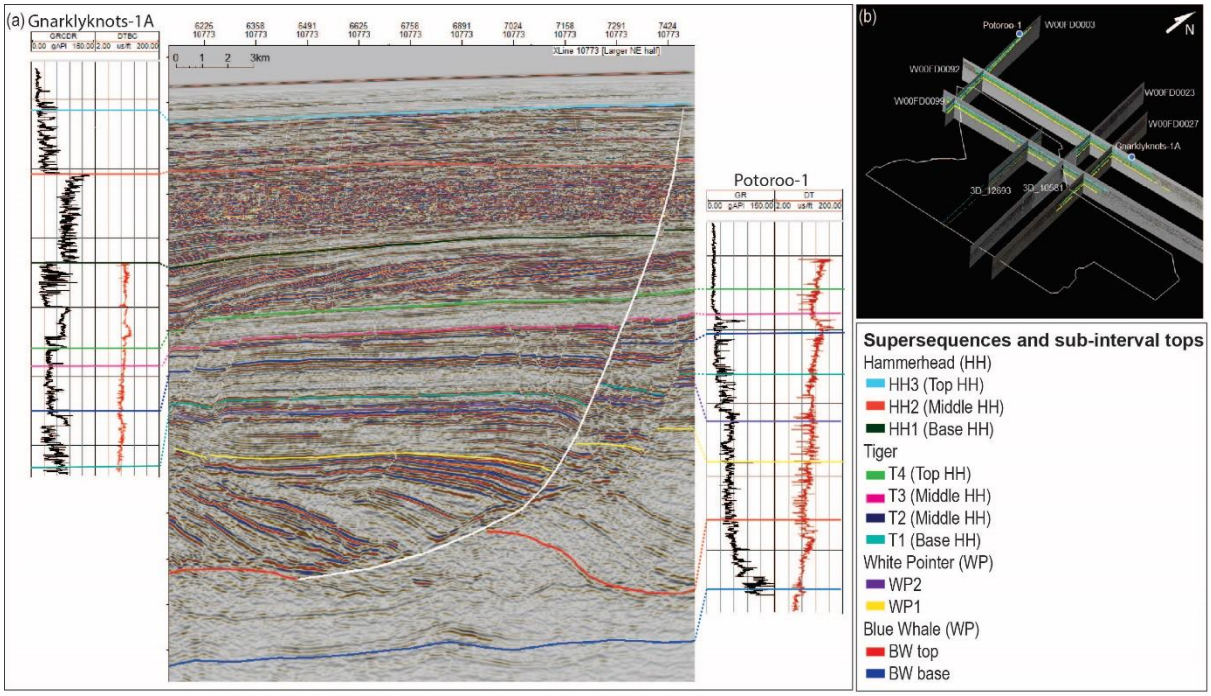

Figure 2: (a) Correlation between steps in Gamma-Ray (GR) and Sonic velocity wireline logs (DT) acquire at Potoroo-1 and Gkarklyknots-1A exploration wells. (b) Major reflectors showing crossline 10773 on the Ceduna 3D MSS seismic survey. The crossline also shows stratigraphic geometries and variations in seismic amplitude

Interpretation of intrusive and extrusive igneous bodies

We interpret the Ceduna 3D seismic survey to identify eruptive centres, lava flows and intrusions within the study area. We identify igneous features in a small region of around 1,141 km^2 to the south of the Ceduna 3D MSS seismic survey. Using as reference preliminary studies of the BBIC, this area is about 32 km southwest from the mounds identified in *Magee et al., (2013)* and 137 km from the Nerites 3D seismic survey that was interpreted in *Reynolds et al., (2017).*

We compare our interpretation with the information from preliminary studies of the BBIC to classify the mapped igneous intrusions (sills) and extrusions (e.g. eruptive centres and lava flows) by morphology and by other characteristics evident in the Ceduna 3D MSS seismic survey *(Magee et al., 2013b; Reynolds et al., 2017a; 2017b)*.

We are aware of certain lithologies within the sedimentary sequence that exhibit similar seismic amplitudes at their boundaries (which co-depend on the adjacent unit) and similar seismic velocities to those of the igneous bodies (in particular, the case of mass transport sediments), which can difficult the recognition of certain horizontal magma emplacements difficult *(Holford et al., 2012; Planke et al., 2017).* The lack of well data and sampling in the study area challenges validation of our interpretation of certain lithologies and true characteristics of the igneous bodies. In addition, we know that seismic data has limitations in terms of a restricted vertical resolution with depth and that can result in difficulties when interpreting small and thin intrusions especially upper and lower terminations of dykes and intrusions *(Magee et al., 2013b; Magee and Jackson, 2020; Phillips et al., 2018).*

Eruptive centres and lava flows

We interpret the top of the principal and minor eruptive centres and lava flows that exhibit a high seismic amplitude in contrast to the surrounding host-rock and represent a seismic peak event ("hard" layer) at the top boundary (representing a step up in acoustic impedance – normal/American polarity). The principal eruptive centres are represented by features with a steepened section of a seismic horizon that co-occurs with an underlying seismic velocity pull-up (timing) distortion and poor signal-noise ratio for reflection events associated with the underlying host-rock, especially towards their centre (Eide et al., 2018). These interpreted extrusions show a discontinuous to semi-continuous character at the Wobbegong Supersequence that is truncated against the Wobbegong and Dugong supersequences *(Reynolds et al., 2017)*. Similarly, lava flows are represented by horizontal to sub-horizontal high boundary amplitude regions around principal eruptive centres. They exhibit strong reflector coherence in comparison to the principal eruptive centres that are also highly reflective that reduce the signal-noise ratio in underlining host-rock *(Eide et al., 2018)*. We classify minor cone morphologies inside the lava flow region as minor eruptive centres, which show smaller diameter and height than the principal eruptive centres.

Magma intrusions

Intrusions are interpreted to have discontinuous (poor coherence) seismic reflectors that represent abrupt reflector terminations. They exhibit horizontal to sub-horizontal geometry or cross-cut upwards through the hosting sedimentary sequence. They also exhibit high boundary reflector amplitudes in comparison to the host rock and top boundaries that represent seismic peak events *(Thomson, 2007; Jackson et al., 2013; Reynolds et al., 2017).* To avoid predefined interpretations from earlier studies in the area, we use the word "intrusions" to refer to sills and sub-horizontal magmatic sheets.

Interpretation of the magma system in the Ceduna 3D seismic survey area

Schofield and Totterdell, (2008) suggest that many volcanoes and lava flows in the GAB are not always related to underlying intrusions. To understand how the magma transport occurred and identify potential relationships between the different igneous bodies in the study area, we create polygons around each sub-horizontal intrusion to identify potential vertical juxtaposition between the intrusions, lava flow regions and eruptive centres. We also use apply a *Automatic Gain Control (AGC)* and generate a variance seismic attribute which was projected in time slices underneath all intrusions and eruptive centres (every 4 ms) to define potential dykes or fissures that could be connected with the mapped igneous bodies. We also generate maximum amplitude surfaces at each intrusion to outline likely magma flow directions from relative amplitude variations and potential assembly of intrusive systems in map view *(Magee et al., 2015).* In addition, to study a potential link between magma transport and the normal growth faults, we generate maximum amplitude and RMS seismic attributes along the fault segments that are located closer to the intrusions (Jackson et al., 2013)

Previous studies suggested that the intrusions and extrusions feed from point sources. For instance, compound intrusions are likely to link at least two different magma sources while saucer-shaped intrusions are expected to have been feed from a single point located at the base of the saucer *(Hansen and Cartwright, 2006)*. Similarly, hybrid intrusions are likely to have been fed by a deeper

hybrid sill complex located at the centre. These source points can be connected to magma conduits (e.g. dykes or other intrusions) which tend to climb away from the magma source such as dykes forming complex magma systems *(Thomson and Hutton, 2004)*. In this paper we will refer as source point to the deeper region of the mapped intrusion from which it might be released outwards and upwards.

Statistical alignment for source points and volcanic cones

To define a potential association between the igneous extrusive and intrusive bodies with the normal growth faults, we use the Continuous Sector Method proposed by *Hammer, (2009)* to detect straight-linear point alignments. This method statistically assesses orientations (azimuths) from the central point to each geological feature (e.g. volcanic cones and source points). The method also includes a radius ('R') that represents the closest boundary around each point and a p-value that indicates the result of the Rayleigh test which quantifies the randomness of spatial distribution. This statistical alignment method measures the orientation from a reference point to other points contained in "R" to statistically define all the potential crossing alignments. In this study we used Intrusion 9 as the reference points as it is placed outside the lava flow perimeters to the east, and the furthers most volcanic cone underlying Volcano B towards the east-southeast boundary of the lava flow region.

For the alignment analysis of the volcanic cones, we use three 'R' values that represent the minimum (0.4 km), intermediate (3 km) and a maximum (5 km) distances between the volcanic cones. As p-value we use a standard value of 0.1 that indicates linear orientations that do not occur randomly. For the intrusion source points, we adopt as input the source points where we measure the minimum (1 km), middle (6 km) and maximum (14.5 km) distance between each point as R values. Here, we use a p-value of 0.5 from the point alignment analysis of the volcanic cones, which agrees with the 0 to 0.5 interval suggested in *Hammer, (2009)* as acceptable for the Continuous Sector Method. It is important to mention that this statistical method is sensitive to the number of points in the study and the maximum distances between each point (Hammer, 2009). For instance, our study included a small number of source points which might reduce the number of statistical iterations.

Results

Interpretation of extrusive features

We interpret the top of the two principal eruptive centres (Volcano A and B) which extends over areas of 0.52 km^2 and 0.36 km^2 and are surrounded by a lava flow region of 24.3 km^2 and 44.6 km^2, respectively (Figure 3a). The lava flows are situated at the base of the Wobbegong Supersequence, while the minor eruptive centres extend from the base to the top of the Wobbegong Supersequence. The floors of the principal eruptive centres spread from the base Wobbegong Supersequence up to the Dugong Supersequence and the eruptive centres themselves attain heights above the present-day seabed in the central region (Figure 3 b and c and Figure 4)

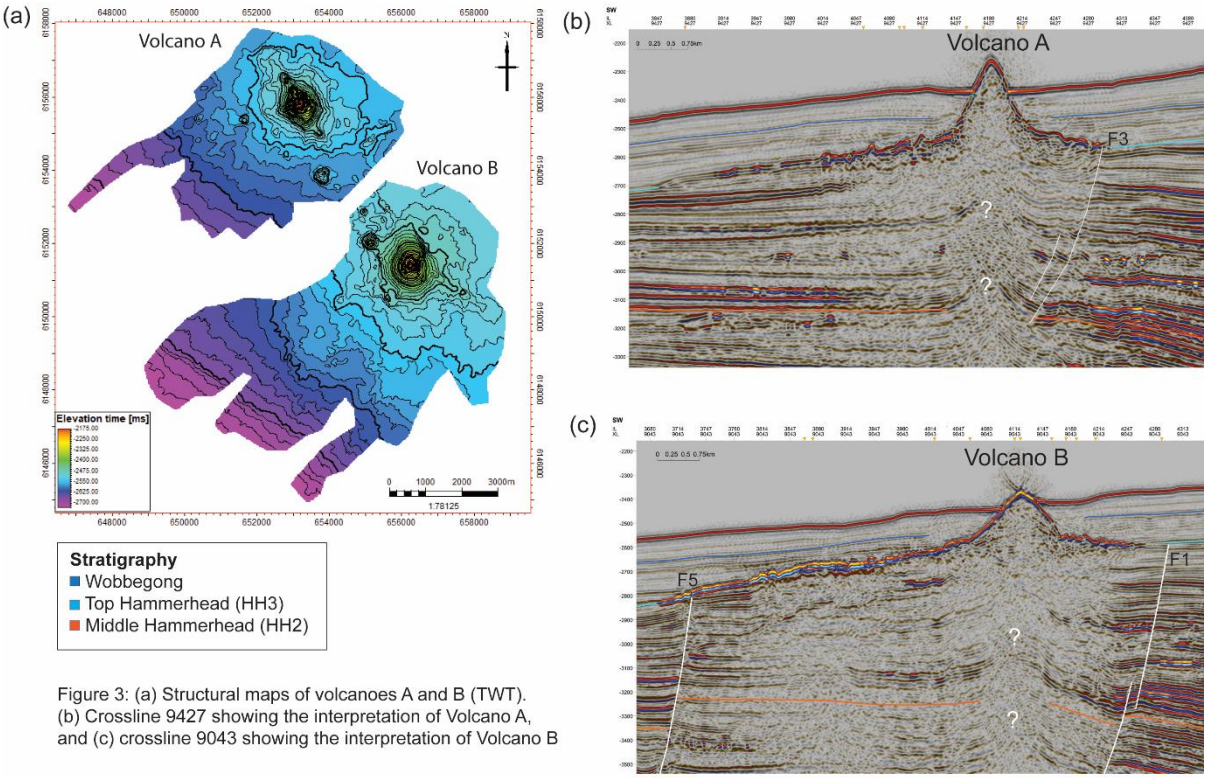

Figure 3: (a) Structural maps of volcanoes A and B (TWT). (b) Crossline 9427 showing the interpretation of Volcano A, and (c) crossline 9043 showing the interpretation of Volcano B

Volcano A includes the eruptive centre A and the surrounding lava flow region. The eruptive centre has a thickness of between 124 and 440 ms and a central height of 2152 ms, with the peak standing above the sea floor at its highest point. The principal eruptive centre exhibits a sub-circular base with slightly sub-angular corners at the southern and northern boundaries (Figure 3a). It shows steep flanks with apparent inclination between 53° and 80° (TWT) (about 20° to 35° in true depth). The lava flow extends with a preferential pathway towards the southwest and south along the base of the Wobbegong Supersequence with minimal changes in seismic amplitude of the top boundary from the central region of the eruptive centre to the lava flow edges. This amplitude is much higher than other reflectors associated with host rock boundaries; eruptive centre A and the lava flow show top boundary amplitudes 780% greater than others associated with the Wobbegong and Dugong supersequences (Figure 3b). Along the lava region we interpret 17 minor eruptive centres that are spread towards the northwest (4), southwest (7) and southeast (3) from the principal eruptive centres. We could not identify reveal dykes or potential fissures underlying Volcano A using seismic attributes that may have suggested a direct feeding source (Figure 3a).

Volcano B contains the eruptive centre B and a surrounding lava flow region. The eruptive centre exhibits a thickness of between 129 and 414 ms that goes from the base of the Wobbegong up to 2207 ms above the present-day seabed. Its flanks display dips of between 40° and 68° (TWT) (18° and 31° in depth) (Figure 3c). Eruptive centre B exhibits a circular to sub-circular geometry with a truncated boundary at the northeast. The lava flow spreads outwards and elongates towards the southwest and south (Figure 3a), showing continuous seismic amplitudes towards the edges 301% greater than the

host-rock (Figure 3c). We map 26 minor eruptive centres cones along the lava flow area that are distributed between the northwest (9), South (5), southwest (1) and southeast (8). Most of the minor eruptive centres are distributed along the lava flow region in Volcano B, except for the minor eruptive centres in the southeast area where they form a visible linear feature with a northwest-southeast orientation (Figure 3c and figure 4).

Additionally, the southwest boundary of the lava flow above two Tiger-HH faults (F8 and F5) do not show any offset of the lava between the footwall and hanging wall sections, but rather a pre-formed step in the topography after nucleation of the faults. The maximum amplitude and seismic attributes from the fault segments do not show any evidence of dykes or intruded magma along the fault planes (Figure 3c)

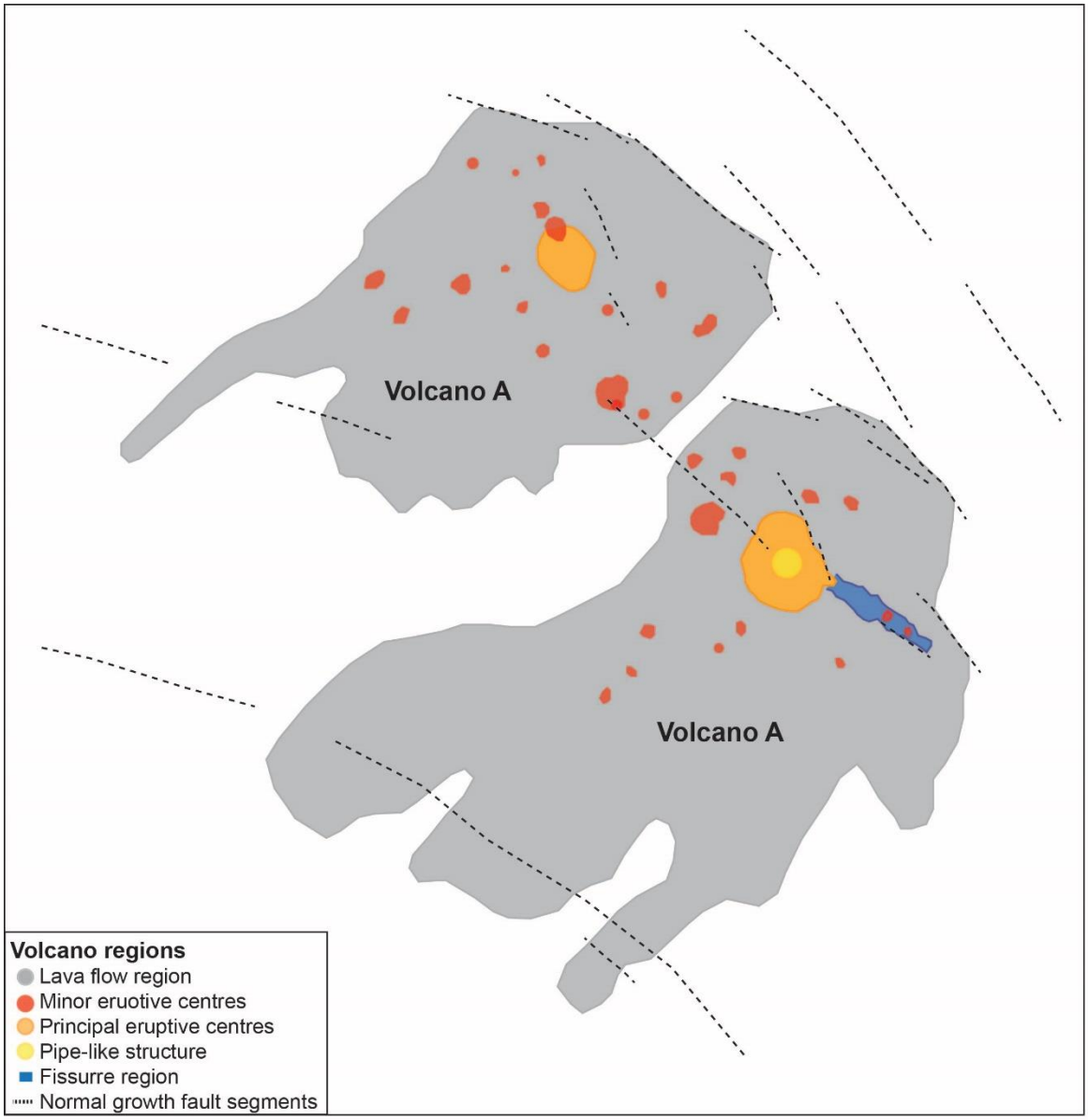

Figure 4: Diagram representing the differet sections in volcanoes A and B including lava flow regions, minor eruptive centres, principal eruptive centres, a pipe-like struture underneath the principal eruptive centre B, and a fissure region.

We interpret seismic time slices surfaces every 4ms, we map a coherent anomaly in the data that potentially can have geological causes such as the presence of a pipe-like geometry underlying volcano B. This pipe-like structure vertically extends between the lower and middle units of the HH (4660 ms to 3680 ms) and it is located exactly below the main eruptive centre B and displays an irregular width that laterally oscillates between 109 and 792 m. In the variance and *Automatic Gain Control (AGC)* seismic attributes in a time slide surfaces, the pipe-like geometry displays a circular to sub-circular geometry that laterally switches position inside a diameter of 0.66 km in map view. The high P-wave velocity and seismic amplitude proximal to the principal eruptive centre makes the interpretation of the pipe-like structure difficult closer to the surface (Figure 5).

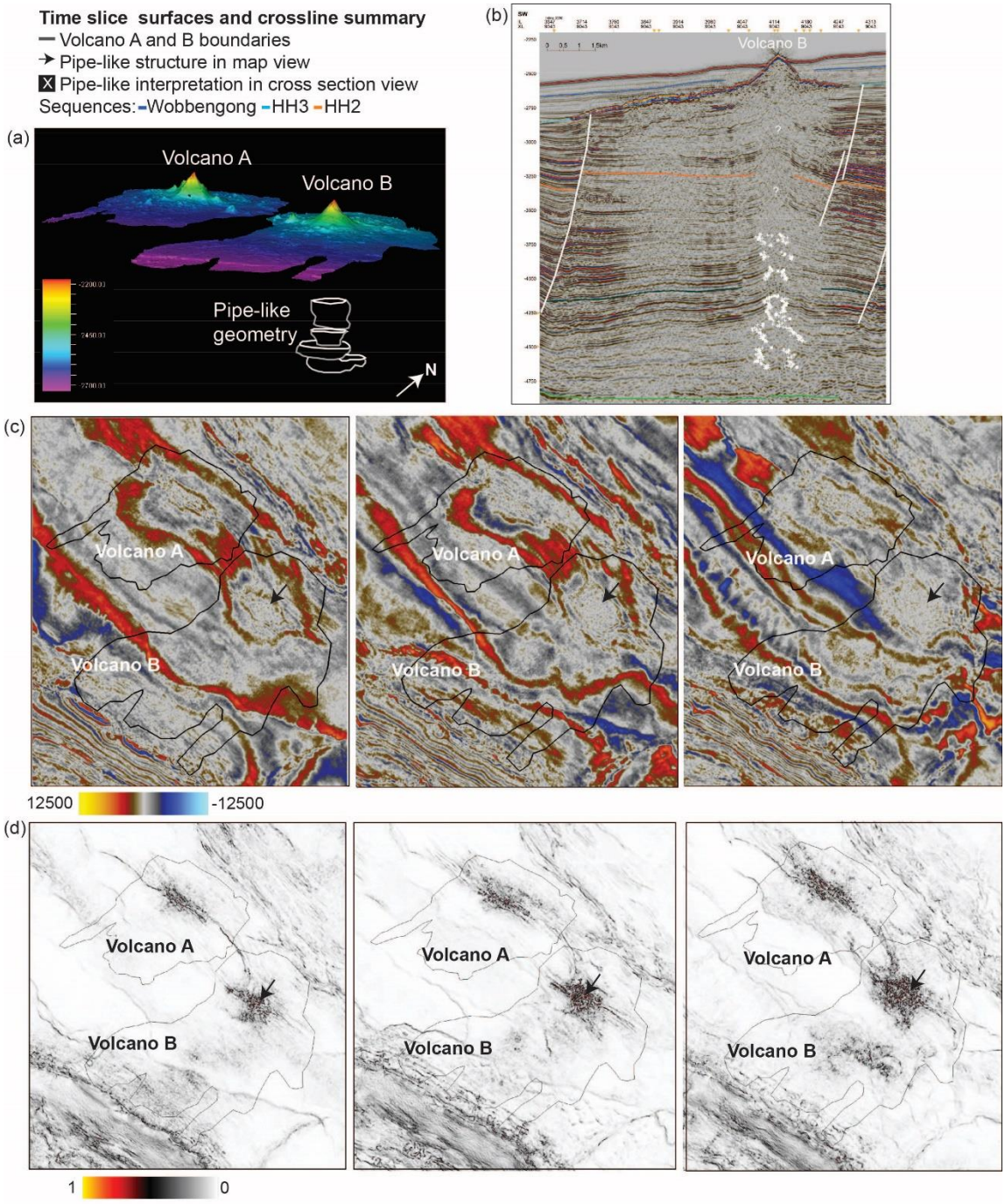

Figure 5: Interpretation of the pipe-like structure underlying Volcano B in (a) 3D map view (b) Crossline 9043 (c) Automatic Gain Control (AGC) seismic attribute over the time-slice surfaces -4204 ms, -4256 ms and -4304 ms (left to right), and (d) Variance seismic attribute over the time-slides surfaces -4204 ms, -4256 ms and -4304 ms (left to right).

Interpretation of intrusions

Intrusions with compound morphology

Intrusions 1, 7, 10 and 13 are located in the HH3 sequence, while Intrusion 4 is situated at the upper section of HH2 (Figure 6a). According to *Reynolds et al., (2017b)* these intrusions are normally elongate with irregular boundaries in map view and concave upwards and concave downwards shapes. In the study area, these intrusions exhibit an irregular geometry and of sub-horizontal to concave shapes. In map view intrusions 1, 4, 7, and 13 are located underneath the lava flow region of volcanos A and B, while intrusion 10 is located between the centre and southern areas of the lava flow region of Volcano B (Figure 6a).

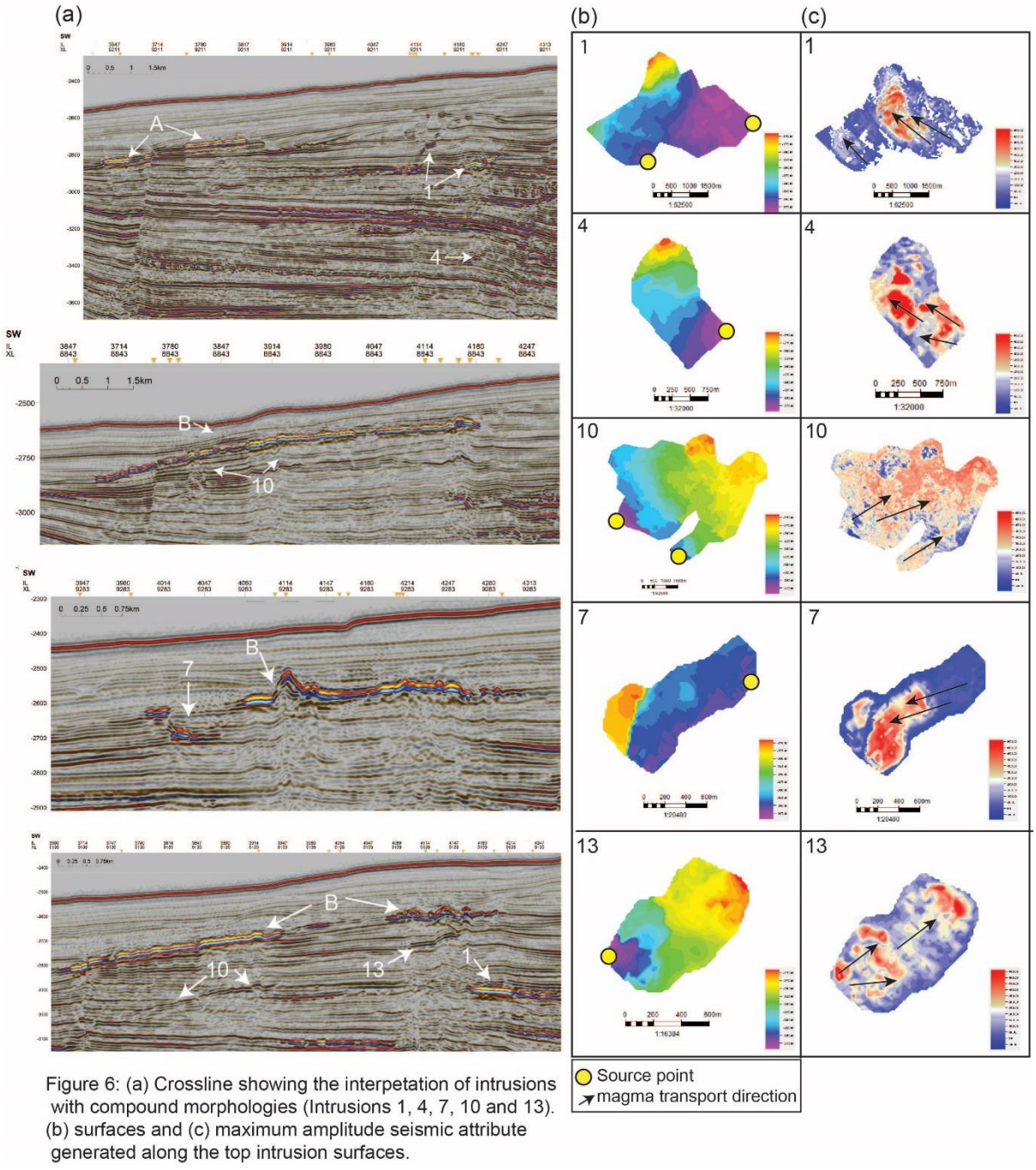

Figure 6: (a) Crossline showing the interpetation of intrusions with compound morphologies (Intrusions 1, 4, 7, 10 and 13). (b) surfaces and (c) maximum amplitude seismic attribute generated along the top intrusion surfaces.

Intrusion 1 is located in the northern corner of the study area between Volcano A and B and underlying their east and northwest lava flows respectively and it is situated between 2920 ms and 2700 ms TWT (Figure 6a). In cross-section, we identify concave upwards to sub-horizontal shapes that cross the host rock towards the northwest in the crosslines. From the maximum amplitude surface and structural maps, we interpret two source points at the eastern and southern edges and a potential magma transport direction towards the northwest. The maximum amplitude seismic attribute displays a series of lobes that seems to be transported laterally from the sources (Figure 6b and c). Intrusion 1 covers a total area of 6.3 km^2 without evidence of a forced-fold overlying the intrusion and exhibits a top boundary seismic reflector amplitude 2070% higher than the host-rock (Figure 6a).

Intrusion 4 is the deepest intrusion of these compound morphologies between 2444 ms and 3296ms, underlying Intrusion 1 at HH2 (Figure 6a). It exhibits sub-horizontal to concave upwards geometries and a top boundary seismic reflector amplitude 230% higher than others associated with the host-rock. From the structural and amplitude maps, we interpret a source point in the southeast and a magma flow direction towards the northwest and north (Figure 6b sand c). In map view the maximum amplitude seismic attribute shows a tabular geometry formed by a series of lobes that extend laterally. In cross-sectional view, Intrusion 4 breaks upwards through the sedimentary record towards the northeast in the crosslines. It also covers an area of 0.94 km^2 without indication of forced-folding in overlying strata (Figure 6a).

Intrusion 7 is located 1.3 km southwest from Intrusion 1 and 1.5 km northwest from Intrusion 3. It reaches HH3 about 0.88 km southeast boundary of Volcano A lava flow covering an area between 0.21 and 0.25 km^2 (Figure 6a). This intrusion has a total area of 0.87 km^2 with a concave upwards and downwards geometry. Its maximum depth is 2700 ms in the northeast directly under the Volcano A lava flow region. It also exhibits a top boundary seismic reflector amplitude 1120% higher with others associated with the surrounding host-rock without evidence of overlying forced-folds (Figure 6a). The maximum amplitude map confirms this lava flow direction towards the southwest that is correlated with the top-most section of Intrusion 7 forming a distinctive upwards step. It also exhibits evidence of lobes stacking laterally in map view (Figure 6 b and c).

Intrusion 10 is located 6 km towards the south of Intrusion 1 and below the lava flow region in volcano B. it covers an area of 22.2 km^2 and it is situated between 2990 ms and 2740 ms. In cross-sectional view, it shows concave upwards and concave downwards geometries that transect the host rock strata towards the northeast. Intrusion 10 shows high top boundary seismic reflector amplitude 220% higher than others associated with the host rock without evidence of forced folds above (Figure 6a). The maximum amplitude surface and structural maps suggest a magma flow direction towards the northeast from two source points in the southwest and south areas (Figure 6b and c).

Intrusion 13 is placed below four minor volcanic cones at the northwest boundary of Volcano B lava flow and above the southern area of Intrusion 1. Vertically, it is placed between 2792 ms and 2652 ms and the top boundary seismic reflector amplitude is 500% higher than others associated with the host rock. Intrusion 13 exhibits a concave downwards and upwards geometry (upwards step). that crosses through the host rock towards the northeast in the crosslines (Figure 6a). From the structural and maximum amplitude maps we interpret a source point in the southwest and a series of lobe geometries that were transported towards the northeast. Intrusion 13 has a total area of 0.87 km^2 without evidence for forced folding of strata overlying the intrusion (Figure 6b and c).

Intrusions with saucer-shaped morphologies

Intrusions 5, 6, 8, 9, 12 were emplaced between the upper and middle Hammerhead intervals (HH3 and HH2) up to the upper Tiger unit (T4). In general, they exhibit a more homogenous shape than the compound intrusions with sub-circular geometry in map view and a bowl-like shape in cross-sectional view *(Reynolds et al., 2017b; Schmiedel et al., 2019)*. The central region of the intrusions is sub-horizontal and exhibits a concave upwards shape at the lateral boundaries. Intrusions 5 and 12 are located underneath the northwest and east-southeast regions of the lava flow of Volcano B, while intrusions 9, 6 and 8 are isolated magmatic bodies outside the perimeter of the igneous volcanoes.

Intrusion 5 is located 2.3 km southeast from Intrusion 1, between 2972ms and 2924ms at HH2 (Figure 7a). It is situated 0.40 km southwest of the F2 fault segment, which exhibits a northwest-southeast strike and a length along strike of 1.2 km. The fault extends vertically between 144 and 292 ms within the HH2 interval with a dip angle >80° and does not seem to offset the intrusion (Figure 7a and b). It exhibits top boundary seismic reflector amplitudes 1000% higher than others associated with the host rock, a flat central region and a pronounced, steep boundary towards the northwest. From the maximum amplitude surface and structural map (Figure 7b and c), we defined a source point at the western edge of the intrusion and a possible sub-radial flow direction towards the northwest and southeast regions. Intrusion 5 exhibits a total area of 0.74 km^2 without evidences of forced folding in the upper host rock sequences.

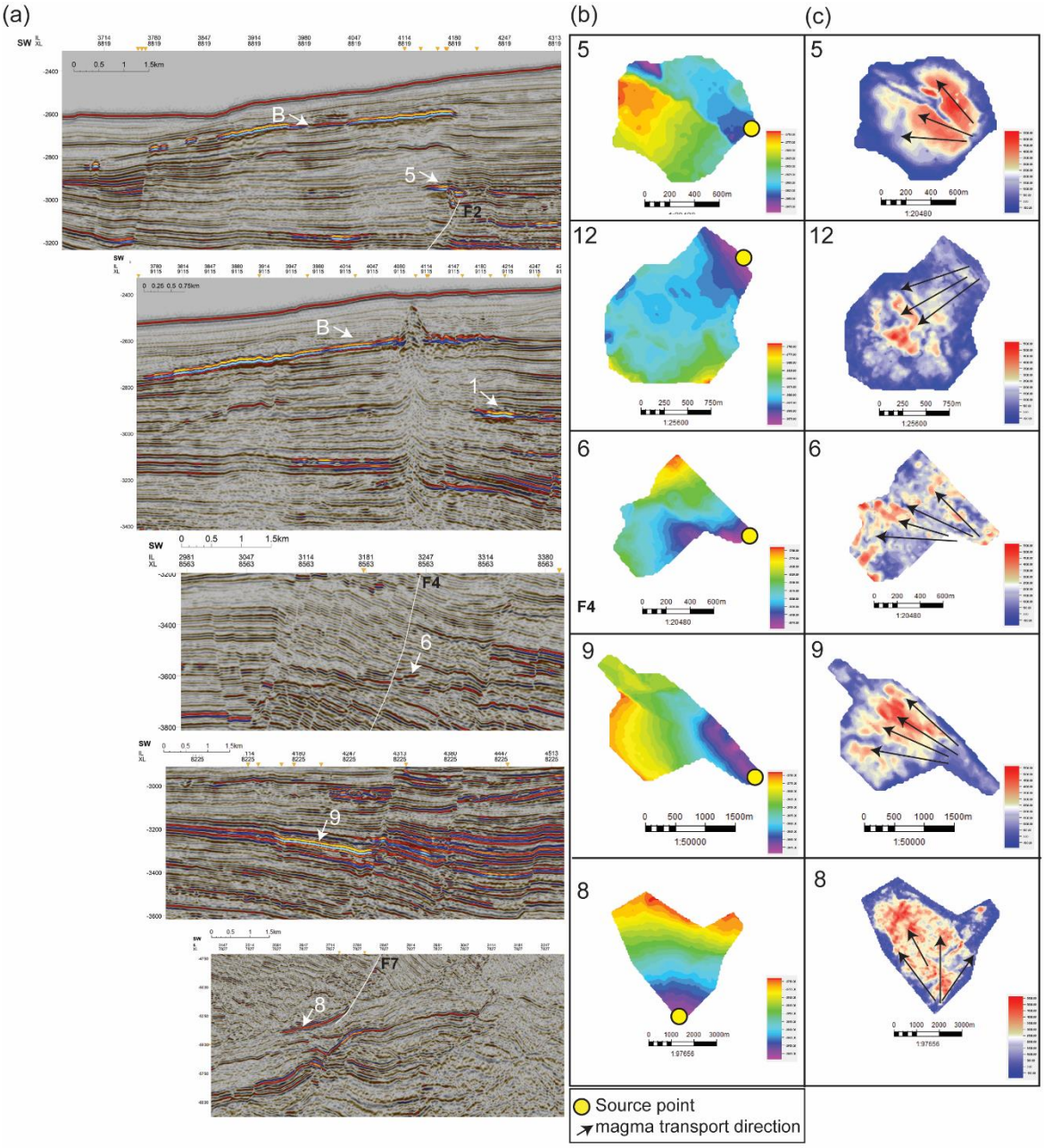

Figure 7: (a) Crossline showing the interpretation of intrusions with Sourcer-shaped morphologies (Intrusions 5, 6, 8, 9, 12). (b) structural maps and (c) maximum amplitude seismic attribute generated along the top intrusion surfaces.

Intrusion 6 is an isolated intrusion situated 8.7 km south of the Volcano B lava flow boundary and 13.8 km from Intrusion 5, between TWTs of 3648 ms and 3580 ms within the middle section of the HH2 sequence (Figure 7a). It shows a top boundary seismic reflector amplitude is400% higher than the host-rock over a total area of 0.65 km^2. It also exhibits a sub-horizontal geometry with lateral concave upwards tips towards the northern and southern edges (Figure 7a). The maximum amplitude surface and structural maps show a potential source point in the west and a sub-radial flow direction towards the north, southwest and south (Figure 7b and c). Intrusion 6 crosses through the normal growth fault F4 from the footwall to hanging wall side following a northeast-southwest pathway and without forced folding in the overlying strata (Figure 7a). This fault has a dip angle of 75° (TWT) at the depth of Intrusion 6 and offsets at the Tiger-HH interval.

Intrusion 8 is located 9.5 km south-southeast from Intrusion 6 and 18.2 km south from the southern lava flow boundary of Volcano B. It sits between 5580 ms and 5556 ms (between T3 and HH1) with a top boundary seismic reflector amplitude 900% greater than the surrounding host rock (Figure 7a). The seismic crosslines and the maximum amplitude surface along the fault planes show that it rests above the base tip of faults F6 and F7, which detach at the upper Tiger detachment over a total area of 16.6 km^2. It shows changes in dip angle between the 10° and 20° that characterise dip angles of the faults at this depth. It also shows a slightly concave upwards and downwards shape away from the bottom tip of the faults in crossline view and a sub-circular geometry in map view (Figure 7a). The structural map and the maximum amplitude surface suggest that the source point is located at the southern edge of the intrusion and fed a sub-radial magma flow in the upper section of the fault towards the north, northwest and northeast regions (Figure 7b and c).

Intrusion 9 is an isolated intrusion 4.8 km east-southeast from Intrusion 5 and outside the volcanic lava flows of volcanos A and B. In map view it exhibits a sub-circular shape and in cross-sectional view a flat geometry in the centre with concave upwards lateral tips. The intrusion exhibits very high to high amplitudes only 70% higher than the massive transport deposits surrounding the intrusion. Intrusion 9 is located at TWTs of 3348 ms and 3228 ms, slightly above the top of HH2 (Figure 7a), and covers an area of 5.2 km^2. We interpret a source point at the western boundary of Intrusion 9 from the maximum amplitude surface and structural maps, with a sub-radial to linear direction of magma flow towards the northwest and southwest (Figure 7b and c). There is not evidences of forced-folds above this intrusion.

Intrusion 12 is located between depths of 3260 ms and 3176 ms, halfway from intrusion 1 at the top and intrusion 4 at the bottom at the bottom of HH3. It exhibits a sub-horizontal shape at the centre but is concave upwards and downwards towards the southwest and northeast in cross-section respectively and has a sub-circular geometry in map view. Intrusion 12 shows a top boundary seismic reflector amplitude that is 210% higher than the host rock, which moderately contrasts with those of surrounding massive transport deposits (Figure 7a). We infer from the maximum amplitude surface and the structural map that the source point is situated at the north-eastern edge of the intrusion with sub-radial magma flow direction towards the southwest, south and southeast regions (Figure 7band c). It has not produced forced fold geometries in the host rock across its total area of 1.9 km^2 (Figure 7a).

Interpretation of normal growth faults

Through general seismic interpretation we map more than 520 normal growth faults using the Ceduna 3D MSS seismic survey. In this paper we focus on 23 segments inside the study area that show strikes towards the northwest-southeast, west-east and northeast-southwest. They extend between 0.5 and 9km along strike and offset the sedimentary record between the Tiger and HH, WP and HH, and WP and Tiger. We use 7 of the closest normal growth fault segments that are in direct contact with magma bodies. For instance, at Volcano A we interpret F3 as the closest fault segment to the northeast boundary of the lava flow region (Figure 3b). At Volcano B, normal growth faults F1 and F5 mark the northeast and southwest boundaries of the lava flow region respectively. In this case F5 forms a step in the lava flow region without showing evidence of fault offset (Figure 3c). In terms of the intrusions, F2 is located 0.4 km southwest of Intrusion 5, F4 passes through the middle of Intrusion 6 without evidence of fault offset, and F6 and F7 are located at the northeast tip of Intrusion 8 (Figure 7a). To

demonstrate possible magma transport along these normal growth fault segments, we generated maximum amplitude and RMS seismic attributes projected along the fault planes (Figure 8). However, our results do not show evidence of magma transport but display lateral variations in seismic amplitude that correspond to the same depth of the massive transport sediments (HH2) (Figure 8a-e). Only F7 and F6 show evidence of magma in contact with the fault planes along the base which agrees with the area where Intrusion 8 becomes steeper (Figure 7a and Figure 8e).

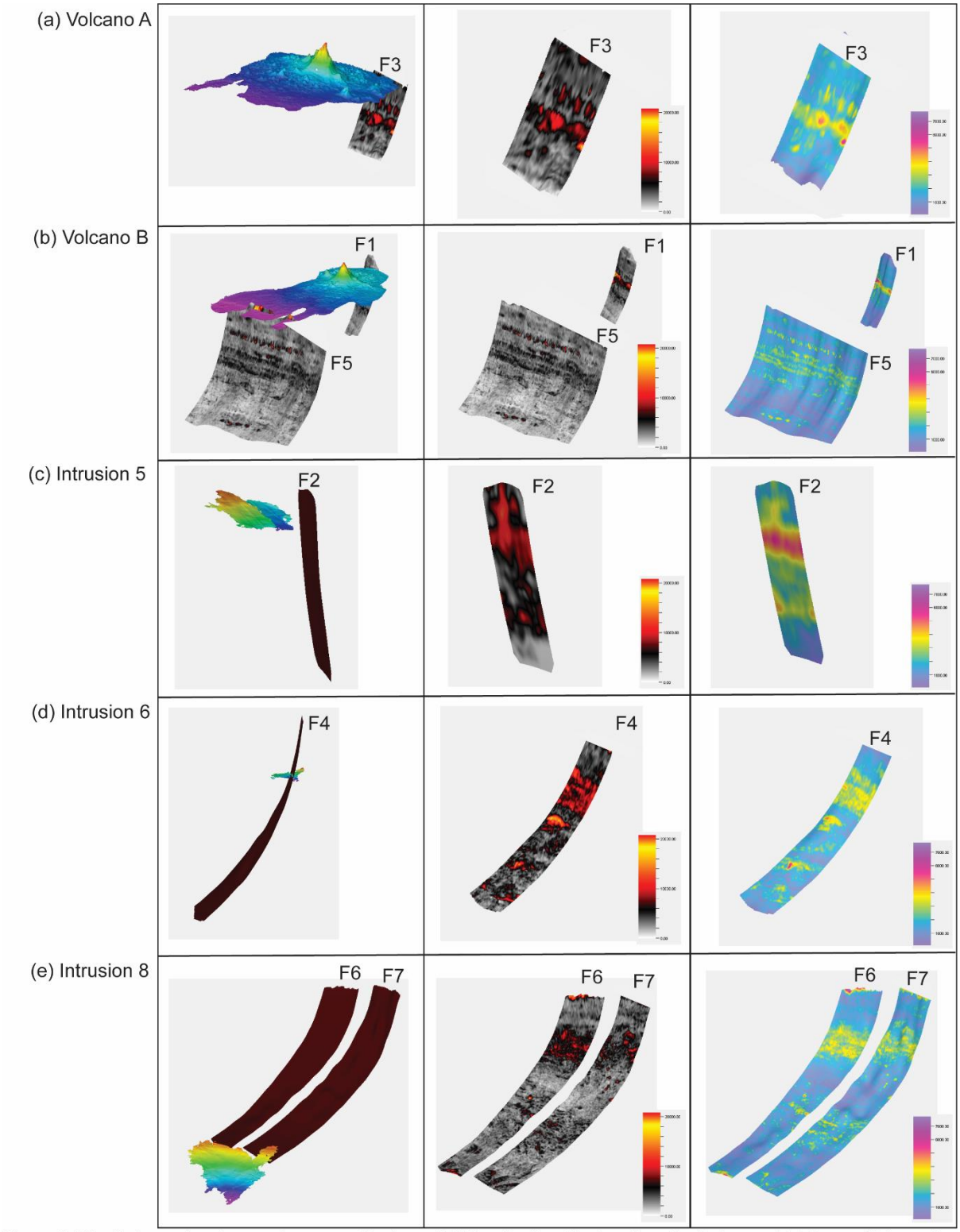

Figure 8: 3D windows showing maximum amplitude and RMS seismic atributes along fault planes. (a) F3 near Volcano A, (b) F1 and F5 near volcano B, (c) F2 near Intrusion 5, (d) F4 near Intrusion 6, and (e) F6 and F7 near Intrusion 8.

Statistical alignment analysis

Eruptive centres

From the structural maps we interpreted two principal eruptive centres, A and B, and a total of 38 smaller eruptive cones across the lava flow region. We find a qualitative correlation between some of the cones and the fault segments with northwest-southeast strikes. To prove this linear correlation, we use the Continuous Sector Method to quantify the degree of alignment between the cones *(Hammer, 2009)*. Our results show that with the minimum 'R' (0.4 km) produces the best fit alignment with an orientation of 145°N while the intermediate 'R' (3 km) shows the best fit alignment between 131°N to 134°N. The maximum 'R' (5.0 km) did not show any alignment results.

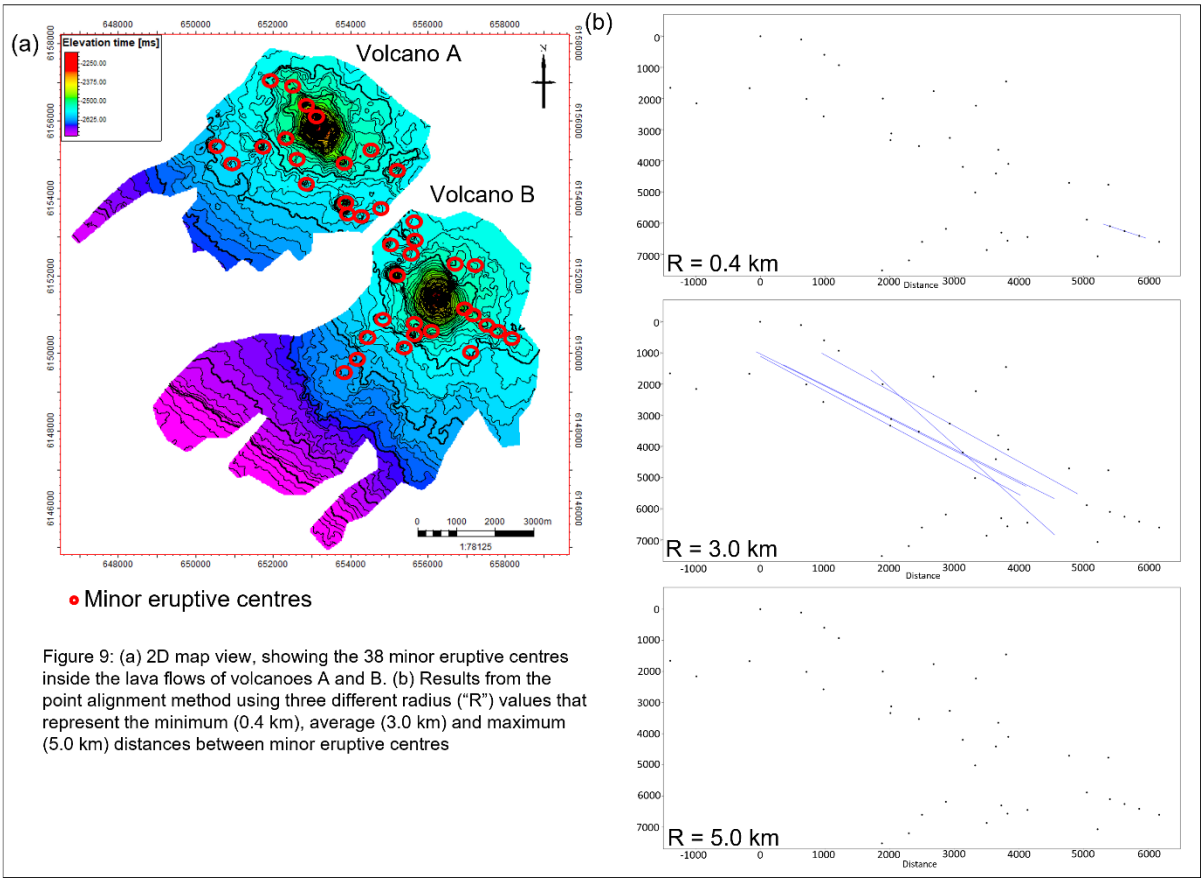

Figure 9: (a) 2D map view, showing the 38 minor eruptive centres inside the lava flows of volcanoes A and B. (b) Results from the point alignment method using three different radius ("R") values that represent the minimum (0.4 km), average (3.0 km) and maximum (5.0 km) distances between minor eruptive centres

Source points

We compare the source points at each intrusion to identify potential linear trends using the Continuous Sector Method, the same as was used for the volcanic cones. In this case, we identify a single alignment at 155°N with a minimum 'R' (1 km) azimuth. The method does not show any results with the intermediate or maximum 'R' (6 and 14.5 km) that we calculated from the distances between the source points in map view (Figure 10). The rose diagram shows a correlation between the statistical alignment of source points and the fault with northwest-southeast strike (Figure 11).

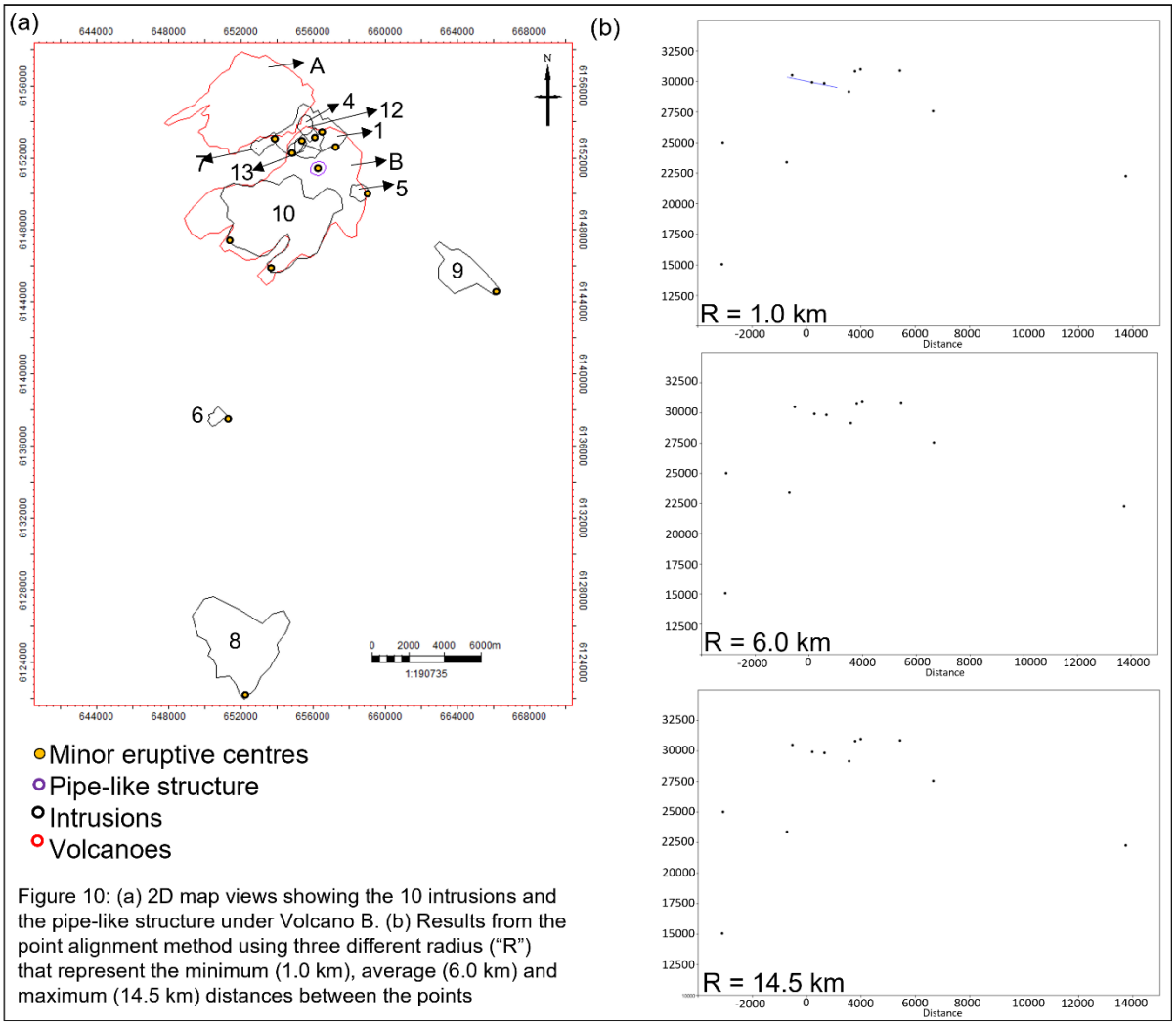

Figure 10: (a) 2D map views showing the 10 intrusions and the pipe-like structure under Volcano B. (b) Results from the point alignment method using three different radius ("R") that represent the minimum (1.0 km), average (6.0 km) and maximum (14.5 km) distances between the points

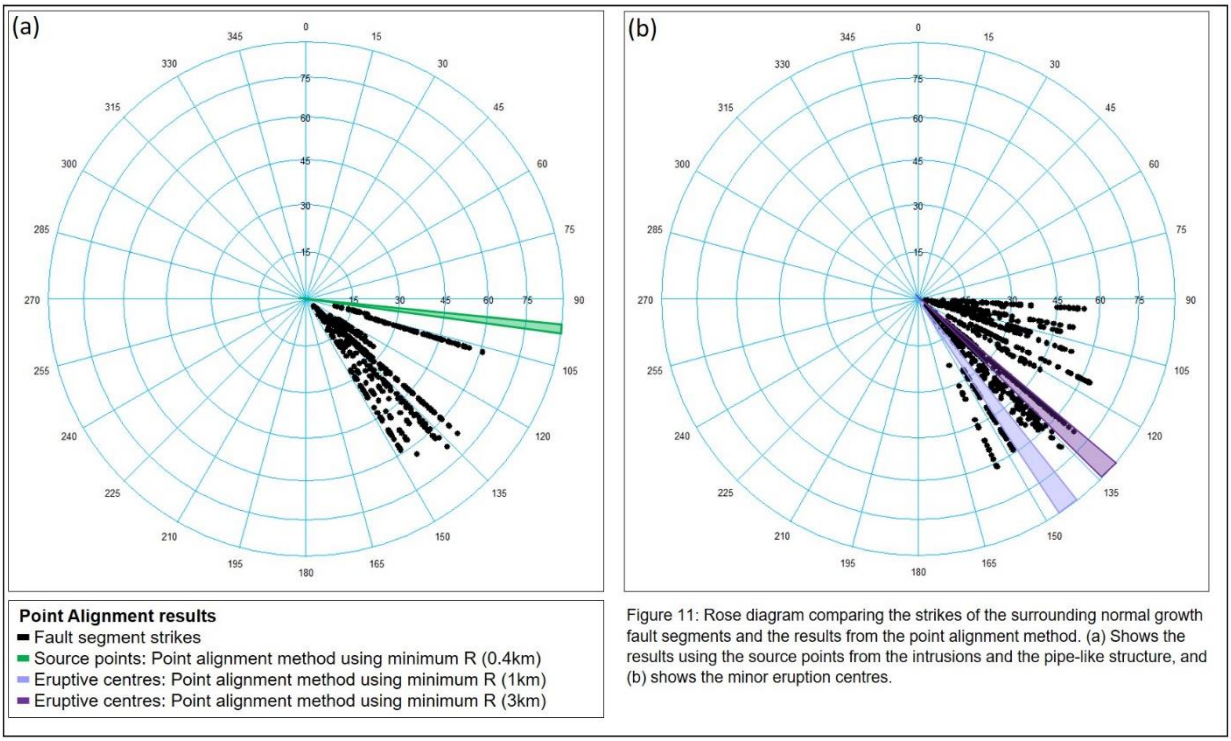

Figure 11: Rose diagram comparing the strikes of the surrounding normal growth fault segments and the results from the point alignment method. (a) Shows the results using the source points from the intrusions and the pipe-like structure, and (b) shows the minor eruption centres.

Discussion of results

Classification of eruptive centres and lava flows

To classify the type of principal eruptive centres A and B, we compare our interpretation results with the preliminary studies in the BBIC. Our results show that the base of the eruptive centres A and B are located in the base of the Wobbegong Supersequence with sediments from the Wobbegong and Dugong supersequences onlapping in cross-section view. These observations suggest that the magma eruption occurred during the Paleogene to Neogene periods. This proposal correlates with other region in the GAB where emplacement is proposed to have taken place in the middle Eocene (Clarke and Alley, 1992; Government of South Australia, 2001). The principal eruptive centres A and B do not exhibit internal changes in the seismic amplitude, with might be related to similarities in density at the interior of the magma flow *(Reynolds et al., 2017a).* This can suggest that they have similar composition (probably mafic) and might respond to a single transport episode *(Reynolds et al., 2018).*

In terms of morphologies, the principal eruptive centres of volcanoes A and B have rounded tops and sub-circular bases and pull-up velocity effects underneath them that diminishes the signal-noise ratio in HH3 and HH2 sequences. Both principal eruptive centres also show steeper flanks (18° to 35°) in comparison to other interpretation studies concerning the BBIC like *Magee et al., (2013b)*, in which they demonstrate gentle dips of less than 12° and classify the extrusive cones they document as shield volcanoes. These volcanoes are described as lava-dominated polygenetic landforms with gentle flanks and commonly basaltic or bimodal composition that erupted from either vents or flanks. In addition, some composite volcanoes with bimodal composition and pyroclastic layers are included in the shield volcanoes class, which can be composed of more viscous lavas and tend to form steeper landforms *(de Silva and Lindsay, 2015)* The steep angles and lack of internal structure at the principal eruptive centres suggest that they are composite volcanoes situated within a shield volcano context. In

addition, eight of the minor eruptive centres in the southeast region of the lava flow associated with Volcano B visibly align, which contrasts with the other 24 minor cones in the lava flow region. This particular alignment can result from a fissure region similar to Mount Schank *(Government of South Australia, 2001)* and/or small faulting underlying the lava flow that could have provided a path to the paleo-surface *(Magee et al., 2013a; Mark et al., 2020)* (Figure 4)

In contrast to the BBIC where the Group 1 volcanoes are characterised by radial lava flows around the eruptive centres *(Magee et al., 2013b),* Volcanoes A and B structural maps show that the lava flow around the eruptive centres is restricted towards the northeast against normal growth faults that nucleate when HH3 was deposited. Additionally, the principal eruptive centres of volcanoes A and B are not entirely circular but rather present with a sub-circular geometry towards the south and southwest boundaries that contrasts with the north-eastern edges where the normal faults terminate. We believe that this may be an outcome of the structural influence that these fault segments had during magma emplacement that not only restricted magma flow to the hanging wall region of the faults, but also controlled the eruption centre geometry. This proposal agrees with *Magee et al., (2013a)* who suggest that pre-existing structures (e.g. faults) can influence the geometry of magma complexes and work as preferential transport pathways (Figure 2).

We do not find evidence of intruded fault segments near the volcanic cones using maximum amplitude and RMS seismic attributes projected to surfaces along the fault planes, which can suggest that (1) magma transport through the fault plane seems to occur in a small scale that it cannot be resolved by the seismic survey data, or (2) that the fault segments act as barriers that do not allow the transport of magma towards the upper footwall section, but rather concentrate the magma at the hanging wall.

Although both principal eruptive centres cause velocity pull-up effects in the host-rock underneath the central region, we identify strong differences in the variance and *Automatic Gain Control (AGC)* seismic attributes (Figure 5) between eruptive centres A and B. In terms of the pipe-like geometry, it appears to exhibit a smooth and regular geometry over the time-slices that might not resulted entirely from a potential velocity-based timing distortion ("pull-up") caused by the overlying Volcano B. Additionally, we do not reject the possibility that this pile-like geometry was been generated inadvertently as part of the seismic data processing workflow. As both main eruptive centres and lava flows exhibit similarly high seismic amplitudes and thicknesses that differ by only 56 ms, we would expect similar underlying structures and distortions in the seismic data beneath both eruptive centres. In the case that this pipe-like geometry has a geological origin, we believe that it can represents a potential feeding network that might permit the transport of magma from deeper to shallower intervals. The lack of a pipe-geometry underlying Volcano A can potentially suggest that it was formed as a result of a different magma transport event. Some possibilities are direct transport of magma from Volcano B, or and interconnection between Volcano A and underlying intrusions or dykes. However, the high-amplitude character of the principal eruptive centres and the lava flows make it difficult to interpret underlying features due to the diminished signal-to-noise ratio of data beneath them. In addition, potential magma conduit elements (e.g., dykes and fissures) are usually sub-vertical in their attitude, which difficult to image in traditional seismic surveys.

Classification of intrusions

We use the classification from *Reynolds et al., (2017a)* to classify the magma intrusions in the study area. Our interpretation shows that there is a 50:50 ratio between compound and saucer-shaped

morphologies. In contrast to the BBIC analysis, we do not recognise any hybrid or laccolith morphologies.

Similar to the BBIC compound intrusions, 1, 4, 7, 10 and 13 are located at shallower depths of the HH3 sequence in comparison to the saucer-shaped intrusions at HH2 and HH1. Compound intrusions are also mainly clustered underneath volcanos A and B, while the majority of the saucer-shaped intrusions are isolated magma bodies outside the lava flow boundaries. Only intrusions 5 and 12 seem to be locally related to the compound intrusion cluster. These two saucer-shaped magma intrusions are also the ones emplaced at shallower depths in relation to the other saucer-shaped morphologies in the study area. In contrast, saucer-shaped intrusions 6, 8 and 9 are isolated magmatic bodies that might have been fed from local sources and do not seem to have a direct relationship with the extrusive cones. These isolated intrusions are also emplaced in deeper areas of the basin between the HH2 and T4 in relation to the BBIC observations. However, they suggest that the intrusions with greater areas (> 1 km^2) were only emplaced in the upper layers. We do not recognise a correlation between the total areas and the emplacement depth, where both morphologies show a wide range of sizes.

As stated previously, Intrusion 7 reaches the base of the Wobbegong Supersequence 1.3 km southwest from the lava flow at Volcano A without showing evidence of eruptive centres. Intrusion 7 is located 1.3 km southwest of Intrusion 1 and 1.5 km northwest Intrusion 10. It reaches HH3 about 0.88 km southeast boundary of Volcano A lava flow covering an area between 0.21 and 0.25 km^2. We propose that Intrusion 7 represents a very small volume of magma with minor volatile content related to a fissure geometry and a small area in comparison to the other saucer-shaped intrusions (Figure 6)

Compound and saucer-shaped intrusions have high to moderate top boundary seismic reflector amplitudes 700 to 2070% higher than the surrounding host rock in the HH and Tiger intervals. Intrusion 9 is the only one with higher top boundary seismic reflector amplitudes comparable to the massive transport deposits at the base of the HH3. Overall, the saucer-shaped intrusions exhibit higher top boundary seismic reflector amplitudes than those of the compound morphologies (Figure 5 and 6).

The interpretation of source points and the overlapping of intrusion areas permit us to identify a cluster of magma intrusions underlying the extrusive cones and lava regions. Even though it is quite difficult to interpret dykes or potential transport feeding channels between the different igneous bodies in the study area using seismic data, this cluster might suggest a potential magmatic complex system along the HH. Isolated intrusions also suggest potential local magma sources in deeper units than those of the cluster.

We show that magmatic extrusions and intrusions in the study area have similar characteristics in terms of morphologies and age to the intrusions and extrusions previously interpreted in the BBIC. From the 10 intrusions we map in the study area, two are located near normal growth faults that offset the sedimentary intervals between the T4 and the HH3 sequences (Figure 8 c and). *Mark et al., (2020)* proposed that intrusions with saucer-shaped morphologies do not propagate upwards through normal fault planes, which agrees with our interpretation at intrusions 6 and 8. Intrusion 8 is the only intrusion that shows a steep dip angle that seems to mimic the fault dip angles of about 10° and 20° above the Tiger Supersequence.

We also showed that there is minimal to no offset of intrusions 5, 6 and 8 by faults, which confirms that the magma activity in the area is younger than the nucleation of the normal growth faults. As the Tiger-HH3 fault segments grew between the Tiger and HH3, we can predict that the magma was

transported during the Cenozoic Period. This interpretation agrees with preliminary studies that suggest the magma activity in the GAB is of a mid-Eocene age and is supported by evidence of onlapping reflectors of the Dugong and Wobbegong intervals against the volcanic cones *(Clarke and Alley, 1992; Schofield et al., 2008; Holford et al., 2012; Reynolds et al., 2018).*

Some intrusions such as intrusion 1 and 5, are associated with "fold" shapes above them that can be traced vertically up to the overlying lava flow region. We propose that these features are related to pull-up time distortion caused by the elevated seismic velocity of the lava flow unit at the upper levels instead of potential forced folds (Figure 7a). The lack of forced folds above the intrusions in the study area, can be a consequence of a combination of different factors such as: (1) the depths where the intrusions were emplaced which sometimes can prevent the formation of forced folds *(Jackson et al., 2013)*; where intrusions such as 1, 4, 5, 6, 8, and 9 are located in deeper layers than sills interpreted using the Nerites3D seismic survey; (2) some intrusions might not develop completely, which might result in partial to non-generation of forced folds *(Thomson, 2007)*; (3) heterogeneity of the overburden host rock including the absence of ductile sequences such as shale or coal-bearing lithologies that can deform by folding *(Jackson et al., 2013)* and/or (4) problems with the seismic imaging where the geometric amplitude of forced folds can be thinner than the vertical seismic resolution (about less than 8 ms TWT thickness). In addition, some authors demonstrate that intrusions are not always associated with forced folds in the overlying strata *(Breitkreuz and Rocchi, 2018)*. A study from *Schofield and Totterdell, (2008)* also proposed that the absence of forced folds in the Western Ceduna Sub-basin can be related to only small volumes of magma intrusion during emplacement. This idea correlates with the marginal location of the Ceduna 3D seismic survey in the Ceduna Sub-basin in comparison to preliminary studies using the Nerites 3D survey area *(Reynolds et al., 2017b)*

Linear correlation between eruptive centres, source points and the strikes of the normal growth faults

We use a statistical point alignment method to define linear spatial correlation between the northwest-southeast strikes of the normal growth faults and (1) eruptive centres, and (2) the source points at each of the 10 intrusions in the study area. In both cases, the maximum radius 'R' did not reveal any spatial statistical alignments ("R" =14.5 km for source points and "R" = 5 km for eruptive centres). These results can be a consequence of the inaccurate 'R' values that might not be representative of the area (very few to no clusters of more than two points with similar distances between them) even though both 'R' values represent the maximum distance we calculated between points. The point alignment study demonstrates a single linear correlation between normal growth faults and source points when we apply a minimum 'R' of 1 km. The small number of results can be attributed to the small amount of data contained in the statistical study. Therefore, we cannot demonstrate evidence of the potential influence of normal growth faults on the transport of magma in the study area. In contrast, we identify evidence of a clear northwest-southeast alignment between the eruptive centres and the strikes of the normal growth faults when using the average radius (3 km). This alignment result agrees with observations in previous studies that propose the magmatic bodies of the BBIC have a northwest-southeast trend *(Schofield and Totterdell, 2008)*, parallel to the normal growth faults.

Comparison between intrusion emplacing depths and the Tiger detachment layer

The Ceduna Sub-basin is well known to contain overpressured shale layers (T4 and BW) that worked as detachment layers for normal growth faults in the extensional region of the Hammerhead and White Pointer Delta Systems. Some authors have proposed that the presence of overpressured shale sequences can facilitate the transport of magma, forming sub-horizontal intrusions when the hot magma dramatically increases pore fluid pressure causing the rock to fracture and dewater the shale sequences permitting additional space for the transport of magma *(Thomson, 2007)*. However, our results demonstrate that the intrusions are mostly emplaced between HH1, HH2 and HH3 where the sedimentary record suggests that the lithology is characterized by thick sandstones intercalated with shales and a continuous lateral sequence of mass transport *deposits (Totterdell and Krassay, 2003; Tapley et al., 2005; Tottendell and Mitchel, 2009)* rather than T4 which that corresponds to the shale detachment of the Hammerhead Delta System.

We believe that there can be different factors that resulted in the emplacement of the interpreted intrusions away from the shale detachment layer. For instance, (1) preliminary studies interpreted fluid chimney geometries at T4 *(Velayatham et al., 2021),* which suggests that the overpressured layer was dehydrated and degassed reducing local pore pressure and resulting in the reduction of overpressure *(Morley et al., 2008; Holford et al., 2017)*. (2) In addition, we identified strong changes in thickness of T4 in the study area where towards the southeast region (where Intrusion 8 is located) (Figure 12a), the thickness drops to 72 and 96ms, which strongly contrasts with the 152 to 192ms below the lava flows (Figure 12b) and between 212and 232ms in the west of the study area (Figure 12c). These changes in thickness in T4 can result from a strong displacement basinwards during the time of fault growth and can substantially affect the volume of fluid and potentially cease the overpressured character of the detachment *(McClay et al., 2003, King and Backé, 2010; MacDonald et al., 2010; King and Morley, 2017).* As a result, the reduced water content and overpressure of T4 would make it a non-preferential layer for magma emplacement *(Thomson, 2007; Schofield et al., 2014)*; T4 is more likely to have acted as any other shale within the HH.

In contrast to T4, the Blue Whale detachment (BW) display a thickness between 700 and 1200m underneath the area where the volcanoes and intrusions are located. The BW also display thrust faulting and folding in this area that can result in a potential local increase on overpressure and the likelihood of magma to be transported and emplaced at the BW. However, the poor signal-noise ratio and the decrease in seismic resolution with depth make it difficult to conduct detailed mapping of potential dykes and intrusions. Therefore, the interactions and implications that the Blue Whale detachment have in the transport and emplacement of magma in the Ceduna Delta System is out of the scope of this paper.

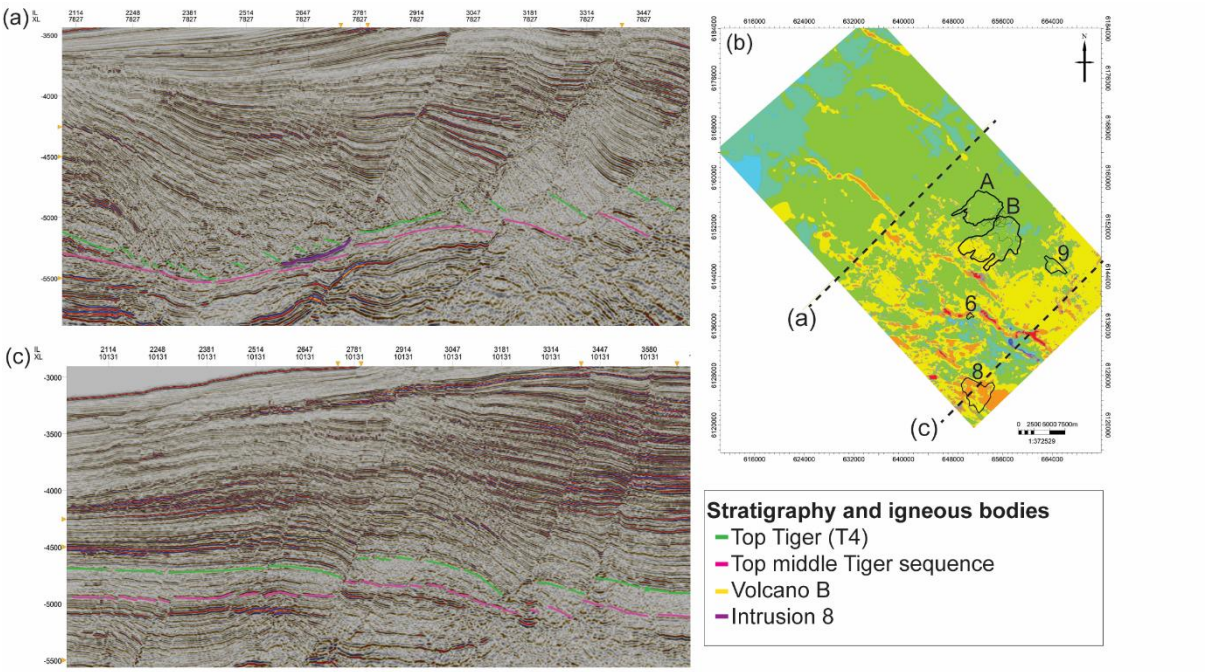

Figure 12: Examples from two differet areas showing the changes in the thickness of the Tiger detachment. (a) Shows a crossline along Intrusion 8, and (d) a crossline to the western of the study area. (c) Shows the thickness map of the Tiger detachment showing regionally how the thickness of the Tiger detachment varies at the southern section of the Ceduna 3D MSS seismic survey.

Conclusions

In this study we interpret the Ceduna 3MSS seismic survey located in the central region of the Ceduna Sub-basin to interpret ancient preserved igneous bodies including eruptive centres, lava flows and intrusions. It is quite difficult to recognize potential correlations between the different igneous bodies and their magma transport history given the poor signal-noise ratio of processed seismic data occurring beneath the eruptive centres and the lava flow regions. Our interpretation underrepresents dykes and connected channels between the different intrusive and extrusive morphologies in the study area. However, our interpretation demonstrates a period of magma transport during the Paleogene that resulted in two principal eruptive centres, Volcano A and Volcano B, associated lava flow regions, 43 minor eruptive centres along the lava flows, five compound and five saucer-shaped intrusions, a potentially pipe-like structure underlying Volcano B, and two potential fissures associated with Intrusion 7 and to the southeast of Volcano B.

We classify the principal eruptive centres (volcanoes A and B) as composite volcanoes within the shield volcano category. Our interpretation agrees with previous studies that classified eruptive centres of the Bight Basin Igneous Complex (BBIC) and in onshore South Australia (Mount Schank) as shield volcanoes, even though the principal eruptive centres in the study area exhibit steeper flanks, and lack of organised internal structures accordingly to our 3D seismic data. It is possible that these paleo-magma eruptions had a similar composition to the samples from much more recent extrusive bodies in South Australia (e.g., Mount Schank) and the Eyre Sub-basin.

The 10 intrusions within the HH were classified as being of compound and saucer-shaped morphologies. Our seismic interpretation is consistent with other studies of the BBIC where the

saucer-shaped intrusions are located within the middle and base of the HH (HH2 and HH1). In the study area they mostly represent isolate intrusions, while the compound intrusions are emplaced in HH3 and are clustered to underlie the lava flows and eruptive centres. Our interpretation suggests that all the intrusions lack overlying forced folds, which can be due to the underdevelopment of some of these intrusions in terms of their lack of heterogeneity and lack of an accommodating ductile hosting rock sequence within the HH. The physical limit of vertical seismic resolution is a factor that probably masks a more fulsome picture of the system. This study concludes with the most geologically recent intrusions in the western part of the Ceduna Sub-basin where small volumes of magma during the emplacement stage likely resulted in the lack of forced folds. We propose that the source point occurs at some deeper location beneath each intrusion that cannot be resolved by our 3D seismic survey dataset.

We investigate the potential emplacement and transport of magma along normal growth fault planes by projecting maximum amplitude and RMS seismic attributes onto fault plane data probes. We demonstrate the strong influence that normal growth faults have had on the formation and morphology of eruptive centres and lava flows in the Ceduna Sub-basin. Our seismic interpretation demonstrates sharp boundaries, and a strong tendency of lava flows to be transported for extended distances along the hangingwall block of major normal growth faults. Our results from the statistical point alignment method and accompanying fault strike rose diagrams allow us to quantify a clear northwest-southeast correlation between the normal growth fault strikes and aligned eruptive centres in the Ceduna Sub-basin.

We also study the relevance of a sub-sequence of the Tiger Supersequence (T4) in the emplacement of intrusions within the study area. In contrast to previous studies where magma is more likely to be transported along through ductile and overpressured layers, intrusions we have interpreted are located within the HH that predominantly comprises sandstones and minor intercalations of shale. We propose that T4 potentially lacked overpressure characteristics at the time when magma was transported, as a consequence of being insufficiently thick or due to potential fluid escape chimneys that dewatered and degassed the detachment layer prior or during intrusion. As a result, T4 acted as any other interval within the stratigraphy rather than being a preferential layer into which magma would intrude.

References

Alzaga-Ruiz, H., Granjeon, D., Lopez, M., Seranne, M., Roure, F., 2009. Gravitational collapse and Neogene sediment transfer across the western margin of the Gulf of Mexico: Insights from numerical models. Tectonophysics 470, 21–41. https://doi.org/10.1016/j.tecto.2008.06.017

Breitkreuz, C., Rocchi, S. (Eds.), 2018. Physical Geology of Shallow Magmatic Systems: Dykes, Sills and Laccoliths, Advances in Volcanology. Springer International Publishing, Switzerland. https://doi.org/10.1007/978-3-319-14084-1

Clarke, J.D.A., Alley, N.F., 1992. Petrologic data on the evolution of the Great Australian Bight (No. 92/21). Department of Mines and Energy South Australia, South Australia.

de Silva, S., Lindsay, J.M., 2015. Primary Volcanic Landforms, in: The Encyclopedia of Volcanoes. Elsevier, pp. 273–297. https://doi.org/10.1016/B978-0-12-385938-9.00015-8

Eide, C.H., Schofield, N., Lecomte, I., Buckley, S.J., Howell, J.A., 2018. Seismic interpretation of sill complexes in sedimentary basins: implications for the sub-sill imaging problem. J. Geol. Soc. 175, 193–209. https://doi.org/10.1144/jgs2017-096

Espurt, N., Callot, J.-P., Totterdell, J., Struckmeyer, H., Vially, R., 2009a. Interactions between continental breakup dynamics and large-scale delta system evolution: Insights from the Cretaceous Ceduna delta system, Bight Basin, Southern Australian margin: CONTINENTAL BREAKUP AND DELTA SYSTEM. Tectonics 28. https://doi.org/10.1029/2009TC002447

Espurt, N., Callot, J.-P., Totterdell, J., Struckmeyer, H., Vially, R., 2009b. Interactions between continental breakup dynamics and large-scale delta system evolution: Insights from the Cretaceous Ceduna delta system, Bight Basin, Southern Australian margin: Continental breakup and delta system. Tectonics, TC6002 28. https://doi.org/10.1029/2009TC002447

GAB 3D Survey Final Report (Seismic Processing), 2012. . PGD Data Processing, Australia.

Gibson, G.M., Totterdell, J., White, L.T., Mitchell, C.R., Stacey, A.R., Morse, M.P., Whitaker, A., 2013. Pre-existing basement structures and its influence on continental rifting and fracture development along Australian's southern rifted margin. J. Geol. Soc. Lond. 170, 365–377. https://doi.org/10.1144/jgs2012-040

Government of South Australia (Ed.), 2001. Volcanoes of the Mount Gambier area.

Hammer, Ø., 2009a. New statistical methods for detecting point alignments. Comput. Geosci. 35, 659–666. https://doi.org/10.1016/j.cageo.2008.03.012

Hammer, Ø., 2009b. New statistical methods for detecting point alignments. Comput. Geosci. 35, 659–666. https://doi.org/10.1016/j.cageo.2008.03.012

Hansen, D.M., Cartwright, J., 2006. Saucer-shaped sill with lobate morphology revealed by 3D seismic data: implications for resolving a shallow-level sill emplacement mechanism. J. Geol. Soc. 163, 509–523. https://doi.org/10.1144/0016-764905-073

Hillman, J.I.T., Crutchley, G.J., Kroeger, K.F., 2020. Investigating the role of faults in fluid migration and gas hydrate formation along the southern Hikurangi Margin, New Zealand. Mar. Geophys. Res. 41, 8. https://doi.org/10.1007/s11001-020-09400-2

Holford, S., Hillis, R., Duddy, I., Green, P., Stoker, M., Tuitt, A., Backé, G., Tassone, D., MacDonald, J., 2011. Cenozoic post-breakup compressional deformation and exhumation of the southern Australian margin. APPEA J. 51, 613. https://doi.org/10.1071/AJ10044

Holford, S., Schofield, N., MacDonald, J., Duddy, I., Green, P., 2012a. Seismic analysis of igneous systems in sedimentary basins and their impacts on hydrocarbon prospectivity: examples from the southern Australian margin. APPEA J. 52, 229. https://doi.org/10.1071/AJ11017

Holford, S., Schofield, N., MacDonald, J., Duddy, I., Green, P., 2012b. Seismic analysis of igneous systems in sedimentary basins and their impacts on hydrocarbon prospectivity: examples from the southern Australian margin. APPEA J. 52, 229. https://doi.org/10.1071/AJ11017

Holford, S.P., Schofield, N., Reynolds, P., 2017. Subsurface fluid flow focused by buried volcanoes in sedimentary basins: Evidence from 3D seismic data, Bass Basin, offshore southeastern Australia. Interpretation 5, SK39–SK50. https://doi.org/10.1190/INT-2016-0205.1

Jackson, C., Schofield, N., Golenkov, B., 2013. Geometry and controls on the development of igneous sill-related forced folds: A 2-D seismic reflection case study from offshore southern Australia. Geol. Soc. Am. Bull. 125, 1874–1890. https://doi.org/10.1130/B30833.1

Jackson, C.A., Magee, C., Schofield, N., Golenkov, B., 2013. Seismic Expression and Petroleum System Implications of Igneous Intrusions in Sedimentary Basins: Examples from Offshore Australia. Presented at the AAPG International Conference and Exhibition, AAPG, Singapore, p. 23.

Jimenez, M., Holford, S., King, R., Bunch, M., 2021. Controls on gravity-driven normal fault geometry and growth in stacked deltaic settings: a case study from the Ceduna Sub-basin. APPEA 61.

King, R., Backé, G., 2010. A balanced 2D strucutral model of the Hammerhead Delta-Deepwater Fold-Thrust Belt, Bight Basin, Australia. Aust. J. Earth Sci. 1005–1012.

King, R.C., Backé, G., 2010. A balanced 2D structural model of the Hammerhead Delta–Deepwater Fold-Thrust Belt, Bight Basin, Australia. Aust. J. Earth Sci. 57, 1005–1012. https://doi.org/10.1080/08120099.2010.509409

King, R.C., Morley, C.K., 2017. Wedge Geometry and Detachment Strength in Deepwater Fold-Thrust Belts. Earth-Sci. Rev. 165, 268–279. https://doi.org/10.1016/j.earscirev.2016.12.012

Kumar, P.C., Niyazi, Y., Eruteya, O.E., Moscariello, A., Warne, M., Ierodiaconou, D., Sain, K., 2022. Anatomy of intrusion related forced fold in the offshore Otway Basin, SE Australia. Mar. Pet. Geol. 141, 105719. https://doi.org/10.1016/j.marpetgeo.2022.105719

MacDonald, J., King, R., Hillis, R., Backé, G., 2010. Structural style of the White Pointer and Hammerhead Delta—deepwater fold-thrust belts, Bight Basin, Australia. APPEA J. 50, 487. https://doi.org/10.1071/AJ09029

Magee, C., Hunt-Stewart, E., Jackson, C.A.-L., 2013. Volcano growth mechanisms and the role of sub-volcanic intrusions: Insights from 2D seismic reflection data. Earth Planet. Sci. Lett. 373, 41–53. https://doi.org/10.1016/j.epsl.2013.04.041

Magee, C., Jackson, C.A.-L., 2020. Seismic reflection data reveal the 3D structure of the newly discovered Exmouth Dyke Swarm, offshore NW Australia. Solid Earth 11, 579–606. https://doi.org/10.5194/se-11-579-2020

Magee, C., Maharaj, S.M., Wrona, T., Jackson, C.A.-L., 2015. Controls on the expression of igneous intrusions in seismic reflection data. Geosphere 11, 1024–1041. https://doi.org/10.1130/GES01150.1

Magee, C., Pichel, L.M., Madden-Nadeau, A.L., Jackson, C.A. -L., Mohriak, W., 2021. Salt–magma interactions influence intrusion distribution and salt tectonics in the Santos Basin, offshore Brazil. Basin Res. 33, 1820–1843. https://doi.org/10.1111/bre.12537

Magee, C., Stevenson, C.T.E., Ebmeier, S.K., Keir, D., Hammond, J.O.S., Gottsmann, J.H., Whaler, K.A., Schofield, N., Jackson, C.A.-L., Petronis, M.S., O'Driscoll, B., Morgan, J., Cruden, A., Vollgger, S.A., Dering, G., Micklethwaite, S., Jackson, M.D., 2018. Magma Plumbing Systems: A

Geophysical Perspective. J. Petrol. 59, 1217–1251. https://doi.org/10.1093/petrology/egy064

Magee, Jackson, C., Schofield, N., 2013. The influence of normal fault geometry on igneous sill emplacement and morphology. Geology 41, 407–410. https://doi.org/10.1130/G33824.1

Mark, N.J., Holford, S.P., Schofield, N., Eide, C.H., Pugliese, S., Watson, D.A., Muirhead, D., 2020. Structural and lithological controls on the architecture of igneous intrusions: examples from the NW Australian Shelf. Pet. Geosci. 26, 50–69. https://doi.org/10.1144/petgeo2018-067

McClay, K., Dooley, T., Zamora, G., 2003. Analogue models of delta systems above ductile substrates. Geol. Soc. Lond. Spec. Publ. 216, 411–428. https://doi.org/10.1144/GSL.SP.2003.216.01.27

Meeuws, F.J.E., Holford, S.P., Foden, J.D., Schofield, N., 2016. Distribution, chronology and causes of Cretaceous – Cenozoic magmatism along the magma-poor rifted southern Australian margin: Links between mantle melting and basin formation. Mar. Pet. Geol. 73, 271–298. https://doi.org/10.1016/j.marpetgeo.2016.03.003

Mitchell, C., Boreham, C.J., Totterdell, J., Geoscience Australia, 2009. Bight Basin geological sampling and seepage survey: RV Southern Surveyor survey SS01/2007. Geoscience Australia, Canberra.

Morley, C.K., King, R., Hillis, R., Tingay, M., Backe, G., 2011. Deepwater fold and thrust belt classification, tectonics, structure and hydrocarbon prospectivity: A review. Earth-Sci. Rev. 104, 41–91. https://doi.org/10.1016/j.earscirev.2010.09.010

Morley, C.K., Tingay, M., Hillis, R., King, R., 2008. Relationship between structural style, overpressures, and modern stress, Baram Delta Province, northwest Borneo. J. Geophys. Res. 113, B09410. https://doi.org/10.1029/2007JB005324

Olivia, S., Ebinger, C., Wauthier, C., Muirhead, D., Roecker, W., Rivalta, E., Heimann, S., 2019. Insights Into Fault-Magma Interactions in an Early-Stage Continental Rift From Source Mechanisms and Correlated Volcano-Tectonic Earthquakes. Geophys. Res. Lett. 46, 2065–2074. https://doi.org/2018GL080866

Phillips, T.B., Magee, C., Jackson, C.A.-L., Bell, R.E., 2018. Determining the three-dimensional geometry of a dike swarm and its impact on later rift geometry using seismic reflection data. Geology 46, 119–122. https://doi.org/10.1130/G39672.1

Pindell, J., Heyn, T., 2022. Dynamo-thermal subsidence and sag–salt section deposition as magma-rich rifted margins move off plume centres along incipient lines of break-up. J. Geol. Soc. 179, jgs2021-095. https://doi.org/10.1144/jgs2021-095

Planke, S., Millett, J.M., Maharjan, D., Jerram, D.A., Abdelmalak, M.M., Groth, A., Hoffmann, J., Berndt, C., Myklebust, R., 2017. Igneous seismic geomorphology of buried lava fields and coastal escarpments on the Vøring volcanic rifted margin. Interpretation 5, SK161–SK177. https://doi.org/10.1190/INT-2016-0164.1

Pollard, D.D., Johnson, M., 1973. Mechanics of growth of some laccolithic inttrusions in the Henry mountains, Utah, II bending and failure of overburden mattion layers and sill -formation. Tectonophysics 18, 311–354.

Reynolds, P., Holford, S., Schofield, N., Ross, A., 2018. The importance of subsurface lithology in controlling magma storage v. eruption: an example from offshore southern Australia. J. Geol. Soc. 175, 694–703. https://doi.org/10.1144/jgs2017-109

Reynolds, P., Holford, S., Schofield, N., Ross, A., 2017. The shallow depth emplacement of mafic intrusions on a magma-poor rifted margin: An example from the Bight Basin, southern Australia. Mar. Pet. Geol. 88, 605–616. https://doi.org/10.1016/j.marpetgeo.2017.09.008

Reynolds, P., Holford, S., Schofield, N., Ross, A., 11/2017a. Three-Dimensional Seismic Imaging of Ancient Submarine Lava Flows: An Example From the Southern Australian Margin. Geochem. Geophys. Geosystems 18, 3840–3853. https://doi.org/10.1002/2017GC007178

Robson, A., 2017. Normal fault growth analysis using 3D seismic datasets located along Australia's southern margin (thesis). University of Adelaide, School of Physical Sciences.

Robson, A., King, R., Holford, S., 2017. Structural evolution of a gravitationally detached normal fault array: analysis of 3D seismic data from the Ceduna Sub-Basin, Great Australian Bight. Basin Res. 29, 605–624. https://doi.org/10.1111/bre.12191

Rowan, M., Jackson, M., Trudgill, B., 1999. Salt-Related Fault Families and Fault Welds in the Northern Gulf of Mexico. AAPG Bull. 83, 1454–1484.

Ryan, L., Magee, C., Jackson, C.A.-L., 2017. The kinematics of normal faults in the Ceduna Subbasin, offshore southern Australia: Implications for hydrocarbon trapping in a frontier basin. AAPG Bull. 101, 321–341. https://doi.org/10.1306/08051615234

Sapin, F., Ringenbach, J.-C., Rives, T., Pubellier, M., 2012. Counter-regional normal faults in shale-dominated deltas: Origin, mechanism and evolution. Mar. Pet. Geol. 37, 121–128. https://doi.org/10.1016/j.marpetgeo.2012.05.001

Sayers, J., Symonds, P.A., Direen, N.G., Bernardel, G., 2001. Nature of the continent-ocean transition on the non-volcanic rifted margin of the central Great Australian Bight. Geol. Soc. Lond. Spec. Publ. 187, 51–76.

Schmiedel, T., Galland, O., Haug, Ø.T., Dumazer, G., Breitkreuz, C., 2019. Coulomb failure of Earth's brittle crust controls growth, emplacement and shapes of igneous sills, saucer-shaped sills and laccoliths. Earth Planet. Sci. Lett. 510, 161–172. https://doi.org/10.1016/j.epsl.2019.01.011

Schofield, A., Totterdell, J., 2008. Distribution, timing and origin of magmatism in the Bight and Eucla Basins. Geosci. Aust., 67359 1–25.

Schofield, N., Alsop, I., Warren, J., Underhill, J.R., Lehné, R., Beer, W., Lukas, V., 2014. Mobilizing salt: Magma-salt interactions. Geology 42, 599–602. https://doi.org/10.1130/G35406.1

Schofield, N.J., Brown, D.J., Magee, C., Stevenson, C.T., 2012. Sill morphology and comparison of brittle and non-brittle emplacement mechanisms. J. Geol. Soc. 169, 127–141. https://doi.org/10.1144/0016-76492011-078

Stoker, M.S., Holford, S.P., Totterdell, J.M., 2022. Stratigraphic architecture of the Cenozoic Dugong Supersequence: implications for the late post-breakup development of the Eucla Basin, southern Australian continental margin. Earth Environ. Sci. Trans. R. Soc. Edinb. 1–34. https://doi.org/10.1017/S1755691022000123

Tapley, D., Mee, B.C., King, S.J., Davis, R.C., Leischner, K.R., 2005a. Petroleum pontetial of the Ceduna Sub-basin: Impact of Gnarlyknots-1A. APPEA J. 45, 365. https://doi.org/10.1071/AJ04029

Tapley, D., Mee, B.C., King, S.J., Davis, R.C., Leischner, K.R., 2005b. Petroleum potential of the Ceduna Sub-Basin: Impact of Gnarlyknots–1A. APPEA J. 45, 365. https://doi.org/10.1071/AJ04029

Thomson, K., 2007. Determining magma flow in sills, dykes and laccoliths and their implications for sill emplacement mechanisms. Bull. Volcanol. 70, 183–201. https://doi.org/10.1007/s00445-007-0131-8

Thomson, K., Hutton, D., 2004. Geometry and growth of sill complexes: insights using 3D seismic from the North Rockall Trough. Bull. Volcanol. 66, 364–375. https://doi.org/10.1007/s00445-003-0320-z

Tottendell, J., Mitchel, C., 2009. Bight Basin geological sampling and seepage survey: RV Southern Surveyor survey SS01/2007. Geosci. Aust., 68689 24, 1–134.

Totterdell, J., Krassay, A., 2003. The role of shale deformation and growth faulting in the Late Cretaceous evolution of the Bight Basin, offshore southern Australia. Geol. Scoeity Lond., Subsurface Sediment Mobilization 216, 429–442.

Totterdell, J., Mitchell, C., 2009. Bight Basin Geological Sampling and Seepage Survey. Geosci. Aust.

Totterdell, J.M., Krassay, A.A., 2003. The role of shale deformation and growth faulting in the Late Cretaceous evolution of the Bight Basin, offshore southern Australia. Geol. Soc. Lond. Spec. Publ. 216, 429–442. https://doi.org/10.1144/GSL.SP.2003.216.01.28

Velayatham, T., Holford, S., Bunch, M., King, R., 2021. Fault controlled focused fluid flow in the Ceduna Sub-Basin, offshore South Australia; evidence from 3D seismic reflection data. Mar. Pet. Geol. 127, 49.

Watson, D., Holford, S., Schofield, N., Mark, N., 2019. Failure to predict igneous rocks encountered during exploration of sedimentary basins: A case study of the Bass Basin, Southeastern Australia. Mar. Pet. Geol. 99, 526–547. https://doi.org/10.1016/j.marpetgeo.2018.10.034

Wood, L.J., 2012. Shale tectonics, in: Regional Geology and Tectonics: Phanerozoic Passive Margins, Cratonic Basins and Global Tectonic Maps. Elsevier, pp. 42–61. https://doi.org/10.1016/B978-0-444-56357-6.00002-0

Conclusions

Conclusions

Normal faults in delta systems, have demonstrated strong control in the distribution of sediments, the geometry and extension of sedimentary systems, and can trap or work as migration paths for fluids including hydrocarbons. However, there is not enough studies related to the analysis of normal growth faults in delta systems where detachment layers are present. Specifically, in the Ceduna Sub-basin, previous studies have used 2D seismic lines and small 3D seismic surveys to define the complexity of the evolution of normal growth faults and the implications that the fault roughness have in the likelihood of reactivation along strike. In addition, there are few studies that have interpreted the influence that normal growth faults and detachment layers can have in the transport and emplacement of magmatic bodies in the Ceduna Sub-basin.

This project aims to address three important gaps in the understanding of normal growth faults in relation with the complexity of their evolution style in delta systems with detachment layers, how the roughness along the fault plane can determine the likelihood of fault reactivation, and the influence that the normal growth fault segments and the detachment layers have in the transport and emplacement of magmatic systems. This project also includes the interpretation of normal growth faults, mapping of the top of the four principal supersequences (Hammerhead, Tiger, White Pointer and Blue Whale) in the Great Australian Bight and a local magma system that includes volcanoes, lava flow areas, and intrusions. It applies innovative and effective techniques such as seismic interpretation of the Ceduna 3D seismic survey to map fault segments sedimentary sequences and magmatic bodies; kinematic analysis to quantify changes in the evolution style of normal faults; *Fault analysis seal technology* (FAST) technique to estimate the likelihood of fault reactivation as a response to the current South Australian Margin; and statistical likelihood of fault reactivation to determine the specific sections along the fault segment that are at higher risk of reactivation; and statistical point alignment method to stablish preferable lineal correlations between fault strike orientation and magmatic bodies.

Characteristics of the normal growth faults and detachment layers

- The broad extension of the Ceduna 3D seismic survey permits the interpretation of 530 fault segments and describes their principal structural characteristics such as changes in strike orientation, dip angle, and displacement. Some of these characteristics were interpreted in previous studies such as strike orientations towards the northwest–southeast strike and west–east. The wide extension of the Ceduna 3D seismic survey also allows to interpret a minor number of normal growth faults with strikes towards the north–south and northeast–southwest. The Ceduna 3D seismic survey also allows the interpretation of displacement and dip angle from 1172ms and 2° in the lower tip of the faults up to 1ms and 85° in the upper tip of the normal growth fault segments.
- Chapter 1 characterise changes on the thickness of the Blue Whale and Tiger detachments (from around 200 in the north, 500 in the centre and up to 1200ms in the south and southeast), dip angle (from 10° in the north to <2° in the south) and structural features (presence of dome-like structures) that strongly influences the changes in the evolution style of normal growth faults. Similarly, the Tiger detachment layer exhibits variations in thickness (from 210 in the north to 430 in the southwest) and a gentle dip angle towards the southeast (about 5° along the study area). This thesis also reveals that to the south and southeast regions of the study area, normal growth

faults are detaching and displacing the top of the Tiger Supersequence towards the south and southeast, where the Tiger detachment is reduced in thickness to 70ms in comparison to the rest of the study area.

- In this thesis the normal growth fault in the Ceduna Sub-basin were classified in three fault groups that represent the sedimentary sequences they displayed: (1) Cenomanian–Late Santonian, (2) Cenomanian–Maastrichtian, and (3) Late Santonian–Maastrichtian. These fault styles are widely distributed in the study area and developed as either located independently or closer to other normal growth faults.

Evolution of normal growth faults

- Like previous studies, this thesis uses kinematic analyses to outline in detail how normal growth faults evolve in the Ceduna Sub-basin. It validates the result from previous studies that describe complex evolution styles of normal growth faults in the Ceduna Sub-basin that include periods of constant growth, dip-linkage and reactivation. This project innovated in the establishment of the implications that these variations in the fault evolution have in the migration and trap of hydrocarbons using 20 fault segments from Chapter 1 and found that Cenomanian–Late Santonian, Late Santonian–Maastrichtian and Cenomanian–Maastrichtian that are located in the northern region constantly grew without periods of reactivation, while the Cenomanian–Maastrichtian fault segments located at the centre region show two periods of dip-linkage in the base and top of the Tiger Supersequence, and Cenomanian–Maastrichtian fault segments located in the south and southeast regions exhibit one period of dip-linkage at the top of the Tiger Supersequence and an event of reactivation during the time that the upper Hammerhead sequence was deposited.
- This project demonstrates that the changes in the evolution style of the Cenomanian-Maastrichtian fault segments can be correlated to the areal location of the faults and with local variations in the accommodation space and the Blue Whale detachment layer geometrical and lithological characteristics (e.g., thickness, lithology, and internal structures). (1) In the northern region of the study area, the Blue Whale detachment is thin (270 to 460 ms), with homogeneous seismic amplitude. In this area, the normal growth faults evolved by continuously growing between the Cenomanian and the Maastrichtian. (2) In the central region of the study area, the Blue Whale detachment shows a medium thickness (565–670 ms) with changes in seismic amplitude and some internal thrust faults and dome-like structures. Here, the fault evolution styles indicated two dip-linkage events, at the base and top of the Tiger Supersequence. (3) In the southern region, the Blue Whale detachment is thicker (685–1430 ms) with strong changes in seismic amplitude and presence of internal dome-like structures and thrust faults. Here, the fault segments evolved by one dip-linkage event at the top of the Tiger Supersequence and one event of reactivation during the deposition of the upper Hammerhead Supersequence interval.

Risk of normal growth faults reactivation

- Chapter 3 in this thesis aims to identify the likelihood of normal growth faults to reactivate as a result of the current active stress field in the Australian Southern Margin and the implications that this reactivation has in potential events of fluid migration and seal breakage. Chapter 3 validates the results from previous studies that effectively use the Fault analysis seal technology (FAST) technique to describe risk of fault reactivation in terms of the pore pressure needed to reactivate fault segments. This thesis also incorporates statistical analysis to confirms the importance of the

fault roughness (changes in dip angle and strike) along the fault plane in the analysis of fault reactivation and highlight the specific sections of the fault that are at higher risk of reactivation.

- Chapter 3 also includes six faults from Chapter 1 where five show a northwest-southeast strike and one a west-east. It demonstrates that the sections of the faults with dip angles >45° and strikes oblique (10° to 15°) to the maximum horizontal stress orientation, are at higher risk of reactivation. This chapter estimate similar results in two leads with closure against two fault segments to demonstrate the importance of a detail risk of fault reactivation analysis in future exploration campaign in the Ceduna Sub-basin.

Influence of normal growth faults in the magmatic systems

- Previous studies have interpreted middle Eocene magma intrusions and extrusion in the Ceduna Sub-basin with similar characteristics to the igneous bodies contained in this thesis. Chapter 4 analyses the geometrical characteristics of magmatic bodies and the influence that normal growth faults have in the transport and emplacement of magma in the south-eastern region of the Ceduna 3D seismic survey. This broad seismic survey allows the interpret in detail two composite volcanoes (within the shield volcanoes morphology) with steep flanks (18 to 35°), sub-radial with lava flows that extend at the base of the Wobbegong Supersequence towards the southwest, and sub-radial lava flows around 43 minor eruptive cones. In all cases, the extrusive igneous bodies show sharp boundaries towards the northeast where several normal growth faults are located. The 3D seismic dataset also enables the interpretation of ten intrusions within the Hammerhead Supersequence that were classified by morphology in saucer-shaped and composite intrusions.
- Chapter 4 details the influence that the northwest–southeast normal growth faults have in the geometry and emplacement of igneous bodies in the Ceduna Sub-basin. It applies a statistical point alignment method to demonstrate a correlation between the distribution of the eruptive centres and the northwest-southeast strike orientation of normal growth faults. This correlation demonstrates the influence that the normal growth faults have in the transport and emplacement of magma in the study area.

Implications of the study for the evolution of passive margins

- There are several examples of delta systems in passive margins that contain detachment layers. Some of these delta systems such as the Gulf of Mexico, Niger Delta, Baram Delta, and Offshore Angola are well known to contain hydrocarbon reserves. However, there is little information regarding the importance of fault kinematics, risk of fault reactivation and structurally characterizing detachment layers in the exploration of hydrocarbons. There is also very little information related to the influence that normal growth faults and detachment layers have in the transport and emplacement of magmatic systems.
- The results contained in Chapter 2 exhibit the complexity of the characteristics of detachment layers in delta systems that have not been described in detail in previous studies. This thesis demonstrates that the structural features of the detachment layers can influence the characteristics and evolution of the fault segments and the potential effectiveness of the normal growth faults in evacuating the detachment towards the centre of the basin. Given the similarities that previous studies have identified between the Ceduna Sub-basin, the Niger Delta, Baram Delta and the Gulf of Mexico, it is likely that these results and techniques can be applicable in other delta systems.

- Chapter 3 provides evidence of the importance of fault roughness (changes in strike and dip angle along strike) to predict potential risk of fault reactivation. The results demonstrate that fault roughness has direct implications in the prediction of tectonic hazards, such as earthquakes, fluid migration and gravity driven movement of sediments that can be applicable in other delta systems with active stress fields.
- This project demonstrates how normal growth faults influence the transport and emplacement of magma in passive margins. For instance, normal growth faults can influence the geometry and alignment of eruptive centres and the flow direction of lava.

Implications for the exploration of hydrocarbons in the Ceduna Sub-basin

- This thesis demonstrates that the evolution style of the normal growth faults in the Ceduna Sub-basin have a strong impact in the petroleum system. The Cenomanian-Late Santonian faults are likely to trap hydrocarbons that have migrated from the Blue Whale, White Pointer, and Tiger source rocks. These hydrocarbons are likely to migrate after the nucleation period at the Late Santonian, therefore, the Cenomanian-Maastrichtian fault segments are likely to present periods of secondary and tertiary hydrocarbon migration due to the events of dip-linkage and reactivation. These fault segments might trap the hydrocarbons that migrated after the Maastrichtian. Similarly, the Late Santonian-Maastrichtian fault segments are likely to trap only the hydrocarbons that migrated after the Maastrichtian.
- The seismic interpretation in the Ceduna Sub-basin shows examples where exploratory leads represent closures against normal growth faults. This project also shows that the current active stress field in the Southern Australian margin can reactivate the normal growth faults in the Ceduna Sub-basin that display sections along strike with steep dip angles (>45°) and oblique strike orientations (between 10° and 15°) from the current Maximum horizontal stress orientation. Therefore, in future exploration campaigns it is vital to include an analysis of the structural characteristics of the fault plane in the exploration risk assessment.

Recommendations for future studies in the Ceduna Sub-basin

- It is recommended that future studies apply kinematic analysis to fault segments located in other sub-basins (like the Eyre Sub-basin) that are located closer to the continent (away from the centre of the basin) in the Great Australian Bight to compare with the kinematics and displacement results contained in this thesis. This comparison can have implications in the analysis of delta systems as it can determinate the changes in the evolution style between faults along different areas of the Ceduna Delta system.
- It is recommended that future studies include the sediment influx rate and compaction with the fault kinematic results to define how if the difference degree of sediment loading of the study area in the Ceduna Sub-basin influence the fault growth changes observed in this thesis between north, centre, and south regions.
- Similar to previous studies, this thesis describes the possibility of a tectonic inversion of some of the normal growth faults as one possible explanation to the thinning of the hangingwall sequences (e.g., Lower Tiger sequence) in the study area. It is recommended to evaluate in more detail the implications that this inversion event might have in the erosion and displacement of the normal growth faults.
- The results exhibited in this thesis demonstrates that the angle of internal friction is the geomechanical parameter with the greater influence in the risk of fault reactivation. Therefore, it

is recommended to obtain measurements of the coefficient of friction in future exploration wells to redefine the likelihood of fault reactivation in the Ceduna Sub-basin.

- This thesis evaluates the influence of the Tiger detachment layer in the transport and emplacement of magma systems. However, it is recommended that future studies determine what influence the Blue Whale detachment layer has in the magma transport in the Ceduna Sub-basin.

Publications

APPEA 2021 Conference publications

AEGC 2021 Conference abstracts

The APPEA Journal 2021, **61**, 632–639
https://doi.org/10.1071/AJ20073

Extended abstract

Controls on gravity-driven normal fault geometry and growth in stacked deltaic settings: a case study from the Ceduna Sub-basin

Monica Jimenez[A,C], *Simon P. Holford*[A], *Rosalind C. King*[B] *and Mark A. Bunch*[A]

[A]Australian School of Petroleum and Energy Resources, University of Adelaide, Australia.
[B]Department of Earth Sciences, University of Adelaide, Australia.
[C]Corresponding author. Email: monica.jimenezlloreda@adelaide.edu.au

Abstract. Kinematics of gravity-driven normal faults exerts a critical control on petroleum systems in deltaic settings but to date has not been extensively examined. The Ceduna Sub-basin (CSB) is a passive margin basin containing the White Pointer (Albian-Cenomanian) and Hammerhead (Campanian-Maastrichtian) delta systems that detach on shale layers of Albian-Cenomanian and Turonian-Coniacian ages, respectively. Here we present evidence for spatially variable fault growth styles based on interpretation of the Ceduna 3D seismic survey and fault kinematic analyses using displacement–distance, displacement–depth and expansion index methods. We identified faults that continuously grew either between the Cenomanian–Santonian or Santonian and the Maastrichtian located throughout the study area and faults that exhibit growth between the Cenomanian–Maastrichtian that are geographically separated into three areas according to their evolution histories: (i) Northern CSB faults exhibit constant growth between the Cenomanian and Maastrichtian. (ii) Central CSB faults show two dip-linkage intervals between (a) Cenomanian and Coniacian–Late Santonian, (b) Coniacian–Late Santonian and Late Santonian–Maastrichtian segments, respectively. (iii) Central and southern CSB faults exhibit dip-linkage intervals between Cenomanian–early Santonian and Late Santonian–Maastrichtian segments. Our study demonstrates a relationship between the location of the Cenomanian–Maastrichtian faults and their evolution history suggesting constant growth evolution at north and dip linkage at the central and south areas.

Keywords: Ceduna Sub-basin, delta systems, kinematic analysis, normal growth faults.

Accepted 18 February 2021, published online 2 July 2021

Introduction

Normal faults in delta systems are an important control on the distribution of source, reservoir and seal rocks, the formation of traps and fluid flow paths for hydrocarbons (Thorsen 1963; Ryan *et al.* 2017). Kinematic analyses (e.g. measurement of displacement–distance, displacement–depth and expansion index [EI]) enable the growth histories of normal faults to be quantified, which can aid the identification of seal failures and fault-related secondary hydrocarbon migration events. However, the implementation of these techniques has been mostly focused on normal fault systems that do not contain a mechanically weak detachment (e.g. salt or overpressured shale) (Walsh and Watterson 1991; Imber *et al.* 2003). This leaves uncertainties related to how normal growth faults evolve in delta systems where detachment layers are present.

Recent studies in the Ceduna Sub-basin (CSB) have used spatially limited seismic datasets and kinematic analysis to provide information about the evolution of normal growth faults within the Cretaceous deltaic sequences. Ryan *et al.* (2017) defined three different fault styles in the CSB based on 2D seismic interpretation (faults in the central CSB that continuously grew between the Cenomanian and Maastrichtian, Cenomanian–Late Santonian fault segments that are either at the northeast CSB and were reactivated at the Campanian–Maastrichtian or at the southwest CSB and were dip linked with Late Campanian–Maastrichtian fault segments). Robson *et al.* (2017) used 3D seismic data and kinematic analysis to conclude that the older Cenomanian–Late Santonian fault segments exert a strong control on the evolution and growth of subsequent younger Late Santonian–Maastrichtian fault segments.

Our study used the Ceduna 3D MSS seismic survey and kinematic analysis to constrain the along-strike evolution of normal growth faults in the CSB. For the purpose of this extended abstract, we describe the main characteristics of the three fault styles we interpreted, which were categorised by the sedimentary stratigraphy they dissect (Cenomanian–Late Santonian, Cenomanian–Maastrichtian and Late Santonian–Maastrichtian). We then explain with more detail the changes in the evolution patterns we identified in the

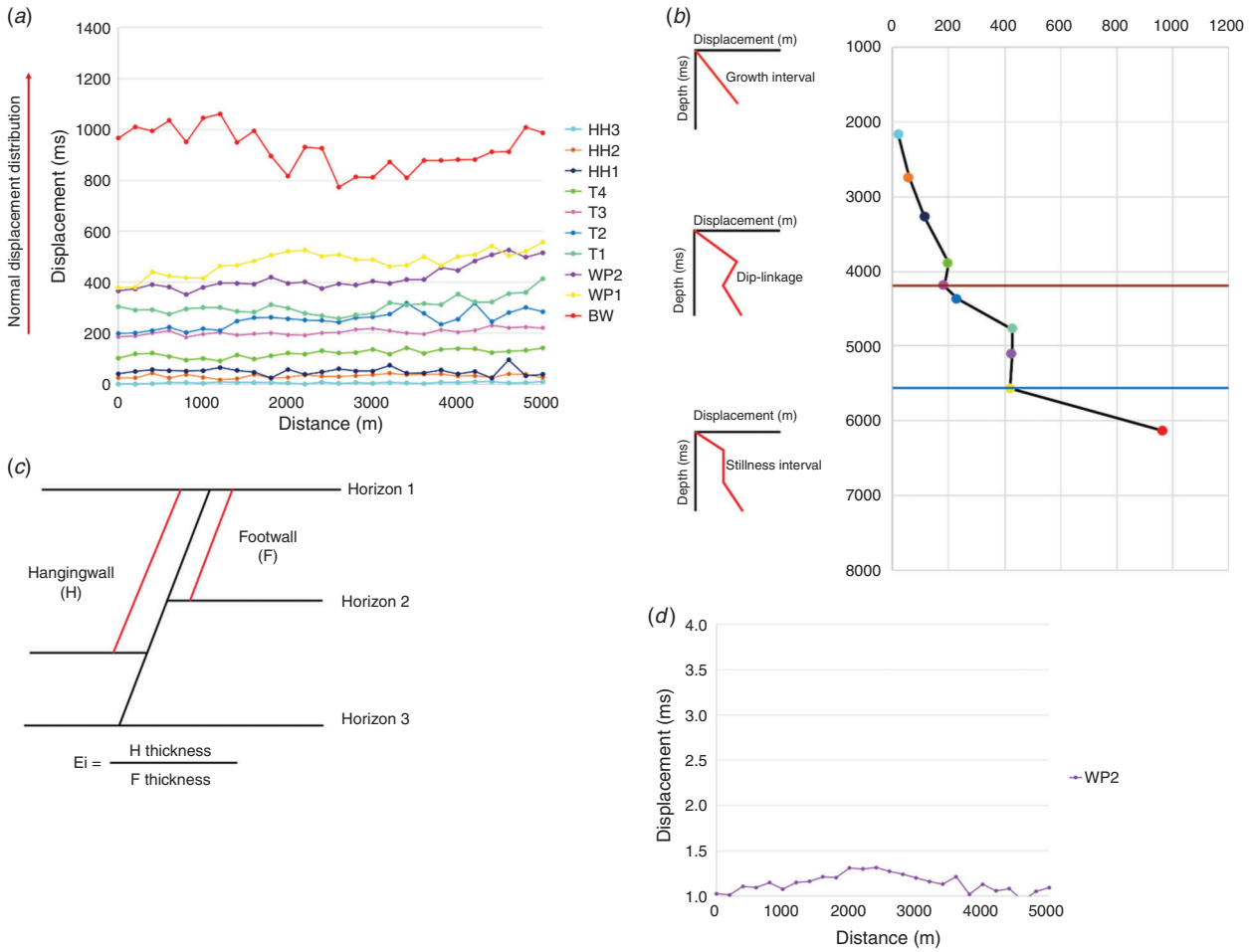

Fig. 1. Description of the kinematic analysis used in the present study. In (*a*), (*b*), and (*d*), the colours represent the seismic horizons where the fault displacement was quantified. (*a*) Example of a fault with normal displacement distribution in the displacement–distance (*D*–*x*) analysis. (*b*) At the left, a schematic representation of evolution patterns that can be identified using the displacement–depth (*D*–*z*) analysis. At the right, an example of a reference point where the fault shows in the *D*–*z* analysis dip-linkage and reactivation events. (*c*) Schematic representation of how the EI is calculated using the hangingwall and footwall thickness at each unit. (*d*) EI results along strike using as example the lower WP unit (EI–*x*).

Cenomanian–Maastrichtian faults that also correlates with the area where each fault is located.

Basin evolution

Large-scale deltaic systems mainly form in passive margins, and their structural characteristics are controlled by factors including sediment loading, subsidence and the nature of underlying detachment layer(s). The CSB in the Great Australian Bight (GAB) has two stacked delta systems (White Pointer [WP] and Hammerhead [HH] deltas) where both exhibit listric growth faults in the delta top that are linked to fold thrust belts at the delta toe (McClay *et al.* 2003; King and Backé 2010; MacDonald *et al.* 2012).

The GAB formed after the initiation of rifting between Australia and Antarctica in the middle Jurassic. This generally NW-SE rifting ended at the Late Santonian with onset of seafloor spreading and the establishment of a passive margin (Totterdell and Mitchell 2009; Holford *et al.* 2011).

The WP delta system encompasses at its base, the overpressured shales of the Blue Whale (BW; Albian–Cenomanian) Supersequence that are overlain by ~4 km deltaic sediments from the WP Supersequence (Cenomanian) during a period of rapid subsidence, which resulted in the development of normal growth faults that detach at the top of the BW (Totterdell *et al.* 2008; Espurt *et al.* 2009; Hughes *et al.* 2009).

The HH Delta system corresponds to the HH Supersequence (Campanian–Maastrichtian) comprising approximately 3 km of deltaic sediments that reactivated some Cenomanian–Late Santonian faults and formed new faults that detach at the top of the Tiger (T) Supersequence (Turonian–Late Santonian) (Reynolds *et al.* 2003; Tapley *et al.* 2005; Totterdell and Mitchell 2009).

Methodology

Seismic interpretation

The first stage of this study involved the interpretation of the Ceduna 3D seismic reflection survey (12 030 km^2). We used

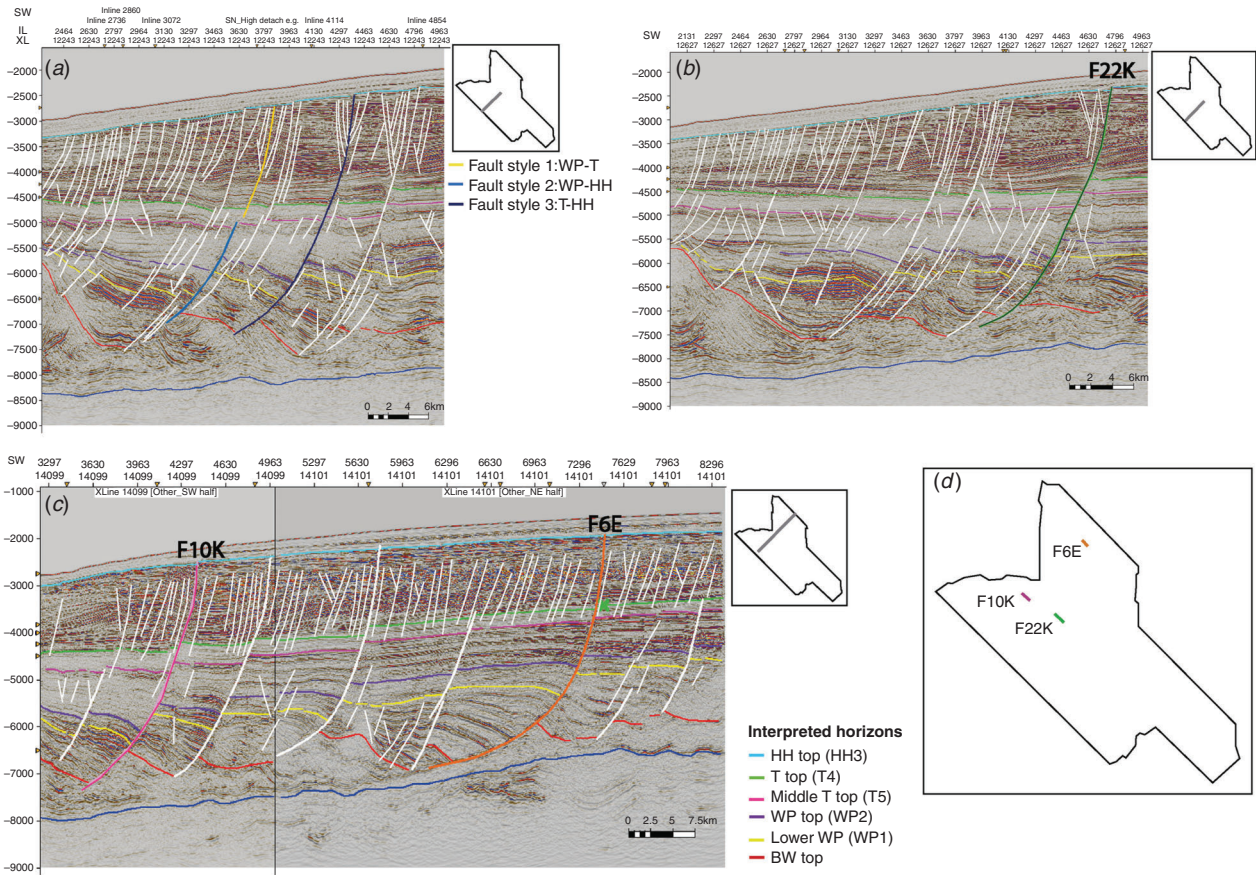

Fig. 2. (*a*) Seismic cross-line 12243 displaying an example of the geometry and offset units that characterise each fault style. (*b*) Cross-line 12627 showing the F22K fault segment that represents the Fault style 2 and evolved by one dip-linkage event. (*c*) Cross-lines 14099 and 14101 showing F10K and F6E fault segments. Both faults correspond to the Fault style 2: F10K grew by two dip-linkage events and F6E by constant growth. (*d*) Location map of F6E, F10K and F22K fault segments within the study area.

well logs from Potoroo-1 and Gnarlyknots-1A, which are the closest drilled wells to the study area (71 and 42.2 km, respectively), to map the HH, T, WP and BW supersequences tops, and seven intra-formational horizons that correlate with changes in the seismic amplitude, which also link to fluctuations in the gamma ray (GR) and sonic log (DT) values.

Kinematic analysis

We first used displacement–distance analysis (*D*–*x*) to describe the changes in along-strike displacement for mapped faults. Second, displacement–depth analysis (*D*–*z*) was employed to identify changes between horizons, where an upwards decrease in displacement represents a growth interval, an upwards increase in displacement corresponds to a dip-linkage event and an interval without changes in displacement coincides to a period of inactivity for the fault. Third, the EI was used to compare the thickness of the strata in hangingwall and footwall of faults. EI $>$ 1 represents a syn-kinematic growth in the hangingwall, and EI $=$ 1 corresponds to a period of no or little resolvable growth in the fault evolution history. We compared the EI results along fault strikes (EI−*x*) to identify fluctuations in syn-kinematic fault growth in map view (Thorsen 1963; Mansfield and Cartwright 1996; Jackson *et al.* 2017) (Fig. 1).

Results

We identified three fault styles in the study area in relation to the sedimentary record they displace. The mapped faults strike north-west to south-east (112–143°N), have a dip direction towards the south-west and their along-strike lengths vary between 1.6 and 11.5 km (Fig. 2).

Fault style 1: Cenomanian–Late Santonian

These faults constantly grew between the Cenomanian and the Late Santonian and are located throughout the study area. They exhibit a listric to planar geometry and contain rotated blocks and rollovers in their hangingwall. The kinematic analyses of these faults show that they constantly grew between the BW and top T horizons.

Fault style 2: Cenomanian–Maastrichtian

These faults grew between the Cenomanian and Maastrichtian, show a listric geometry with rollovers in their hangingwall and are well distributed across the study area. Kinematic analysis indicates three different evolution patterns: (a) constant growth, (b) three fault segments that grew by two events of dip linkage and (c) two fault segments that grew by one dip-linkage event.

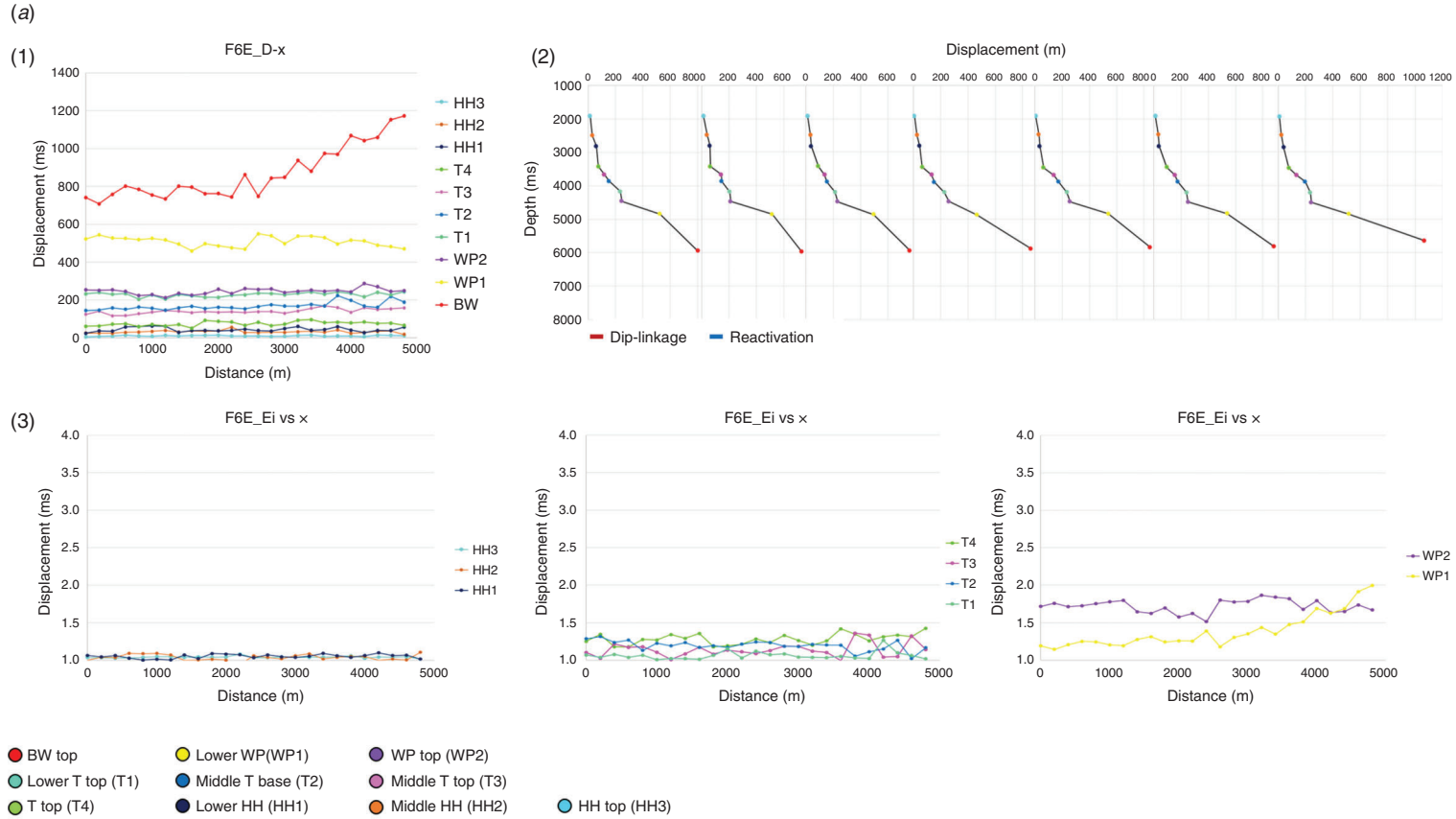

Fig. 3. Continued

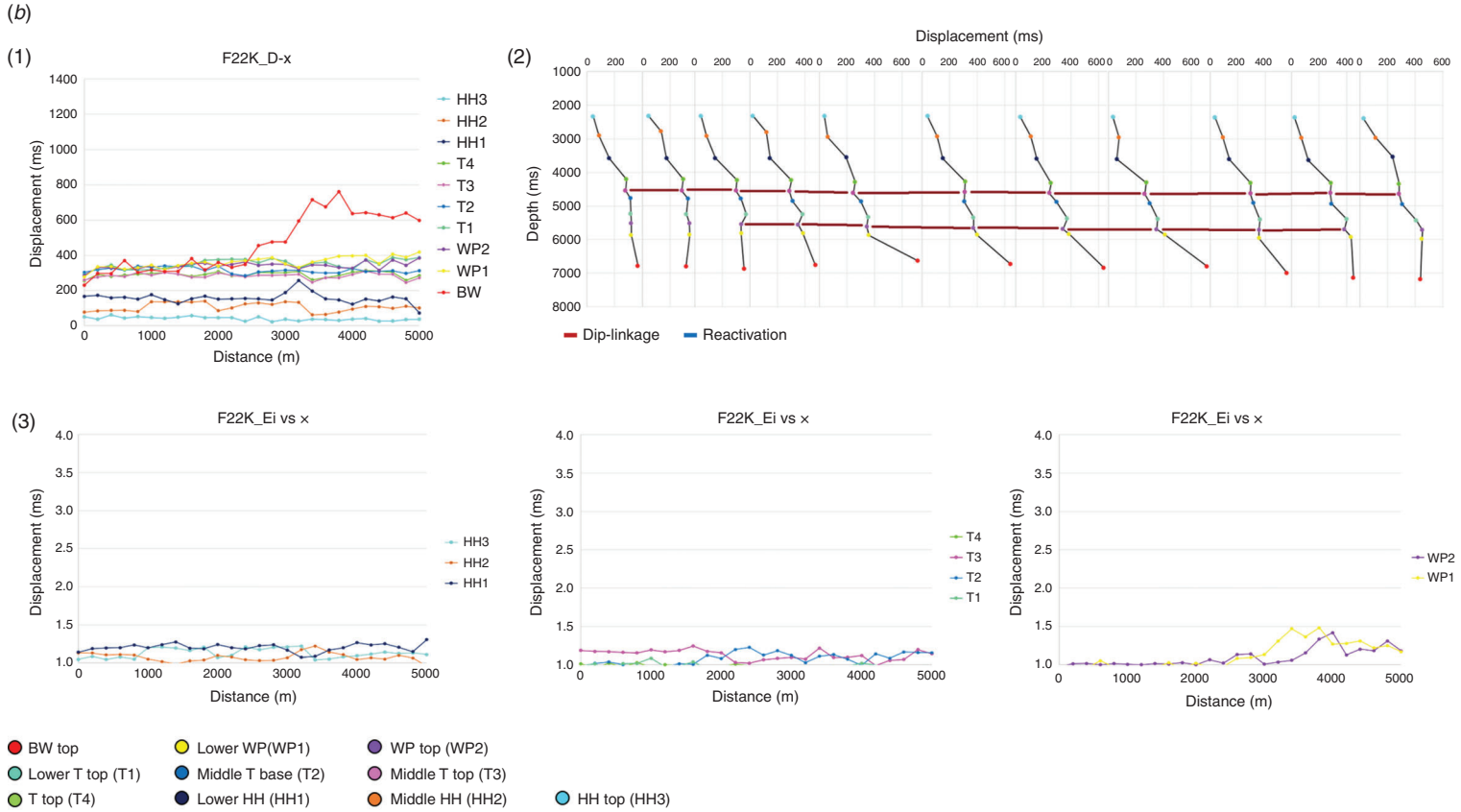

Fig. 3. Continued

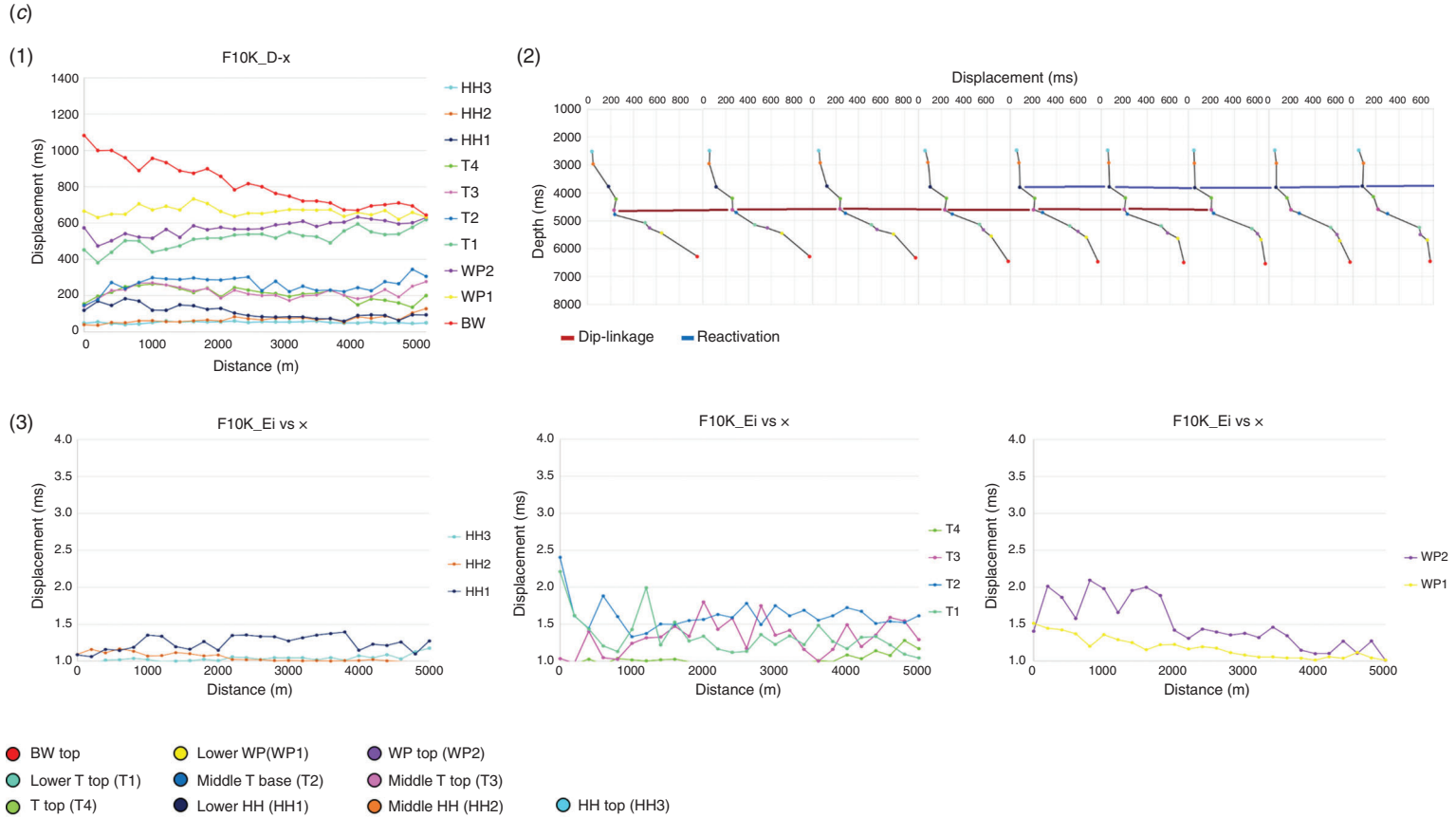

Fig. 3. Kinematic analysis: (1) *D–x*, (2) *D–z* and (3) EI—*x* of three fault segments from the fault style 2 (F6E, F22K, F10K) showing evidence to define each evolution pattern. (*a*) F6E evolved by continuous growth during the deposition of WP-HH. (*b*) F22K grew by two dip-linkage events at the lower T unit and upper T unit. The three dip-linked fault segments correspond to BW-WP top, middle T unit and HH interval. (*c*) F10K evolved by one dip-linkage event at the upper T unit. The two fault segments that were dip linked correspond to BW top to middle T top and HH interval.

The fault segments that constantly grew during the deposition of the WP and the HH are mainly located in the northern part of the study area. The *D–x* analysis of these faults shows a steady decrease in displacement between the BW top and the upper HH unit, which resembles the constant decrease in displacement from the base of WP to the top of HH at the *D–z* analysis. The EI−*x* analysis indicates that the thickest syn-kinematic interval is within the WP that gradual decrease toward the HH top.

The faults that have grown through two dip-linkage events are located at the central section of the study area. Their *D–x* analysis indicates an uneven distribution of displacement in-side view, where the top of the WP shows lower displacement values than the lower T top. Similarly, the lower T top displays lower displacement values than the T top. Both results demonstrate dip-linkage events revealed by the *D–z* analysis, where we identified an upwards increase in displacement gradient at the same periods. The EI−*x* analysis shows thicker syn-kinematic intervals at the WP interval and minimum changes in EI between the T and HH intervals.

The fault segments that evolved by one dip-linkage event are located at the central and southern sections of the study area. Their *D–x* analysis displays the highest displacement at BW top, lower WP and lower T, moderate values in the middle and T top and lower displacement values within the HH interval. In all the faults, the upper T unit shows higher displacement values at the top than the base. This result resembles the *D–z* analysis where the upper T unit represents an upwards increase in the displacement gradient that indicates a dip-linkage event (Fig. 3*a–c*).

Fault style 3: Late Santonian–Maastrichtian

These faults constantly grew between Late Santonian–Maastrichtian. They are either above Cenomanian–Late Santonian fault segments (at the north and central parts of the study area) or are detached at the upper T unit (at the south and south-eastern areas). Kinematic analysis of these faults shows that they constantly grew during the deposition of the T top and the HH upper unit.

Interpretation of results

From the seismic interpretation and the kinematic analysis, we identified three different fault styles according to the ages of sedimentary strata they displaced (Cenomanian–Late Santonian, Cenomanian–Maastrichtian and Late Santonian–Maastrichtian). These northwest-southeast strike fault segments show similar listric and listric to planar geometries and dip directions towards the south-east.

The faults segments that evolved between the Cenomanian–Late Santonian and Late Santonian–Maastrichtian periods show constant growth during their evolution history and are distributed throughout the study area.

Our results agree with earlier studies that suggest a correlation between the evolution histories of faults that grew between the BW-HH and their geographic location (Ryan *et al.* 2017). However, our results indicate that faults that show constant growth are located in the northern CSB, faults at the central area represent three fault segments that were dip linked, and the faults in the central and southeast areas evolved as two fault segments that were dip linked. In contrast to previous studies, we did not find evidence for faults that grew through reactivation during HH deposition.

Conflicts of interest

The authors declare that no conflicts of interest exist.

Declaration of funding

This research is part of a PhD project that is funded by an Australian Government Research Training Program Scholarship and the Australian Society of Exploration Geophysicists (ASEG).

References

Espurt, N., Callot, J.-P., Totterdell, J., Struckmeyer, H., and Vially, R. (2009). Interactions between continental breakup dynamics and large-scale delta system evolution: Insights from the Cretaceous Ceduna delta system, Bight Basin, Southern Australian margin. *Tectonics* **28**, TC6002. doi:10.1029/2009TC002447

Holford, S., Hillis, R., Duddy, I., Green, P., Stoker, M., Tuitt, A., Backé, G., Tassone, D., and MacDonald, J. (2011). Cenozoic post-breakup compressional deformation and exhumation of the southern Australian margin. *The APPEA Journal* **51**, 613. doi:10.1071/AJ10044

Hughes, M., Nichol, S., Przeslawski, R., Totterdell, J., Heap, A., Fellows, M., and Daniell, J. (2009). Ceduna sub-basin: Environmental summary. *Geoscience Australia* 65838 09147.

Imber, J., Childs, C., Nell, P. A. R., Walsh, J. J., Hodgetts, D., and Flint, S. (2003). Hanging wall fault kinematics and footwall collapse in listric growth fault systems. *Journal of Structural Geology* **25**, 197–208. doi:10.1016/S0191–8141(02)00034-2

Jackson, C. A.-L., Bell, R. E., Rotevatn, A., and Tvedt, A. B. M. (2017). Techniques to determine the kinematics of synsedimentary normal faults and implications for fault growth models. *Geological Society* London, Special Publications **439**, 187–217. doi:10.1144/SP439.22

King, R. C., and Backé, G. (2010). A balanced 2D structural model of the Hammerhead Delta–deepwater fold-thrust belt, Bight Basin, Australia. *Australian Journal of Earth Sciences* **57**, 1005–1012. doi:10.1080/08120099.2010.509409

MacDonald, J., Holford, S., and King, R. (2012). Structure and prospectivity of the delta-deep-water fold-thrust belt systems, Bight Basin, Australia. In 'New understanding of the Petroleum Systems of Continental Margins of the World'. (Eds N. C. Rosen *et al.*) pp. 779–816. (SEPM Society for Sedimentary Geology.) doi:10.5724/gcs.12.32.0779

Mansfield, C. S., and Cartwright, J. A. (1996). High resolution fault displacement mapping from three-dimensional seismic data: evidence for dip linkage during fault growth. *Journal of Structural Geology* **18**, 249–263. doi:10.1016/S0191–8141(96)80048-4

McClay, K., Dooley, T., and Zamora, G. (2003). Analogue models of delta systems above ductile substrates. *Geological Society* London, Special Publications **216**, 411–428. doi:10.1144/GSL.SP.2003.216.01.27

Reynolds, S., Hillis, R., and Paraschivoiu, E. (2003). In situ stress field, fault reactivation and seal integrity in the Bight Basin, South Australia. *Exploration Geophysics* **34**, 174–181. doi:10.1071/EG03174

Robson, A. G., King, R. C., and Holford, S. P. (2017). Structural evolution of a gravitationally detached normal fault array: analysis of 3D seismic data from the Ceduna Sub-Basin, Great Australian Bight. *Basin Research* **29**, 605–624. doi:10.1111/bre.12191

Ryan, L., Magee, C., and Jackson, C. A.-L. (2017). The kinematics of normal faults in the Ceduna Subbasin, offshore southern Australia: Implications for hydrocarbon trapping in a frontier basin. *Bulletin* **101**, 321–341. doi:10.1306/08051615234

Tapley, D., Mee, B. C., King, S. J., Davis, R. C., and Leischner, K. R. (2005). Petroleum potential of the Ceduna Sub-Basin: Impact of Gnarlyknots–1A. *The APPEA Journal* **45**, 365. doi:10.1071/AJ04029

Thorsen, C. E. (1963). Age of growth faulting in Southeast Louisiana. *AAPG, Gulf Coast Association of Geological Societies Transactions* **13**, 103–110.

Totterdell, J., and Mitchell, C. (2009). Bight Basin Geological Sampling and Seepage Survey. RV Southern Surveyor SS01/2007. Geoscience Australia Record 2009/24.

Totterdell, J. M., Struckmeyer, H. I. M., Boreham, C. J., Mitchell, C. H., Monteil, E., and Bradshaw, B. E. (2008). Mid–Late Cretaceous organic-rich rocks from the eastern Bight Basin: implications for prospectivity. In 'PESA Eastern Australian Basins Symposium III, Sydney, 14–17 September 2008'. pp. 137–160.

Walsh, J. J., and Watterson, J. (1991). Geometric and kinematic coherence and scale effects in normal fault systems. *Geological Society* London, Special Publications **56**, 193–203. doi:10.1144/GSL.SP.1991.056.01.13

The authors

Monica Jimenez is a PhD candidate at the Australian School of Petroleum and Energy Resources, University of Adelaide. She graduated with BSc-Hons (2007) from the National University of Colombia and MSc (2012) from the Royal Holloway. She has 7 years of experience in the oil and gas industry, working on seismic interpretation, structural and static modelling. Her research is focused on the fault evolution in deltaic settings and its implications for petroleum systems. Memberships: AAPG, ASEG, PESA and SACOME. Email: monica.jimenezlloreda@adelaide.edu.au

Simon P. Holford is an associate professor of Petroleum Geoscience at the University of Adelaide's Australian School of Petroleum and Energy Resources. Simon has published ~90 papers on the prospectivity and tectonics of rifted margins, petroleum geomechanics and magmatism in basins. Simon has successfully supervised ~10 PhD students and ~50 Honours and Masters Students. Simon has a PhD from the University of Birmingham and a BSc (Hons) from the Keele University. Simon has won multiple awards, including Best Paper prizes at APPEA 2012 and AEGC 2019 and the Geological Society of Australia's Walter Howchin and ES Hills medals. Email: simon.holford@adelaide.edu.au

Rosalind C. King is an associate professor and head of the Department of Earth Sciences, University of Adelaide. She graduated with a BSc-Hons (2001) and a PhD (2006) from the University of Liverpool. Her research interests include structural geology, deepwater fold-thrust belts, detachments, fault and fracture mechanics, fault controlled permeability and petroleum geomechanics.
Email: rosalind.king@adelaide.edu.au

Mark A. Bunch is a senior lecturer in Petroleum Geoscience at the Australian School of Petroleum and Energy Resources (ASPER), University of Adelaide. He graduated with a BSc-Hons (2000) from the Durham University, MSc (2001) and PhD (2006) from the University of Birmingham. His research interests include formation evaluation and seismic geomorphology. Memberships: AAPG, ASEG and PESA.
Email: mark.bunch@adelaide.edu.au

How do detachment properties influence the kinematics of normal growth faults? Insights from 3D seismic reflection data from the Ceduna sub-basin

Monica Jimenez
ASPER- University of Adelaide
Santos building, University of Adelaide, Adelaide SA (5001)
monica.jimenezlloreda@adelaide.edu.au

Simon Holford
ASPER- University of Adelaide
Santos building, University of Adelaide, Adelaide SA (5001)
simon.holford@adelaide.edu.au

Rosalind King
Earth Sciences – University of Adelaide
Mawson building – University of Adelaide, Adelaide SA (5001)
rosalind.king@adelaide.edu.au

Mark Bunch
ASPER- University of Adelaide
Santos building, University of Adelaide, Adelaide SA (5001)
mark.bunch@adelaide.edu.au

SUMMARY

The growth of gravity-driven normal faults exerts a critical control on multiple elements and processes of the petroleum system. However, there is still a poor understanding of the interactions between the properties of detachment layers and the evolution of growth faults in delta systems underlain by mechanically-weak detachments. This study is focused on the White Pointer Delta system in the Ceduna sub-basin, which detaches on an overpressure shale layer deposited during the Albian-Cenomanian. Using the Ceduna 3D seismic survey, we present evidence of how changes in thickness, dip angle and geometry of the Albian-Cenomanian detachment influences the kinematics of overlying, detachment-linked growth faults. In the proximal region of the study, the detachment is relatively thin (0.2 to 0.5 s) with basal dips of 5°-10°. Normal faults located at this region, show constant growth during the Cenomanian-Maastrichtian. In central and distal areas of the seismic survey, the thicker detachment has basal dips <2° with thrust faulting and 'dome' structures. Faults at this area grew by dip-linkage. Our study shows that a more consistent and active evacuation of the detachment resulted in non-interrupted fault growth, while a thicker and more complex detachment can outcome in minimum accumulation that caused irregular fault growth.

Key words: Delta systems, growth normal faults, detachment, fault evolution.

INTRODUCTION

The kinematics of gravity-driven normal faults in deltaic settings exert strong controls on the deposition of reservoir rocks, the formation of trapping structures and the development of fluid flow paths for hydrocarbons. The growth of such faults is controlled by aspects including sediment loading, subsidence and the characteristics of any underlying detachment layer (McClay et al., 2003; King and Backé, 2010; MacDonald et al., 2012). A large body of work has advanced the knowledge of the kinematic analysis of normal fault systems that do not feature a mechanically weak detachment layer (such as is formed by an interval of salt or overpressured shale; Walsh and Watterson, 1991; Imber et al., 2003). However, the same degree of attention has not been paid to documenting the kinematic development of gravity-driven normal faults in sedimentary basins that contain delta systems underlaying a detachment layer. As such, there is little information available concerning the relationship between such faults and the characteristics of their associated underlying detachment (e.g. thickness under the fault segments, changes in lithology and 'dome' like and thrust fault structures) and the evolution style of growth faults.

This study is focused on the Ceduna Sub-basin (CSB), the main depocentre within the Great Australian Bight (GAB), which contains up to 15 km of Cretaceous strata. The basin formed after the beginning of rifting between Australia and Antarctica during the middle Jurassic, with major subsidence continuing until the Late Santonian when the passive margin was established (Sayers et al., 2001; Totterdell and Mitchell, 2009, Holford et al., 2011). The CSB stratigraphy comprises two stacked delta systems: the older Cenomanian-age White Pointer Delta, and the younger Hammerhead Delta, which accumulated from the Late Santonian-Maastrichtian. Both delta systems exhibit listric growth faults in the delta tops and fold-thrust belts at the delta toes. In both cases, growth faults detach on overpressured shale layers (the Albian-Cenomanian Blue Whale Supersequence and the Late Santonian Tiger Supersequence respectively) (Totterdell and Krassay, 2003, MacDonald et al., 2012).

Large scale delta systems in passive margins typically approximate the characteristics and behaviour of a critical-taper wedge model, where a weak detachment such as salt or overpressured shale, slides basinwards due to the load of overlying sediments. This results in normal growth faults at the delta top that are linked to deep water fold-trust belts at the delta toe (Stewart, 1996, Alzaga-Ruiz et al., 2009; Espurt et al., 2009; Morley et al., 2011; Sapin et al., 2012). Analogue models suggest that the gravity sliding of the detachment layer depends on the net balance between sedimentation and horizontal extension rates (Bally et al., 1981; Vendeville and Cobbold, 1988, McClay et al., 2003). There are several examples of delta systems where growth faults have been proven to form effective trapping structures for hydrocarbon accumulation, such as those of the Niger Delta, the Gulf of Mexico, and in offshore Angola. Some studies have also suggested that the GAB basin features similar structural characteristics that define such prospective delta systems elsewhere (King and Backé, 2010; MacDonald et al., 2012).

We have used the Ceduna 3D seismic survey to interpret multiple growth faults in the CSB and ten different horizons including the top and base of the Blue Whale detachment layer.

We generated structural and thickness maps to characterize the White Pointer delta system and its detachment layer to identify local changes in dip angle, dip direction and thickness throughout the study area. Our analysis shows that uniform detachment thickness, consistent seismic amplitude expression and lack of internal structures (e.g. folds, dome'-like features and folds) in the proximal section (northern region of the study area) are features associated with fault segments that grew continuously during the Cenomanian-Maastrichtian, throughout the period of accumulation for both major delta systems. A thicker (greater than 0.5 s two-way time; TWT) underlying Blue Whale detachment interval with more complex features (e.g. thrust faults and 'dome'-like features) is associated with Cenomanian-Maastrichtian fault segments with more complex growth histories encompassing dip-linkage and reactivation. Our findings highlight the importance of constraining detachment morphology when investigating the growth history of normal faults in deltaic settings.

METHODOLOGY

To evaluate the influence that the Blue Whale detachment characteristics (lithology, thickness and content of internal structures such as folds and thrust faults) have on the kinematics of overlying detached normal faults, we correlated ten well tops picked using wireline log data acquired at the Potoroo-1 and Gnarlyknots-1A wildcat wells (71 km and 42.2 km to the north of the study area respectively) to seismic reflector horizons evident in regional 2D seismic lines. The main seismic horizons correspond to the tops of: the Hammerhead (HH) Supersequence that were deposited from the Late Santonian-Maastrichtian, the Tiger (T) Supersequence that accumulated from the Turonian-Late Santonian, the White Pointer (WP) Supersequence that was deposited during the Cenomanian, and the top and base of the Blue Whale (BW) Supersequence – the major detachment unit – that accumulated from the Albian-Cenomanian. The six additional seismic horizons are intra-formational and represent changes in the sonic (DT) and gamma-ray (GR) wireline logs that correlate with distinct seismic reflection response. Subsequently, we interpreted the Ceduna 3D MSS reflection seismic survey (~12,200 km^2) in TWT, mapping these eleven horizons and 520 fault segments that grew simultaneously with the deposition of the Cenomanian-Late Santonian, Cenomanian-Maastrichtian or the Late Santonian-Maastrichtian intervals. In this extended abstract, we focus our analysis on the influence of the Albian-Cenomanian detachment on the Cenomanian-Maastrichtian fault segments.

We generated time-structure maps (in TWT) of the tops of the main supersequences and then we computed thickness maps from different intervals to recognize changes in the stratal architecture. In the case of the Blue Whale detachment layer, we used the seismic data, thickness and structural maps to define possible structures (e.g. faults, 'dome'-like features and folds), changes in thickness and seismic amplitude variations that then can be correlated to the results of fault kinematic analyses (e.g. Displacement-distance, Displacement-depth, and Expansion Index). Finally, we compared our interpretation of the Blue Whale detachment thickness variations, presence of thrust and folds, and local changes in lithology with the detailed kinematic analyses of three fault segments that offset the Cenomanian-Maastrichtian sedimentary record, as described by Jimenez et al., (2021) (F6E, F22K and F10K).

RESULTS

Blue Whale detachment layer characteristics

Our mapping indicates that the top surface of the Blue Whale detachment unit is characterised by a regional dip angle of about 5 to 10 degrees towards the south-west. The Blue Whale exhibits its shallowest TWTs in the north, south-west and far south-southeast (between 5.3 to 6.5 s) and appears deepest in the central and southern areas (7.3 to 8 s). We observed local-scale changes in depth and dip angle that are related either to fault segments that displace the top detachment surface between 0.04 and 1.2 seconds (around 35 to 1050 meters), or small 'dome'-like structures that we interpret to be the result of a vertical stack of detachment unit material that did not evacuate effectively towards the ocean basin.

The basal surface of the Blue Whale detachment exhibits a regional dip angle between 5 and 12 degrees towards the south-west. The dip shallows towards the south and south-east areas, where the base surface is almost horizontal (less than 2 degrees). The base of the detachment presents fewer local changes in dip angle and depth in comparison to the top of the detachment, and in most cases the local-scale variations are associated with underlying structures. For instance, in the south-east of the study area, the base of the Blue Whale unit mimics an antiformal structure at the basement level forming a dome'-like structure at the detachment layer, where several planar to listric faults detach (Figure 1 a and b).

Variations in thickness of the Blue Whale detachment are observed with thinnest sections in the north and thicker intervals in the south, south-west and east. Locally, 'dome' and 'depression'-like structures strongly change the detachment thickness in certain sections of the study area. We believe that the 'dome'-like structures (especially those located in the south and south-east regions) may have inhibited accumulation of the White Pointer and Tiger Supersequences, resulting in thinner overlying layers. In contrast, the 'depression'-like structures are associated with a thickening of the Blue Whale Supersequence that do not seem to have affected deposition of the overlying White Pointer and Tiger Supersequence intervals above. (Figure 2).

Based on our seismic interpretation we also identified strong changes in the seismic amplitude within the Blue Whale detachment layer. Whilst the lack of direct lithological data prevented confirmation of the causes of such changes, we believe that they may be related to variations in lithology, which are more evident towards the central and southern regions of the study area. We also interpreted thrust faults inside the Blue Whale detachment layer associated with the vertical stacking of the detachment which may explain its local thickening in the central and south to south-eastern areas.

Based on our observations of the Blue Whale detachment, we sub-divided the study area into three main regions:

(a) A northern region where the Blue Whale detachment unit has a TWT thickness of less than 0.5 s and dips between 5 to 10 degrees. The seismic facies suggest uniform lithology within the detachment and lack of thrust faults or 'dome'-like features.

(b) A central region where the Blue Whale detachment unit has a TWT thickness of between 0.65 and 0.7 s and dips

between 5 and 10 degrees. There is evidence for thrust fault ing and variability in the seismic amplitude mostly in the distal region. Locally, there are several 'dome'-like structures, particularly to the western section of the study area. These have altered the dip angle and thickness of the detachment unit.

(c) To the south and south-east, the BW detachment shows strong changes in seismic amplitude and structural complexity that includes thrust faulting, 'dome'-like features, and a progressive flattening in the dip angle towards the south-east (e.g., from 10 at the south-west and south to 2 at the south-east). To the south-east, we identified a large domal shape that mimics an antiformal structure in the underlying basement.

Correspondence between detachment characteristics and faults kinematics

A recent study of fault growth by Jimenez et al., (2021) used the Ceduna 3D MSS seismic survey and kinematic analysis techniques such as Displacement-Distance (D-x), Displacement-depth (D-z) and Expansion Index (EI), to demonstrate that faults offsetting the Cenomanian-Maastrichtian sedimentary record evolved by three different evolutionary styles. Examples demonstrating these three different styles are faults F6E in the north, F22K in the centre and F10K in the south of the study area. Fault F6E exhibits a history of constant growth during deposition of the Cenomanian-Maastrichtian interval. By contrast, F22K grew by two dip-linkage events in the lower and upper Tiger intervals (T1 and T4) respectively. F10K exhibits one dip-linkage event in the upper Tiger interval (T4) with possible evidence for reactivation at the middle Hammerhead unit (HH2) along central and eastern sections of the fault, along strike. Here we compare the growth of these faults with the characteristics of the underlying Blue Whale detachment.

Fault F6E in the north exhibits a listric geometry along-strike with a pronounced rollover in the hangingwall. The kinematic analyses show that the fault evolved by constant growth, reaching its maximum length during the Cenomanian. We suggest that this might be related to a strong basinwards evacuation of the Blue Whale detachment unit layer that left behind a thinner layer between 0.25 and 0.3s TWT in the northern section of the study area. In addition, it is likely that the lack of thrust and 'dome'-like structures within the Blue Whale detachment unit imply that no lateral barrier developed that otherwise would have inhibited constant growth and slide of the fault hangingwall segment during the deposition of the Cenomanian-Maastrichtian units. (Figure 3a).

In the central area, fault F22K exhibits a listric geometry and a rollover in the hangingwall. Kinematic analyses suggest two dip-linkage events during its growth (at the base and top intervals of the Tiger Supersequence), with an older fault segment from the Cenomanian dip-linking with a younger Turonian-Coniacian fault segment. Later, this Cenomanian-Coniacian fault nucleated and dip-linked again with a younger Late Santonian-Maastrichtian fault segment. We infer that the thicker detachment layer (between 0.5 and 0.6s), with thrust structures and possible variations in lithology might have affected the basinward gravity sliding of the detachment, resulting in a fault segment that grew by three discrete increments of growth. (Figure 3b)

To the south, the F10K fault segment exhibits a listric geometry and a gentler rollover in comparison to the other two faults. The kinematic analyses of this fault imply that it evolved by the dip-linkage between an older Cenomanian-Late Santonian fault segment and a younger Late Santonian-Maastrichtian fault segment. In this case, the fault also shows a reactivation event during the middle Hammerhead interval (HH2) along the eastern and central sections of the fault. 3D seismic survey data show strong occurrence of thrust and dome'-like structures in the Blue Whale detachment unit with pronounced changes in seismic amplitude. It may be the case that the development of thrust and 'dome'-like features during the early evolution of the fault between the Cenomanian-Late Santonian, resulted in minimal accumulation of the upper Tiger unit and subsequent nucleation of the fault in the Late Santonian. (Figure 3c).

CONCLUSIONS

Our analyses show that there is a strong correlation between the characteristics of the Blue Whale detachment layer and the evolutionary history of Cenomanian-Maastrichtian fault segments in the Ceduna sub-basin. For example, faults that exhibit simpler, constant growth histories appear to correspond with parts of the basin where the Blue Whale detachment unit is relatively consistent, whilst regions where the detachment has a more complex morphology and internal structure are associated with faults that have a more complex kinematic history.

ACKNOWLEDGMENTS

This research is part of a PhD project that is funded by an Australian Government Research Training Program Scholarship and the Australian Society of Exploration Geophysicists (ASEG).

REFERENCES

Alzaga-Ruiz, H., Granjeon, D., Lopez, M., Seranne, M., Roure, F., 2009. Gravitational collapse and Neogene sediment transfer across the western margin of the Gulf of Mexico: Insights from numerical models. Tectonophysics 470, 21–41. https://doi.org/10.1016/j.tecto.2008.06.017

Bally, A.W., Bernoulli, D., Davis, G.A., Montadert, L., 1981. Listric Normal Faults. Oceanology. Acta 16.

Espurt, N., Callot, J.-P., Totterdell, J., Struckmeyer, H., Vially, R., 2009. Interactions between continental breakup dynamics and large-scale delta system evolution: Insights from the Cretaceous Ceduna delta system, Bight Basin, Southern Australian margin: Continental breakup and delta system. Tectonics, TC6002 28. https://doi.org/10.1029/2009TC002447

Holford, S., Hillis, R., Duddy, I., Green, P., Stoker, M., Tuitt, A., Backé, G., Tassone, D., MacDonald, J., 2011. Cenozoic post-breakup compressional deformation and exhumation of the southern Australian margin. APPEA J. 51, 613. https://doi.org/10.1071/AJ10044

Imber, J., Childs, C., Nell, P.A.R., Walsh, J.J., Hodgetts, D., Flint, S., 2003. Hanging wall fault kinematics and footwall collapse in listric growth fault systems. Journal Structural Geology. 25, 197–208. https://doi.org/10.1016/S0191-8141(02)00034-2

Jimenez, M., Holford, S., King, R., Bunch, M., 2021. Controls on gravity-driven normal fault geometry and growth in stacked deltaic settings: a case study from the Ceduna Sub-basin. APPEA 61.pp. na. https://doi.org/10.1071/AJ20073

King, R.C., Backé, G., 2010. A balanced 2D structural model of the Hammerhead Delta–Deepwater Fold-Thrust Belt, Bight Basin, Australia. Aust. J. Earth Sci. 57, 1005–1012. https://doi.org/10.1080/08120099.2010.509409

MacDonald, J., Holford, S., King, R., 2012. Structure and Prospectivity of the Delta-Deep-Water Fold-Thrust Belt Systems, Bight Basin, Australia, in: New Understanding of the Petroleum Systems of Continental Margins of the World: 32nd Annual. Society of Economic palaeontologist and mineralogists, pp. 779–816.

McClay, K., Dooley, T., Zamora, G., 2003. Analogue models of delta systems above ductile substrates. Geological Society of London. Special Publication.216,411–428. https://doi.org/10.1144/GSL.SP.2003.216.01.27

Morley, C.K., King, R., Hillis, R., Tingay, M., Backe, G., 2011. Deepwater fold and thrust belt classification, tectonics, structure and hydrocarbon prospectivity: A review. Earth-Science.Rev.104,41–91. ttps://doi.org/10.1016/j.earscirev.2010.09.010

Sapin, F., Ringenbach, J.-C., Rives, T., Pubellier, M., 2012. Counter-regional normal faults in shale-dominated deltas: Origin, mechanism and evolution. Marine and PEtroleum Geology.37,121–128. https://doi.org/10.1016/j.marpetgeo.2012.05.001

Sayers, J., Symonds, P.A., Direen, N.G., Bernardel, G., 2001. Nature of the continent-ocean transition on the non-volcanic rifted margin of the central Great Australian Bight. Geological Society of London. Special Publication. 187, 51–76.

Stewart, S.A., 1996. Influence of detachment layer thickness on style of thin-skinned shortening. Journal Structural. Geology. 18,1271–1274. https://doi.org/10.1016/S0191-8141(96)00052-1

Totterdell, J., Mitchell, C., 2009. Bight Basin Geological Sampling and Seepage Survey. Geoscience Australia.

Totterdell, J.M., Krassay, A.A., 2003. The role of shale deformation and growth faulting in the Late Cretaceous evolution of the Bight Basin, offshore southern Australia. Geological Society of London. Special Publication. 216, 429–442. https://doi.org/10.1144/GSL.SP.2003.216.01.28

Vendeville, B., Cobbold, P., 1988. How normal faulting and sedimentation interact to produce listric fault profiles and stratigraphic wedges. Journal Structural Geology. 10, 649–659.

Walsh, J.J., Watterson, J., 1991. Geometric and kinematic coherence and scale effects in normal fault systems. Geological Society of London. Special Publication. 56, 193–203. https://doi.org/10.1144/GSL.SP.1991.056.01.13

Figures

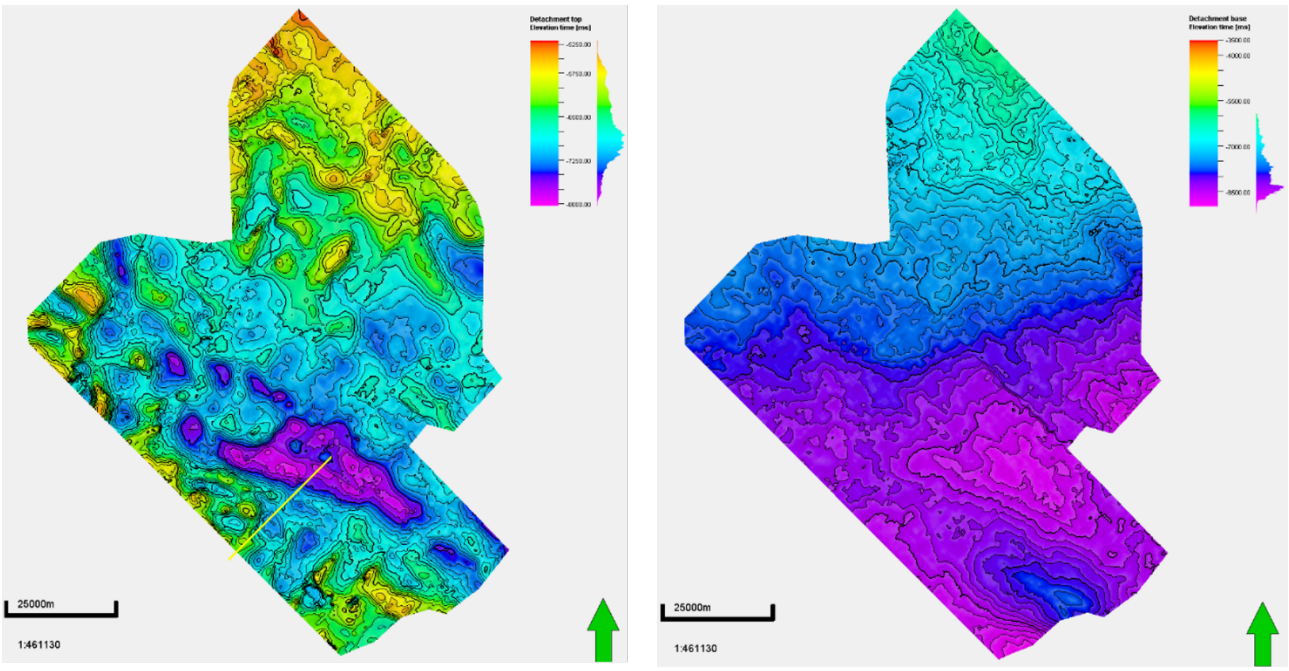

Figure 1. (a) Structural map of the BW top and (b) BW base. Both maps present the contours every 100 ms.

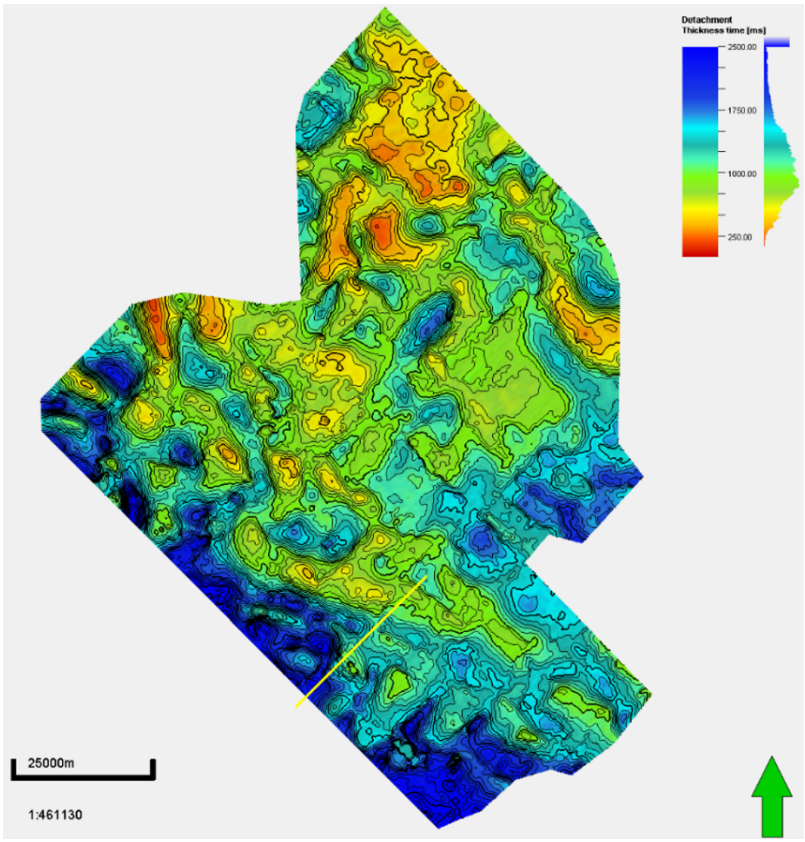

Figure 2. Thickness map of the BW detachment layer. Contours every 100 ms.

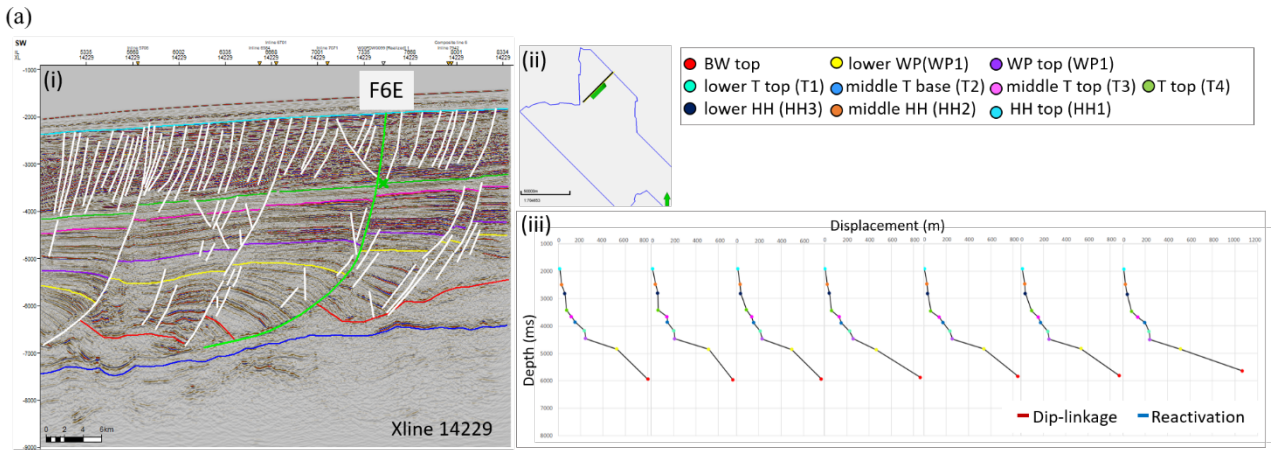

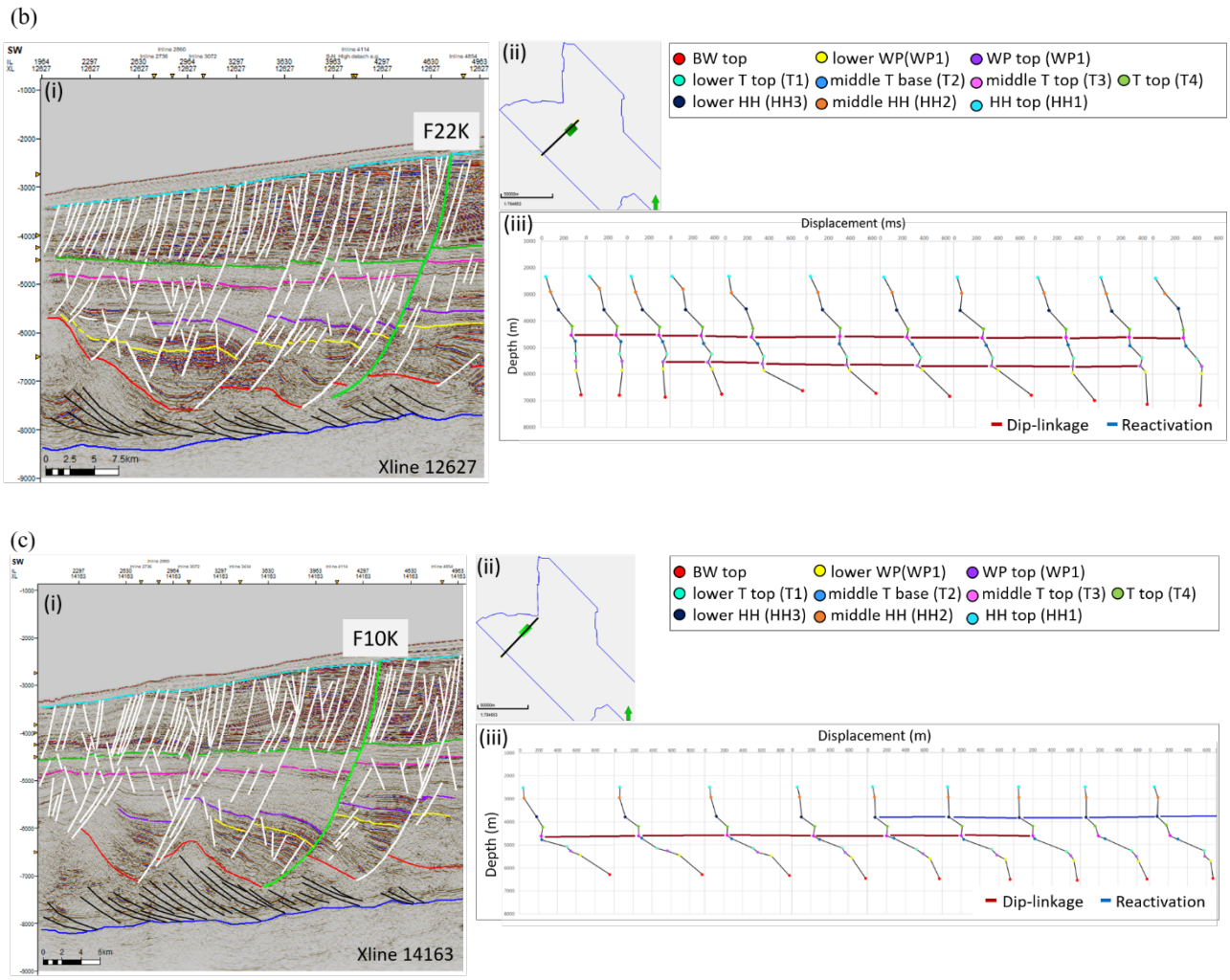

Figure 3: (a) Example of the F6E fault segment showing (i) a seismic cross-line with the interpreted fault segment and the interpretation of the BW detachment, (ii) localization map with F6E and the cross-line, (iii) Displacement-distance kinematic analysis showing that the F6E constantly grew between the BW and HH. (b) Example of the F22K fault segment showing (i) a seismic cross-line with the interpreted fault segment and the interpretation of the BW detachment, (ii) localization map with F22K and the cross-line, (iii) Displacement-distance kinematic analysis presenting two dip-linkage events at the lower and upper Tiger units. (c) Example of the F10K fault segment showing (i) a seismic cross-line with the interpreted fault segment and the interpretation of the BW detachment, (ii) localization map with F10K and the cross-line, (iii) Displacement-distance kinematic analysis showing one dip-linkage event at the upper Tiger and a reactivation event at the central and east sections of the fault along strike. For more information about the kinematic analysis for these faults refer to Jimenez et al., (2021) – APPEA extender abstract.